

CHEMICAL TRANSFORMATION OF NANOCRYSTALS
TOWARD ENERGY APPLICATIONS

A Dissertation

Presented to the Faculty of the Graduate School

of Cornell University

In Partial Fulfillment of the Requirements for the Degree of

Doctor of Philosophy

by

Don-Hyung Ha

January 2015

© 2015 Don-Hyung Ha

CHEMICAL TRANSFORMATION OF NANOCRYSTALS
TOWARD ENERGY APPLICATIONS

Don-Hyung Ha

Cornell University 2015

Chemical transformations of as-synthesized nanocrystals (NCs) are an emerging and powerful method to tailor the composition and morphology of NCs. Nanosynthetic chemistry has centered on creating new NCs using these transformations. However, beyond works employing empirical qualitative analysis, few works have addressed the underlying atomic mechanisms for these transformations. Works using chemical transformations of NCs for applications are also an under-studied field. This dissertation spans from fundamental understandings of the atomic structural evolutions and mechanisms in chemical transformations for NCs, to use of these methods to create and characterize new structures, to the final “applied” stage of device integration of these chemically transformed materials.

To advance the mechanistic understanding of chemical transformations of NCs and to develop new characterization methodologies, several analytic tools are used in combination to access unique and redundant information. Specifically, x-ray absorption spectroscopy (XAS), transmission electron microscopy, x-ray diffraction, and superconducting quantum interference device characterization, are implemented to investigate several chemical transformation systems and nanoscale behaviors. The materials research findings from these investigations include: 1) In the nanoscale

Kirkendall effect it was discovered that a two-step diffusion process is involved due to a crystal-phase-dependent diffusivities, that results in a switching of the favorable diffusion species that leads to NC hollowing during the transformation from ϵ -Co to Co_2P NC.; 2) The use of tri-*n*-octylphosphine ligands to promote stabilization and coordination in Ni NC synthesis can lead to undesired phosphorus doping. The phosphorus atoms are preferentially located on the Ni fcc lattice as substitutional dopants.; 3) By utilizing XAS, a structural characterization method is developed to elucidate and define distinct crystalline and amorphous structures in NC materials.; 4) During the phase transition from NC ϵ -Co to CoO and Co_3O_4 the oxygen inward-diffusion is led by an indirect exchange-mechanism through interstitial O and vacancies of type I Co sites, and the lattice orientations during the transformation show preferential orderings after the single crystalline ϵ -Co NCs are transformed to polycrystalline CoO and Co_3O_4 NCs. 5) Through cation exchange, a dual interface formation in NCs is demonstrated by creating epitaxial heterostructures within spherical NCs. In addition, this heterostructured NC demonstrates that ion diffusion generated by a cation exchange reaction can initiate a solid-solid phase transition, and tune the phase of NCs.

To engineer the nanomaterials for energy devices, a simple and robust method is developed to fabricate carbon-free and polymer-free, lightweight colloidal films for lithium-ion battery electrodes through the chemical transformation from Co to Co_3O_4 . The lack of additives can lead to enhancements in battery performance. By adapting the electrophoretic deposition method, NCs assemble on a current collector showing superior mechanical stability when compared to films fabricated by conventional

battery-making methods with binders. Due to the absence of additive materials, this method can provide a promising template system to investigate the physical mechanisms and understand the reactions during lithiation/delithiation steps. Furthermore, this additive free NC film provides opportunities to utilize colloidal NCs for battery electrodes in a simple and robust manufacturing process.

To My Family

ACKNOWLEDGMENTS

First I would like to express my appreciation to my advisor, Professor Richard D. Robinson, for his encouragement and support throughout my graduate career. He has given me opportunities through which I have grown as an independent researcher, and for which I am immensely grateful.

I would also like to thank Professor Frank DiSalvo and Professor Richard Hennig for their helpful comments and support as a thesis committee member. In addition, I would like to thank my lab mates and collaborators for their fruitful discussions and help.

I am beyond grateful for my parents and brother, my biggest supporters, who taught me that hard work can make dreams become reality.

Finally I would like to thank my wife Hyo Jung for all of her encouragement, help, support, and love to allow me to complete my Ph.D.

TABLE OF CONTENTS

ACKNOWLEDGMENTS	vii
TABLE OF CONTENTS	viii
LIST OF FIGURES	xii
LIST OF TABLES	xvii
1 INTRODUCTION.....	1
1.1 Colloidal Nanocrystals and their Synthesis.....	1
1.2 Chemical Transformation of Nanocrystals.....	4
1.2.1 Classes of Chemical Transformations of Nanocrystals.....	4
1.2.2 XAS Characterization.....	14
1.3 Chemical Transformation of NCs for Energy Applications.....	19
1.3.1 Colloidal NCs for Battery Applications	19
1.3.2 Chemical Transformation of NCs for Battery	20
1.4 References	22
2 The Structural Evolution and Diffusion during the Chemical Transformation from Cobalt to Cobalt Phosphide Nanoparticles	28
2.1 Abstract.....	28
2.2 Introduction	29

2.3	Methods	34
2.3.1	Synthesis and Characterizations	34
2.3.2	Calculation of Diffusion Activation Barriers.....	39
2.4	Results.....	42
2.5	Discussion.....	59
2.6	Conclusion.....	67
2.7	References	70
3	Unintended Phosphorus Doping of Nickel Nanoparticles during Synthesis with TOP: A Discovery through Structural Analysis	104
3.1	Abstract.....	104
3.2	Introduction	105
3.3	Results.....	108
3.4	Discussion.....	129
3.5	Conclusion.....	135
3.6	References	136
4	Defining Crystalline/Amorphous Phases of Nanoparticles through X-ray Absorption Spectroscopy and X-ray Diffraction: The Case of Nickel Phosphide.....	168
4.1	Abstract.....	168
4.2	Introduction	169
4.3	Methods	173

4.4	Results.....	174
4.5	Discussion.....	193
4.6	Conclusion.....	197
4.7	References	199
5	The Oxidation of Cobalt Nanoparticles into Kirkendall-Hollowed CoO and Co ₃ O ₄ : the Diffusion Mechanisms and Atomic Structural Transformations	226
5.1	Abstract.....	226
5.2	Introduction	227
5.3	Methods	230
5.4	Results and Discussion	235
5.5	Conclusion.....	252
5.6	References	254
6	The Interplay between Cation Diffusion and Strain to Induce Solid-Solid Phase Transformations in 2D Heterostructured Nanocrystals	274
6.1	Abstract.....	274
6.2	Introduction	275
6.3	Results.....	278
6.4	Discussion.....	300
6.5	Methods	302
6.6	References	309

7	Binder-free and Carbon-free Nanoparticle Batteries: A Method for Nanoparticle Electrodes without Polymeric Binders or Carbon Black...	339
7.1	Abstract.....	339
7.2	Introduction	340
7.3	Results and Discussion	346
7.4	Conclusion.....	362
7.5	References	364
8	CONCLUSIONS AND OUTLOOK	377
8.1	Chemical Transformation of NCs through Redox Addition	377
8.2	Heterostructured NCs through Cation Exchange	382
8.3	Additive-Free NC Film for Battery Electrodes.....	385

LIST OF FIGURES

Figure 1.1 (A) Schematic diagrams of energy vs. density of states comparing metal and semiconductors across bulk, nanoscale, and atomic size regimes. (B) Schematic diagram of density of states vs. energy showing one idealized band of a semiconductor as a function of its dimension. ¹	2
Figure 1.2(A) Schematics of the stages of nucleation and growth for the synthesis of monodisperse NCs in the framework of the La Mer model. (B) A diagram of an apparatus employed in the synthesis of monodisperse NC samples. ⁵	3
Figure 1.3 Categories of chemical transformation pathways in nanocrystals.....	5
Figure 1.4 Redox addition reactions and accompanying nanoscale Kirkendall effect. .	8
Figure 1.5 TEM images and corresponding schematics of cation exchange reactions in NCs.	11
Figure 1.6 Schematics and corresponding TEM images during the anion exchange reaction.	13
Figure 1.7 Typical raw absorption coefficient data and its Fourier-transformed k-weighted EXAFS and simulated fitting result.	16
Figure 1.8 TEM images and battery cycling performance of Sn-Ge nanorods. ⁶⁶	21
Figure 2.1 The evolutional schematics of transition from cobalt to cobalt phosphide nanocrystals.....	32

Figure 2.2 TEM images of the samples A–F (top) and corresponding crystal structures (bottom).	44
Figure 2.3 X-ray diffraction patterns of samples from A to F. ϵ -Co, Co ₂ P and CoP crystal phase matched well with sample A, D, and F respectively.	46
Figure 2.4 Fourier-transformed <i>k</i> -weighted EXAFS data and simulated fitting results for samples A–F.	47
Figure 2.5 The coordination numbers of Co–Co and Co–P from the fitting results and those of bulk theoretical values.	55
Figure 2.6 The magnetic hysteresis loops of the samples at 2K.	56
Figure 2.7 The HRTEM image of the intermediate NP between ϵ -Co and Co ₂ P.	60
Figure 2.8 Formation energy per atom for Co _{1-x} P _x structures illustrating the proposed path between the ϵ -Co, Co ₂ P, and CoP structures.	62
Figure 2.9 Supercells illustrating a possible path between the Co ₂ P and CoP structures are shown, viewed along the [0 1 0] direction.	64
Figure 2.10 Two pathways for the transition from sample Co ₂ P to CoP.	66
Figure 3.1 TEM images and XRD spectrum of Ni nanoparticles.	110
Figure 3.2 Ni nanoparticles XAS data and EXAFS fitting model.	112
Figure 3.3 Deviation of inter-atomic distance from reference Ni pathways:	117

Figure 3.4 Implications of synthetic parameters on Ni nanoparticle P atomic % and corresponding XRD peak shifts.	122
Figure 3.5 DFT calculations for phosphorus doping in transition metals (TMs): magnetization, formation energies, and diffraction patterns.	127
Figure 3.6 Magnetization data for Ni nanoparticles.	131
Figure 3.7 Bulk Ni density of states (DOS) near the Fermi surface.	134
Figure 4.1 TEM images and XRD spectra of the nanoparticles.	177
Figure 4.2 HAADF STEM images of nanoparticles from reaction II.	178
Figure 4.3 HRTEM images of the samples.	179
Figure 4.4 XAS spectra of Ni ₂ P nanoparticles from Ni foil standard (red), reaction I (blue) and reaction II (green).	180
Figure 4.5 EXAFS models of the nickel phosphide nanoparticle spectra.	184
Figure 4.6 Magnetization vs. applied field hysteresis loops measured at 2 K.	189
Figure 4.7 FC and ZFC magnetization curves and susceptibility plot.	192
Figure 4.8 Offsets in inter-atomic distance for the modeled pathways versus bulk reference distances.	193
Figure 5.1 TEM images of the samples during the oxidation at 200 °C in air.	236

Figure 5.2 (a) XRD and (b) EXAFS results of the NP samples. The pink, turquoise, blue, light green, and black lines represent the starting cobalt NPs, oxidized for 5 mins, 10 mins, 30 mins, and 90 mins samples, respectively.....	239
Figure 5.3 The oxygen concentrations and the average inter-atomic distances of the samples during the oxidation process.....	242
Figure 5.4 The high-resolution TEM images of the samples.....	243
Figure 5.5 The photograph and TEM image of the Co_3O_4 NP samples re-dispersed in an organic solvent after oxidation process.	246
Figure 5.6 The proposed indirect exchange-mechanism of O diffusion in the ϵ -Co phase takes place over four steps (a) – (d).	249
Figure 5.7 The migration energy diagram of the indirect-exchange mechanism.	249
Figure 6.1 Cation exchange transformation of copper sulfide nanoparticles into dual-interface heterostructured particles with zinc sulfide caps.	280
Figure 6.2 HRTEM and HAADF images of the cation exchange reaction final sample.	282
Figure 6.3 XRD structural evolution of heterostructured particles.	285
Figure 6.4 XANES structural evolution of heterostructured NCs.	286
Figure 6.5 Characterization of the heterointerface.	292

Figure 6.6 Phase stability calculation and diffusion pathways.	293
Figure 6.7 Modeled strain in the heterostructured nanocrystals.	296
Figure 6.8 Absorption spectra of nanocrystal samples.	298
Figure 7.1 Schematic of process for fabrication of binderless, carbon-free nanoparticle film battery electrodes:	345
Figure 7.2 EPD-formed nanoparticle film:	347
Figure 7.3 Materials characterization of EPD-formed nanoparticle electrodes:.....	350
Figure 7.4 Electrochemical performance of EPD Co_3O_4 NP films without carbon black and polymeric additives:	353
Figure 7.5 Mechanical stability test of Co_3O_4 nanoparticle films:	358
Figure 7.6 Relationship between average film thickness and the charge capacity for different applied voltages during EPD:	360
Figure 7.7 TEM images and schematic of nanoparticles through lithiation/delithiation process:	362

LIST OF TABLES

Table 2.1 The reaction conditions of the samples B-F.....	36
Table 2.2 The sum of experimental path degeneracies (coordination number).....	48
Table 2.3 Co K-Edge EXAFS structure fitting parameters of samples A-F.....	49
Table 2.4 The formation energy, migration barrier, and diffusion activation barrier for Co and P diffusing through ϵ -Co	56
Table 2.5 The formation energy, migration barrier and diffusion activation barrier for Co and P diffusing through vacant sites in Co_2P	57
Table 3.1 First and second shell path parameters.	116
Table 3.2 Summary of Ni and P content from EXAFS modeling and ICP.	120
Table 3.3 The elemental composition of Ni nanoparticles synthesized through standard techniques based on ICP measurements.....	120
Table 3.4 Formation energy calculation results. Calculated formation energies for octahedral (o), tetrahedral (t), and substitutional (s) P, for Ni, Co, and Fe.....	126
Table 4.1 Nickel phosphide nanoparticle synthetic conditions.	173
Table 4.2 First shell path parameters from EXAFS fitting models.	183

Table 4.3 Ni and P contributions and associated error within the nanoparticles from EXAFS modeling and ICP.	185
Table 4.4 Average $\Delta R/R$ % and standard deviation for EXAFS fitting models.....	195
Table 5.1 The structural contributions (atomic %) from the EXAFS fitting models for the samples	240
Table 5.2 The formation energy, migration barrier and diffusion activation barrier for Co and O diffusing through ϵ -Co.	248
Table 5.3 The formation energy, migration barrier and diffusion activation barrier for Co and O diffusing through CoO.....	250
Table 6.1 Diffusion activation barrier for Cu, Zn, and Cd.....	293
Table 7.1 Thickness and volume analysis of three samples with different thicknesses.	352

CHAPTER 1

1 INTRODUCTION

1.1 Colloidal Nanocrystals and their Synthesis

Materials at nanoscale dimensions (between 1 and 100 nm) can present unique properties, fundamentally different from those found in bulk materials that follow classical theories.¹⁻⁸ These new properties are the result of the high surface-to-volume ratio in nanoscale materials as well as size confinement effects. The new properties are the focus of nanoscience and nanotechnology. Controlling the physical size of materials enables control of material properties. For example, the electronic and optical properties of semiconductors strongly depend on crystallite size and shape in the nanometer size regime (**Figure 1.1**).¹ In metals, the relevant energy level spacing is small even at the nanoscale. However in semiconductors, the Fermi level lies between valence and conduction bands such that the band edges govern the low-energy optical and electronic behavior leading to optical excitations across the band gap that are highly dependent on the size of materials in the nanoscale regime.

Nanocrystals (NCs) exhibit interesting size-dependent electronic, optical, magnetic, and chemical properties that cannot be achieved by their bulk counterparts.^{5, 9-11} To make efficient use of these properties in applications, the synthesis of a homologous batch of NCs with a narrow size distribution (monodisperse with a size distribution $\leq 5\%$) is required, since the electronic, optical, and magnetic properties of these NCs are highly dependent on their size and shape.^{5, 12}

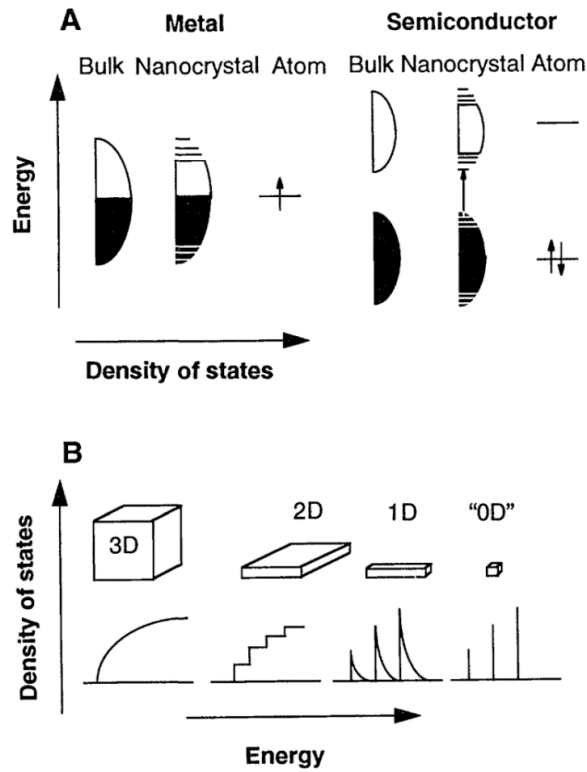


Figure 1.1 (A) Schematic diagrams of energy vs. density of states comparing metal and semiconductors across bulk, nanoscale, and atomic size regimes. (B) Schematic diagram of density of states vs. energy showing one idealized band of a semiconductor as a function of its dimension.¹

The colloidal synthesis of NCs involves two important processes, the nucleation followed by the growth of the NCs. La Mer and his coworkers showed the synthesis of monodisperse colloids requiring a short burst of nucleation followed by slower particle growth of the existing nuclei.¹³ Often referred to as “the separation of nucleation and growth,” this model for colloidal nanoparticle syntheses is depicted schematically in the simple diagram shown in **Figure 1.2**. The “burst nucleation” is

initiated when the concentration of monomer exceeds the nucleation threshold and is achieved through the rapid addition of the monomer into the coordinating solvent. At the onset of nucleation, the degree of monomer supersaturation is high enough to overcome the energy barrier for the nucleation event, resulting in the formation of stable nuclei. As the monomer is consumed and its concentration decreases below the nucleation threshold, the system exhibits a growth stage called Ostwald ripening. In this phase, nucleation is effectively halted, and particles continue to grow since the high surface energy of small particles promotes their dissolution thereby providing monomer species which deposit on larger particles. As such, this Ostwald ripening process leads to a decrease in the number of particle in the reaction vessel.

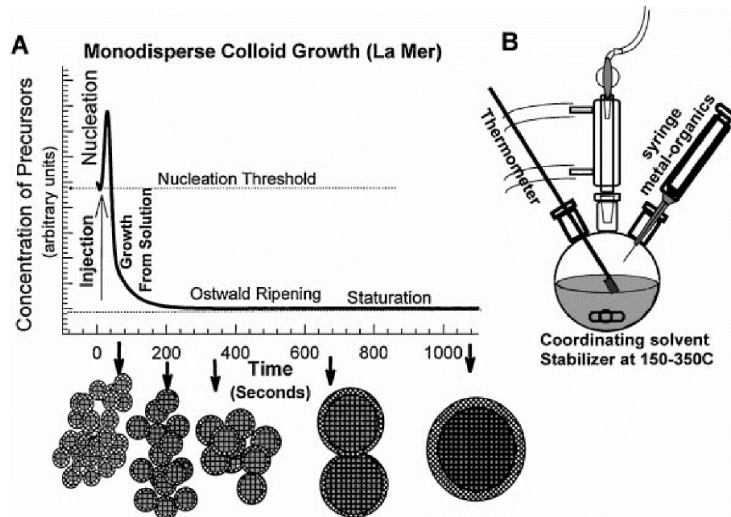


Figure 1.2(A) Schematics of the stages of nucleation and growth for the synthesis of monodisperse NCs in the framework of the La Mer model. (B) A diagram of an apparatus employed in the synthesis of monodisperse NC samples.⁵

1.2 Chemical Transformation of Nanocrystals

The chemical transformation of as-synthesized NCs is an emerging and powerful method to tailor NC composition and morphology.^{2, 4, 14-23} The chemical transformation process in bulk solids is generally very slow because of the high activation energy for the diffusion of reactant atoms and ions. Such reactions are restricted to the surface region of bulk materials. In contrast, the large surface-to-volume ratio of nanomaterials allows for a lowering of phase transition temperatures.⁴ This unique nanoscale phenomenon allows for both complete and partial chemical transformations of nanomaterials, which are difficult or inaccessible using conventional NC syntheses. In addition, chemical transformations of NCs can induce metastable phases²⁴ and novel morphologies such as striped nanorods,⁷ and hollow NCs². However, few works have addressed the atomic mechanisms for these transformations beyond empirical qualitative analysis.

1.2.1 Classes of Chemical Transformations of Nanocrystals

Solid state chemical transformation of NCs can be classified by reaction type as summarized in **Figure 1.3**. The four categories are: 1) redox addition (oxidative diffusion), 2) galvanic replacement, 3) cation exchange, and 4) anion exchange.

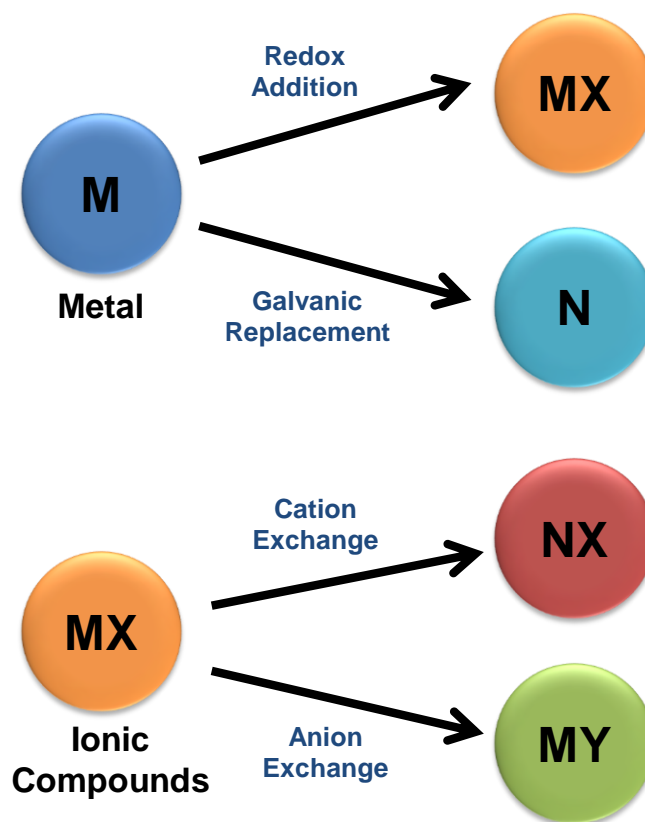


Figure 1.3 Categories of chemical transformation pathways in nanocrystals

1.2.1.1 Redox Addition

Redox addition reactions can be performed on NCs of a particular metal to form the corresponding metal chalcogenides^{2, 25, 26}, phosphides^{27, 28}, and oxides^{2, 29, 30}. The main driving force for the transformation can be attributed to the enthalpy of formation of metal chalcogenides (or phosphides/oxides), which is much lower than those of the pure components³¹. These oxidative diffusion transformations are effective pathways to create various metal chalcogenides (or phosphides/oxides).

Additionally, these conversion reactions often involve the nanoscale Kirkendall effect, which plays a pivotal role in controlling the product morphology.

Alivisatos and coworkers demonstrated that Co metal NCs reacted with O₂ result in hollow CoO NCs through an oxidation of Co metal and the reduction of the oxygen.² This hollowing, an example of the nanoscale Kirkendall effect, is caused by the fast outward diffusion of Co atoms in contrast to the slower inward diffusion of oxygen atoms. Similarly, hollow cobalt sulfide NCs (Co₃S₄ and Co₉S₈) were obtained through sulfurization with elemental sulfur in a mixture of *o*-dichlorobenzene, tri-*n*-octylphosphine oxide, and oleic acid at 455K (**Figure 1.4a**). The benefit of utilizing the Kirkendall effect to create hollow NCs is that no sacrificial template is needed. Furthermore, monodisperse metal NCs produce monodisperse hollow chalcogenides (or oxides), so the size and shape of the product can be controlled by the template metal NCs. However, the products often result in polycrystalline shells despite the single-crystalline nature of the template metal NCs.

Tracy and coworkers investigated the size-dependent oxidation of Ni NCs and demonstrated that NiO shell formation results in single voids for smaller NCs (9 and 26 nm) whereas multiple voids form in larger NCs (96 nm) since self-diffusion is not fast enough to cause the voids to merge into a single void.³² In addition, they concluded that the formation of a single void at the core/shell interface causes anisotropic outward diffusion of Ni resulting in a non-uniform NiO shell thickness (**Figure 1.4b**).

In addition, a study by Pileni and coworkers demonstrated that the crystallinity and crystal structure of the starting metal NCs influence their morphology significantly.³³⁻³⁵ The oxidation process was carried on Co NCs with different crystallinity or phases, which are amorphous, FCC (face centered cubic), HCP (hexagonal close packed), and the epsilon phase of cobalt NC.³⁵ Amorphous Co NCs have showed no hollow structures, meaning that the difference in the diffusion rates between oxygen and cobalt atoms is not significant as in the crystalline cobalt NCs that always transform to a hollow morphology upon oxidation at 260 °C. Additionally, different crystal structures of the starting Co NCs yield distinct morphologies upon oxidation, indicating that oxygen diffusion is strongly dependent on the crystal structure of initial metal NCs.

Recently, *in-situ* TEM studies on the oxidation of Bi metal NCs by Alivisatos and coworkers have provided insight into understanding the mechanism of Kirkendall hollowing (**Figure 1.4c**).³⁶ The dynamics of Bi diffusion through the bismuth oxide shell were captured *in-situ* using a TEM and liquid cell. They found that the diffusion coefficient of bismuth in the bismuth oxide shell is 3–4 orders of magnitude higher than that of bulk Bi. The complex reaction kinetics were observed to depend on various parameters such as the size of the initial Bi NCs and the reaction temperature.

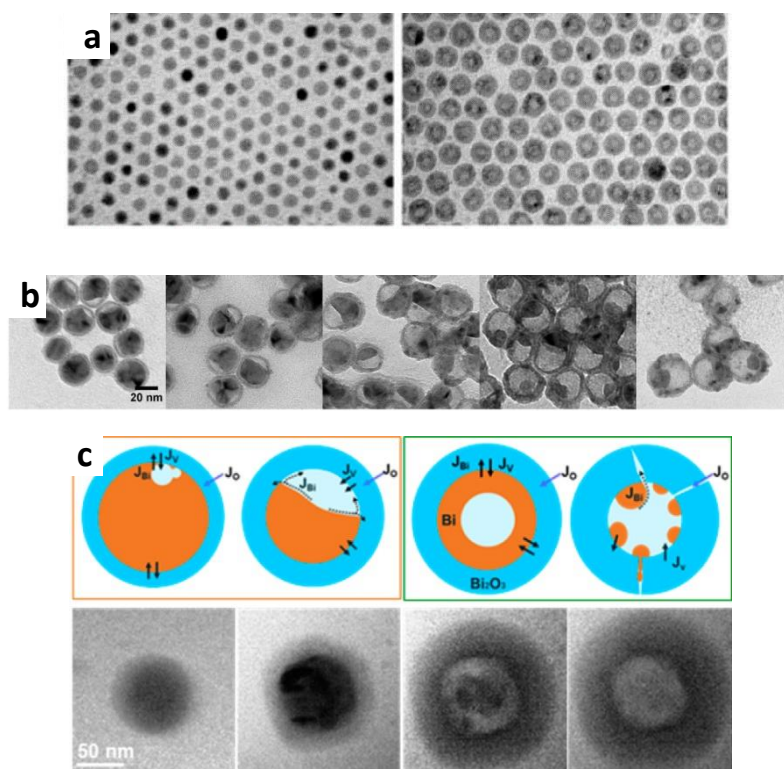


Figure 1.4 Redox addition reactions and accompanying nanoscale Kirkendall effect. (a) TEM image show that the cobalt NCs (left) transform to cobalt sulfide (right) phase with hollow structures.² (b) TEM images show the morphological change through the Kirkendall effect during the oxidation of 26 nm Ni NCs at 300 °C in air for 90 mins to 210 mins (left to right)³² (c) TEM images and corresponding graphical depictions of in the in-situ oxidation of bismuth NCs in a TEM liquid cell.³⁶ The different sizes of initial Bi NCs lead to different diffusion mechanisms.

1.2.1.2 Galvanic Replacement

Galvanic replacement is a versatile method to create hollow metal NCs through the different reduction potentials of two elemental metals.^{18, 22, 37} The galvanic

reaction leads to the deposition of a more noble metal (lower reduction potential) and dissolution of a less noble metal. For example, Ag NCs have been used to form hollow Au NCs in aqueous and organic media due to the different reduction potentials between Ag and Au. Xia and coworkers demonstrated the transformation of various Ag nanostructures into Au or Au/Ag alloy nanomaterials.²² Ag nanocubes stabilized with poly(vinyl pyrrolidone) have served as a sacrificial template for the synthesis of hollow Au nanoboxes or nanocages.

1.2.1.3 Cation Exchange

In ionic NCs, cation exchange is a powerful method to chemically transform NCs through the substitution of cations.^{4, 7, 17, 24, 38-40} The smaller ionic radius of cations than anions facilitates diffusion of cations while maintaining the overall morphology of the template ionic NCs through the preservation of the anion lattice.^{4, 19, 39, 41} The cation exchange reaction has gained attention due to its capacity to induce metastable phases and form unconventional heterostructures.^{7, 24} Partial cation exchange reactions can also lead to the fine-tuning of NC optical properties, making such reactions useful for photovoltaic⁴² and plasmonic applications⁴³. In general, cation exchange reactions are driven by the relative K_{sp} value, which is an equilibrium constant between an ionic solid and its dissolved state.^{41, 44} Once the reactants and products are solvated in a solution, the relative solubility difference between them determines if exchange reactions are thermodynamically favorable.^{19, 39, 44} Ions in a

solid with a higher relative solubility can be exchanged by other ions if the product has a lower solubility.

The first comprehensive study of cation exchange in NCs was carried out by Alivisatos and coworkers.⁴ Exposing CdSe NCs to a methanol solution of Ag⁺ ions induces the formation of Ag₂Se NCs with the liberation of Cd²⁺ ions from the reactant host NC lattice such that the original size and shape are preserved (Figure 5 top). In addition, the reverse exchange reaction from Ag₂Se to CdSe was achieved in the presence of complexing molecules such as tri-n-butylphosphine. A critical NC size to retain the anionic subframe for conserving the shape of the NCs during cation exchange was identified as well.

Cation exchange of NCs often results in metastable phases and unusual NC shapes which are not easily accomplished by conventional NC syntheses.^{7, 17, 24, 38} For example, TiS₂ nanodisks have been shown to transform to Cu₂S toroids through a heteropitaxial TiS₂-Cu₂S intermediate (**Figure 1.5** bottom left).¹⁷ This result demonstrates that cation exchange on 2D layered nanomaterials can lead to hollow toroids due to the high reactivity for the transformation at the edge of the nanodisks. Partial cation exchange has also been utilized to produce striped CdS-Ag₂S (**Figure 1.5** bottom right) and CdS-Cu₂S nanorods starting from CdS nanorods.⁷ Strain energy has been found to be critical for inducing the spontaneous formation of periodic structures in CdS- Ag₂S nanorods.

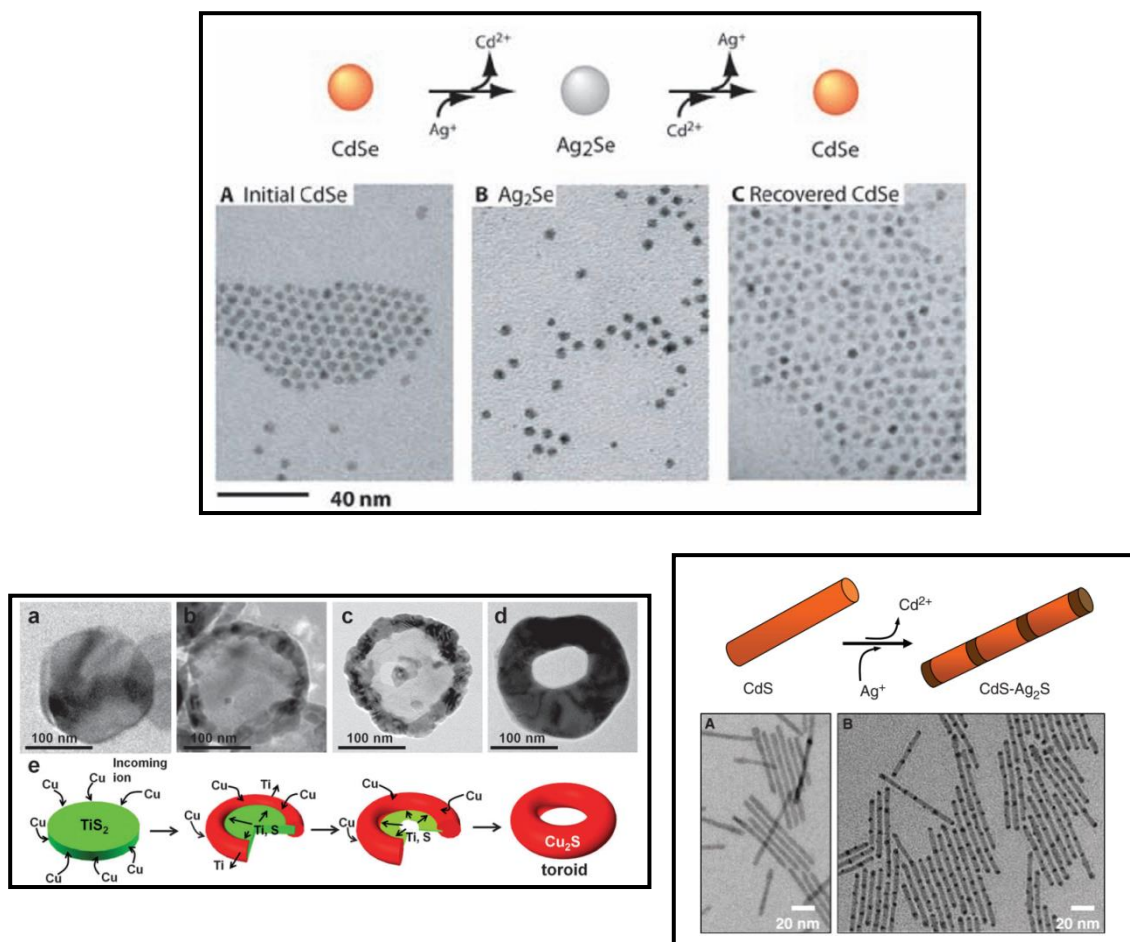


Figure 1.5 TEM images and corresponding schematics of cation exchange reactions in NCs. (Top) TEM images and corresponding schematics of cation exchange from CdSe to Ag₂Se and back to CdSe NCs.⁴ (Bottom left) TEM images and corresponding schematics of cation exchange from TiS₂ nanoplate to Cu₂S toroid.¹⁷ (Bottom right) TEM images and corresponding schematics of superlattices formed through partial cation exchange from CdS to Ag₂S.⁷

1.2.1.4 Anion Exchange

The anion exchange of NCs is less common compared to cation exchange since anions generally possess larger ionic radii than those of cations.^{21, 45, 46} Anion exchange reactions are made more difficult by slower anion diffusion, which often requires longer reaction times and higher temperatures than cation exchange reactions. Moreover, the slower reaction kinetics of anion exchange compared to cation exchange may be due to a smaller selection of reactive anion-supplying reagents. Recently, Robinson and coworkers demonstrated an anion exchange reaction from cobalt oxide NCs to cobalt sulfide NCs by introducing the highly reactive molecular precursor ammonium sulfide ((NH₄)₂S) as shown in **Figure 1.6**.⁴⁶ The high reactivity of (NH₄)₂S allowed for a relatively low temperature for the anion exchange reaction (70 °C). Subsequent annealing at 200 °C led to polycrystalline Co₃S₄ NCs and the formation of a larger void compared to the initial void of the CoO NCs. This increase in the void size is caused by the faster diffusion of Co²⁺ and O²⁻ than that of the incoming S²⁻ during the anion exchange.

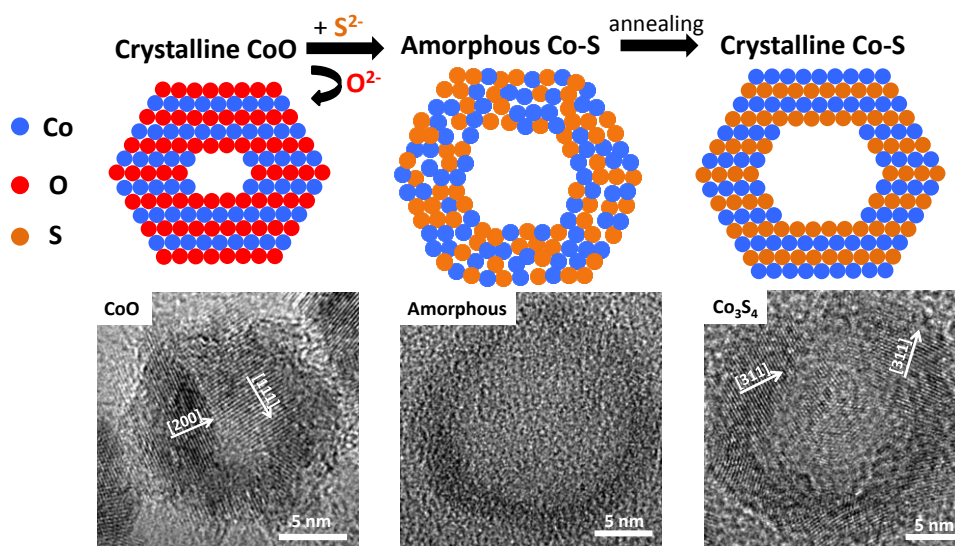


Figure 1.6 Schematics and corresponding TEM images during the anion exchange reaction. Ammonium sulfide exhibits high reactivity in anion exchange reactions, transforming CoO to amorphous Co-S NCs, which are subsequently converted into crystalline Co₃S₄ NPs by annealing at 200 °C.⁴⁶

1.2.2 XAS Characterization

One of the major challenges in nanoscience is to fully understand and characterize transformation mechanisms. Chemical transformations in bulk systems follow pathways that can be described by classical thermochemical and kinetic models. Nanoscale systems, on the other hand, often exhibit intriguing and complex transformation kinetics, providing new opportunities to manipulate the crystal phase, composition, and morphology of NCs. Moreover, chemical transformations can lead to new nanomaterials with unusual patterns or morphologies which cannot be obtained through direct synthesis. However, the mechanisms and kinetics of these chemical transformations are not well established for NCs. It is essential to understand these reaction processes and diffusion mechanisms in order to optimize the control of nanomaterial properties and access new NC-based material compositions and morphologies. A more complete understanding of transformation pathways would enable both the prediction and manipulation of the unique products resulting from the chemical transformations of NCs.

X-ray absorption spectroscopy (XAS) is the ideal technique with which to address these challenges and to resolve the local atomic structure during chemical transformations. XAS is a powerful tool to probe the atomic structure of a material with short-range order.⁴⁷⁻⁴⁹ When combined with other tools such as X-ray diffraction (XRD) and transmission electron microscopy (TEM), a nearly complete structural and morphological picture of a NC sample can be assembled. XAS is an essential characterization method for NCs that have undergone chemical transformations

because XAS can characterize intermediate disordered structures during the transformations, which are not fully accessible by other common tools.

XAS is a synchrotron-based characterization technique that can be separated into near edge spectroscopy (XANES) and extended X-ray absorption fine structure (EXAFS) as shown in **Figure 1.7a**. In terms of energy level, the XANES is generally in the range where the potential is 50 eV above the edge where sharp absorption occurs, and the EXAFS is in where the potential is between 50 - 1000 eV above the edge. In the X-ray absorption process, a core electron is excited to an empty state by synchrotron X-rays, and as such, X-ray absorption probes the unoccupied part of the electronic structure of the system. In the EXAFS region, the excited electron has kinetic energy in the form of a photoelectron, and EXAFS analysis yields for many systems an accurate determination of the local radial structures, such as bond length, coordination number, and elemental composition. The XANES structure can also provide details on a geometric structure of specific element in the system, such as electronic transition, ligand coordination, and oxidation state. The intensity of an X-ray beam passing through a material of thickness t is given by the absorption coefficient μ :

$$I = I_0 e^{-\mu t} \quad (1)$$

where I_0 is the X-ray intensity striking the material, and I is the intensity transmitted through the material. μ has a sharp absorption edge corresponding to the characteristic core-level energies of specific atom. μ depends on X-ray energy E , atomic number Z , density ρ , and atomic mass A :

$$\mu \approx \frac{\rho Z^4}{A E^3} \quad (2)$$

presenting that μ is highly sensitive to the atomic number.

For further analysis of EXAFS, the spectra are typically converted from E-space to k-space by Fourier transform (FT). In the FT spectrum, peaks appear at real space positions related to particular interatomic distances from the absorbing atom (**Figure 1.7b**). Additionally, by fitting well-matched theoretical pathways to the experimental spectra by allowing structural parameters to deviate from the theoretical bulk structures, specific structural information could be determined, such as coordination number, spacing, and mean-square disorder, in accordance with the EXAFS equation (**Figure 1.7b**).

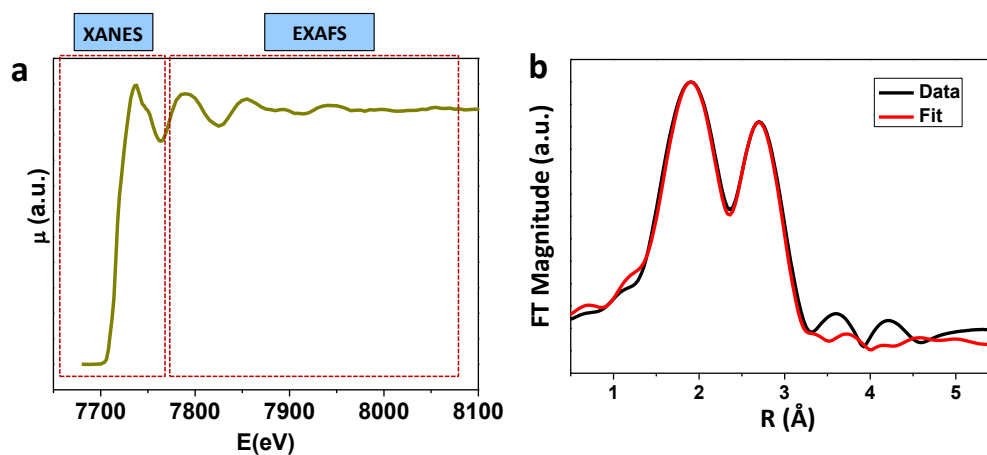


Figure 1.7 Typical raw absorption coefficient data and its Fourier-transformed k-weighted EXAFS and simulated fitting result. (a) Co K-edge XAS spectrum, which can be divided to XANES and EXAFS, of Co NC sample. (b) Fourier-transformed k-weighted EXAFS data of Co NC sample (black line) and simulated fitting result (red line).

Generally, the data processing and modelling are carried out with analysis softwares. The raw spectra are averaged and processed using the ATHENA software.⁵⁰ This processing includes edge determination from the first inflection point in the absorption data, background subtraction using the AUTOBK algorithm, and normalization of the EXAFS modulations (greater than 150 eV above the edge).⁵¹ For nanoparticle samples during the transformation from cobalt to cobalt phosphide, a k-weight of 1 is chosen for both the FT of the experimental data and the theoretical fitting because phosphorus and oxygen are low-Z scattering elements which will scatter mainly at lower k-values.⁵² Also, use of a higher k-weight is not compensate for the damping in amplitude due to the high variations in absorber-scatterer distance characteristically observed in nanoparticle spectra.⁵³ Additionally, as fitting is performed only to the first coordination shell, there was no need to use a higher k-weighting to emphasize high k behavior.⁵⁴ The spectra are converted from E-space, to k-space by Fourier transform, according to standard procedure⁵⁴ and fitted to theory.⁵⁵ In the FT spectrum, peaks appear at the real space position related to a particular shell from the absorbing atom.⁵⁶ The data, after processing, are then analyzed by the ab-initio method with ARTEMIS.⁵⁰ Crystal structures from theory are input using ATOMS.⁵⁷ By fitting well-matched theoretical pathways to the experimental spectra by allowing structural parameters to deviate from the theoretical bulk structures, specific structural information can be determined such as coordination number, spacing, and mean-square disorder, in accordance with the EXAFS equation^{55, 56, 58, 59}

$$\chi(k) = \sum_{\Gamma} \left[\frac{N_{\Gamma} S_0^2 F_{\Gamma}(k)}{2kR_{\Gamma}^2} e^{-2k^2\sigma_{\Gamma}^2} e^{-2R_{\Gamma}/\lambda(k)} \times \sin(2kR_{\Gamma} + \phi_{\Gamma}(k)) \right] \quad (3)$$

Equation (3) above describes the parameters that comprise the EXAFS model. Knowledge of particular parameters enables the determination of others. Γ counts the individual scattering pathways that are summed over. Parameter k is the photoelectron wavevector. $F_I(k)$, the scattering amplitude, and $\lambda(k)$, the mean free path of inelastically-scattered photoelectrons which contribute to the reduction of the scattering amplitude, are computed by the analysis program. The phase shift $\phi_I(k)$ is a function of the absorbing and scattering atom and takes into account the fact that the electron is in the presence of potentials.⁵⁶ The amplitude reduction factor, S_0^2 , theoretically accepted to be between 0.7 and 1 was set to 0.85 for purposes of extracting the coordination number.⁵⁸ The parameters allowed to float during fitting were degeneracy N_I , which represents the number of atoms at the same distance from the absorbing atom, R_I , the effective distance from the absorbing atom to the scattering atom, and σ_I^2 , the mean square disorder, which includes components from structural disorder as well as thermal disorder (Debye-Waller factor).⁵⁶

1.3 Chemical Transformation of NCs for Energy Applications

Chemical transformation reactions of NCs provide an access to a wide range of metal phosphide, sulphide, selenide, telluride, and oxide NCs with unique architectures, including heterostructures, which may be inaccessible to capture utilizing other traditional fabrication techniques. Moreover, chemical transformation pathways often lead to a metastable phase and provide a precise phase tunability of materials phase which might unlock new and enhanced properties. These NCs designed through chemical transformations are of interest for a broad range of energy applications because of their novel catalytic, electronic, optical, magnetic, and electrochemical properties.

1.3.1 Colloidal NCs for Battery Applications

Nanomaterials have shown to be an alternative format for lithium-ion battery (LIB) electrodes due to their greatly reduced diffusion length for ionic transport and their capability to accommodate strain through cycles.^{10, 20, 60-64} In particular, colloidal NC are emerging building blocks for creating and designing LIB electrodes with enhanced electrochemical performance.^{20, 65-67} Colloidal synthesis of NC offers a wide range of materials, such as metal, metal oxide, and various semiconducting materials, that are well established to finely tune the size and shapes. In addition, the solution processability of colloidal NCs is a huge advantage for the fabrication of complicated devices and for development for a mass production such as roll-to-roll manufacturing process.

1.3.2 Chemical Transformation of NCs for Battery

Chemical transformation of NCs is an emerging strategy for utilization of NCs in battery electrodes since chemical transformations can offer a noble architecture of NCs. For example, Kovalenko and coworkers synthesized heterostructured Sn-Ge nanorods colloiddally using Sn NCs as low-melting point catalyst for the solution-liquid-solid growth (**Figure 8a,b**).⁶⁶ The heterostructured Sn-Ge showed that there is a synergistic effect of both components onto the Li-ion battery electrode performance of the entire nanocomposite. Figure 8c exhibits the comparison for the discharge capacities of Sn-Ge nanorods and Sn NCs demonstrating that the Sn-Ge heterostructured nanorods gain ~50% higher capacity compared to Sn NCs. This enhancement of electrochemical property may originate from a stepwise lithiation and delithiation of Sn and Ge which can reduce the mechanical stress during electrochemical cycling.

Another huge advantage of chemical transformation for NCs is accessibility of complex phases of NCs to optimize their properties. For instance, Hyeon and coworkers demonstrated galvanic replacement reactions on metal oxide NCs.²⁰ Fe(II) oxidized to Fe(III) and was deposited as γ -Fe₂O₃ onto the Mn₃O₄ nanocubes. At the same time, Mn(III) in Mn₃O₄ dissolved into a reaction solution as it was reduced to Mn²⁺, creating γ -Fe₂O₃ nanocages. During this galvanic replacement reaction, intermediate phases between Mn₃O₄ and γ -Fe₂O₃ could be isolated as Mn_{2.0}Fe_{1.0}O₄, Mn_{1.5}Fe_{1.5}O₄, Mn_{1.1}Fe_{1.9}O₄, Mn_{0.6}Fe_{2.4}O₄, and Mn_{0.3}Fe_{2.7}O₄ through partial galvanic replacements. Among these phases, Mn_{1.1}Fe_{1.9}O₄ NCs showed the highest reversible capacity of ~1000 mAh/g up to 50 cycles. This high cycling performance of

$Mn_{1.1}Fe_{1.9}O_4$ NC phase may attribute to the electronic conductivity enhancement resulting from the mixed valency of the multicomponent $Mn_{3-x}Fe_xO_4$.

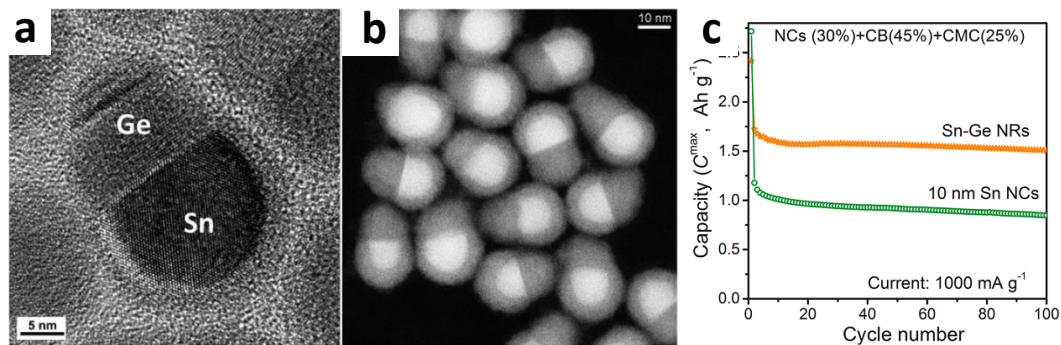


Figure 1.8 TEM images and battery cycling performance of Sn-Ge nanorods.⁶⁶

(a) High-resolution TEM image. (b) high-angle annular darkfield scanning transmission electron microscopy (HAADF-STEM) image of Sn-Ge nanorods. (c) Discharge capacities for anodes containing Sn-Ge NRs and, for comparison, the same weight percentage of Sn NCs.

1.4 References

1. Leutwyler, W. K.; Bürgi, S. L.; Burgli, H. *Science* **1996**, 271, (5251), 933-937.
2. Yin, Y. D.; Rioux, R. M.; Erdonmez, C. K.; Hughes, S.; Somorjai, G. A.; Alivisatos, A. P. *Science* **2004**, 304, (5671), 711-714.
3. Yin, Y.; Alivisatos, A. P. *Nature* **2005**, 437, (7059), 664-670.
4. Son, D. H.; Hughes, S. M.; Yin, Y. D.; Alivisatos, A. P. *Science* **2004**, 306, 1009-1012.
5. Murray, C. B.; Kagan, C. R.; Bawendi, M. G. *Annu. Rev. Mater. Sci.* **2000**, 30, (1), 545-610.
6. Scholl, J. A.; Koh, A. L.; Dionne, J. A. *Nature* **2012**, 483, (7390), 421-427.
7. Robinson, R. D.; Sadtler, B.; Demchenko, D. O.; Erdonmez, C. K.; Wang, L. W.; Alivisatos, A. P. *Science* **2007**, 317, (5836), 355-358.
8. Jacobs, K.; Zaziski, D.; Scher, E. C.; Herhold, A. B.; Paul Alivisatos, A. *Science* **2001**, 293, (5536), 1803-1806.
9. Murray, C. B.; Norris, D. J.; Bawendi, M. G. *J. Am. Chem. Soc.* **1993**, 115, (19), 8706-8715.
10. Poizot, P.; Laruelle, S.; Grugeon, S.; Dupont, L.; Tarascon, J. M. *Nature* **2000**, 407, (6803), 496-499.
11. Tolbert, S. H.; Alivisatos, A. P. *Science* **1994**, 265, (5170), 373-376.

12. Park, J.; Joo, J.; Kwon, S. G.; Jang, Y.; Hyeon, T. *Angew. Chem., Int. Ed.* **2007**, *46*, (Copyright (C) 2011 American Chemical Society (ACS). All Rights Reserved.), 4630-4660.
13. LaMer, V. K.; Dinegar, R. H. *J. Am. Chem. Soc.* **1950**, *72*, (11), 4847-4854.
14. Fayette, M.; Robinson, R. D. *J. Mater. Chem. A* **2014**, *2*, (17), 5965-5978.
15. Vasquez, Y.; Henkes, A. E.; Chris Bauer, J.; Schaak, R. E. *Journal of Solid State Chemistry* **2008**, *181*, (7), 1509-1523.
16. Carbone, L.; Cozzoli, P. D. *Nano Today* **2010**, *5*, (5), 449-493.
17. Jeong, S.; Han, J. H.; Jang, J.-t.; Seo, J.-w.; Kim, J.-G.; Cheon, J. *J. Am. Chem. Soc.* **2011**, *133*, (37), 14500-14503.
18. Moon, G. D.; Ko, S.; Min, Y.; Zeng, J.; Xia, Y.; Jeong, U. *Nano Today* **2011**, *6*, (2), 186-203.
19. Rivest, J. B.; Jain, P. K. *Chem. Soc. Rev.* **2013**, *42*, (1), 89-96.
20. Oh, M. H.; Yu, T.; Yu, S.-H.; Lim, B.; Ko, K.-T.; Willinger, M.-G.; Seo, D.-H.; Kim, B. H.; Cho, M. G.; Park, J.-H. *Science* **2013**, *340*, (6135), 964-968.
21. Park, J.; Zheng, H.; Jun, Y.-w.; Alivisatos, A. P. *J. Am. Chem. Soc.* **2009**, *131*, (39), 13943-13945.
22. Sun, Y.; Xia, Y. *Science* **2002**, *298*, (5601), 2176-2179.
23. Anderson, B. D.; Tracy, J. B. *Nanoscale* **2014**.

24. Li, H.; Zanella, M.; Genovese, A.; Povia, M.; Falqui, A.; Giannini, C.; Manna, L. *Nano Lett.* **2011**, 11, (11), 4964-4970.
25. Yin, Y. D.; Erdonmez, C. K.; Cabot, A.; Hughes, S.; Alivisatos, A. P. *Adv. Funct. Mater.* **2006**, 16, (11), 1389-1399.
26. Cabot, A.; Smith, R. K.; Yin, Y.; Zheng, H.; Reinhard, B. r. M.; Liu, H.; Alivisatos, A. P. *ACS Nano* **2008**, 2, (7), 1452-1458.
27. Ha, D.-H.; Moreau, L. M.; Bealing, C. R.; Zhang, H.; Hennig, R. G.; Robinson, R. D. *J. Mater. Chem.* **2011**, 21, (31), 11498-11510.
28. Brock, S. L.; Perera, S. C.; Stamm, K. L. *Chem.-Eur. J.* **2004**, 10, (14), 3364-3371.
29. Cabot, A.; Ibáñez, M.; Guardia, P.; Alivisatos, A. P. *J. Am. Chem. Soc.* **2009**, 131, (32), 11326-11328.
30. Cabot, A.; Puentes, V. F.; Shevchenko, E.; Yin, Y.; Balcells, L.; Marcus, M. A.; Hughes, S. M.; Alivisatos, A. P. *J. Am. Chem. Soc.* **2007**, 129, (34), 10358-10360.
31. Deore, S.; Xu, F.; Navrotsky, A. *American Mineralogist* **2008**, 93, (5-6), 779-783.
32. Railsback, J. G.; Johnston-Peck, A. C.; Wang, J.; Tracy, J. B. *ACS Nano* **2010**, 4, (4), 1913-1920.
33. Yang, Z.; Walls, M.; Lisiecki, I.; Pileni, M.-P. *Chem. Mater.* **2013**, 25, (11), 2372-2377.

34. Yang, Z.; Lisiecki, I.; Walls, M.; Pileni, M.-P. *ACS Nano* **2013**, 7, (2), 1342-1350.
35. Yang, Z.; Yang, J.; Bergstrom, J.; Khazen, K.; Pileni, M.-P. *Phys. Chem. Chem. Phys.* **2014**, 16, (21), 9791-9796.
36. Niu, K.-Y.; Park, J.; Zheng, H.; Alivisatos, A. P. *Nano Lett.* **2013**, 13, (11), 5715-5719.
37. Sun, Y. G.; Xia, Y. N. *J. Am. Chem. Soc.* **2004**, 126, (12), 3892-3901.
38. Miszta, K.; Dorfs, D.; Genovese, A.; Kim, M. R.; Manna, L. *ACS Nano* **2011**, 5, (9), 7176-7183.
39. Beberwyck, B. J.; Surendranath, Y.; Alivisatos, A. P. *J. Phys. Chem. C* **2013**, 117, (39), 19759-19770.
40. Sadtler, B.; Demchenko, D. O.; Zheng, H.; Hughes, S. M.; Merkle, M. G.; Dahmen, U.; Wang, L.-W.; Alivisatos, A. P. *J. Am. Chem. Soc.* **2009**, 131, (14), 5285-5293.
41. Beberwyck, B. J.; Alivisatos, A. P. *J. Am. Chem. Soc.* **2012**, 134, (49), 19977-19980.
42. Mao, B.; Chuang, C.-H.; Lu, F.; Sang, L.; Zhu, J.; Burda, C. *J. Phys. Chem. C* **2012**, 117, (1), 648-656.
43. Kriegel, I.; Rodríguez-Fernández, J.; Wisnet, A.; Zhang, H.; Waurisch, C.; Eychmüller, A.; Dubavik, A.; Govorov, A. O.; Feldmann, J. *ACS Nano* **2013**, 7, (5), 4367-4377.

44. Wark, S. E.; Hsia, C. H.; Son, D. H. *J. Am. Chem. Soc.* **2008**, 130, (29), 9550-9555.
45. Dawood, F.; Schaak, R. E. *J. Am. Chem. Soc.* **2008**, 131, (2), 424-425.
46. Zhang, H.; Solomon, L. V.; Ha, D.-H.; Honrao, S.; Hennig, R. G.; Robinson, R. D. *Dalton Transactions* **2013**, 42, (35), 12596-12599.
47. Frenkel, A. I. *Chem. Soc. Rev.* **2012**, 41, (24), 8163-8178.
48. De Groot, F. *Chem. Rev.* **2001**, 101, (6), 1779-1808.
49. Koningsberger, D. C.; Mojet, B. L.; van Dorssen, G. E.; Ramaker, D. E. *Top. Catal.* **2000**, 10, (3), 143-155.
50. Ravel, B.; Newville, M. *J. Synchrotron Radiat.* **2005**, 12, (4), 537-541.
51. Kelly, S. D.; Ravel, B. *AIP Conf. Proc.* **2007**, 882, (1), 132-134.
52. Koningsberger, D. C.; Mojet, B. L.; van Dorssen, G. E.; Ramaker, D. E. *Top. Catal.* **2000**, 10, (3), 143-155.
53. Cheng, G.; Carter, J. D.; Guo, T. *Chem. Phys. Lett.* **2004**, 400, (1-3), 122-127.
54. Bunker, G., *Introduction to XAFS: a practical guide to X-ray absorption fine structure spectroscopy*. Cambridge University Press: Cambridge, 2010; p 260.
55. Stern, E. A. *Phys. Rev. B* **1974**, 10, (8), 3027-3037.
56. Stern, E. A. *Contemp. Phys.* **1978**, 19, (4), 289 - 310.
57. Ravel, B. *J. Synchrotron Radiat.* **2001**, 8, (2), 314-316.
58. Ravel, B.; Kelly, S. D. *AIP Conf. Proc.* **2007**, 882, (1), 150-152.

59. Scott, R., *Physical Methods in Bioinorganic Chemistry: Spectroscopy and Magnetism*. University Science Books: 2000.
60. Chan, C. K.; Peng, H. L.; Liu, G.; McIlwrath, K.; Zhang, X. F.; Huggins, R. A.; Cui, Y. *Nat. Nanotechnol.* **2008**, 3, (1), 31-35.
61. Liu, N.; Lu, Z.; Zhao, J.; McDowell, M. T.; Lee, H.-W.; Zhao, W.; Cui, Y. *Nat. Nanotechnol.* **2014**, 9, (3), 187-192.
62. Chen, J.; Xu, L.; Li, W.; Gou, X. *Adv. Mater.* **2005**, 17, (5), 582-586.
63. Lu, J.; Lei, Y.; Lau, K. C.; Luo, X.; Du, P.; Wen, J.; Assary, R. S.; Das, U.; Miller, D. J.; Elam, J. W.; Albishri, H. M.; El-Hady, D. A.; Sun, Y.-K.; Curtiss, L. A.; Amine, K. *Nat Commun* **2013**, 4.
64. Lou, X. W.; Deng, D.; Lee, J. Y.; Feng, J.; Archer, L. A. *Adv. Mater.* **2008**, 20, (2), 258-262.
65. Ha, D.-H.; Islam, M. A.; Robinson, R. D. *Nano Lett.* **2012**, 12, (10), 5122-5130.
66. Bodnarchuk, M. I.; Kravchyk, K. V.; Krumeich, F.; Wang, S.; Kovalenko, M. V. *ACS Nano* **2014**, 8, (3), 2360-2368.
67. Kravchyk, K.; Protesescu, L.; Bodnarchuk, M. I.; Krumeich, F.; Yarema, M.; Walter, M.; Guntlin, C.; Kovalenko, M. V. *J. Am. Chem. Soc.* **2013**, 135, (11), 4199-4202.

CHAPTER 2

2 THE STRUCTURAL EVOLUTION AND DIFFUSION DURING THE CHEMICAL TRANSFORMATION FROM COBALT TO COBALT PHOSPHIDE NANOPARTICLES *

2.1 *Abstract*

We report the structural evolution and the diffusion processes which occur during the phase transformation of nanoparticle (NP) ϵ -Co to Co_2P to CoP, from a reaction with tri-*n*-octylphosphine (TOP). Extended X-ray absorption fine structure (EXAFS) investigations were used to elucidate the changes in the local structure of cobalt atoms which occur as the chemical transformation progresses. The lack of long-range order, spread in interatomic distances, and overall increase in mean-square disorder compared with bulk structure reveal the decrease in the NP structural order compared with bulk structure, which contributes to their deviation from bulk-like behavior. Results from EXAFS show both the Co_2P and CoP phases contain excess Co. Results from EXAFS, transmission electron microscopy, X-ray diffraction, and density functional theory calculations reveal that the inward diffusion of phosphorus is more favorable at the beginning of the transformation from ϵ -Co to Co_2P by forming of an amorphous Co-P shell, while retaining a crystalline cobalt core. When the major phase of sample turns to Co_2P , the diffusion processes reverse and cobalt atom out-

* Originally Published as: Ha, D.-H.; Moreau, L. M.; Bealing, C. R.; Zhang, H.; Hennig, R. G.; Robinson, R. D., The Structural Evolution and Diffusion During the Chemical Transformation from Cobalt to Cobalt Phosphide Nanoparticles. *J. Mater. Chem.* **2011**, 21, 11498-11510. Reprinted with Permission from The Royal Society of Chemistry.

diffusion is favored, leaving a hollow void, characteristic of the nanoscale Kirkendall effect. For the transformation from Co₂P to CoP theory predicts an outward diffusion of cobalt while the anion lattice remains intact. In real samples, however, the Co-rich nanoparticles continue Kirkendall hollowing. Knowledge about the transformation method and structural properties provides a means to tailor the synthesis and composition of the NPs to facilitate their use in applications.

2.2 Introduction

Complexity is an emerging and important area for chemical research. Just as living systems have adapted by demonstrating a hierarchical organization of structure and function over many length scales, materials can display very different properties depending on their length scale. While bulk materials are generally well understood and characterization methods to study them are mature, materials on the nanoscale can display complex behavior due to the emergence of novel and non-bulk properties that result from their small size.

Chemical transformations in bulk systems follow pathways that can be described by standard thermochemical kinetic models. Nanoscale systems, however, can display interesting and unpredictable transformation kinetics that increase the structural complexity of the original material.¹⁻¹⁰ Characterization of the transformation routes to form the complex final structure is one of the major challenges in nanoscience. A more complete understanding of the transformation

pathways would enable the prediction of the unique products resulting from chemical transformations of nanoparticles.

Structural characterization of nanoparticles is a multifaceted problem. Nanoscale materials present a challenge to both experimental and theoretical methods due to their small size and the importance of their surfaces. The finite size of nanoparticles creates broadened features in the experimental data from typical characterization tools, blurring distinctions between the features. In addition, the high surface to volume ratio places greater emphasis on knowing the structure of the surface and near-surface layers, which are difficult to characterize. For theoretical methods it is the lack of translational symmetry and the importance of the surfaces that complicate the study of nanoparticles. A combination of experimental and theoretical methods can overcome these problems and enable the determination of atomic ordering, kinetic changes and structural aspects of nanoparticles. Experimental methods based on X-rays and electron microscopy can provide important structural information. Computational studies such as density functional theory (DFT) calculations can provide information about the energetics and atomistic structures of surfaces and diffusion barriers.

X-ray absorption spectroscopy (XAS) is a powerful and versatile means to study structures of materials. When combined with other tools such as X-ray diffraction (XRD) and transmission electron microscopy (TEM), a nearly complete structural and morphological picture of a nanoparticle sample can be assembled. EXAFS measures real-space structural information, probing local range (within $\sim 8 \text{ \AA}$) around a central atom (in our case cobalt), and determining the partial radial distribution of atoms which are neighbors to the central atom.¹¹⁻¹² EXAFS and XRD

are complementary techniques: EXAFS probes local structure about a central atom while XRD reports long-range order.

EXAFS is a useful tool for probing the structural properties of nanoparticles.¹²⁻
¹³ Multiple-scattering path degeneracies can be reliably extracted from nanoparticle EXAFS data to yield information on size, shape, coordination number of the first shell, and surface orientation of nanoclusters.^{11, 14-15} Surface structure and coordination number at the surface can be determined for nanoparticles if the interior is assumed to have bulk-like coordination values.¹⁵⁻¹⁶ EXAFS has been used successfully to characterize structures in nanoparticle metal and bi-metallic clusters made through gas-phase synthesis on supports,^{11, 17-20} and metal and semiconductor nanoparticles made through solution-phase chemistry.^{15-16, 21-25}

The use of EXAFS to characterize chemical transformations in nanoparticles (NPs) is relatively rare. One study related to our work used EXAFS to characterize CoPt core-shell nanoparticles formed from a chemical transformation of Co metal NPs.²¹ In that study, the nanoparticle Co metal core is partially oxidized and the Pt ion is reduced (due to the favorable redox potential) on the core's surface to form the shell. Characterization of the core-shell nanoparticles was performed, however, only on fully-transformed samples of $\text{Co}_{\text{core}}\text{Pt}_{\text{shell}}$ nanoparticles. No attempt to document the intermediate stages was reported, therefore the information about the chemical transformation mechanism in this report is limited.

The precise structural characterization and understanding of chemical transformations in nanoparticles is not well understood. This is due partly to the lack

of well-defined model systems and difficulties in characterization. We have chosen the cobalt phosphide system as a model system to investigate this topic. Here we report on the chemical transformation of nanoparticle ϵ -Co metal into two phases of cobalt phosphide, Co_2P and CoP , studied through a combined analytical effort involving EXAFS, XRD, TEM, SQUID, and DFT. In this study the nanoparticles of Co metal are transformed to cobalt phosphide phases by the addition of tri-*n*-octylphosphine (TOP) (**Fig. 2.1**). The nanoparticle Co metal core is reacted with TOP to successively transform the nanoparticle into Co_2P and then CoP . Six samples are prepared that represent different stages of this transformation: samples are arrested during sequential reaction stages and cleaned and prepared for analysis.

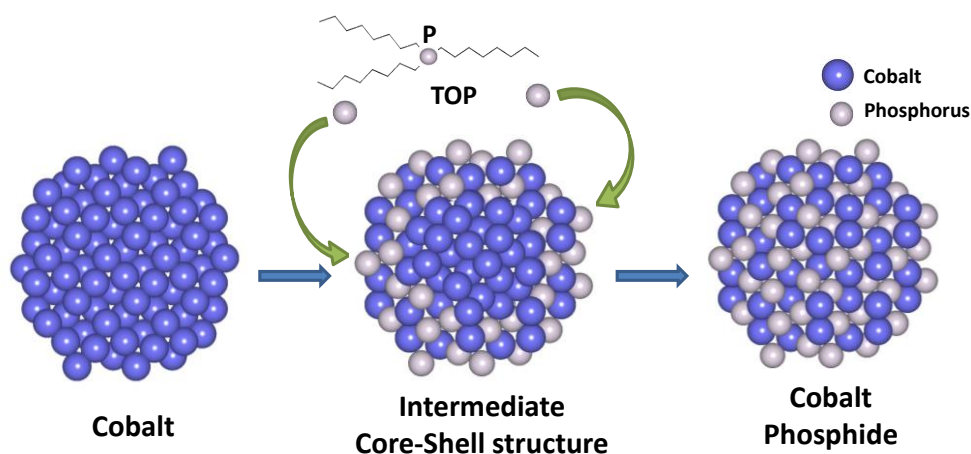


Figure 2.1 The evolutional schematics of transition from cobalt to cobalt phosphide nanocrystals.

Metal phosphides are particularly interesting materials due to their wide range of unique properties including ferromagnetism, superconductivity, catalytic activity, magnetoresistance, and magnetocaloric effects.²⁶⁻²⁹ Cobalt phosphides have recently received increased attention due to their catalytic and magnetic properties as well as their potential as a promising anode material.³⁰⁻³⁴ Recently, we have reported a controlled synthesis of hyperbranched Co₂P using tri-*n*-octylphosphine oxide (TOPO) as a phosphorus source.³⁵ Previously reported syntheses of cobalt phosphides, however, displayed a lack of pure phase control mainly due to having multiple energetically favorable stoichiometries.³⁶⁻³⁷ The changes in nanoparticle properties during this phase transition also remained unknown, which inhibits improvement of the synthesis and functionalization of these promising nanostructures.

In particular, in the cobalt to cobalt phosphide transformation reaction we seek to understand: 1) kinetics of the nanoscale Kirkendall transformation, 2) diffusion processes during chemical conversion, 3) shell growth through the nanoscale Kirkendall effect, 4) structural changes that occur during chemical transformation, 5) structural comparison between nanoparticles and bulk materials, and 6) structural effects on magnetic behavior.

Our findings through this study include various structural and behavioral insights into the Co metal to cobalt phosphide transformation reaction. During the transformation from ϵ -Co to Co₂P, an interesting crossover point was determined for the diffusivities of cobalt and phosphorus: phosphorus is the faster diffusing species in ϵ -Co, while cobalt is the faster diffusing species in Co₂P. In Co₂P NPs the Co–Co coordination remains higher than expected due to retention of a cobalt-rich core. The

transformation process from Co_2P to CoP is different from that of $\epsilon\text{-Co}$ to Co_2P . Theoretical calculations predicted no further hollowing for this transformation, but excess Co in real samples led to further Kirkendall hollowing. The information obtained from this study of nanoparticle transformation from cobalt to cobalt phosphide provides a means to improve synthesis techniques as well as provide insight into the control of structural and magnetic properties, in order to optimize the nanoparticles for use in applications.

2.3 Methods

2.3.1 Synthesis and Characterizations

All synthesis was carried out in a dry, oxygen-free, di-nitrogen atmosphere by employing standard Schlenk line and glove box techniques. Acetone ($\geq 99.5\%$), hexanes ($\geq 98.5\%$), ethanol ($\geq 99.5\%$), oleic acid (99%), tri-*n*-octylphosphine oxide (TOPO, 99%), oleylamine (70%), 1,2-dichlorobenzene (99%, anhydrous) and 1-octadecene (90%) were purchased from Aldrich. Tri-*n*-octylphosphine (TOP, 97%) and $\text{Co}_2(\text{CO})_8$ were purchased from Strem Chemicals and Alfa Aesar respectively. Six samples were produced at distinct stages throughout the chemical transformation of Co metal into Co_2P and CoP . The samples are labeled from **A** to **F**, with **A** corresponding to $\epsilon\text{-Co}$ metal, **B** to **E** corresponding to intermediate structures and **F** corresponding to CoP (as determined through XRD). Details of the synthesis are as follows.

The synthesis of ϵ -Co NPs (sample **A**) followed standard procedures.³⁸ A N_2 fluxed flask was filled with TOPO (0.1 g). After adding 0.09 g (0.32 mmol) of oleic acid, which is used as a surfactant, dissolved in 12 mL of 1,2-dichlorobenzene, the solution was heated. When the temperature of the solution reached 180 °C, 0.52 g (1.52 mmol) of $Co_2(CO)_8$ dissolved in 4 mL of 1,2-dichlorobenzene was quickly injected. After the reaction progressed for 4 mins, the heating mantle was removed and the reaction solution was cooled down in a water bath. The Co NPs were purified by adding ethanol and centrifuged. The supernatant was removed, and the NPs were redispersed in hexanes. The precipitation/redispersion process was performed twice overall.

To synthesize the intermediate phases and Co_2P NPs (samples **B-E**) a flask which was vacuumed and fluxed with N_2 , was filled with 12 mL of 1-octadecene and 3 mL of tri-*n*-octylphosphine. After the solution was heated up to 300 °C, the pre-synthesized ϵ -Co NPs (~150 mg) dispersed in the mixture of 3 mL 1-octadecene and 3 mL oleylamine were quickly injected into the solution and the reaction proceeded for varied amounts of time, as described in **Table 2.1**. The solution was cooled to room temperature by removal of the heating mantle. The NPs were separated by centrifugation and washed twice with acetone/hexanes.

Table 2.1 The reaction conditions of the samples B-F

	B	C	D (Co₂P)	E	F (CoP)
Reaction time	7mins	10mins	1hr	2hr	2.5hr
Temperature(°C)	300	300	300	300	350
TOP (mL)	3	3	3	3	15
Oleylamine (mL)	3	3	3	3	6
1-octadecene(mL)	15	15	15	15	

In order to prepare CoP phase (sample **F**), slightly more aggressive reaction conditions compared to previous samples were necessary.³⁹ A mixture of ϵ -Co NPs (~150 mg), 15 mL TOP, and 6 mL oleylamine was heated to 350 °C and kept for 2.5 hr. The solution was cooled to room temperature by removal of the heating mantle. The NPs were separated by centrifugation and washed twice with acetone/hexanes.

Nanoparticles were characterized by conventional and high-resolution TEM, X-ray powder diffraction (XRD), EXAFS, and SQUID magnetometry. The conventional TEM images were recorded on an FEI Tecnai T12 operating at 120 kV; the high-resolution TEM images were collected on an FEI Tecnai F20 operating at 200 kV. For statistical analysis at least 200 particles were analyzed. XRD data was collected on a Scintag Theta-Theta X-ray diffractometer (Cu K α radiation).

XAS spectra of the Co K-edge were obtained using the C-line station at the Cornell High Energy Synchrotron Source (CHESS) using a Si(111) monochromator over an energy range of 7.68 – 8.20keV. The nanoparticle samples were diluted to a concentration of 25 mM suspended in toluene, and placed in a 2 mm diameter

cylindrical quartz capillary. The spectra were obtained using a four-element fluorescence detector, calibrated with a Co metal foil. An Fe filter was used to control the signal level. For each sample, a minimum of 16 scans at 4 spectra/scan over these 16 scans were averaged for the accuracy of the results, accommodating outliers. Self-absorption was not a concern with the fluorescence detection because the samples were sufficiently dilute in solution at 25 mM. Also, the absorption length of cobalt at 7.7 keV is on a μm scale, which is much larger than the particle size. The fluorescence measurements were proportional to the absorption coefficient, $\mu(E)$, which produces a spectrum which describes the strength of X-ray absorption as a function of energy.¹²

The raw spectra were averaged and processed using the ATHENA software.⁴⁰ This processing included edge determination from the first inflection point in the absorption data, background subtraction using the AUTOBK algorithm, and normalization of the EXAFS modulations (greater than 150 eV above the edge).⁴¹ A k-weight of 1 was chosen for both the Fourier transform (FT) of the experimental data and the theoretical fitting because phosphorus and oxygen are low-Z scattering elements which will scatter mainly at lower k-values.⁴² Also, use of a higher k-weight did not compensate for the damping in amplitude due to the high variations in absorber-scatterer distance characteristically observed in nanoparticle spectra.²⁴ Additionally, as fitting was performed only to the first coordination shell, there was no need to use a higher k-weighting to emphasize high k behavior.¹² The spectra were converted from E-space, to k-space, and then Fourier transformed, according to standard procedure¹² and fitted to theory (see supplementary materials).¹³ In the FT

spectrum, peaks appear at the real space position related to a particular shell from the absorbing atom.⁴³ A phase shift was applied by adding the appropriate pair of known phase shifts of the absorbing and backscattering atom (Co and Co or P respectively).

The data, after processing, were then analyzed by the ab-initio method with ARTEMIS.⁴⁰ Crystal structures from theory were input using ATOMS.⁴⁴ By fitting well-matched theoretical pathways to the experimental spectra by allowing structural parameters to deviate from the theoretical bulk structures, specific structural information could be determined such as coordination number, spacing, and mean-square disorder, in accordance with the EXAFS equation^{13, 43, 45-46}

$$\chi(k) = \sum_{\Gamma} \left[\frac{N_{\Gamma} S_0^2 F_{\Gamma}(k)}{2kR_{\Gamma}^2} e^{-2k^2\sigma_{\Gamma}^2} e^{-2R_{\Gamma}/\lambda(k)} \times \sin(2kR_{\Gamma} + \phi_{\Gamma}(k)) \right] \quad (1)$$

Equation (1) above describes the parameters that comprise the EXAFS model. Knowledge of particular parameters enables the determination of others. Γ counts the individual scattering pathways that are summed over. Parameter k is the photoelectron wavevector. $F_{\Gamma}(k)$, the scattering amplitude, and $\lambda(k)$, the mean free path of inelastically-scattered photoelectrons which contribute to the reduction of the scattering amplitude, are computed by the analysis program. The phase shift $\phi_{\Gamma}(k)$ is a function of the absorbing and scattering atom and takes into account the fact that the electron is in the presence of potentials.⁴³ The amplitude reduction factor, S_0^2 , theoretically accepted to be between 0.7 and 1 was set to 0.85 for purposes of extracting the coordination number.⁴⁵ The parameters allowed to float during fitting were degeneracy N_{Γ} , which represents the number of atoms at the same distance from the absorbing atom, R_{Γ} , the effective distance from the absorbing atom to the

scattering atom, and σ_F^2 , the mean square disorder, which includes components from structural disorder as well as thermal disorder (Debye-Waller factor).⁴³

2.3.2 Calculation of Diffusion Activation Barriers

Diffusion activation barriers were calculated as

$$E^{diffusion\ activation} = E^f + E^{barrier} \quad (2)$$

where E^f is the formation energy of the cell including the defect, and $E^{barrier}$ is the energy barrier to migration of the diffusing species, calculated using the nudged elastic band (NEB) method. Formation energies and migration barriers were calculated using the density functional theory (DFT) in each case. Further details are given below.

An ϵ -Co cell which included a single vacancy defect was created by removing either a type I or type II Co atom from the 20-atom ϵ -Co cell (see supplementary materials for detailed structure information). Formation energies for the vacancy defects were calculated as

$$E_{V(A)}^f = E[\epsilon\text{-Co}_{19}\text{V}(A)] - \frac{19}{20}E[\epsilon\text{-Co}_{20}] \quad (3)$$

where $E[\epsilon\text{-Co}_{20}]$ denotes the total energy of the 20-atom ϵ -Co cell, and $E[\epsilon\text{-Co}_{19}\text{V}(A)]$ denotes the total energy of the same cell including a vacancy on a site of type A = I or II. The calculated formation energies are $E_{\epsilon\text{-Co}_{19}\text{V}(I)}^f = 1.34$ eV and $E_{\epsilon\text{-Co}_{19}\text{V}(II)}^f = 1.79$ eV. Since the formation energy of vacancies in type I sites is significantly lower than that for type II sites, only diffusion of Co through type I sites was considered. Note that the type I sublattice forms a network of nearest neighbor

sites such that it is possible for an atom to diffuse through an entire crystal of ϵ -Co on the type I site sublattice.

The barrier to migration of Co atoms from a type I site to a neighboring type I vacancy $E_{Co(I)\leftrightarrow V(I)}^{barrier}$ was calculated using the NEB method. Initial atomic coordinates used for the images in the NEB calculation were generated by linearly interpolating between those of the endpoints. The total activation barrier for Co atoms through vacant type I sites was calculated as

$$E_{Co(I)\leftrightarrow V(I)}^{diffusion\ activation} = E_{V(I)}^f + E_{Co(I)\leftrightarrow V(I)}^{barrier} \quad (4)$$

This value was calculated as $E_{Co(I)\leftrightarrow V(I)}^{diffusion\ activation} = 1.40$ eV.

P atoms can diffuse through the ϵ -Co crystal through either a substitutional or interstitial mechanism. Considering first substitutional defects, the formation energy for an ϵ -Co cell including a P atom substituted for a type I Co atom was calculated as $E_{P(I)}^f = -1.00$ eV compared to $E_{P(II)}^f = -0.37$ eV for type II substitution. Since the formation energy $E_{P(I)}^f$ is significantly lower than $E_{P(II)}^f$, only diffusion of P through type I Co sites was considered. An ϵ -Co cell including both a single vacancy at a type I site, and a P atom substituted for a type I Co atom (which neighbors the vacancy) was created. The formation energy of this cell was calculated as

$$E_{V(I)P(I)}^f = E[\epsilon\text{-Co}_{18}V(I)P(I)] - \frac{18}{20}E[\epsilon\text{-Co}_{20}] - \frac{1}{4}E[\text{b-P}_4] \quad (5)$$

where $E[\text{b-P}_4]$ denotes the reference energy of a cell of black phosphorus (used to provide a reference chemical potential for P in our calculations), containing four P atoms. With the barrier to migration calculated in the same way as described for Co

diffusion, the total diffusion activation barrier for P atoms through vacant type I sites was found to be $E_{P(I)\leftrightarrow V(I)}^{diffusion\ activation} = 0.58\text{ eV}$.

A number of interstitial P sites within the ϵ -Co cell were attempted, in order to find favorable interstitial defects. The most favorable site attempted for the P atom for the ϵ -Co₂₀ cell is given by the fractional coordinates (0.375, 0.375, 0.375). Symmetry equivalent positions within the cell are given by the fractional coordinates (0.875, 0.125, 0.625), (0.625, 0.875, 0.125), and (0.125, 0.625, 0.875). The formation energy for a ϵ -Co₂₀ cell containing an interstitial P defect at this position is given by

$$E_{P(int)}^f = E[\epsilon\text{-Co}_{20}\text{P}(int)] - E[\epsilon\text{-Co}_{20}] - \frac{1}{4}E[\text{b-P}_4] \quad (6)$$

The NEB method was used to calculate the barrier to migration between adjacent interstitial sites within the ϵ -Co₂₀ cell, and the total diffusion activation barrier for P atoms through interstitial sites was found to be $E_{P(int)\leftrightarrow P(int)}^{diffusion\ activation} = 1.97\text{ eV}$.

The diffusion of Co and P atoms in Co₂P was also investigated. Firstly a Co₂P structure containing a vacancy defect was created; this was achieved by the removal of one of the four type I-Co₂P Co atoms, or of one of the four type II-Co₂P atoms from a Co₈P₄ cell. The defect formation energies relative to that of the Co₂P structure are

$$E_{Co_7P_4V(I-Co_2P)}^f - E_{Co_2P}^f = 0.55\text{ eV}, \text{ and } E_{Co_7P_4V(II-Co_2P)}^f - E_{Co_2P}^f = 0.65\text{ eV}, \text{ hence}$$

only diffusion of Co through type I-Co₂P sites was considered. The barrier to migration of the Co atom was calculated using the NEB method; the total diffusion

activation barrier for Co through type I-Co₂P sites was found to be

$$E_{Co(I-Co_2P) \leftrightarrow V(I-Co_2P)}^{diffusion\ activation} = 2.24\text{ eV.}$$

The diffusion activation barrier for P in Co₂P was calculated in a similar way. A P atom was removed from the Co₈P₄ cell to create a vacancy; the barrier to migration of a neighboring P atom into the vacancy was calculated using the NEB method. The diffusion activation barrier for P in Co₂P was found to be 5.80 eV.

2.4 Results

TEM was used to characterize the nanoparticle morphology through the phase transformations (**Fig. 2.2A-F** and **Fig. A.2**). The ϵ -cobalt nanoparticles of sample **A** are monodisperse in shape and size (11.9 nm, std. dev. 8%) with a spherical morphology (**Fig. 2.2A**). Such particle monodispersity is particularly important for EXAFS analysis, which gives insight into average structure.⁴³ The NPs in sample **B** increase slightly in size and dispersity (12.4 nm, std. dev. 10%) but retain the similar spherical morphology of **A** (**Fig. 2.2B**). The nanoparticles of sample **C** further increase in size and dispersity (13.1 nm, std. dev. 12%), and begin to transform into polyhedrons of irregular shape (**Fig. 2.2C**). Some of the particles (ca. 10%) in sample **C** show a darker core, indicating the onset of the nanoscale Kirkendall effect. The Kirkendall effect arises from the asymmetric diffusivities of atoms and ions in a material.¹ A dark center is commonly seen at the onset of Kirkendall structural hollowing within the nanoparticle core, after transformation is initiated and a shell begins to develop.^{1, 47} Completely hollow structures are observed in sample **D** (ca.

70% of the NPs are hollow with hole size 3.5 nm, std. dev. 17%) as the Kirkendall effect proceeds (**Fig. 2.2D**). The NP size distribution of sample **D** increases (12.8 nm, std. dev. 16%). Sample **E** shows an increase in the average nanoparticle size and dispersity (15.7 nm, std. dev. 20%) (**Fig. 2.2E**). Additionally, only about 30% of the nanoparticles in **E** show hollow structure and there is an increase in the average size of hollow voids (5.5 nm, std. dev. 32%). Finally, sample **F** shows a slight size increase from sample **E** (16.2 nm, std. dev. 20%) (**Fig. 2.2F**). However, only some of **F** (ca. 20%) show clear hollow voids. The average size of voids decreases from sample **E** to sample **F** (void size for **F** ~4 nm, std. dev. 24%).⁴⁸ This morphological difference between samples **E** and **F** might be the consequence of different reaction conditions: sample **F** is synthesized at a higher temperature for a longer time so it is possible that an annealing of the particle occurred, or the slightly modified reaction conditions for sample **F** favored smaller void formation. **Fig. 2.2** shows the TEM images of these particles with corresponding unit cells for the three distinct phases as determined by XRD (see **Fig. A.1** for the summary of the results).

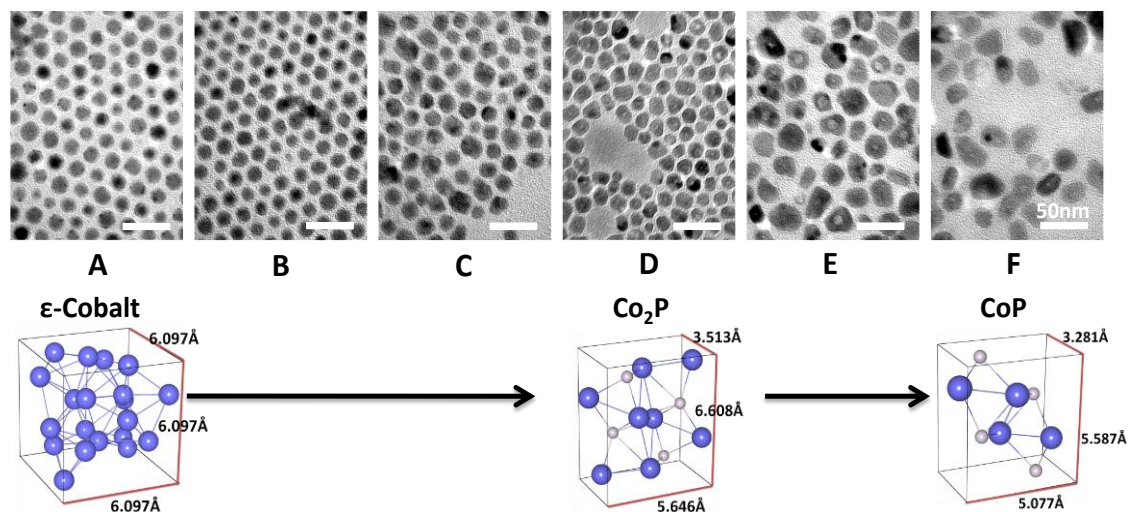


Figure 2.2 TEM images of the samples A–F (top) and corresponding crystal structures (bottom). The crystal structures shown at bottom (right to left ϵ -Co, Co_2P and CoP) correspond to sample **A**, **D**, and **F** respectively, as determined from XRD. All scale bars are 50 nm. The larger blue atoms correspond to cobalt, the smaller gray atoms are phosphorus.

XRD (**Fig. 2.3**) data show a phase transformation from pure Co metal to two different cobalt phosphide phases (Co_2P and CoP). Sample **A** shows ϵ -Co, which is the phase of Co metal most commonly reported for nanoparticles (**Fig. 2.3**, spectrum A).^{38, 49} The XRD pattern of sample **B** shows the ϵ -Co phase still present as the majority phase (**Fig. 2.3**, spectrum B). The pattern of sample **C** shows a dramatic transition from **B**; there is a strong peak at 41° , and two additional peaks at 52° and 56° (**Fig. 2.3**, spectrum C). These peaks correspond to the Co_2P phase. The intensities of these peaks are dominant in the spectrum indicating that Co_2P is the majority phase. A small presence of ϵ -Co crystal remains in sample **C**, but the

strongest peak of ϵ -Co at 44.6° (seen clearly in samples **A** and **B**) is decreased significantly and the ϵ -Co peaks at 47.1° and 49.6° also are greatly diminished. The broadness of the peak at 44.6° is attributed to overlapping of the contribution from both ϵ -Co and Co_2P . The XRD pattern of **D** shows a crystalline Co_2P phase with no evidence of any other crystal phases (**Fig. 2.3**, spectrum D). Also, new Co_2P peaks emerge at higher 2θ in sample **D** which are very weak in sample **C**, indicating the improved crystallinity. The XRD pattern of sample **E** exhibits a mixture of Co_2P and CoP phase (**Fig. 2.3**, spectrum E). Unlike the two other intermediate samples **B** and **C**, which do not show well-ordered crystallinity, the intensities of the peaks are stronger in sample **E**, indicating there is a mixture of relatively well-ordered Co_2P and CoP crystalline phases. The XRD spectrum of sample **F** confirms that its phase is CoP with well-defined crystalline order (**Fig. 2.3**, spectrum F).

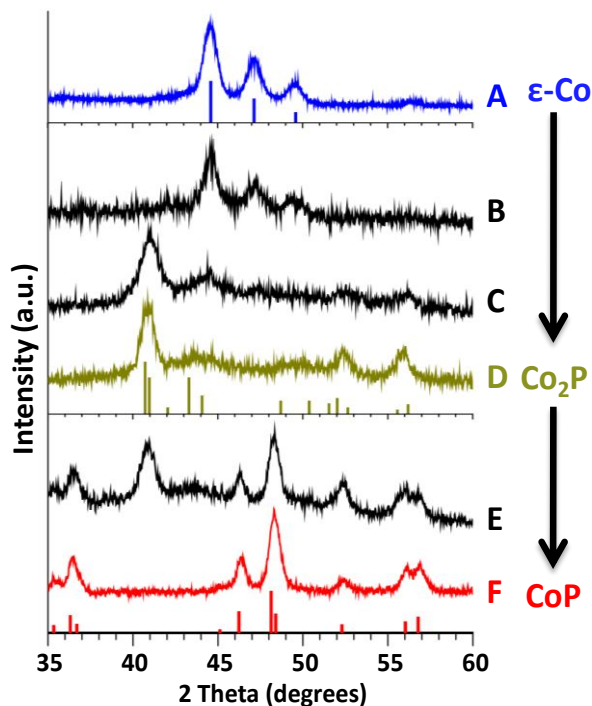


Figure 2.3 X-ray diffraction patterns of samples from A to F. ϵ -Co, Co_2P and CoP crystal phase matched well with sample A, D, and F respectively.

Co K-edge EXAFS was used to investigate the local atomic radial structure around a central cobalt atom through the ϵ -Co to Co_2P and CoP chemical phase transformation. Only fitting to the first coordination shell (first peak in the FT spectrum, shown in **Fig. 2.4**) was performed due to the sharp decrease in the EXAFS amplitude for second and higher order shells because of increased disorder in addition to the presence of low-Z scatterers.¹² Qualitative changes in the overall first shell FT spectrum for the transformation are as follows (**Fig. 2.4a**): 1) the first shell peak evolves from a doublet in sample **A**, to an asymmetric singlet in **B** and **C**; 2) two small peaks appear in sample **D** but the doublet is less defined than that of sample **A**; 3) the

peaks merge into one broad peak in sample **E**; and 4) the peak is sharpened in sample **F** with a significant second shell contribution.

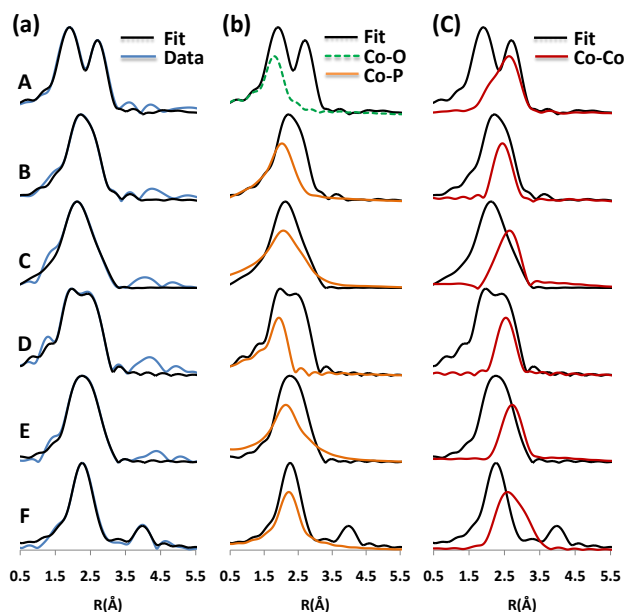


Figure 2.4 Fourier-transformed k -weighted EXAFS data and simulated fitting results for samples A–F. (a) Co K-edge FT-EXAFS experimental data (blue) and first-shell fitting results (dotted black). (b) First-shell fitting (dotted black) and the contributions of the Co–O (dashed green) and Co–P (orange) pathways. (c) First-shell fitting (dotted black) and the contributions of the Co–Co (red) pathways. The sums are normalized path contributions. The intensities of the Co–O, Co–P, and Co–Co contributions are scaled for convenient viewing and do not represent absolute intensities. Vertical axis is FT magnitude in arbitrary units. The Co–Co and Co–P pathways can be again broken down into contributions from the ϵ -Co, Co_2P , and CoP phases (not shown here: see supporting information).

Table 2.2 The sum of experimental path degeneracies (coordination number)

	Co-Co		Co-P	
	Results	Bulk theoretical value	Results	Bulk theoretical value
A	11.1	12		
B	10.2		3.4	
C	10.2		4.4	
D	9.9	9	4.7	4.5
E	8.1		5.9	
F	7.5	6	5.5	6

The EXAFS spectrum from sample **A** displays two distinct peaks. The first strong peak at a short distance is attributed to cobalt-oxygen bonding (**Fig. 2.4b**, spectrum **A**). Cobalt oxide is known to form on the surface of Co metal nanoparticles directly after synthesis, and has previously been found on the surface of ϵ -Co NPs.^{24, 49-50} Since cobalt oxide is not evident in the XRD spectrum of **A** it may exist as only a few monolayers with amorphous or polycrystalline order. From our experimental EXAFS fittings, the degeneracy of the cobalt-oxygen path is 0.98. This value can be compared to the bulk value of 6 (**Table 2.2**). The degeneracy value is a quantitative measure of the average multiplicity for an individual scattering path. Since the value found here is about 1/6 of the bulk value, it indicates that fewer oxygen atoms are located around the cobalt, on average. The concentration of the atoms on the surface can be calculated by a simple model.⁵¹ Based on the model, the fraction of the atoms on the surface compared to the total number of atoms in one of our 11.9 nm ϵ -Co NP is approximately 9% (see Appendix A). When we consider the degeneracy of Co-O

in our NPs which is 1/6 (~0.17) of bulk, this equals approximately two unit cell layers of cobalt oxide on the surface. These results support the argument that only several atomic layers become oxidized.

Table 2.3 Co K-Edge EXAFS structure fitting parameters of samples A-F

Sample	Path ^a	N ^b	ΔE_0 (eV)	ΔR (Å) ^c	$\sigma^2 (\times 10^{-3} \text{ \AA}^2)$
A	Co _I – Co _I	1.12	8.31	-0.14	15.0
	Co _I – Co _{II} /	7.73	9.99	0.02	17.3
	Co _{II} – Co _I				
	Co _{II} – Co _{II}	2.23	-7.01	0.04	11.8
	Co – O	0.98	-8.74	-0.23	2.1
B	Co _I – Co	4.32	-4.66	0.14	9.9
	Co _{II} – Co	5.88	6.90	-0.02	9.1
	Co _A – P	2.45	-8.96	-0.16	7.4
	Co _B – P	0.96	-9.99	0.02	11.5
C	Co _A – P	3.33	-10	-0.15	11.9
	Co _B – P	1.08	-7.47	-0.07	5.8
	Co _A – Co	7.30	-1.27	-0.02	12.7
	Co _B – Co	2.85	-5.79	-0.16	6.1
D	Co _A – P	2.83	-10	-0.11	10.5
	Co _B – P	1.84	-6.44	-0.07	2.7
	Co _A – Co	6.30	-1.55	-0.08	5.4
	Co _B – Co	3.59	-4.12	-0.03	23.7
E	Co _A – P	3.08	-10	-0.09	17.3
	Co _B – P	2.84	-2.55	-0.02	6.9
	Co _A – Co	4.90	1.59	-0.06	20.0
	Co _B – Co	3.19	-0.64	0.02	12.4
F	Co – P shell 1	5.52	-3.03	-0.04	8.6
	Co – Co shell 1	7.52	-6.49	-0.13	10.0
	Co – P shell 2	8.48	5.08	-0.06	3.8
	Co – Co shell 2	2.46	1.45	0.05	3.0

^a I and II correspond to type I and II in ϵ -Co and A and B correspond to type I and II in Co₂P

^b Reasonable estimates of the errors are $\pm 10\%$ ^{16, 64}

^c Reasonable estimates of the errors are $\pm 0.01 \text{ \AA}$ ⁶⁴

Significant atomic change is apparent between the EXAFS spectra of samples **A** and **B**. Through first-shell fittings (**Fig. 2.4** and **Table 2.3**) we are able to assign the doublet peaks in **A** to a Co–O contribution with a shorter bonding distance and Co–Co. Two distinct peaks in sample **A** around 1.9 Å and 2.7 Å merge into one broad peak with a small shoulder and longer radial distance in sample **B**. In sample **B** we are able to deconvolve this asymmetric single peak into contributions from Co–P and Co–Co bonds with shorter and longer bond lengths, respectively. If we include the cobalt-oxygen scattering pathway into the fit for sample **B** a more accurate fit is not achieved, implying that the cobalt-oxygen bonds are removed during the reaction of TOP with the nanoparticle surface.

In sample **C**, Co₂P is the majority phase detected from the XRD pattern with minor contributions from ε-Co metal, but fittings of the EXAFS data show that there is significant ε-Co metal remaining (**Fig. 2.4b,c** spectrum C, and supporting information, and **Table 2.3**). We determine that there is significant ε-Co present by comparing the experimental Co–Co degeneracy and R spacing values to those in the ε-Co and Co₂P theoretical structures. Our experimental Co–Co degeneracy (10.2) is much higher than theoretical values of Co₂P (9). We are able to distinguish Co–Co contributions from ε-Co and Co₂P because the Co–Co average interatomic distance from ε-Co metal (our experimental value: 2.54 Å, theoretical value: 2.51 Å) is shorter than that from Co₂P (experimental value: 2.67 Å, theoretical value: 2.70 Å). The EXAFS and XRD data imply that the remaining ε-Co metal in sample **C** is composed of very small crystalline domains. The ε-Co core starts as a single crystal. It is unlikely that the

remaining metal core is being transformed into a polycrystalline form. Most likely, the ϵ -Co metal has been reduced in size to only a very small domain.

The EXAFS data show a clear transition from sample **C** to **D**; sample **D** shows two peaks which correspond to the two distinct interatomic pathways, Co–P at 2.26 Å and Co–Co at 2.67 Å, while the EXAFS data only shows one peak for sample **C** (**Fig. 2.4**, spectrum C and D). As shown in total sums of pathways for Co–P (**Fig. 2.4b**, spectrum C and D), the Co–P contribution in sample **D** is narrower than in **C** implying more uniform Co–P distances in sample **D**, which is characteristic of a crystal. (Broad peaks generally indicate that atoms are not well organized into exact crystal positions.)⁵² The coordination number (CN) of cobalt to phosphorus is lower in sample **C** than in sample **D** (4.4 in **C** vs. 4.7 in **D**, **Table 2.2**). The bulk value for coordination in Co₂P is 4.5. The slightly higher CN for **D** could imply a thin shell of phosphorus-rich cobalt phosphide on the surface. The high crystalline order of sample **D** provides two distinct, narrow peaks from Co–P and Co–Co pathways in the EXAFS spectrum, which is not the case for the Co–P pathways in intermediate phases **B** and **C** (compare **Fig. 2.4b** spectra B, C, D and **Fig. 2.4c** spectra B, C, D), nor the Co–Co pathways in sample **C**, with increased deviation from the ϵ -Co structure. The narrowness of the peaks from both contributions in sample **D** implies that the interatomic distances are well organized which results in a well ordered crystallinity, as a favorable stoichiometric ratio is reached. The EXAFS and XRD data confirm that sample **D** is a converted, well-ordered phase of Co₂P. Despite the increased order within the structure, and pure Co₂P phase shown from XRD results, EXAFS data reveal excess cobalt (experimental CN: 9.9 vs. theoretical CN: 9). This may be a result

of retention of a Co-rich core, resulting in a particle that, although more well-ordered than intermediate samples **B** and **C**, still lacks a perfect crystalline Co₂P structure.

The EXAFS data for sample **E** reveal a broad distribution of Co–P bonds, similar to that seen in the intermediate sample **C** (**Fig. 2.4b**, spectrum E). The Co–P and Co–Co interatomic distances of sample **E** (2.28 Å and 2.69 Å respectively) are slightly larger than those of sample **D** (2.26 Å and 2.67 Å respectively). The overall shape is a single, broad peak centered roughly between the two peaks of sample **D**. The shape change of the peak from sample **D** to **E** (two peaks to one peak) shows the change in atomic positions, which overlap over a broad distribution instead of forming two distinct contributions. Such a change in distribution indicates a decrease in ordered crystallinity⁵² in **E** compared to sample **D**, despite the fact that the average length of both Co–P and Co–Co increased.

XRD data show that sample **F** is fully converted to CoP. However, EXAFS results indicate that the sample has more cobalt than that of a perfect CoP phase. The average sum of path degeneracies (CN) of Co–P and Co–Co in sample **F** are 5.5 and 7.5, respectively, while the theoretical bulk values for both are 6 (**Table 2.2**). Even when we take into account the ~10% error in the degeneracy value, the Co–Co coordination is higher than that of perfect CoP crystal. This indicates that there is a small excess of Co–Co bonds with short range order that cannot be detected by XRD. Nevertheless, this sample has the best crystallinity of all the samples, evident in the 2nd shell peak in the EXAFS data which is indicative of long range order (**Fig. 2.4a**, spectrum F).¹² The superior crystallinity is likely because the reaction was carried out for a longer time and at a higher temperature than the other reactions, leading to

conditions more favorable for crystal formation. This well-defined crystallinity present in sample **F** results in a sharp first shell EXAFS peak and well defined second shell peak. This sample has the largest NP size among the samples, which corresponds to more bulk-like behavior with greater long range order.

In order to further explore structural evolution, the EXAFS spectrum for each sample was analyzed for changes in radial structure. The average interatomic distance for Co–P and Co–Co were calculated from the EXAFS data by examining an average of the path distances experimentally found to compose the structures and examining their deviation from bulk/standard distances (see Appendix A). Such data reveal the general trends in interatomic spacing as the transformation progresses. An interesting result emerges: the Co–Co distances gradually increase from sample **A** to **F** while those of Co–P stay relatively constant. These results indicate that the interatomic distances between cobalt atoms are lengthened by introducing phosphorus atoms into the system. The Co–Co bond lengths reflect those of bulk materials, as the Co–Co spacings in CoP are longer on average than those of Co₂P, which are longer than those of ϵ -Co. It appears that the Co–P bonds form at energetically stable distances initially, even as additional phosphorus atoms diffuse into the system, and remained fixed in their positions, resulting in a constant average interatomic distance for Co–P pathways.

The average degeneracies of the Co–Co and Co–P scattering pathways present in the nanoparticle samples and those expected for bulk materials are plotted in **Fig. 2.5**. The overall trend of the Co–Co and Co–P coordination mirrors that observed in bulk materials: the Co–Co coordination decreases gradually and the Co–P increases

gradually, as the reaction continues to transform from Co metal into Co₂P and then CoP. The slight deviation between NPs and bulk materials for sample **A** (**Fig. 2.5**) may be attributed to the surface oxidation of the cobalt NPs, and also for the decrease in coordination as a result of the large number of surface atoms.⁵³⁻⁵⁴ For samples **D** and **F**, some parts of the NPs may contain an amorphous Co-rich region due to the faster outward diffusion of cobalt, resulting in greater cobalt coordination than expected stoichiometrically. Additionally, the mean square disorder term is overall significantly higher than that expected for cobalt bonding in bulk structure ($\sigma^2 \sim 0.003 \text{ \AA}^2$) (see **Table 2.3**).⁵⁵ This is an observation typically seen in nanoparticles, whose bonds reveal a greater amount of structural disorder due to surface defects.^{24,55} This is likely a result of both large spreads in interatomic distances compared to bulk structure, which are observed also from the FTs of the spectral data (particularly for intermediate phases). It is also possible that thermal disorder, which increases with higher values of k is contributing to this increase in addition to the greater characteristic structural disorder which our spectral data support. R-factor values between 0.0002 and 0.0082 for each of the theoretical fittings as well as ΔE_0 , which represents energy shift,^{12,41} values within 10 eV support data reliability (see Appendix A and **Table 2.3**).

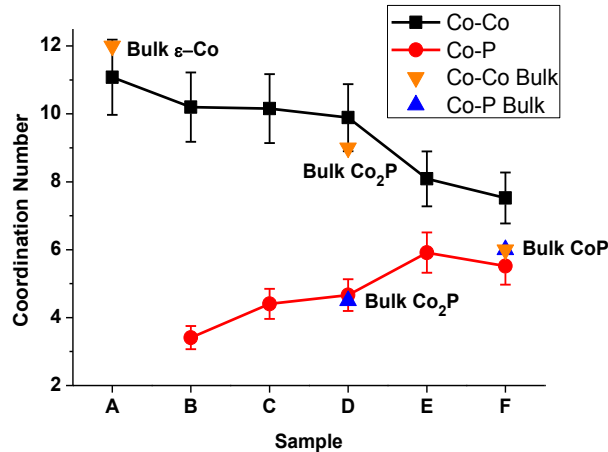


Figure 2.5 The coordination numbers of Co–Co and Co–P from the fitting results and those of bulk theoretical values. Labels have been added to clarify the bulk phases (e.g., At sample **A** Co–Co bonding corresponds to that in ϵ -Co phase). Reasonable estimates of the errors are $\pm 10\%$ ^{16, 64}

The transition in magnetic properties from sample **A** to **F** was analyzed by utilizing superconducting quantum interference device (SQUID, Quantum Design MPMS-XL). **Fig. 2.6** shows magnetic hysteresis loops of samples measured at 2K. Sample **A** shows ferromagnetic behavior, with a coercivity of 1800 Oe. There is a significant coercivity drop observed in sample **B** compared to **A** (~280 Oe). Even though the major phase of sample **B** is ϵ -Co from XRD, the ferromagnetic behavior was suppressed greatly which indicates the magnetic properties are sensitive. A gradual decrease in ferromagnetic behavior was shown in sample **C** (coercivity ~200 Oe). Samples **D** and **F** showed paramagnetic behavior which corresponds to the behavior characteristic to bulk Co_2P and CoP , which are both known as paramagnetic

materials.⁵⁶ Sample **E** which is an intermediate sample between sample **D** and **F**, also appeared to be paramagnetic.

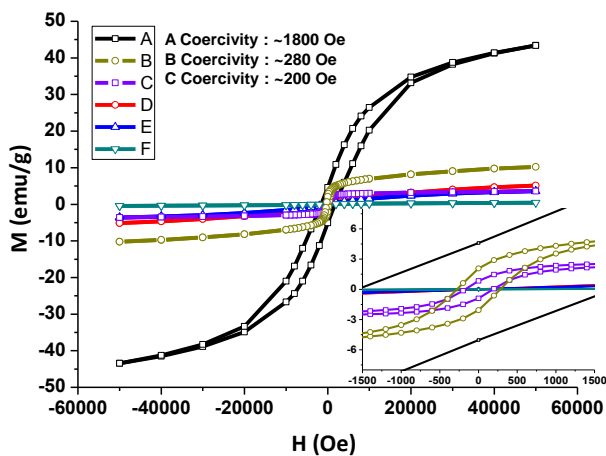


Figure 2.6 The magnetic hysteresis loops of the samples at 2K. The hysteresis loops gradually shrink from sample **A** through **B** to **C**. Coercivities of sample **A**, **B**, and **C** are 1800, 280, and 200 Oe respectively. Sample **D**, **E**, and **F** which are paramagnetic show no hysteresis loop.

Table 2.4 The formation energy, migration barrier, and diffusion activation barrier for Co and P diffusing through ϵ -Co

Diffusion type	Formation energy (eV)	Barrier to migration (eV)	Diffusion activation barrier (eV)
Co(I) \leftrightarrow V(I)	1.34	0.06	1.40
P(I) \leftrightarrow V(I)	0.05	0.53	0.58
P(int) \leftrightarrow P(int)	-0.63	2.60	1.97

Table 2.5 The formation energy, migration barrier and diffusion activation barrier for Co and P diffusing through vacant sites in Co₂P

Diffusion type	Formation energy (eV)	Barrier to migration (eV)	Diffusion activation energy (eV)
Co(I-Co ₂ P) ↔ V(I-Co ₂ P)	0.55	1.69	2.24
P ↔ V	2.81	2.99	5.80

In order to determine the transformation path from ϵ -Co to Co₂P in the nanoparticle, diffusion activation barriers for Co and P diffusing through vacant sites in bulk ϵ -Co were determined, as well as the diffusion activation barrier for P diffusing through interstitial sites in bulk ϵ -Co. Co atoms are more likely to diffuse through type I sites than type II sites, due to the lower formation energy for a vacancy at a type I site. Diffusion of P atoms through type I sites was also found to be favorable; diffusion through interstitial sites was prohibited by the high barrier to migration. Since the lowest diffusion activation barrier calculated was for P atoms through vacant type I sites, P is expected to diffuse more quickly than Co in the ϵ -Co crystal. Details of the activation barrier calculations are given in the Methods section. **Table 2.4** gives the formation energy, migration barrier, and diffusion activation barrier for Co and P diffusing through ϵ -Co.

Diffusion activation barriers were also calculated for Co and P through Co₂P. **Table 2.5** gives the formation energy, migration barrier and diffusion activation barrier for Co and P diffusing through vacant sites in Co₂P.

The calculated diffusion activation barriers suggest that P diffuses more quickly than Co through the ϵ -Co structure, while conversely, Co diffuses faster than P through the Co₂P structure. This shows that the fastest diffusing species switches from P to Co somewhere in between ϵ -Co and Co₂P. The calculated diffusion activation energy values also suggest that Co diffusion through type I-Co₂P sites is more favorable than P diffusion in Co₂P and type II-Co₂P Co (see **Table 2.5** and Methods section). This has important consequences for the mechanism governing the transformations from ϵ -Co to Co₂P, and from Co₂P to CoP, which will be discussed in the Discussion section.

Density of states (DOS) calculations were carried out for the Co₂P and CoP phases, using the GGA PBE⁵⁷ exchange correlation functional and the hybrid HSE06⁵⁸ functional. DOS plots are shown in **Fig. A.13** in the supporting information. The Fermi level is indicated by the dashed green line in each case. Contrary to a recent experimental study of Co₂P and CoP nanocrystals,⁵⁹ the Co₂P and CoP structures are metallic and no band gap is observed for either phase. Semilocal density functionals such as the PBE often underestimate the bandgap and sometimes even predict metallic structures instead of the observed semiconducting phases. However, we confirm the predicted metallic structures using the HSE06 hybrid exchange-correlation functional,^{58, 60} which has been shown to be highly accurate for the prediction of semiconductor bandgaps.⁶¹

2.5 Discussion

The ϵ -Co to Co₂P to CoP chemical transformation was investigated through a combination of TEM, XRD, SQUID, and EXAFS. Defect formation energies and migration barriers were calculated using DFT; the sum of these two quantities gives the full diffusion activation barrier for the defects considered, which may be used to infer the most likely diffusion mechanism during the transformation. To discuss the mechanisms for transformation we divide the transformations into two sections: (I) ϵ -Co to Co₂P and (II) Co₂P to CoP. We do this in part because the diffusivities change depending on the chemical environment. For example, the cobalt atoms/ions diffuse faster in Co₂P than in ϵ -Co when reacted with excess phosphorus.

(I) ϵ -Co to Co₂P

We believe that two steps are involved in the phase transformation from ϵ -Co to Co₂P. The first step is inward diffusion of phosphorus atoms into ϵ -Co NPs, forming Co-rich Co₂P. The second step is outward diffusion of Co from a Co₂P compound, leaving a hollow void through the Kirkendall mechanism.

Step 1, inward P diffusion: From our calculations of diffusion activation barriers, the phosphorus atoms diffuse much faster than cobalt atoms in ϵ -Co (see **Table 2.4**). Considering the calculated diffusion activation barriers, diffusion is likely to take place in the ϵ -Co nanoparticle by P atoms taking vacant type I sites. Despite the lower barrier to migration for Co atoms traveling through type I sites, P atoms will diffuse more quickly due to a lower formation energy for the defect of a P atom /

vacancy pair, compared to a vacancy alone. Interstitial P diffusion is ruled out due to the far higher barrier to migration, which is a result of the relatively high density of ϵ -Co. Therefore, phosphorus atoms diffuse into ϵ -Co NPs and form a Co_2P phase and/or a Co-rich Co–P phase, while the diffusion of cobalt atoms is not significant. The inward-diffusing P atoms form an amorphous shell of Co–P around the ϵ -Co core (see **Fig. 2.7**), which then transforms to crystalline Co_2P . Our theoretical modeling suggests that an outer shell of Co_2P is formed around the nanoparticle by the inward diffusion of P atoms through a mechanism of substitutional hopping and vacancy formation.

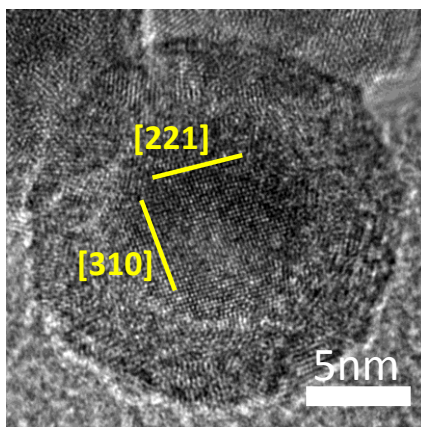


Figure 2.7 The HRTEM image of the intermediate NP between ϵ -Co and Co_2P . The core shows ϵ -Co phase as indicated by the (221) and (310) lattice planes. The reaction conditions of this sample followed that of sample **B**.

Step 2, outward Co diffusion: However, when the phase approaches crystalline Co_2P , the diffusion speeds invert, causing the Kirkendall hollowing. From

our calculations, in the Co_2P phase the outward diffusion of Co is faster than inward diffusion of P (see **Table 2.5**). There is a critical point during the phase transition from ϵ -Co to Co_2P after which the relative diffusivity of Co exceeds that of P atoms. After this point the Kirkendall effect dominates and the Co from the Co-rich core diffuses outward faster than P can diffuse inward, leaving a hollow center.

Experimental data confirms both of these process steps (step 1 and 2). We see that the phosphorus atoms diffuse through the surface of the cobalt NPs, initially replacing the cobalt oxide native layer, and then forming a phosphorus-rich amorphous shell (EXAFS of **A** to **B**). ϵ -Co crystal is the majority phase while the Co-P shell is forming (XRD of **B**), then ϵ -Co co-exists with the Co_2P phase (XRD of **C**), and finally the NP transforms into a dominant Co_2P phase, albeit with a higher concentration of Co atoms (XRD and EXAFS of **D**). TEM images of the transformation show a solid core until the dominant phase Co_2P NP, which is hollow (**D**). That is: until the Co_2P phase appears in crystalline form (**C**) there is no void formation, which corresponds well to our theoretical predictions that asymmetric outward diffusion of Co is minimal until a Co_2P phase appears.

In the pre-crystalline Co_2P the core-shell intermediate stage has an amorphous shell and a crystal core, which was characterized by HRTEM and modeled through DFT. HRTEM images of the intermediate stage between ϵ -cobalt and Co_2P showed NP cores of pure epsilon phase confirmed by analyzing the lattice planes (**Fig. 2.7**). The outer shell exhibited poor crystallinity with nearly no lattice planes evident in HRTEM, indicating an amorphous structure. It is possible that this amorphous outer shell layer might be composed of short orderings of the cobalt-phosphorus bonds.

These HRTEM results correlate well with the EXAFS results which reveal the presence of Co–P coordination while XRD results show no evidence of cobalt phosphide phases. Theoretical modeling of this shell confirms the experimental observations. DFT calculations of the formation energy of an amorphous structure with stoichiometry Co_2P was -0.49 eV per atom, compared to -0.57 eV per atom for crystalline Co_2P . The relatively low energy of the amorphous phase suggests that the transformation to Co_2P in the nanoparticle shell may take place through the amorphous structure (Fig. 2.8).

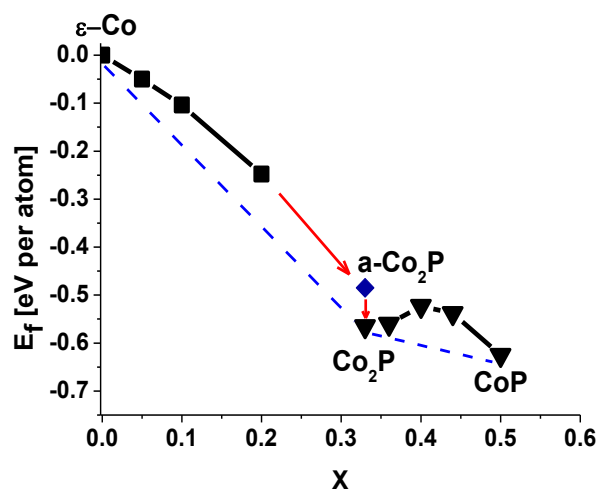


Figure 2.8 Formation energy per atom for $\text{Co}_{1-x}\text{P}_x$ structures illustrating the proposed path between the $\epsilon\text{-Co}$, Co_2P , and CoP structures. The black squares indicate structures in which P atoms have been substituted for type I Co atoms in the $\epsilon\text{-Co}$ crystal. The blue diamond indicates an amorphous structure with stoichiometry Co_2P (a- Co_2P), through which the transformation to crystalline Co_2P may take place. The black triangles indicate the proposed path from Co_2P to CoP ; for the intermediate structures between one and three type I- Co_2P Co atoms have been removed from the Co_2P cell. The blue dashed tie line connects the stable phases.

As crystalline Co_2P forms, structural hollowing occurs due to the nanoscale Kirkendall effect (transformation of sample **C** to **D**). The Co_2P crystal must initially form on the outside of the NP sphere since Co metal coexists with the Co_2P phase (XRD of **C**), and HRTEM of previous NPs show a solid core of ϵ -Co metal. (From our calculations and HRTEM data it is very unlikely that the Co metal diffuses outward as crystalline Co metal clusters. Therefore, the majority of the Co metal is in the core.) Once the Co_2P crystal is formed, the Co atoms in the Co-rich core diffuse out faster than P atoms diffuse in, leaving a void (TEM of **D**, **Fig. 2.2**). This is an intriguing finding and suggests that the inner hollow void size could be tuned if the rate of Co_2P crystal formation on the outer shell could be controlled. (For example, one could introduce a limited amount of P into the system and allow a defined shell of Co_2P to form, then introduce more P to instigate Kirkendall hollowing. From our results, one should expect that the initial thickness of the shell of Co_2P will define the void size.)

(II) Co_2P to CoP

Based on the calculation of the diffusion activation barriers of Co and P in Co_2P , the transformation from Co_2P to CoP most likely takes place through the de-intercalation of Co from type I- Co_2P sites, while the connectivity of the anion sublattice remains intact, as shown in **Fig. 2.9**. **Fig. 2.9** illustrates a possible path by which ideal Co_2P can transform to CoP: type I- Co_2P Co atoms are successively removed from the initial Co_2P cell. This is consistent with the diffusion of Co atoms

out from the center of the nanoparticle towards the surface. This transformation involves a deformation in the shape of the P sublattice, as indicated by the red highlighted bonds in **Fig. 2.9**. The anion sublattice retains connectivity, however, which is consistent with what is seen during cation exchange reactions in nanocrystals.³⁻⁴ That is: in an ideal transformation from Co_2P to CoP , no hollowing due to Kirkendall effects would take place; the only shape change would be additional layers of CoP forming at the outer surface of the nanoparticle. However, a nanoparticle containing a Co-rich core and a Co_2P shell would result in Kirkendall hollowing (as detailed in the previous sections) from the center of the nanoparticle, and thus the transformation should result in the creation or enlargement of a pore at the nanoparticle center.

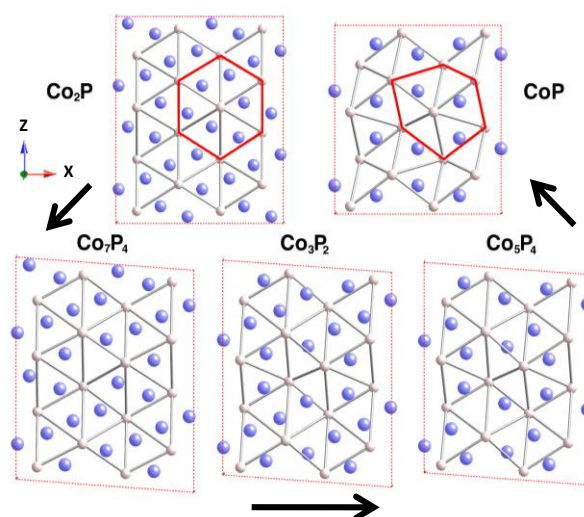


Figure 2.9 Supercells illustrating a possible path between the Co_2P and CoP structures are shown, viewed along the $[0\ 1\ 0]$ direction. The structure was relaxed using DFT after successively removing type I- Co_2P Co atoms, resulting in a deformation of the P sublattice. After the removal of four Co atoms the CoP structure

was achieved. The bonds highlighted in red indicate the P sublattice associated with the Co₂P and CoP structures, which retains connectivity during the transformation.

The actual NP samples, however, showed slightly different behavior compared to the theoretical predictions of pure Co₂P, and were more similar to the latter case with a Co-rich core. In the transition from Co₂P (sample **D**) to the interphase Co₂P/CoP (sample **E**) the NPs become more polydisperse, the hollow voids increase in diameter, and the percentage of hollow particles decreases by more than half (from 70% with hollow centers in **D** to 30% in **E**). Clearly more is occurring than the simple shuttling of Co through the anion lattice predicted for perfect crystals. Based on our experimental results we believe in our samples there is 1) a Co-rich inner region which leads to the continued void expansion and 2) a fracturing of hollow particles which leads to the increase in polydispersity and decrease in percentage of hollow particles. Though not mutually exclusive, these two phenomena will create two pathways for the transition from our NP Co₂P to CoP (**Fig. 2.10**).⁶²

In the first path (**Fig. 2.10** path a) the CoP NPs grow in diameter by diffusion of cobalt atoms from the Co-rich Co₂P interior, forming additional CoP on the surface. This accounts for the void size increase and the increase in overall particle size. The void size *should* remain fixed after the initial ϵ -Co to Co₂P Kirkendall reaction since the Co₂P to CoP reaction is expected to maintain a structural integrity through the anion sub-lattice (see previous theoretical section). However, our Co₂P NPs (sample **D**) are not perfect Co₂P: EXAFS results show that the degeneracy of the Co–Co coordination (9.9) is higher than that of theoretical value (9), which means that the

concentration of cobalt atoms is higher than a perfect Co_2P crystal. This higher concentration of cobalt atoms should occur as a gradient from the interior to the exterior, with the interior having the highest concentration and the exterior having the lowest. These excess cobalt atoms facilitate a continued Kirkendall effect and result in bigger voids in the intermediate phase between Co_2P and CoP (sample **E**). SQUID and XRD results indicate that metal Co clusters are not present in samples **D-F** so the Co_2P and CoP are Co-rich and *do not* contain a significant amount of Co metal clusters, which should be detected by SQUID.⁶³

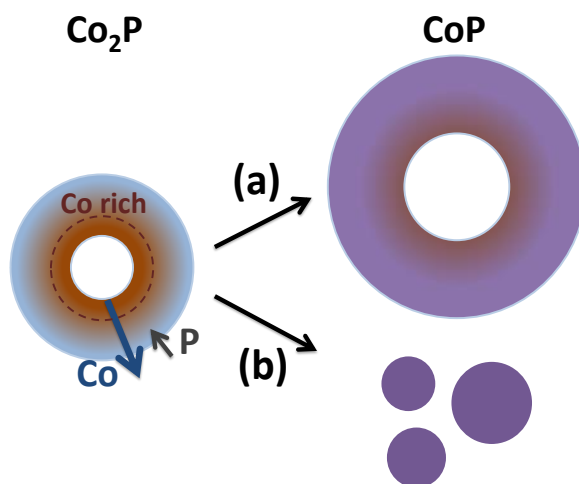


Figure 2.10 Two pathways for the transition from sample Co_2P to CoP . In Co_2P NP (left), inner brown region indicates the cobalt rich part. Longer Co arrow symbolizes the larger diffusivity of Co over P (shorter arrow). (a) NPs grow by diffusion of cobalt atoms from inside of NPs to surface. (b) NPs break into small particles during the reaction.

In the second path for our Co₂P to CoP transformation (**Fig. 2.10** path b) the NPs fracture into smaller pieces during the reaction (**Fig. 2.2** D and E). Fracturing of hollow NPs into smaller NPs is commonly seen in hollow NP systems.^{1, 47} The increase in size deviation in our samples (std. dev. of 16% in **D** to 20% in **E**) is then due to this fracturing since new small NPs are formed that skew the size deviations. The small pieces may then undergo Ostwald ripening as they dissolve and the new material is added to the larger NPs. This would also increase polydispersity and explain the increase in irregular shapes (TEM of sample **E**). The fracturing also explains the decrease in the percentage of hollow NPs (from 70% to 30%) because newly formed small NPs are not hollow.

In sample **F**, with a longer reaction time and higher temperatures, re-annealing is observed for a majority of the nanoparticles, increasing the crystalline order with increased phosphorus diffusion. This resulted in a significant second shell contribution to the EXAFS spectrum which indicates that sample **F** acts as more bulk-like than other samples. It is interesting to note that higher temperatures and longer reaction times lead to such large morphological differences with this sample compared to the others. For instance, hollowing is lessened in these particles compared to the intermediate Co₂P/CoP particles.

2.6 Conclusion

A thorough means to elucidate nanoparticle atomic and morphological structure through a chemical transformation is presented, with the use of X-ray

absorption spectroscopy, XRD, TEM, and DFT calculations. Atomic coordination and structural evolution, including diffusion processes, throughout the transformation of NP ϵ -Co to Co_2P and CoP are reported.

EXAFS and XRD analysis revealed that the NPs which show pure Co_2P and CoP phase in XRD spectra were not perfect structures: the Co–Co coordination number was greater in NPs than in bulk, resulting in a cobalt-rich gradient from the interior to exterior of the NPs.

We propose that the transformation from ϵ -Co to Co_2P occurs through two sequential diffusion steps: 1) inward diffusion of phosphorus with negligible movement of cobalt and 2) outward diffusion of cobalt which results in a hollow structure. During the first step, cobalt phosphide first forms an amorphous shell layer in the exterior portion of the NP before a complete transformation occurs. When ϵ -Co is the majority phase the P atoms diffuse inward faster than Co diffuses outward. After the transformation progresses and Co_2P becomes the majority phase in the NPs, the diffusivity of Co exceeds that of P, resulting in outward diffusion of cobalt atoms and the formation of hollow voids as is characteristic of the nanoscale Kirkendall effect.

As Co_2P transforms into CoP a different transformation mechanism is involved. Cobalt atoms de-intercalate from interstitial sites while the anion lattice remains intact. Although theoretical calculations predict no further structural hollowing within the NPs, in the real samples the cobalt-rich interior causes further hollowing. This residual metal has implications for other nanoscale Kirkendall systems and the

properties of the resulting compounds. In the final CoP nanoparticle structure, re-annealing occurs, resulting in NPs with long-range order that lack hollow voids.

Our findings provide an elucidation of cobalt to cobalt phosphide NP transformation and structure. Knowledge about the transformation method and structural properties provides a means to fine-tune the synthesis and composition of the NPs and facilitate the optimization of such NPs for use in applications. We predict that it is possible to tailor the void size in Co₂P hollow nanoparticles by varying the initial Co₂P shell size. The Co diffusion through the Co₂P anion lattice is an intriguing mechanism that deserves further study. It may be possible to use CoP for ionic conduction of Co.

2.7 References

1. Yin, Y. D.; Rioux, R. M.; Erdonmez, C. K.; Hughes, S.; Somorjai, G. A.; Alivisatos, A. P. *Science* **2004**, 304, (5671), 711-714.
2. Sun, Y. G.; Xia, Y. N. *J. Am. Chem. Soc.* **2004**, 126, (12), 3892-3901.
3. Son, D. H.; Hughes, S. M.; Yin, Y. D.; Alivisatos, A. P. *Science* **2004**, 306, 1009-1012.
4. Robinson, R. D.; Sadtler, B.; Demchenko, D. O.; Erdonmez, C. K.; Wang, L. W.; Alivisatos, A. P. *Science* **2007**, 317, (5836), 355-358.
5. Demchenko, D. O.; Robinson, R. D.; Sadtler, B.; Erdonmez, C. K.; Alivisatos, A. P.; Wang, L. W. *ACS Nano* **2008**, 2, (4), 627-636.
6. Sadtler, B.; Demchenko, D. O.; Zheng, H.; Hughes, S. M.; Merkle, M. G.; Dahmen, U.; Wang, L. W.; Alivisatos, A. P. *J. Am. Chem. Soc.* **2009**, 131, (14), 5285-5293.
7. Wark, S. E.; Hsia, C. H.; Son, D. H. *J. Am. Chem. Soc.* **2008**, 130, (29), 9550-9555.
8. Tang, Z. Y.; Kotov, N. A.; Giersig, M. *Science* **2002**, 297, (5579), 237-240.
9. Cho, K. S.; Talapin, D. V.; Gaschler, W.; Murray, C. B. *J. Am. Chem. Soc.* **2005**, 127, (19), 7140-7147.
10. Chan, E. M.; Marcus, M. A.; Fakra, S.; ElNaggar, M.; Mathies, R. A.; Alivisatos, A. P. *J. Phys. Chem. A* **2007**, 111, (49), 12210-12215.
11. Frenkel, A. Z. *Kristallogr.* **2007**, 222, (11), 605-611.

12. Bunker, G., *Introduction to XAFS: a practical guide to X-ray absorption fine structure spectroscopy*. Cambridge University Press: Cambridge, 2010; p 260.
13. Stern, E. A. *Phys. Rev. B* **1974**, 10, (8), 3027-3037.
14. Frenkel, A. I.; Hills, C. W.; Nuzzo, R. G. *J. Phys. Chem. B* **2001**, 105, (51), 12689-12703.
15. Aruguete, D. M.; Marcus, M. A.; Li, L. S.; Williamson, A.; Fakra, S.; Gygi, F.; Galli, G. A.; Alivisatos, A. P. *J. Phys. Chem. C* **2007**, 111, (1), 75-79.
16. Marcus, M. A.; Flood, W.; Stiegerwald, M.; Brus, L.; Bawendi, M. *J. Phys. Chem.* **1991**, 95, (4), 1572-1576.
17. Hwang, B. J.; Sarma, L. S.; Chen, J. M.; Chen, C. H.; Shih, S. C.; Wang, G. R.; Liu, D. G.; Lee, J. F.; Tang, M. T. *J. Am. Chem. Soc.* **2005**, 127, (31), 11140-11145.
18. Nashner, M. S.; Frenkel, A. I.; Adler, D. L.; Shapley, J. R.; Nuzzo, R. G. *J. Am. Chem. Soc.* **1997**, 119, (33), 7760-7771.
19. Nashner, M. S.; Frenkel, A. I.; Somerville, D.; Hills, C. W.; Shapley, J. R.; Nuzzo, R. G. *J. Am. Chem. Soc.* **1998**, 120, (32), 8093-8101.
20. Frenkel, A. I. *J. Synchrotron Radiat.* **1999**, 6, (3), 293-295.
21. Park, J. I.; Kim, M. G.; Jun, Y. W.; Lee, J. S.; Lee, W. R.; Cheon, J. *J. Am. Chem. Soc.* **2004**, 126, (29), 9072-9078.

22. Sarma, L. S.; Chen, C.-H.; Kumar, S. M. S.; Wang, G.-R.; Yen, S.-C.; Liu, D.-G.; Sheu, H.-S.; Yu, K.-L.; Tang, M.-T.; Lee, J.-F.; Bock, C.; Chen, K.-H.; Hwang, B.-J. *Langmuir* **2007**, *23*, (10), 5802-5809.
23. Rodriguez, J. A.; Hanson, J. C.; Kim, J. Y.; Liu, G.; Iglesias-Juez, A.; Fernandez-Garcia, M. *J. Phys. Chem. B* **2003**, *107*, (15), 3535-3543.
24. Cheng, G.; Carter, J. D.; Guo, T. *Chem. Phys. Lett.* **2004**, *400*, (1-3), 122-127.
25. Rockenberger, J.; Troger, L.; Kornowski, A.; Vossmeier, T.; Eychmuller, A.; Feldhaus, J.; Weller, H. *J. Phys. Chem. B* **1997**, *101*, (14), 2691-2701.
26. Brock, S. L.; Perera, S. C.; Stamm, K. L. *Chem.-Eur. J.* **2004**, *10*, (14), 3364-3371.
27. Kelly, A. T.; Rusakova, I.; Ould-Ely, T.; Hofmann, C.; Luttge, A.; Whitmire, K. H. *Nano Lett.* **2007**, *7*, (9), 2920-2925.
28. Gregg, K. A.; Perera, S. C.; Lawes, G.; Shinozaki, S.; Brock, S. L. *Chem. Mater.* **2006**, *18*, (4), 879-886.
29. Li, Y.; Malik, M. A.; O'Brien, P. *J. Am. Chem. Soc.* **2005**, *127*, (46), 16020-16021.
30. Souza, D. C. S.; Pralong, V.; Jacobson, A. J.; Nazar, L. F. *Science* **2002**, *296*, (5575), 2012-2015.
31. Ni, Y. H.; Li, J.; Jin, L.; Xia, J.; Hong, J. M.; Liao, K. M. *New J. Chem.* **2009**, *33*, (10), 2055-2059.

32. Ni, Y.; Li, J.; Zhang, L.; Yang, S.; Wei, X. *Mater. Res. Bull.* **2009**, 44, (5), 1166-1172.
33. Lucas, I.; Perez, L.; Aroca, C.; Sánchez, P.; López, E.; Sánchez, M. C. *J. Magn. Magn. Mater.* **2005**, 290-291, (Part 2), 1513-1516.
34. Burns, A. W.; Layman, K. A.; Bale, D. H.; Bussell, M. E. *Appl. Catal., A* **2008**, 343, (1-2), 68-76.
35. Zhang, H.; Ha, D.-H.; Hovden, R.; Kourkoutis, L. F.; Robinson, R. D. *Nano Lett.* **2011**, 11, (1), 188-197.
36. Lukehart, C. M.; Milne, S. B.; Stock, S. R. *Chem. Mater.* **1998**, 10, (3), 903-908.
37. Schlesinger, M. E. *Chem. Rev.* **2002**, 102, (11), 4267-4301.
38. Puentes, V. F.; Krishnan, K. M.; Alivisatos, A. P. *Science* **2001**, 291, (5511), 2115-2117.
39. The mixture of Co₂P and CoP was obtained when the reaction continues for 5hrs using the same conditions for sample B-E
40. Ravel, B.; Newville, M. *J. Synchrotron Radiat.* **2005**, 12, (4), 537-541.
41. Kelly, S. D.; Ravel, B. *AIP Conf. Proc.* **2007**, 882, (1), 132-134.
42. Koningsberger, D. C.; Mojet, B. L.; van Dorssen, G. E.; Ramaker, D. E. *Top. Catal.* **2000**, 10, (3), 143-155.
43. Stern, E. A. *Contemp. Phys.* **1978**, 19, (4), 289 - 310.

44. Ravel, B. J. *Synchrotron Radiat.* **2001**, 8, (2), 314-316.
45. Ravel, B.; Kelly, S. D. *AIP Conf. Proc.* **2007**, 882, (1), 150-152.
46. Scott, R., *Physical Methods in Bioinorganic Chemistry: Spectroscopy and Magnetism*. University Science Books: 2000.
47. Yin, Y. D.; Erdonmez, C. K.; Cabot, A.; Hughes, S.; Alivisatos, A. P. *Adv. Funct. Mater.* **2006**, 16, (11), 1389-1399.
48. The average size of hollow voids in sample F is not accurate due to their irregular shapes.
49. Dinega, D. P.; Bawendi, M. G. *Angew. Chem. Int. Ed.* **1999**, 38, (12), 1788-1791.
50. Jia, S.; Hsia, C.-H.; Son, D. H. *J. Phys. Chem. C* **2011**, 115, (1), 92-96.
51. Johnston, R. L., *Atomic and Molecular Clusters*. Taylor & Francis: 2002; p 256.
52. Nietubyc, R.; Czerwosz, E.; Diduszko, R.; Dluzewski, P.; Kozlowski, M.; Welter, E. *J. Alloys Compd.* **2009**, 484, (1-2), 896-901.
53. Cezar, J.; uacute;lio, C.; Tolentino, H.; eacute;lio, C. N.; Knobel, M. *Phys. Rev. B* **2003**, 68, (5), 054404.
54. Calvin, S.; Riedel, C. J.; Carpenter, E. E.; Morrison, S. A.; Stroud, R. M.; Harris, V. G. *Phys. Scr.* **2005**, T115, (T115), 744-748.
55. Chen, L. X.; Rajh, T.; Jager, W.; Nedeljkovic, J.; Thurnauer, M. C. *J. Synchrotron Radiat.* **1999**, 6, (3), 445-447.

56. Sprouster, D. J.; Giulian, R.; Araujo, L. L.; Kluth, P.; Johannessen, B.; Cookson, D. J.; Foran, G. J.; Ridgway, M. C. *J. Appl. Phys.* **2010**, 107, (1), 014313-10.
57. Fujii, S.; Ishida, S.; Asano, S. *J. Phys. F: Met. Phys.* **1988**, 18, (5), 971-980.
58. Perdew, J. P.; Burke, K.; Ernzerhof, M. *Phys. Rev. Lett.* **1996**, 77, (18), 3865.
59. Paier, J.; Marsman, M.; Hummer, K.; Kresse, G.; Gerber, I. C.; Angyan, J. G. *J. Chem. Phys.* **2006**, 124, (15), 154709-13.
60. Maneepprakorn, W.; Malik, M. A.; O'Brien, P. *J. Mater. Chem.* **2010**, 20, (12), 2329-2335.
61. Heyd, J.; Scuseria, G. E.; Ernzerhof, M. *J. Chem. Phys.* **2003**, 118, (18), 8207-8215.
62. Heyd, J.; Peralta, J. E.; Scuseria, G. E.; Martin, R. L. *J. Chem. Phys.* **2005**, 123, (17), 174101-8.
63. This explanation is mainly based on the sample D and E because the synthetic conditions of sample F are slightly different (Table 2.1).
64. Barea, E.; Batlle, X.; Bourges, P.; Corma, A.; Fornes, V.; Labarta, A.; Puntès, V. F. *J. Am. Chem. Soc.* **2005**, 127, (51), 18026-18030.

APPENDIX A

A SUPPLEMENTARY INFORMATION FOR CHAPTER 2

Summary

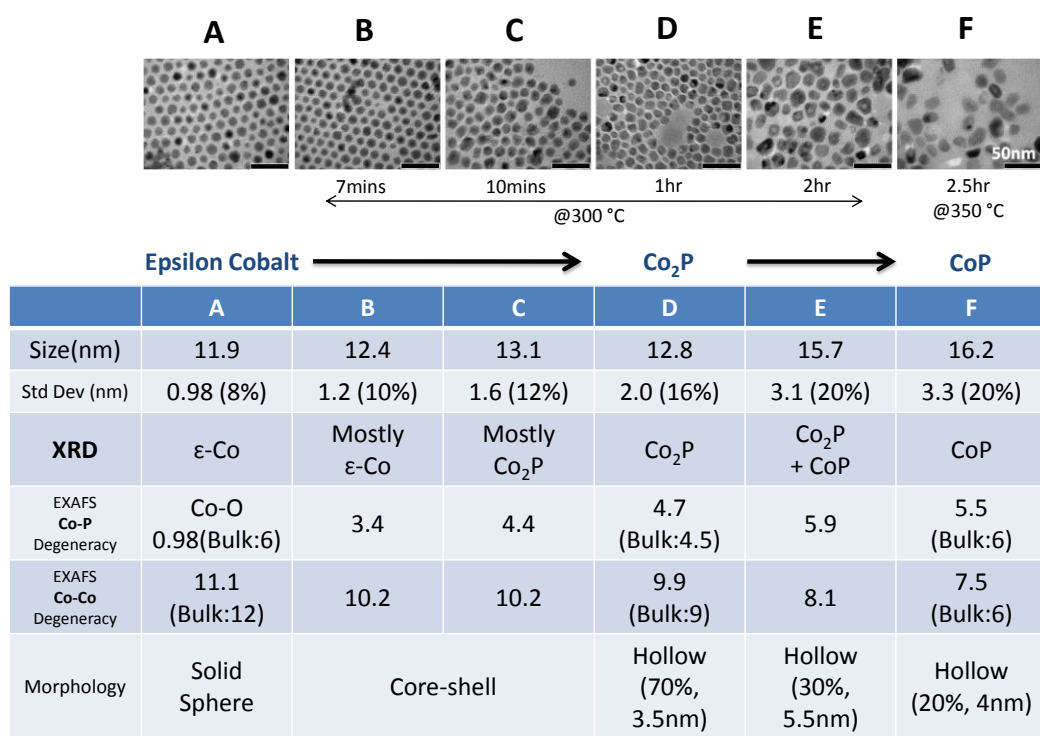


Figure A.1 Summary of reaction conditions for NP samples with corresponding TEM images directly above, and summary of XRD, EXAFS and other characterizations below.

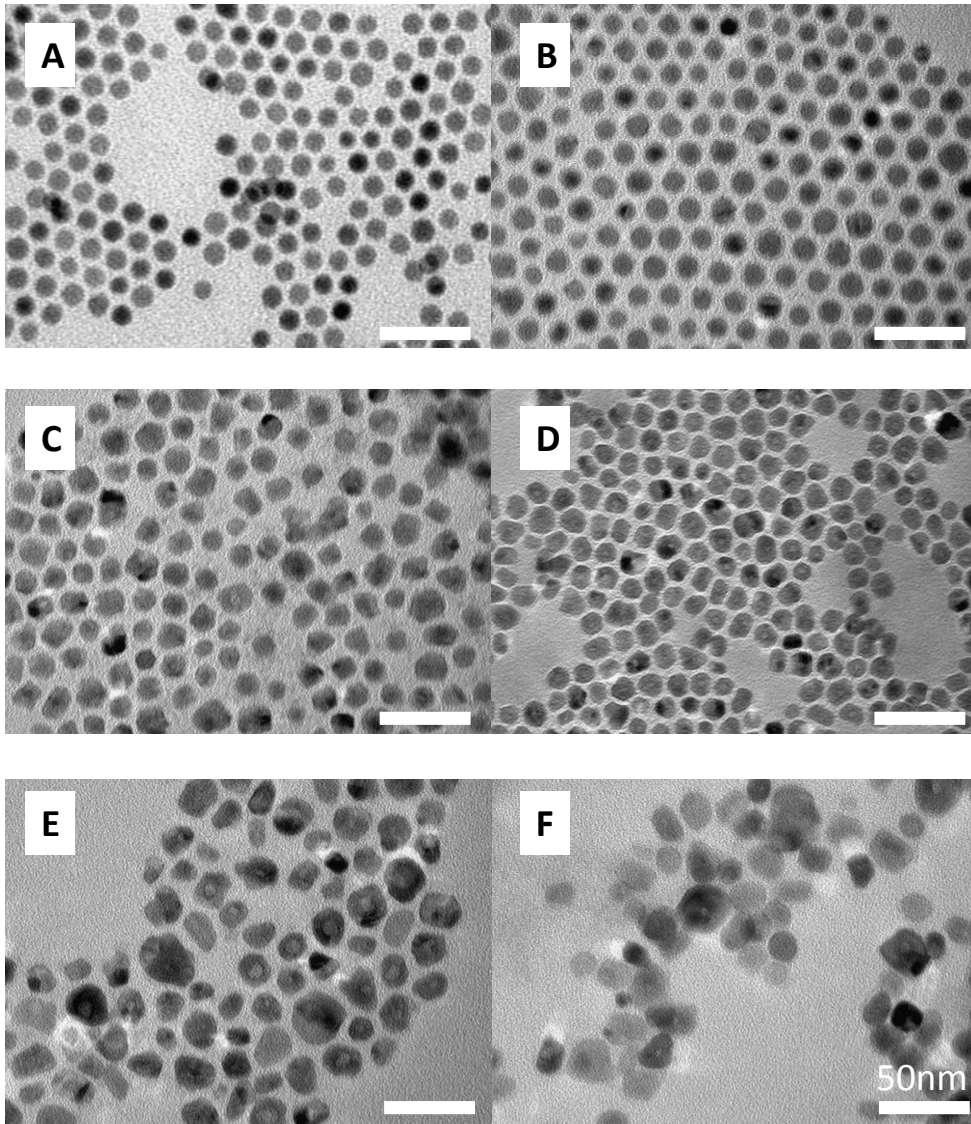


Figure A.2 Low magnification TEM images of sample A-F

Structure details

1) ϵ -Co

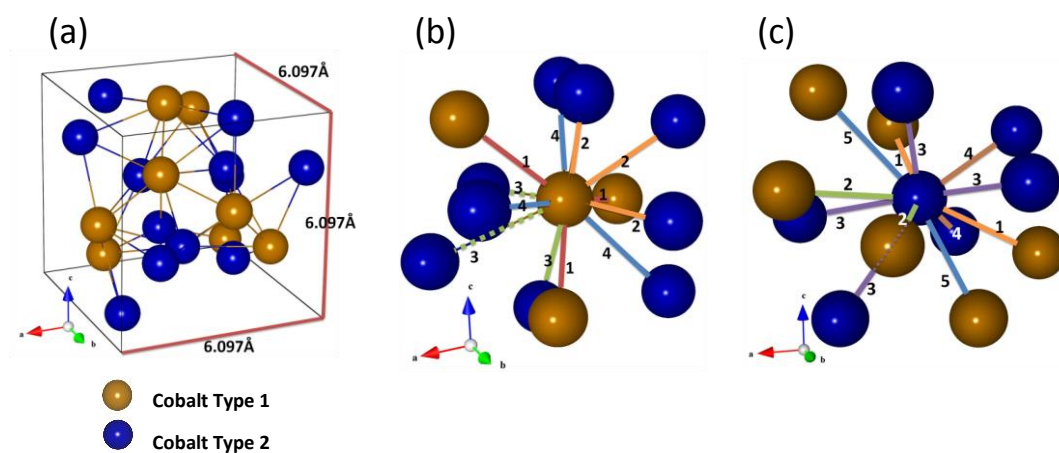


Figure A.3 (a) A schematic representation of the ϵ -Co crystal structure. The gold atom and blue atom are cobalt type I and II respectively. (b) Scattering pathways from cobalt type I atom in ϵ -Co (c) Scattering pathways from cobalt type II atom in ϵ -Co. Paths of the same length are represented with lines of the same color.

Table A.1 The conditions of scattering pathways from cobalt type I atom in ϵ -Co

Numbers corresponding to Fig. A.3 (b)	Pathway Distance(\AA)	Number of Pathways	Scattering Atom
1	2.28	3	Co(I)
2	2.49	3	Co(II)
3	2.54	3	Co(II)
4	2.59	3	Co(II)

Table A.2 The conditions of scattering pathways from cobalt type II atom in ϵ -Co

Numbers corresponding to Fig. A.3 (c)	Pathway Distance(\AA)	Number of Pathways	Scattering Atom
1	2.49	2	Co(I)
2	2.54	2	Co(I)
3	2.55	4	Co(II)
4	2.58	2	Co(II)
5	2.59	2	Co(I)

2) Co₂P

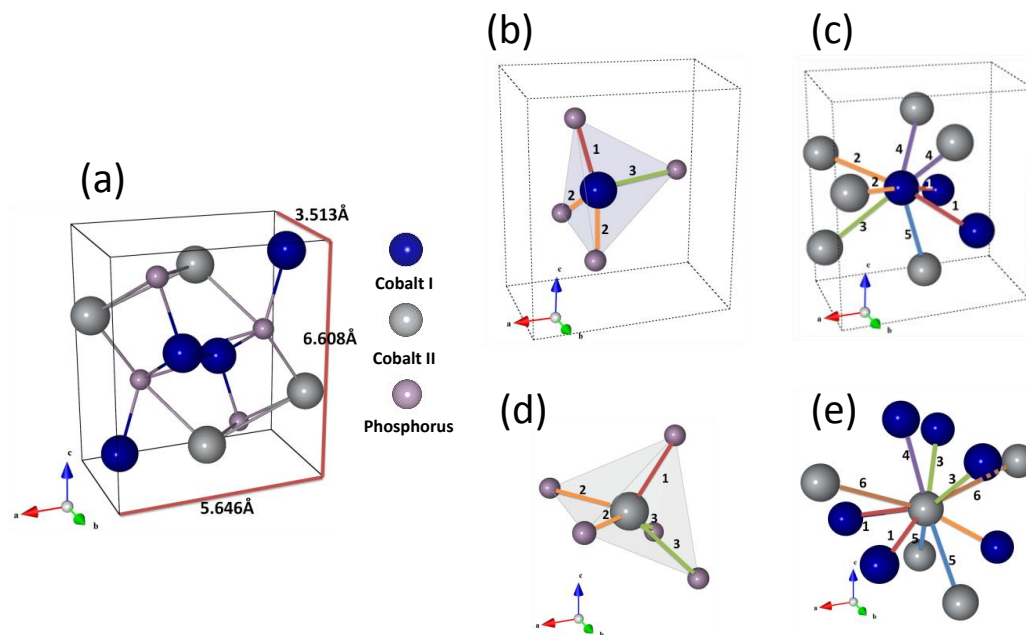


Figure A.4 A schematic representation of the Co₂P crystal structure. The blue, gray, and purple atoms are cobalt type I, II, and phosphorus respectively. (b) Co-P Scattering pathways from cobalt type I atom of Co₂P (c) Co-Co Scattering pathways from cobalt type I atom of Co₂P (d) Co-P Scattering pathways from cobalt type II atom of Co₂P (e) Co-Co Scattering pathways from cobalt type II atom of Co₂P.

**Table A.3 The conditions of Co-P scattering pathways from cobalt type I atom in
Co₂P**

Numbers corresponding to Fig. A.4 (b)	Pathway Distance(Å)	Number of Pathways	Scattering Atom
1	2.14	1	P
2	2.23	2	P
3	2.24	1	P

**Table A.4 The conditions of Co-Co scattering pathways from cobalt type I atom
in Co₂P**

Numbers corresponding to Fig. A.4 (c)	Pathway Distance(Å)	Number of Pathways	Scattering Atom
1	2.54	2	Co(I)
2	2.62	2	Co(II)
3	2.67	1	Co(II)
4	2.69	2	Co(II)
5	2.71	1	Co(II)

**Table A.5 The conditions of Co-P scattering pathways from cobalt type II atom
in Co₂P**

Numbers corresponding to Fig. A.4 (d)	Pathway Distance(Å)	Number of Pathways	Scattering Atom
1	2.29	1	P
2	2.40	2	P
3	2.54	2	P

**Table A.6 The conditions of Co-Co scattering pathways from cobalt type II atom
in Co₂P**

Numbers corresponding to Fig. A.4 (e)	Pathway Distance(Å)	Number of Pathways	Scattering Atom
1	2.62	2	Co(I)
2	2.67	1	Co(I)
3	2.69	2	Co(I)
4	2.71	1	Co(I)
5	2.83	2	Co(II)
6	3.03	2	Co(II)

2) CoP

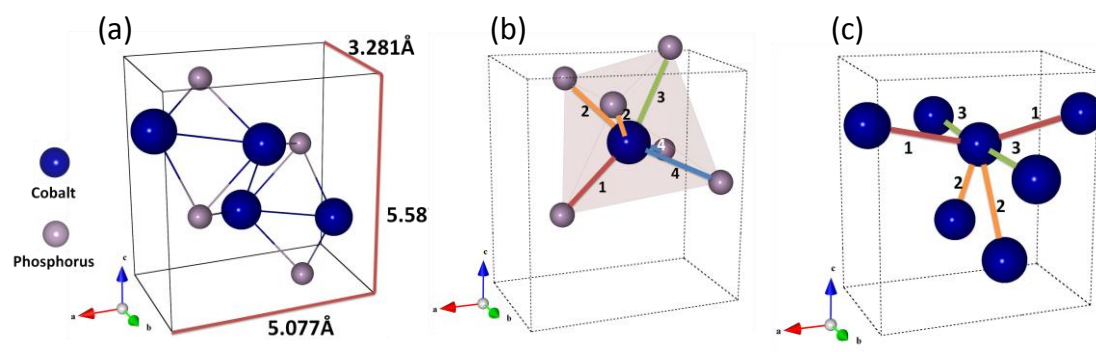


Figure A.5 (a) A schematic representation of the CoP crystal structure. The blue atom and purple atom are cobalt and phosphorus respectively. (b) Co-P Scattering pathways from cobalt atom in CoP (c) Co-Co Scattering pathways from cobalt atom in CoP.

Table A.7 The conditions of Co-P scattering pathways from cobalt atom in CoP

Numbers corresponding to Fig. A.5 (b)	Pathway Distance(Å)	Number of Pathways	Scattering Atom
1	2.21	1	P
2	2.27	2	P
3	2.35	1	P
4	2.36	2	P

Table A.8 The conditions of Co-Co scattering pathways from cobalt atom in CoP

Numbers corresponding to Fig. A.5 (c)	Pathway Distance(\AA)	Number of Pathways	Scattering Atom
1	2.60	2	Co
2	2.76	2	Co
3	3.28	2	Co

EXAFS Analysis Methods

The raw absorption spectra obtained (Fig. A.6) at the beamline were averaged and processed using the ATHENA software. This processing included edge determination from the first inflection point in the absorption data, background subtraction using the AUTOBK algorithm, and normalization of the EXAFS modulations (greater than 150 eV above the edge). A k-weight of 1 was chosen in order to emphasize the first coordination shell for fitting due to the presence of low-Z scatterers. The spectra were converted from E-space, to k-space, and then underwent a phase shift specific to the scattering element and Fourier transformation into R-space using the Hanning-type window, in order to better visualize the spacing and fit to theory. In a Fourier transform of the raw spectral data, each peak appears at the relative spacing of that particular shell from the scattering atom. The data, after processing, was then analyzed by the ab-initio method with use of the ARTEMIS software. Crystal structures from theory were inputted using ATOMS. By fitting well-matched theoretical pathways to the experimental spectra by loosening variables to deviate from the theoretical bulk structures, specific structural information was determined such as coordination number, spacing, and mean square disorder.

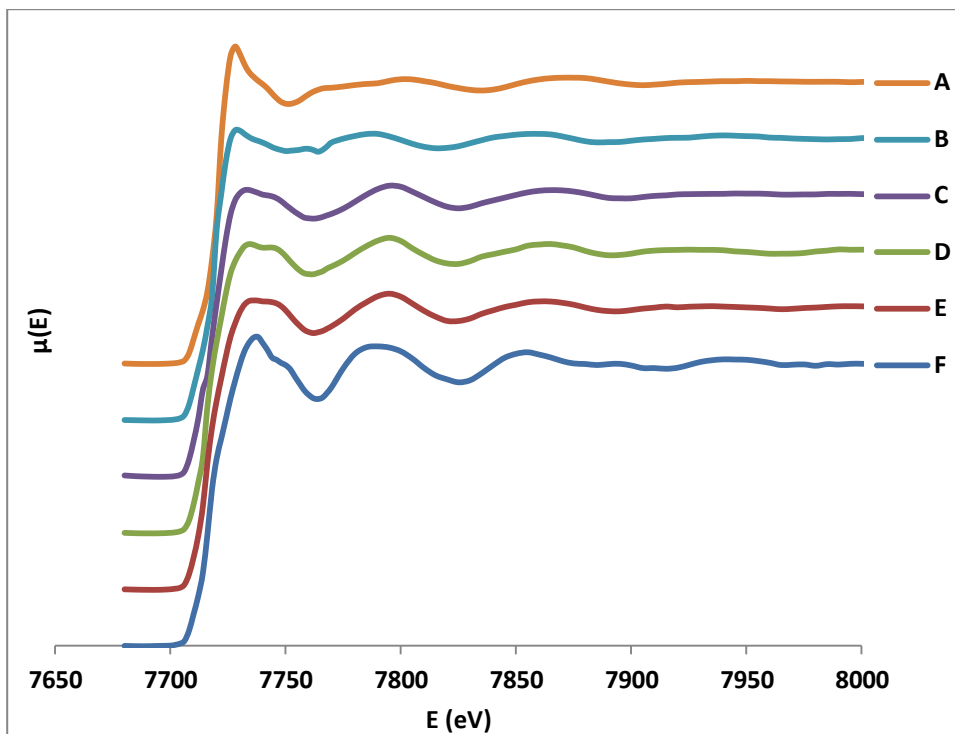


Figure A.6 Co K-edge XAS spectra: Samples A to F. The waterfall plot shows the absorption data obtained at the beamline. Even before analysis, a visual difference can be traced as the reaction progresses in the shape and definition of each spectrum.

EXAFS fitting details and procedure

The following EXAFS plots show the Fourier Transformations of the absorption spectrum obtained for each sample, their respective fitting using theoretical pathways, and residual pathway summations. The pathway summations shown were those used in the fitting process. Separate residuals represent a separate set of variables allowed to float during the fit.

1) Sample A

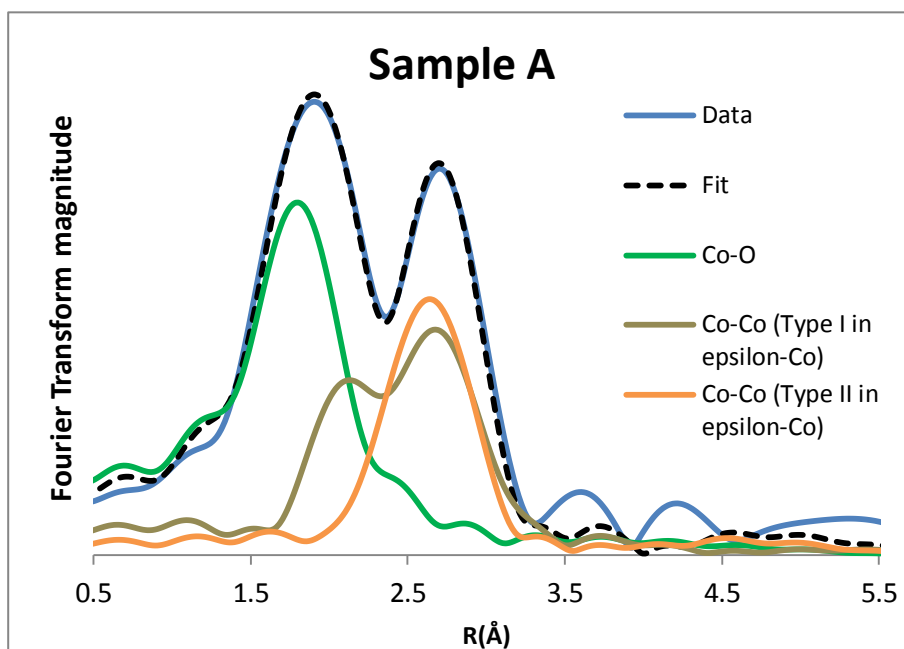


Figure A.7 The residual sums for sample A include the Co-O contribution at a short distance from the absorbing atom as well as Co-Co contributions using both type I and type II cobalt as the core.

Table A.9 Sample A pathways and associated variable summary

Pathways	Total Average Degeneracy	ΔE_0 (eV)	ΔR (Å)	σ^2
Co ₁ to Co ₁	1.12	8.3098	-0.1387	0.015019
Co ₁ to Co ₂ / Co ₂ to Co ₁	7.728	9.999318	0.01906	0.017342
Co ₂ to Co ₂	2.23	-7.01082	0.04101	0.011824
Co to O	0.978	-8.739076	-0.229	0.0021

Table A.10 Summary of fit parameters for Sample A.

	Values
Total Co-Co average coordination number	11.1
Total Co-O average coordination number	0.98
Reduced chi square value	288.68
R-factor	0.001410295
Path Used for Phase Shift	Co-Co

2) Sample B

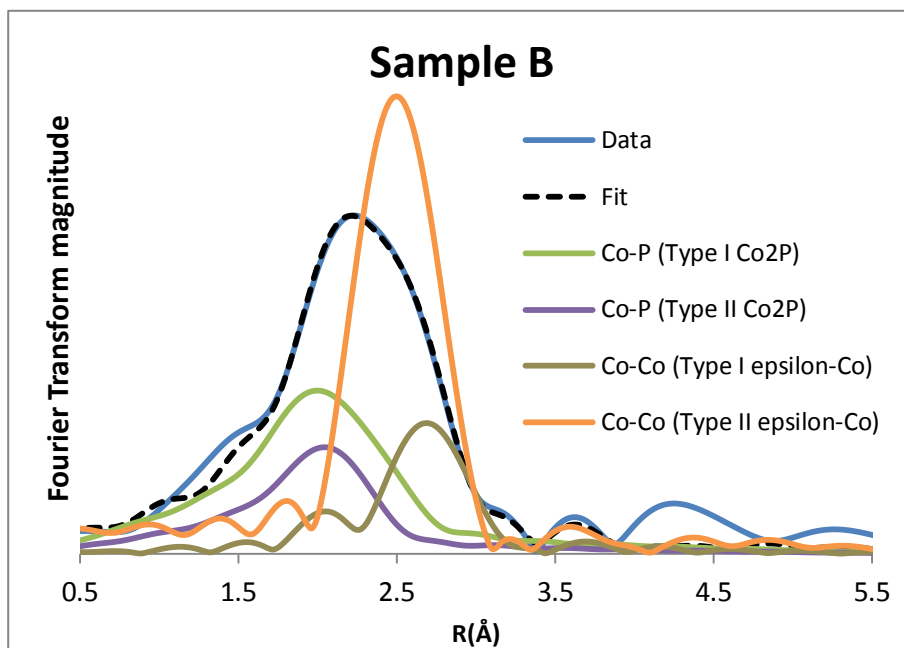


Figure A.8 The contributions to the Sample B spectrum include pathways from epsilon cobalt as well as a smaller amount of Co-P at a shorter bonding distance

Table A.11 Sample B pathways and associated variable summary

Pathways	Total Average Degeneracy	ΔE_0 (eV)	ΔR (Å)	σ^2
Co ₁ to Co	4.32	-4.659989	0.14266	0.00996
Co ₂ to Co	5.88	6.902365	-0.023126	0.009057
Co _a to P	2.45	-8.955041	-0.16	0.007392
Co _b to P	0.96	-9.999989	0.020076	0.011527

Table A.12 Summary of fit parameters for Sample B.

	Values
Total Co-Co average coordination number	10.2
Total Co-P average coordination number	3.41
Reduced chi square value	<i>99.577537</i>
R-factor	0.000874373
Path Used for Phase Shift	Co-Co

3) Sample C

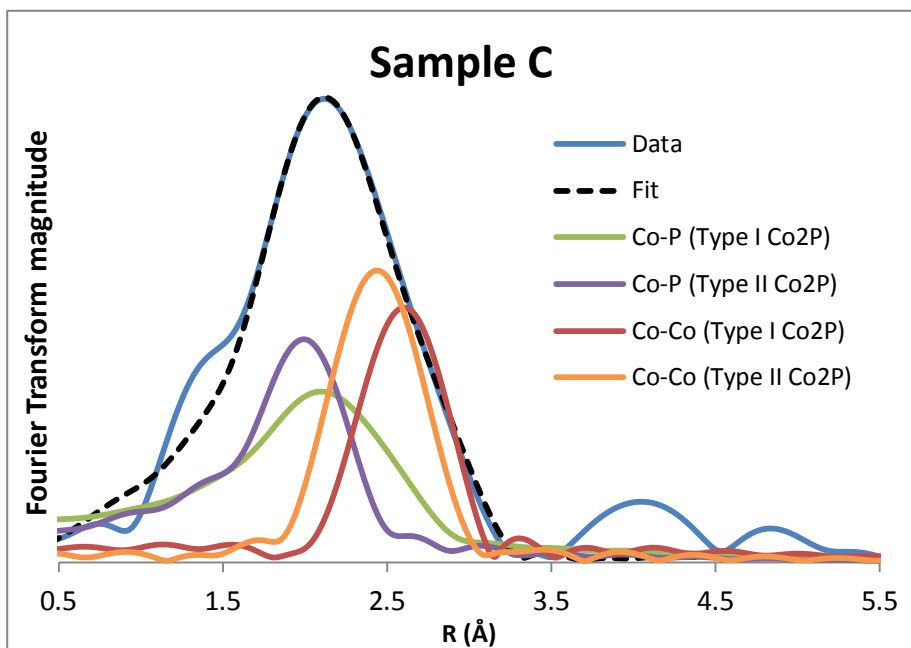


Figure A.9 The residual sums associated with sample C reveal the increased Co-P contribution due to increased Phosphorus diffusion

Table A.13 Sample C pathways and associated variable summary

Pathways	Total Average Degeneracy	ΔE_0 (eV)	ΔR (Å)	σ^2
Co _A to P	3.325	-10	-0.152932	0.011932
Co _B to P	1.08	-7.471694	-0.069252	0.005759
Co _A to Co	7.3	-1.269713	-0.017524	0.012653
Co _B to Co	2.8548	-5.788145	-0.159	0.006055

Table A.14 Summary of fit parameters for Sample C.

	Values
Total Co-Co average coordination number	10.2
Total Co-P average coordination number	4.4
Reduced chi square value	480.6568
R-factor	0.001654547
Path Used for Phase Shift	Co-Co

4) Sample D

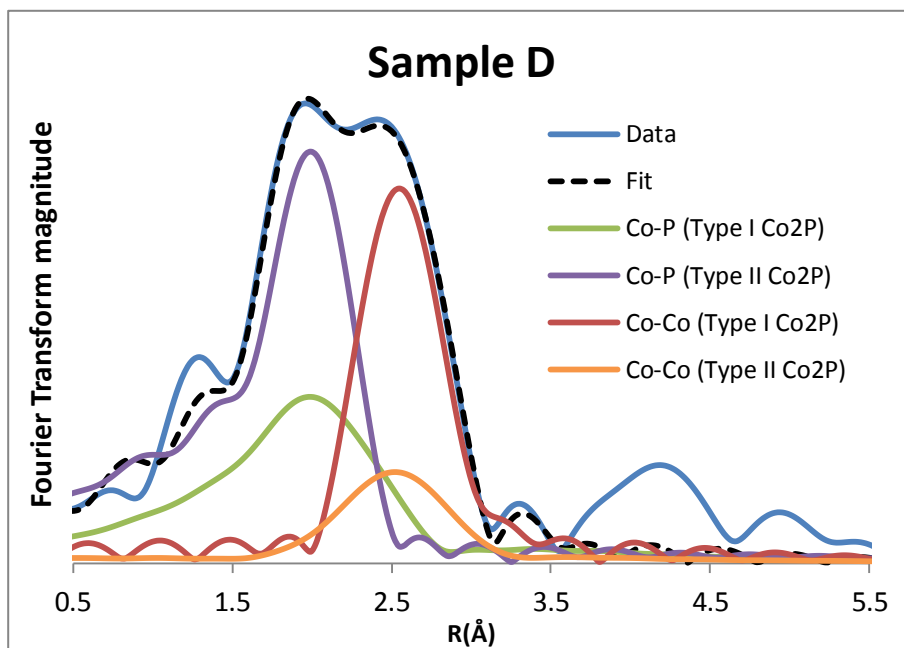


Figure A.10 The FT for sample D reveals two distinct peaks, associated with **Co-P** and **Co-Co** contributions. This reveals increased crystalline order within the structure, as the contributions become distinct.

Table A.15 Sample D pathways and associated variable summary

Pathways	Total Average Degeneracy	ΔE_0 (eV)	ΔR (Å)	σ^2
Co _A to P	2.825	-10	-0.105952	0.010464
Co _B to P	1.84	-6.44098	-0.066952	0.002659
Co _A to Co	6.3	-1.545924	-0.075272	0.005416
Co _B to Co	3.58904	-4.121373	-0.025223	0.023724

Table A.16 Summary of fit parameters for Sample D.

	Values
Total Co-Co average coordination number	9.9
Total Co-P average coordination number	4.7
Reduced chi square value	86.900344721
R-factor	0.000639151
Path Used for Phase Shift	Co-Co

5) Sample E

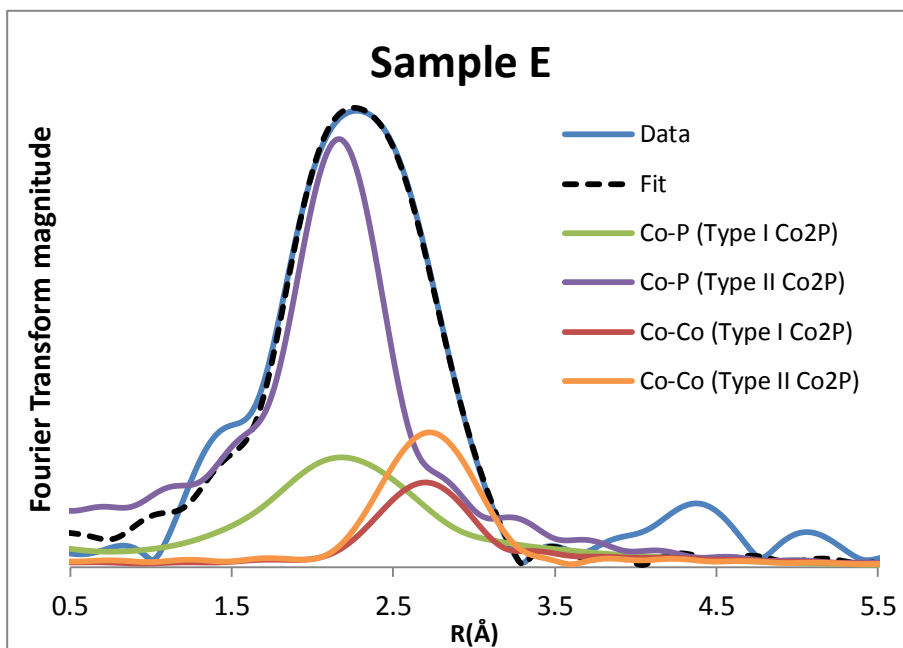


Figure A.11 The residual sums which contribute to sample E reveal a decrease in order, as the two distinct contributions are no longer distinguishable at separate distances as observed in sample D

Table A.17 Sample E pathways and associated variable summary

Pathways	Total Average Degeneracy	ΔE_0 (eV)	ΔR (Å)	σ^2
Co _A to P	3.075	-10	-0.088822	0.017251
Co _B to P	2.84	-2.546812	-0.014710	0.006905
Co _A to Co	4.9	1.596878	-0.060017	0.02000
Co _B to Co	3.188984	-0.64398	0.0158	0.012375

Table A.18 Summary of fit parameters for Sample E.

	Values
Total Co-Co average coordination number	8.1
Total Co-P average coordination number	5.9
Reduced chi square value	86.900344721
R-factor	0.000639151
Path Used for Phase Shift	Co-P

6) Sample F

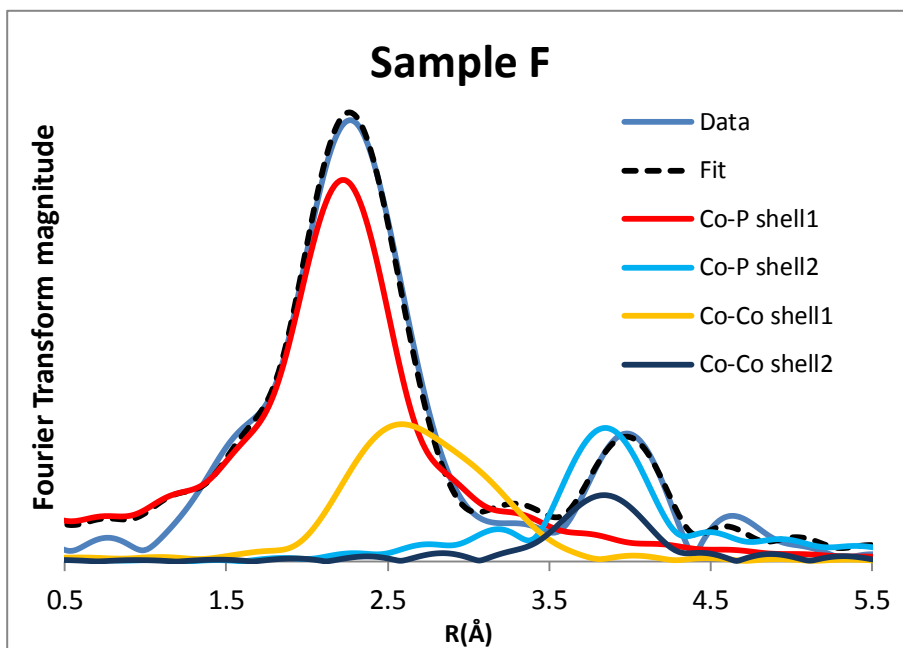


Figure A.12 The FT for sample F shows an apparent second shell contribution, associated with long-range order with increased crystallinity.

Table A.19 Sample F pathways and associated variable summary

Pathways	Total Average Degeneracy	ΔE_0 (eV)	ΔR (Å)	σ^2
Co to P shell 1	5.52	-3.032113	-0.036685	0.008577
Co to Co shell 1	7.524	-6.497283	-0.132	0.010045
Co to P shell 2	8.48	5.084003	-0.061169	0.003803
Co to Co shell 2	2.46	1.452831	0.049239	0.002997

Table A.20 Summary of fit parameters for Sample F.

	Values
Total Co-Co average coordination number	7.5
Total Co-P average coordination number	5.5
Reduced chi square value	355.397899926
R-factor	0.008133337
Path Used for Phase Shift	Co-P

Calculation of the concentration of atoms on the surface in a nanoparticle

The average nanoparticle size was estimated by TEM. Spherical Cluster

Approximation (SCA) was used in this calculation.¹ We assumed that the NPs are spherical.

$$V_{\text{cluster}} \approx NV_{\text{atom}} \quad (1)$$

$$\frac{4}{3}\pi(R_{\text{cluster}})^3 = N\frac{4}{3}\pi(R_{\text{atom}})^3 \quad (2)$$

Where N is the total number of atoms in the cluster, V is cluster/atom volume, and R is radius of cluster/atom. After rearranging, we obtain:

$$R_{\text{cluster}} = N^{1/3}R_{\text{atom}} \quad (3)$$

By using R_{cluster} as 5.95nm which was obtained by TEM analysis and R_{cobalt} as 0.135nm, the number of atoms in NP is 85615.

$$S_{\text{cluster}} = 4\pi R_{\text{cluster}}^2 \quad (4)$$

S is the surface area of cluster/atom. The number of surface atoms N_s in a cluster is given by dividing the surface area of the cluster by the cross-sectional area of an atom (A_a). After rearranging, we obtain:

$$N_s = \frac{4\pi(R_{\text{cluster}})^2}{\pi R_{\text{atom}}^2} = 4N^{2/3} \quad (5)$$

From this equation, the number of surface atoms is 7770. Therefore, the fraction of the surface atoms is about 9%. ($\approx 7770/85615$)

Calculation Details

Total energy calculations were carried out using the Vienna Ab-initio Software Package (VASP),²⁻⁵ within the framework of DFT. The gradient- corrected PBE exchange-correlation functional was employed,⁶ along with the Projector Augmented Wave (PAW) method.^{7,8} For density of state calculations the hybrid HSE06 functional was also employed.⁹ Calculations were carried out with periodic boundary conditions, with wave functions expanded on a plane-wave basis set. K-sampling of the Brillouin zone was performed using special k-points generated using the method of Monkhorst and Pack.¹⁰ For density of states (DOS) calculations in which the PBE functional was employed, K-point meshes of $12 \times 12 \times 12$ and $13 \times 21 \times 11$ were employed, for the ϵ -Co and Co₂P/ CoP cells, respectively. For DOS calculations in which the HSE06 functional was employed, K- point meshes of $6 \times 6 \times 6$ and $8 \times 12 \times 6$ were employed, for the ϵ -Co and Co₂P/CoP cells, respectively. The kinetic energy cutoff for the wave functions was set to 351.0 eV for DOS calculations in which the PBE functional was employed, and 270.0 eV for DOS calculations in which the HSE06 functional was employed. The corresponding cutoff energies for the augmentation functions were set to 621.2 eV and 477.8 eV. For nudged elastic band (NEB) calculations, the same k-point meshes and cutoff energies were used as for the HSE06 DOS calculations. The corresponding cutoff energies for the augmentation functions were set to 621.2 eV and 477.8 eV.

Density of States for Co₂P and CoP

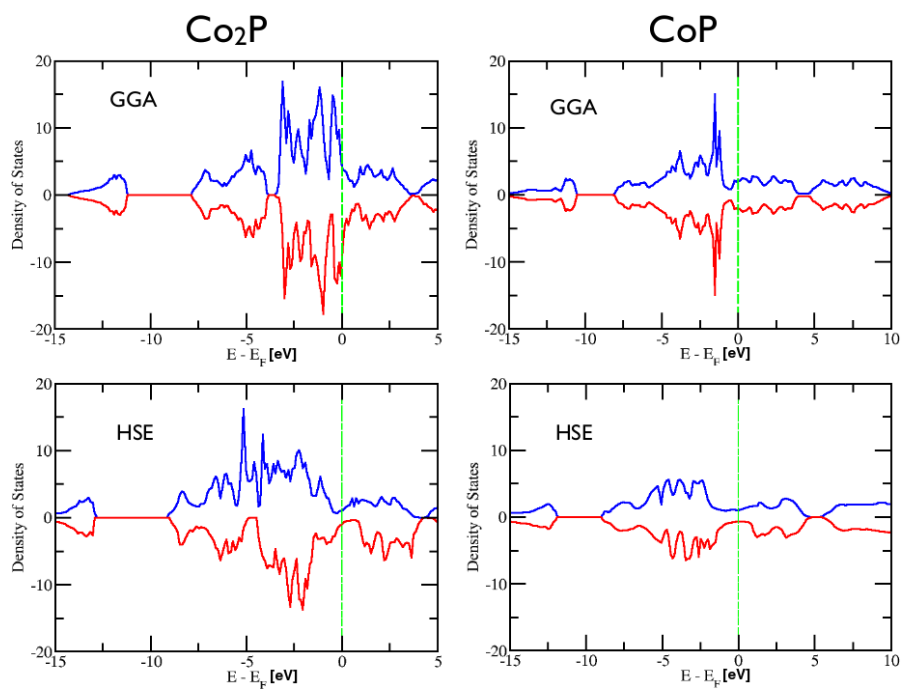


Figure A.13 Total DOS plots for the Co₂P and CoP structures for the GGA PBE exchange-correlation functional and HSE06 hybrid functional. Spin up (blue lines) and spin down (red lines) contributions are represented in each case.

References

1. Johnston, R. L., *Atomic and Molecular Clusters*. Taylor & Francis: 2002; p 256.
2. Kresse, G.; Hafner, J. *Phys. Rev. B* **1993**, 47, (1), 558.
3. Kresse, G.; Hafner, J. *Phys. Rev. B* **1994**, 49, (20), 14251.
4. Kresse, G.; Furthmüller, J. *Comput. Mater. Sci.* **1996**, 6, (1), 15-50.
5. Kresse, G.; Furthmüller, J. *Phys. Rev. B* **1996**, 54, (16), 11169.
6. Perdew, J. P.; Burke, K.; Ernzerhof, M. *Phys. Rev. Lett.* **1996**, 77, (18), 3865.
7. Blöchl, P. E. *Phys. Rev. B* **1994**, 50, (24), 17953.
8. Kresse, G.; Joubert, D. *Phys. Rev. B* **1999**, 59, (3), 1758.
9. Paier, J.; Marsman, M.; Hummer, K.; Kresse, G.; Gerber, I. C.; Angyan, J. G. *J. Chem. Phys.* **2006**, 124, (15), 154709-13.
10. Monkhorst, H. J.; Pack, J. D. *Phys. Rev. B* **1976**, 13, (12), 5188.

CHAPTER 3

3 UNINTENDED PHOSPHORUS DOPING OF NICKEL NANOPARTICLES DURING SYNTHESIS WITH TOP: A DISCOVERY THROUGH STRUCTURAL ANALYSIS *

3.1 *Abstract*

We report the discovery of unintentional phosphorus (P) doping when tri-*n*-octylphosphine (TOP) ligands are used in Ni nanoparticle synthesis, which is the most common method for monodisperse Ni nanoparticle synthesis. The nanoparticles appear pure *fcc* Ni in X-ray diffraction despite the surprisingly high level (5 at. %) of P. We find that the P doping follows a direct relationship with increased reaction time and temperature and that the P doping can be estimated with the degree of lattice expansion shown from a peak shift in the XRD spectrum. Through EXAFS modeling and density-functional (DFT) calculations of defect formation energies we find that the P atoms are preferentially located on the *fcc* lattice as substitutional dopants, with oxidation state of zero. Magnetic and catalytic properties are shown to be greatly affected by this doping: DFT calculations show magnetization losses in the Ni system, as well as in Fe and Co systems. These findings are likely relevant for other metal syntheses that employ phosphine ligands.

* Originally Published as: L. M. Moreau,* D.-H. Ha,* C. R. Bealing, H. Zhang, R. G. Hennig and R. D. Robinson, "Unintended Phosphorus Doping of Nickel Nanoparticles during Synthesis with TOP: A Discovery through Structural Analysis," *Nano Lett.* **12**, 4530 (2012) Reprinted with Permission from American Chemical Society. (* = equally contributed)

3.2 Introduction

For nearly two decades the backbone of colloidal nanoparticle synthesis has been the organic molecules that serve as both surfactants and solvents for the nanoparticles and precursors.¹⁻³ The common ligands and solvents used are bulky hydrocarbon molecules, such as oleic acid, tri-*n*-octylphosphine oxide (TOPO), tri-*n*-octylphosphine (TOP), and phosphonic acids. These coordinating molecules play a crucial role in controlling the size and morphology of the nanoparticles, stabilizing the nanoparticles, and solvating the precursors.^{2, 4, 5} These reagents had generally been considered pure and were believed to play only a supporting role in the synthesis. However, recent papers have provided a more complex story,⁶ such as elucidating the role of impurities^{7, 8} and coordination groups,⁹ and even identifying the unexpected reactivity of TOPO being used as a phosphorus source.¹⁰ In this work we find that a commonly used surfactant in Ni nanoparticle synthesis, TOP, can act as a P source during synthesis, leading to unintended P doping.

Nickel nanostructures are of increasing interest for their novel magnetic and catalytic properties. Nickel nanoparticles have been shown to decrease the activation energy of hydrogen desorption by surface activation, enhancing catalytic activity.¹¹ They have also demonstrated functionality as catalysts for the decomposition of hydrazine¹² and hydrogenation reactions,^{13, 14} and enhance the hydrogen storage capacity of carbon nanotubes by up to three times.¹⁵⁻¹⁸ In recent years, organic-phase synthesis of Ni nanoparticles using TOP as a surfactant¹⁹⁻²⁴ has resulted in better control of particle size and morphology. This is an important achievement because catalytic activity has been shown to increase in liquid phase dehydrogenation reactions

with smaller particles²⁵ and magnetic properties of Ni nanoparticles are highly dependent on particle size.²⁶ For instance, Carenco *et al.* performed a specific study of Ni nanoparticle synthesis using TOP as a surfactant.²⁷ They determined that TOP was crucial to achieve monodisperse Ni nanoparticles in comparison to other methods, and report the synthesis of monodisperse Ni nanoparticles with a tunable size range from 2 to 30 nm. Based on X-ray diffraction (XRD), all previous studies characterized their Ni nanoparticles as pure *fcc* Ni.^{19, 21-24, 27}

In our study, we have synthesized Ni nanoparticles following similar procedures involving TOP and have found that the composition is not pure Ni. In particular we discover that the Ni particles, despite their characterization as pure *fcc* Ni based on XRD, contain a significant amount of phosphorus. The excess P content has property implications not previously realized, especially with respect to magnetism and catalysis. We determine by density-functional calculations that magnetic properties dramatically decrease with increasing P content. Catalytic behavior should also be affected: we find that there are some significant differences in the electronic density of states (DOS) near the Fermi energy with P doping. Equally surprising is the location and charge of the P atoms in the lattice: a majority of P atoms sit substitutionally on the *fcc* lattice sites and were found through calculations to be charge neutral (P^0).

Although techniques which enable the structural characterization of bulk material have been well-developed, the dominance of surface facets, small size, and poor crystalline order makes characterization of nanoparticles difficult. X-ray absorption spectroscopy (XAS) is a powerful method to study local atomic

arrangements and has been used to resolve the structure of colloidal nanocrystals.²⁸⁻³⁵ With the use of high energy, white-light synchrotron radiation, sensitive XAS spectra can be obtained and used to gain insight into materials' structural properties.^{36, 37} Using both the lower-energy X-ray absorption near edge structure (XANES) portion of the spectrum to resolve electronic and geometric structure, and the higher-energy quasi-periodic EXAFS (extended X-ray absorption fine structure) modulations to resolve radial structure, the structure of both XRD-detectable and XRD-amorphous materials can be determined in fine detail.³⁸

XAS in combination with other characterization methods – such as XRD, density-functional theory (DFT), inductively coupled plasma (ICP), transmission electron microscopy (TEM), and superconducting quantum interference device (SQUID) measurements – allows for resolution of composition, structure, and property relationships in complex nanomaterials. EXAFS and XRD complement each other by providing insight into short-range and long-range order, respectively. DFT enables calculation of formation energies to determine lowest-energy compositional configurations and charge analysis for dopant atoms.^{39, 40} TEM provides morphological and size-distribution insight, ICP provides the atomic composition, and SQUID enables the study of magnetic properties. Thus a complete picture of the nanoparticle structural properties can be obtained through cooperative use of these methods.

In this investigation, we (1) report a surprisingly high amount of P present in the *fcc* Ni nanoparticles that results from routine synthesis and show that the P doping in the *fcc* Ni nanoparticles increases as a function of reaction time and temperature, (2)

present the structural attributes (inter-atomic distances, distortion, coordination, and composition) of the Ni nanoparticles resulting from the P atom doping, (3) demonstrate the feasibility of significant phosphorus stability within an *fcc* Ni lattice without significant lattice distortion, (4) reveal the effects of excess P content on the magnetic and catalytic properties, and the stability of both amorphous and crystalline phases that comprise transition metal nanoparticles, (5) compare the long-range structural characterization by XRD with the radial structure information obtained from EXAFS analysis, and (6) propose a method to determine the P content of the nanoparticles based as a function of XRD peak position. Due to the intimate connection between nanoscale structural attributes and their resulting properties, control over nanoparticle structure and doping will enable the tailoring of their properties for magnetic and catalytic applications.

3.3 Results

We briefly describe the synthesis conditions for the nanoparticles. Complete descriptions of all characterization and analysis methods can be found in the supplementary materials. Synthesis of the Ni nanoparticle samples was based on thermal decomposition of a Ni-TOP complex as outlined by Muthuswamy *et al.*²¹ Under air-free conditions, 1.17 g (4 mmol) of nickel acetylacetonate (Ni(acac)₂) and 4.48 mmol of tri-*n*-octylphosphine (TOP) were mixed into a flask containing 10 mL of octyl ether (solvent) and 4 mL oleylamine (surfactant). The solution was heated to

230 °C and the particles were allowed to grow for 1 hour. After the reaction the nanoparticle products were isolated by centrifugation with excess ethanol.

Our Ni nanoparticle recipe falls within the range of conditions previously reported for pure-phase Ni.^{19, 21, 23, 27} Methods from the literature for the synthesis of Ni nanoparticles using this same synthetic method use TOP/Ni(acac)₂ ratios from 0.8 to 3, temperatures ranging from 200 °C to 240 °C, and oleylamine/Ni(acac)₂ ratios from 3 to 10.^{19, 21, 23, 27} Thus, our results, in which we find surprisingly high P concentrations in the Ni nanoparticles, should be applicable to these previous works.

TEM images show that the Ni particles are monodisperse, in agreement with previous studies which use TOP as a surfactant (**Fig. 3.1a**).²⁷ The Ni nanoparticles (22.2 nm, std. dev. 8.9%) have a quasi-spherical morphology. HRTEM (high-resolution TEM) results of these particles show them to be polycrystalline (**Fig. 3.1b**) and XRD results show that each of the Ni nanoparticle peaks matches well with the *fcc* Ni structure (**Fig. 3.1c**). The slight contrast on the surface of the nanoparticle sample in **Fig. 3.1b** is likely due to surface oxidation during the oxygen plasma cleaning procedure (see supplementary materials for method). Prior to plasma cleaning, the nanoparticles have no contributions from nickel phosphide or nickel oxide detected by XRD. From the Scherrer equation the grain size in these Ni particles is about 5.5 nm, indicating that the Ni particles are polycrystalline, each consisting of several grains, which is consistent with our HRTEM images.

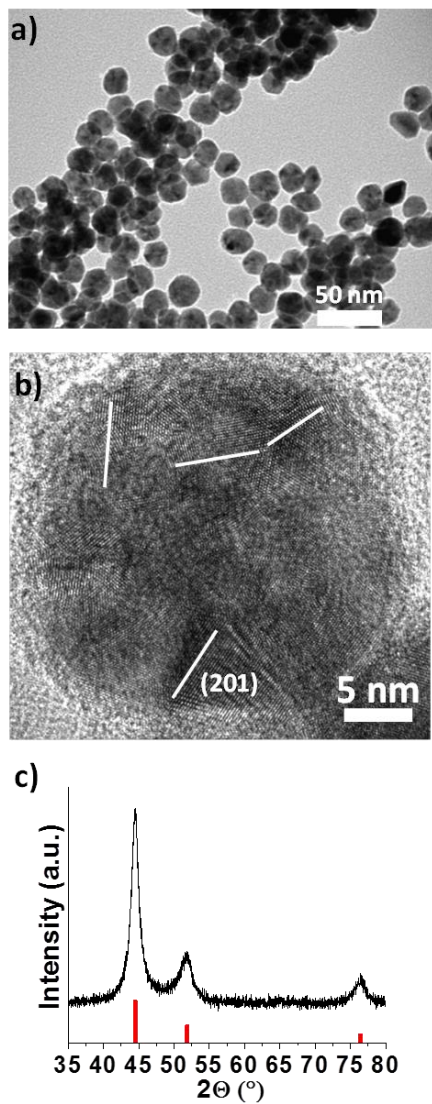


Figure 3.1 TEM images and XRD spectrum of Ni nanoparticles. (a) TEM images show monodisperse Ni nanoparticles with quasi-spherical morphology. (b) HRTEM image reveals that the Ni nanoparticles are polycrystalline and that they are not core-shell structures. The white lines in the particle present nickel (201) lattice planes indicating multigrains within the nanoparticle. (c) XRD spectrum shows crystalline *fcc* Ni (red bars correspond to JCPDS 65-2865.)

The Ni nanoparticle sample and Ni foil XAS spectra (**Fig. 3.2a**) share similar features especially within the lower energy XANES region, and therefore exhibit similar electronic structure. The K-edge in both samples is 8334 eV, a value associated with the $1s-3d$ atomic line.^{41, 42} Although the spectra for the Ni nanoparticles and the Ni foil show similar features throughout the near-edge and EXAFS regime, there is a noticeable reduction in the Ni nanoparticle sample's EXAFS oscillation amplitude. Also, the Ni nanoparticle spectrum features a white line peak and EXAFS oscillations that are broadened compared to the sharp features in the Ni foil spectrum.

The shape and phase of both the k -space and R -space XAS spectra are very similar for the Ni nanoparticles and Ni foil (**Fig. 3.2b,c**). Both samples show significant contributions beyond the first coordination shell, observable in the R -space spectrum (**Fig. 3.2c**). This display of long-range order is characteristic of a crystalline structure.³⁶ The spectral intensity amplitudes of the Ni nanoparticles, however, are considerably reduced compared to bulk. There is a known amplitude reduction associated with nanoscale effects.^{43, 44} Theory predicts an intensity reduction of about 8% due to nanoscale effects for our 5.5 nm grains.⁴⁵ Experimental reports in related material systems have seen intensity reductions as large as 25% in k -space and 20% in R -space for 6 nm NiO nanocrystals.⁴³ Our crystal domains, at 5.5 nm, should show comparable intensity reductions to these works but we find much larger reductions of ~41% in both k - and R -space.

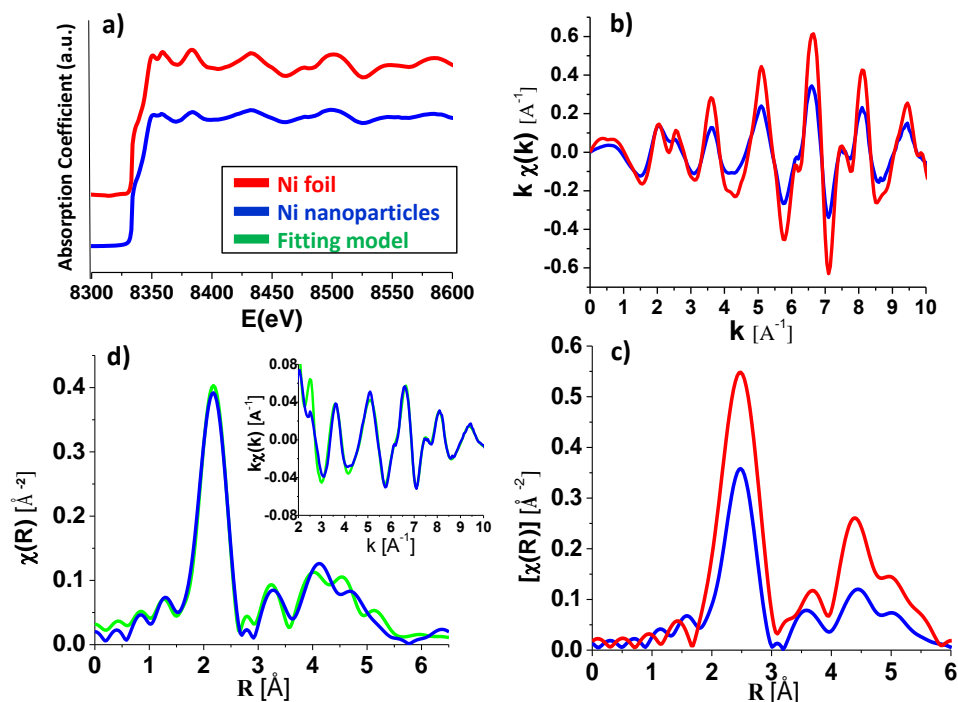


Figure 3.2 Ni nanoparticles XAS data and EXAFS fitting model. (a) The spectra of the Ni foil (red) and Ni nanoparticles (blue) are shown. Observable broadening is noticeable in the Ni nanoparticle sample. (b) Plots of the Ni foil and nanoparticle sample spectra in k -space. The shapes of the curves are similar but there is a reduction in amplitude between the Ni foil and Ni nanoparticle sample. (c) Non-phase shifted R -space spectra. A high degree of crystallinity is noticeable in the Ni foil and Ni nanoparticle samples, despite significant reduction in the Ni nanoparticle sample peak heights. (d) The theoretical fitting model using *fcc* Ni and substitutional P is shown in R -space and k -space (inset). The fitting results (green) are well-matched to the experimental spectra (blue).

The amplitude reduction can be explained by P content. In bulk Ni a reduction in k - and R -space intensity was previously observed when P was introduced into the lattice.⁴¹ With 8 at.% P the reduction was about 20% and at 10 at.% P the reduction increased to 47%.⁴¹ In both cases the lattice retained the fcc structure despite this high level of P content. It is likely that the intensity reductions in our nanoparticle system result from a combination of nanoscale effects and P doping (discussed below).

Through the EXAFS fitting process we found that it was impossible to resolve the Ni sample with a model that included only a pure, well-ordered fcc Ni crystal structure (see **Fig. B.2a**). Degeneracy values reveal that pure fcc Ni alone does not provide an accurate model, despite XRD results, which suggest a pure-phase fcc structure. Using only fcc pathways in the fitting model, for the first shell, the degeneracy of the model is only 74% that of bulk, meaning that 26% of the Ni–Ni pathway degeneracies are missing (see **Table B.1**). This degeneracy reduction is unphysical for fcc Ni and cannot be ascribed to nanosize effects: using the method proposed by Calvin *et al.* to estimate reduction in coordination number due to nanoscale effects, the degeneracy value in our 5.5 nm crystal domains should be 92% of the accepted bulk degeneracy value.⁴⁵ Thus the 74% obtained using pure fcc Ni is far too low of a contribution to be accounted for by nanoscale effects, even when the typical 10% error in the coordination numbers determined by the fitting is considered.^{29, 46, 47} Additional structural contributions must therefore exist.

Surface oxidation also does not account for the missing structural contributions. In our previous studies of the Co-P nanoparticle system, additional contributions to the ϵ -Co structure were attributed to surface oxidation.⁴⁸ However,

using a combination of Ni *fcc* and NiO pathways, the fit was also poor (**Fig. B.2b**). Much larger degeneracy values were obtained for the second shell than for the first shell for all permutations of the model fit (**Table B.2**), which is unreasonable since the degeneracy values should remain constant or decrease for higher order shells.⁴³

A reasonable model was found using a combination of *fcc* Ni and Ni₂P pathways (see supplementary materials **Fig. B.3**, **Table B.3**). Using this combination the *fcc* pathways became well-ordered, but there was extreme distortion observed in the Ni₂P fitting and atomic positions, particularly for higher shells of Ni₂P. This suggests that the positions of the P atoms do not correspond closely to those in the Ni₂P structure. We examined the radial distances (see **Table B.4**) and realized that a majority (63%) of the Ni–P pathways was within a distance of 3.6% from substitutional *fcc* positions, and a smaller percentage (17%) corresponded to octahedral interstitial site distances. Using this knowledge we proposed that the P atoms were located primarily on substitutional sites, and created a new EXAFS model based on this assumption.

To achieve the best-fit model for the Ni nanoparticle sample we used single and multiple scattering pathways from a combination of *fcc* Ni and an artificially created *fcc* lattice built with three Ni atoms and one P atom substituted on the fourth Ni *fcc* site (*e.g.*, *fcc* Ni₃P, see **Fig. 3.3** and **Fig. B.4**). The *fcc* Ni₃P contributions simulate the P substitution within the Ni *fcc* lattice, and also enable distortion of the Ni atoms surrounding the substitutional P. Thus, the additional degeneracies for the Ni–Ni pathways are accounted for by pathways which are distorted from their Ni *fcc* positions. These two factors – additional Ni–P pathways and allowing neighboring Ni

positions to distort – improved the goodness of the fit to acceptable levels compared to the poor fit from using only a pure-phase *fcc* Ni model. The substitutional P and particularly the neighboring Ni–Ni pathways deviated from ideal positions, with large differences in inter-atomic distance (exceeding 5% of the average inter-atomic distance, as shown in **Fig. 3.3**). The large deviations from ideal positions and the decreased degeneracy of these pathways (see **Table 3.1**) indicate that the substitutional P contribution present within the crystalline *fcc* Ni lattice distorts the surrounding atoms in the lattice, creating somewhat disordered pathways within the well-ordered *fcc* structure.

The *fcc* Ni + substitutional P model has a high quality fit (low *R*-factor) to the experimental data in both *R*-space (**Fig. 3.2d**) and *k*-space (**Fig. 3.2d**, inset). **Table 3.1** contains the parameters used to construct the fitting model for the Ni nanoparticles. The parameters included in the table are the reference degeneracy value found in bulk structure (N_{theory})⁴⁹ (the number of atoms located at a specified distance from the central scattering atom), the degeneracy value determined by the fit to the experimental spectra (N_{exp}), the reference inter-atomic distance from the scattering atom found in bulk (R),⁴⁹ the nanoparticle deviation from the bulk reference inter-atomic distance resulting from the fit (ΔR), the energy shift parameter (E_0), which was fixed for pathways consisting of the same absorbing and scattering atom, and the mean-squared disorder (σ^2). A reasonable estimate of the error associated with the degeneracy and mean-squared disorder values (N_{exp} and σ^2) is 10%^{29, 46, 47} and an estimate of error for ΔR and E_0 is 5%.⁴⁷ Additional higher-order shell pathway parameters are included in **Table B.5**.

Table 3.1 First and second shell path parameters. Parameters are listed for *fcc* Ni and for the artificial Ni₃P *fcc* model used to construct the best-fit EXAFS model for the Ni nanoparticle sample.

Ordered Ni-Ni Pathways from <i>fcc</i>						
Pathway	N_{theory}	N_{exp.}	R (Å)	ΔR (Å)	E₀ (eV)	σ² (Å²) x 10⁻³
Ni–Ni (shell 1)	12	9.49	2.49	-0.003	6.26	7.73
Ni–Ni (shell 2)	6	4.72	3.52	-0.008	6.26	12.0
Ni-Ni pathways (Ni₃P <i>fcc</i> model)						
Pathway	N_{theory}	N_{exp.}	R (Å)	ΔR (Å)	E₀ (eV)	σ² (Å²) x 10⁻³
Ni–Ni (shell 1)	8	1.68	2.49	0.277	6.26	13.8
Ni–Ni (shell 2)	6	1.25	3.52	-0.280	6.26	14.0
Ni-P pathways (Ni₃P <i>fcc</i> model)						
Pathway	N_{theory}	N_{exp.}	R (Å)	ΔR (Å)	E₀ (eV)	σ² (Å²) x 10⁻³
Ni–P (shell 1)	4	0.83	2.49	-0.194	-8.70	8.95
Ni–P(shell 2)	8	1.65	4.32	0.094	-8.70	9.13

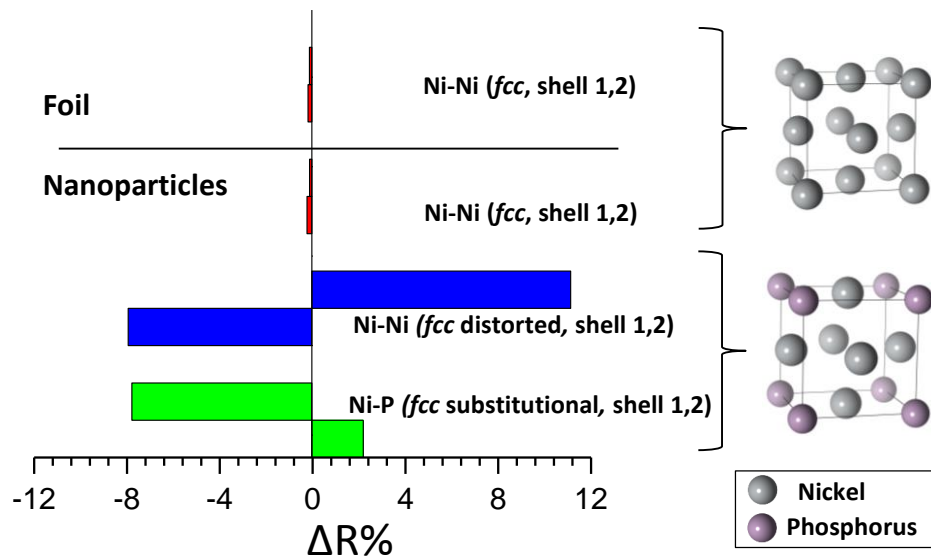


Figure 3.3 Deviation of inter-atomic distance from reference Ni pathways: red

bars correspond to well-ordered Ni-Ni pathways from the *fcc* Ni phase, blue bars correspond Ni-Ni pathways in the Ni₃P *fcc* model, and green bars correspond to Ni-P pathways in the Ni₃P *fcc* model. Deviations in inter-atomic distance between the fitting model and bulk are given for the first two shells, expressed as a percentage of shell distance. Note the large deviations associated with the Ni and P positions in the Ni₃P model. Atomic structures at right show the EXAFS models used for the fitting. At top is the *fcc* Ni lattice, and on the bottom is the artificial Ni₃P *fcc* model used to account for P doping and Ni positional distortions, based on *fcc* Ni with substitutional

P atoms.

We can use the *fcc* Ni + substitutional P model to estimate the amount of P in the nanoparticles by examining the degeneracy of the pathways. The P content is determined by summing the degeneracy values (*i.e.*, N_{exp}) for the Ni–P pathways and dividing by the sum of the degeneracies for all pathways (see supporting information for methods). This same method is used to determine the number of Ni atoms in ordered and disordered *fcc* positions. The first three columns of **Table 3.2** show the estimated percentages of each type of contribution (Ni in ordered *fcc* positions, Ni in distorted *fcc* positions surrounding the substitutional P atoms, and P from substitution on *fcc* sites). The estimated P percentage in the structure from the model fit, based on the number of phosphorus atoms in the 5.57 Å radial shell, is 5.3%. This is a large amount of P and an unexpected result considering that XRD only shows the *fcc* phase and no detectable phosphide compounds. Furthermore, the result is important considering that many groups have used this synthetic method for their Ni nanoparticles, which they assume to be pure *fcc* Ni. In a similar finding in bulk materials, retention of the Ni *fcc* lattice has been observed in bulk Ni–P alloys with atomic percentage of P up to 14%.⁴¹ In these bulk Ni–P samples the Ni *fcc* lattice was maintained with good crystallinity despite the high phosphorus content.⁴¹ This suggests that such phosphorus incorporation on substitutional sites may also be possible at the nanoscale.

To confirm that the P contribution is not from TOP surface ligands, ICP-OES (inductively coupled plasma - optical emission spectrometry) was performed on Ni nanoparticles for Ni, P, and C contents. The atomic percentages in the sample were found to be 83.3%, 5%, and 11.7% for Ni, P, and C, respectively (**Table 3.3**). If we

consider that all the detected carbon atoms are from TOP, which has twenty-four C atoms and one P atom in its molecule, then the C/P ratio should be 24/1. But the C/P ratio from our ICP is nearly an order of magnitude smaller than what would be expected from the TOP ligand molecules. This confirms that most of the P atoms are contained within the Ni nanoparticles and not located on the surface in the form of TOP molecules.

This high P content is repeatable across multiple syntheses. Results from ICP analysis on five Ni samples from eight identical synthesis conditions results in an average of 6.4 at.% P in the Ni nanoparticles (**Table 3.2**, column 4), with a standard deviation of 1.9 at.% P.

We also calculate the surface coverage by TOP ligands of our Ni nanoparticles. Using the carbon content as a guide we find that only 12% of the surface Ni atoms are connected with TOP molecules. A comparable surface ligand coverage has been previously observed,⁵⁰ and nanoparticle phosphine ligand coverage has been shown to decrease with increasing particle size,⁵¹ which is relevant to our larger nanoparticles. The low TOP coverage explains the slow precipitation behavior of the Ni nanoparticles in a non-polar solvent such as hexane.

As another test to prove that the P contribution is not from surface TOP surfactant, a ligand exchange was performed on the Ni nanoparticles, exchanging the existing ligands for oleic acid (see supporting information for methods). ICP analysis was then performed on both the as-prepared (with TOP surfactant) nanoparticles and the nanoparticles after ligand exchange. Results of P content between the two samples

showed negligible changes (5.0 at.% P before ligand exchange vs. 5.2 at.% P after ligand exchange) confirming that the P content measured by ICP is not dominated by surface phosphine.

Table 3.2 Summary of Ni and P content from EXAFS modeling and ICP. The first two columns show the % contribution of the Ni atoms in both ordered and distorted positions with respect to the *fcc* Ni lattice. In the third column is the phosphorus atomic percentage calculated from EXAFS modeling. The P is located on substitutional *fcc* sites. The final column lists the average phosphorus content determined from ICP results.

% atoms Ni <i>fcc</i>, ordered	% atoms Ni <i>fcc</i>, distorted	% atoms P (substitutional)	% atoms P from ICP results
79.2%	15.5%	5.3%	6.4%

Table 3.3 The elemental composition of Ni nanoparticles synthesized through standard techniques based on ICP measurements. From these results the carbon content is an order of magnitude too small in comparison to the phosphorus at.% for the phosphorus to be a result of TOP surface ligand contributions.

Element	Ni	P	C
Atomic %	83.3	5.0	11.7

To further investigate the synthetic conditions for P inclusion, the effects of reaction temperature and time on the P content of the Ni nanoparticles were studied. Plotting P content for reactions at 210, 220 and 230 °C, with samples taken at 20, 40 and 60 minutes, shows a consistent increase in P content within the nanoparticles as a function of reaction temperature and time (**Fig. 3.4a**). This result further confirms that the P content is incorporated into the nanocrystal and not merely on the surface. Additionally, the wide variance of P content in the 230 °C samples (open red symbols in **Fig. 3.4a**) demonstrates that P incorporation at higher reaction temperatures is sensitive to minor changes in synthetic conditions. TEM images of the nanoparticles synthesized with varied conditions are included in the supplementary materials (**Fig. B.5**).

A trend of lattice expansion due to the P doping is clearly shown in **Fig. 3.4b**. The (111) 2-theta peak from reference (JCPDS 65-2865) is 44.5°. The P doped nanoparticle samples show XRD peaks shifted toward lower angles. The black line in **Fig 3.4b** is linearly fitted with the results from P doped Ni nanoparticles and the Ni reference ($Y = -0.0535X + 44.522$, $R^2=0.7445$). From this equation it is possible to roughly predict the P content of Ni nanoparticles from an XRD pattern. The d-spacing is also calculated based on the peak position (**Fig 3.4b**). At a P content of ~10 at. %, there is a ~1% expanded lattice constant.

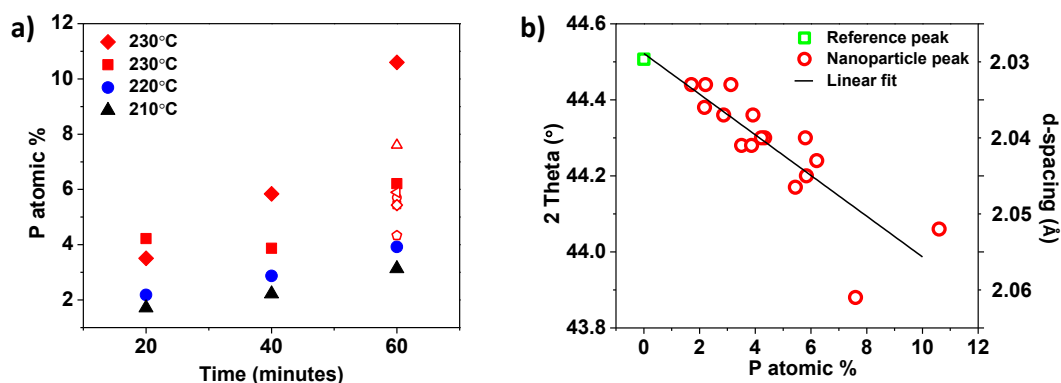


Figure 3.4 Implications of synthetic parameters on Ni nanoparticle P atomic % and corresponding XRD peak shifts. (a) Correlations between reaction temperature and time: The black, blue, and red solid symbols represent the P at. % of samples synthesized at 210, 220, and 230 °C, respectively, for different reaction times. All of the open symbols exhibit P at. % from the samples synthesized at 230 °C for 60 mins. (b) The correlation between the P at. % and the (111) peak position of Ni nanoparticle samples and the Ni reference: The green open square represents the (111) 2-theta peak position (44.5°) of Ni reference (JCPDS 65-2865). The red open circles represent the (111) 2-theta peak positions of the samples which show P contents. The d-spacing of (111) plane is also calculated based on the peak positions, showing the lattice expansion due to P doping.

Fig. 3.3 shows the deviations in atomic position as a percentage of the reference crystalline atomic positions ($\Delta R\%$) for the first and second shell atoms. The atoms are categorized by structural contributions: 1) Ni–Ni from *fcc* Ni, 2) Ni–P from substitutional P on *fcc* sites, and 3) Ni–Ni from Ni on *fcc* sites which are allowed to distort, representing the Ni atoms which surround the substitutional P. For our Ni nanoparticle samples the majority (79.2%) of the *fcc* Ni pathways deviate minimally from the bulk inter-atomic distances, with $\Delta R/R < 0.25\%$. These deviations are similar in magnitude to the Ni foil deviations (compare red bars in **Fig. 3.3**, Ni foil versus Ni nanoparticles). This means that the majority of Ni atoms are located on the *fcc* lattice. As a result, the bulk-like *fcc* Ni contributions within the Ni nanoparticle sample are detectable by XRD. A smaller portion of the Ni–Ni pathways within the nanoparticles (blue bars in **Fig. 3.3**), have large ΔR values, representing Ni atoms that deviate from their *fcc* positions, likely as a result of nearby substitutional P. These Ni–Ni contributions are described by the *fcc* Ni₃P component of the model. The Ni–P pathways resulting from P substitution on the *fcc* lattice (green bars in **Fig. 3.3**) also show deviations from ideal *fcc* positions, yet they are smaller than the deviations of the distorted Ni–Ni pathways. The P atoms may not be sitting in ideal *fcc* sites because: 1) a small number of the P atoms may be positioned in octahedral sites, as suggested by our Ni/Ni₂P EXAFS model (see supplementary materials), 2) the P atoms may be positioned slightly off the *fcc* lattice sites, or 3) the P atoms may take the form of dimers within the structure, as suggested by our density-functional calculations (*vide infra*). All aforementioned phenomena would cause the inter-atomic distances to deviate slightly from the value of the ideal *fcc* Ni phase. The possibility

of the P atoms sitting in grain boundaries within the nanoparticles was considered. This is unlikely because the grain boundaries effectively act as a surface, at which the degeneracy values of higher order shells is known to be significantly diminished due to the surface termination effect,^{43, 45} and we do not observe this effect in our EXAFS model. Comparing the average mean-squared disorder values (**Table 3.1, Fig. B.6**), we see that the disorder is larger for the nanoparticles than for bulk (foil), meaning that the nanoparticle pathways have a higher degree of structural disorder. In addition, the distorted Ni–Ni pathways show larger values than the ordered Ni–Ni pathways, revealing that these pathways not only show greater distance deviation, but also are distributed in a less-uniform manner.

The unusually high P content in the Ni nanoparticles (6.4 at.% by ICP (average), 5.3 at.% by EXAFS) raises the question about the oxidation state of the P, and the feasibility of P substitution at such high concentrations, with relative retention of the structural integrity of the *fcc* lattice. DFT calculations including spin-polarization (see supplementary materials for computational details) of the charge density and Bader analysis⁵² for a *fcc* Ni supercell containing a single substituted P atom (Ni₁₀₇P) show only a small amount of charge transfer of less than 0.25 e between the P and the Ni atoms. A small Bader charge transfer of 0.25 electrons between P and Ni indicates that the bonding is mostly covalent in nature with some ionic character, which is consistent with the electronegativity values of P and Ni (see supplementary materials). This suggests that the P has an oxidation state of zero within the *fcc* Ni phase. This is confirmed by our XAS results, which reveal little

deviation from *fcc* Ni in the near edge region (XANES), showing that the Ni atoms (and therefore P atoms, due to charge-neutrality) have an oxidation number of zero.

The positions of the P atoms in the Ni lattice were also compared between the relaxed structures from the DFT calculations and our EXAFS models. Through EXAFS modeling, it was found that P atoms sit primarily on substitutional sites. DFT defect formation energies were calculated to determine the energetics of various possible positions of phosphorus atoms in *fcc* Ni. The formation energy for a P atom to sit substitutionally on a *fcc* lattice site is 0.8 eV (see **Table 3.4**). The formation energy for the interstitial sites is higher. It is 2.7 eV for the octahedral site and 3.9 eV for the tetrahedral site. Based on the formation energies, it is not surprising that the majority of the P atoms are found by the EXAFS analysis in both the *fcc* Ni + Ni₂P and the *fcc* Ni + substitutional P models, to be located on substitutional sites. However, the results of the *fcc* Ni + Ni₂P EXAFS modeling suggesting that ~17% of the Ni-P pathways correspond to octahedral position radial distances, is somewhat unexpected. Together, the EXAFS analysis and the DFT defect formation energies show that the majority of the P atoms are positioned on *fcc* lattice sites.

The analysis of the P location in Ni was extended to several other important transition metal (TM) systems. **Table 3.4** shows the formation energies for the P-doped ferromagnetic transition metals (TMs, TM = Ni, Co, Fe), where P is present at tetrahedral or octahedral interstitial lattice positions, or substituted for a TM atom. Total energies were calculated using (spin-polarized) DFT. Formation energies, E_f , were calculated as $E_f = [E[\text{TM}_n\text{P}_m] - (n\mu_{\text{TM}} + m\mu_{\text{P}})/m]$, where $E[\text{TM}_n\text{P}_m]$ denotes the total energy of the cell containing n TM atoms and m P atoms, and μ_{TM} and μ_{P} denote

the chemical potentials of TM and P, respectively. μ_{TM} was taken as the total energy per atom of TM in the appropriate crystal structure (*i.e.* *fcc*, *hcp*, *bcc*, for TM = Ni, Co and Fe, respectively), and μ_{P} was calculated as $\mu_{\text{P}} = (E[\text{TM}_3\text{P}] - (24\mu_{\text{TM}}))/8$, where $E[\text{TM}_3\text{P}]$ is the total energy of the TM_3P phase, calculated for a unit cell containing 24 TM ions and 8 P ions. Even when considering that the diffusion of a P atom as a substitutional impurity into a transition metal nanoparticle will require the formation of a vacancy and comparing the combined formation energy of a TM vacancy and a P atom substituted for a TM atom, substitutional rather than interstitial doping is significantly favored in all three TMs. Similarly, ϵ -phase Co has been found experimentally to favor substitutional rather than interstitial P-doping.⁴⁸

Table 3.4 Formation energy calculation results. Calculated formation energies for octahedral (o), tetrahedral (t), and substitutional (s) P, for Ni, Co, and Fe.

TM	Supercell	E_f (eV)
Ni	Ni ₁₀₈ P (o)	2.7
	Ni ₁₀₈ P (t)	3.9
	Ni ₁₀₇ P (s)	0.8
Co	Co ₉₆ P (o)	3.3
	Co ₉₆ P (t)	3.5
	Co ₉₅ P (s)	0.7
Fe	Fe ₁₂₈ P (o)	3.4
	Fe ₁₂₈ P (t)	3.4
	Fe ₁₂₇ P (s)	0.4

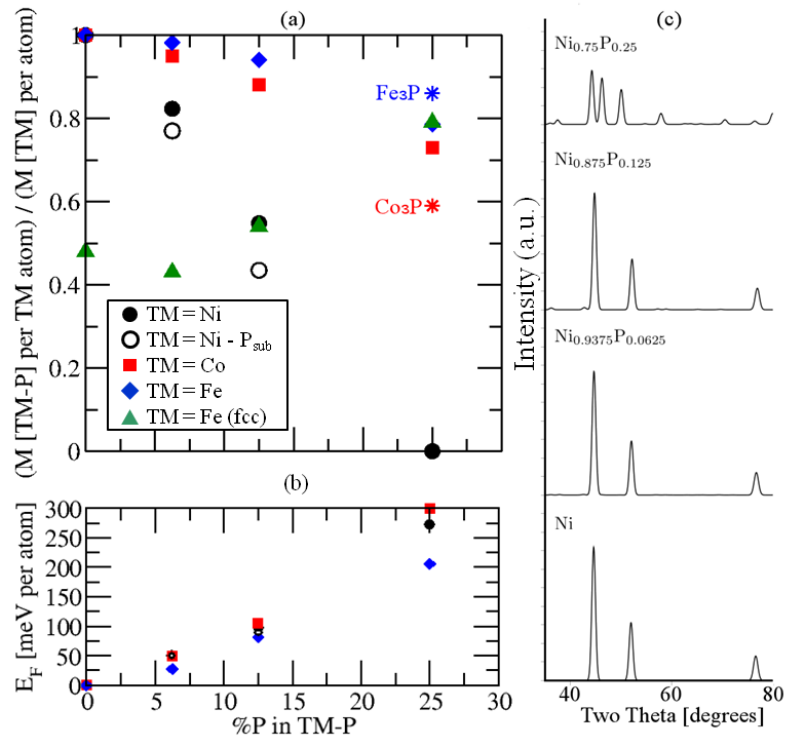


Figure 3.5 DFT calculations for phosphorus doping in transition metals (TMs): magnetization, formation energies, and diffraction patterns. (a) Magnetization M per TM atom for the TMs Ni (filled black circles), Co (red squares), and Fe (blue diamonds), substitutionally doped with P. The green triangles give the magnetization for P-doped *fcc* Fe. Magnetizations for the Co₃P and Fe₃P crystal structures are indicated by the red and blue stars, respectively. Empty black circles give the magnetization for Ni containing substitutional P dimers. (b) Formation energies E_f for P-doped Ni (filled black circles), Co (red squares), and Fe (blue diamonds). Empty black circles give the formation energy for Ni containing substitutional P dimers. Formation of P dimers in Ni was found to be energetically slightly favorable with respect to evenly-distributed P. (c) Calculated XRD patterns for pure and P-doped Ni.

Figure 3.5b shows the formation energies calculated for P-doped TM at concentrations of 6.25, 12.5, and 25 at.%. At 6.25 at.% P, the formation energies for the P-doped TMs are small (within 60 meV per atom), suggesting that P may be accommodated within the TM lattice at this concentration. As the concentration of P increases, the formation energy of the doped TM also increases, indicating that substitutional doping becomes less favorable. At 12.5 at.% P, the formation energy is still less than ~100 meV per atom, which is consistent with the observation of *fcc* Ni doped at 14 at.% P.³⁵ Formation of P dimers (empty black circles) in Ni was found to be energetically slightly favorable with respect to evenly-distributed P (filled black circles), for concentrations of 6.25 and 12.5 at.% P, supporting the hypothesis of P-clustering.

Experimentally, Ni has been found to accommodate up to 14 at.% P without departing significantly from the *fcc* crystal structure.⁴¹ Calculated XRD patterns for the relaxed Ni–P cells (**Fig. 3.5c**) are consistent with this result, indicating that the *fcc* structure is retained at P concentrations of 6.25 and 12.5 at.%, for which the XRD patterns are almost indistinguishable from that of pure Ni. At 25 at.% P the relaxed cell is deformed significantly with respect to the *fcc* structure, as is reflected in the altered XRD pattern. The Ni–P compound with the lowest phosphorus concentration in bulk materials is Ni₃P, which has 25 atomic percent P and exhibits a tetragonal structure.⁵³

Surprisingly, in contrast to our experimental results, the calculated lattice constant and bulk modulus for P-doped Ni, for concentrations of 6.25 and 12.5 at.% P indicate that the lattice undergoes a contraction as the concentration of P is increased,

consistent with the smaller covalent radius of P compared to Ni. The bulk modulus is increased by ~1% for Ni doped at 12.5 at.% P compared to pure Ni (see **Table B.6**). Because the experimental results show a lattice expansion rather than contraction, this implies that some of the P formation may occur on octahedral interstitial sites, instead of solely *fcc* substitutional sites. This finding is consistent with the EXAFS positions analyzed using the *fcc* Ni + Ni₂P model.

Phosphorus doping is expected to reduce the magnetism of Ni nanoparticles. **Figure 3.5a** shows the calculated magnetization M against the concentration of substitutional P, for *fcc* Ni (filled black circles). P is substituted for Ni and the atomic positions and cell size and shape are relaxed until the forces on all ions are less than 0.03 eV/Å. The calculations were carried out with periodic boundary conditions using supercells containing a single P atom, for P concentrations of 6.25, 12.5, and 25 at.%. The magnetization decreases for the P-doped Ni with increasing P doping. The decrease in magnetization with P concentration is considerable, falling to zero by 25 at.% P, exhibiting paramagnetism in Ni₃P.⁵⁴

3.4 Discussion

Through our DFT calculations we can estimate the P effect on magnetization to be expected in our nanoparticles. For Ni doped with 6.25 at.% P, which is close to the concentration measured to be present in the nanoparticles described in this article, M is calculated as 0.49 μ_B per Ni atom, which is equivalent to 45 emu/g, compared to the value obtained using a SQUID of ~29.5 emu/g (see **Fig. 3.6**). This discrepancy

might be explained by P clustering. The empty black circles in **Fig. 3.5a** give the magnetization for P dimers within the Ni lattice. The dimers lead to slightly lower magnetizations than the evenly-distributed P for the same concentration. For the dimers, P was substituted for two adjacent Ni atoms, in a supercell which is twice as large as that used for the calculations corresponding to the evenly-distributed P (*i.e.*, the filled black circles). The lower magnetization of the Ni doped with P dimers indicates that clusters of P within the Ni lattice would disrupt the ferromagnetism more than evenly-distributed P; P clustering might therefore be expected to lead to a greater reduction in M , leading to closer agreement with the measured saturation moment.

The loss of magnetization due to P content is also supported by our experimental data. Magnetization versus applied-field (M vs. H) hysteresis loops for the Ni nanoparticle sample at 2K are shown in **Fig. 3.6a**. The Ni nanoparticles show lower remnant magnetization (M_r) (6.4 emu/g) and saturation magnetization (M_s) (29.5 emu/g) than those observed in bigger Ni nanoparticles reported previously.^{55, 56} This decrease, although likely due in part to the size of domains in our Ni nanoparticles, which are smaller than the critical size for superparamagnetism,^{55, 57, 58} may also be a function of phosphorus content within the nanoparticle structure, as suggested by our theoretical calculations. Zero field cooling (ZFC) – field cooling (FC) measurements also display significant changes in magnetic properties (**Fig. 3.6b**). The blocking temperature (T_b) of the Ni nanoparticles is around 260 K, which is lower than that observed in the bulk structure.

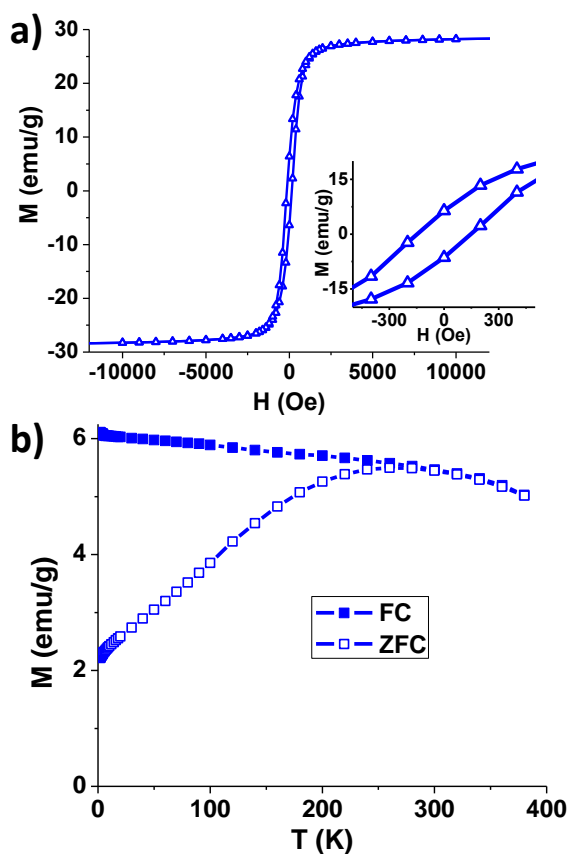


Figure 3.6 Magnetization data for Ni nanoparticles. (a) Magnetization vs. applied field hysteresis loops measured at 2 K. (b) FC and ZFC magnetization curves for Ni nanoparticles. The curves represent temperature dependence of the magnetization for samples under a magnetic field of 100 Oe after zero-field-cooling (open square) and field-cooling (filled square).

Two additional samples were synthesized to investigate the effects of phosphorus on the magnetic properties: (1) Ni nanoparticles synthesized without TOP and (2) Ni nanoparticles synthesized with half the amount of TOP (2.24 mmol) compared to the standard Ni nanoparticle synthesis TOP concentration (4.48 mmol).

Compared to the “standard” Ni synthesis, nanoparticles synthesized with less TOP are larger and irregular in morphology (size: 32.8 nm, std. dev: 14.4%) (**Fig. B.7**, left). Nanoparticles synthesized without TOP (**Fig. B.7**, right) exhibit an even greater polydispersity and a larger average size compared to the “standard” Ni nanoparticles (size: 32.3 nm, std. dev: 27.8%). The samples synthesized with less TOP and without TOP do not clearly show the T_b point within our measurement temperature range (2 K – 380 K) indicating that these samples exhibit more bulk-like (higher blocking temperature) magnetic behavior (**Fig. B.8**).⁵⁹ Additionally, field dependence of the magnetization results of the samples with lower TOP concentrations show a larger hysteresis loop with higher M_r (Ni without TOP: 15.9 emu/g, Ni with less TOP: 10.34 emu/g) and M_s (Ni without TOP: 34.5 emu/g, Ni with less TOP: 36.2 emu/g) than that of standard Ni nanoparticles. However it is not clear whether or not this effect is solely a result of phosphorus content, since ferromagnetic behavior is highly sensitive to size effects.⁶⁰⁻⁶² This change in magnetic behavior with increasing phosphorus content suggests that changes in the nanoparticle properties may result from the presence of excess phosphorus within the structure.

DFT calculations were carried out to investigate whether the P doping effects on magnetization may be applicable to other transition metal systems. **Fig. 3.5a** shows the calculated magnetization against substitutional P concentration for *hcp* Co (red squares) and *bcc* Fe (blue diamonds). As with Ni, the magnetization decreases for Co and Fe with increasing P doping, although there is a weaker sensitivity of the ferromagnetism in these TMs to P doping compared to Ni. This effect is consistent with the fact that the TM_3P phase exhibits ferromagnetism rather than paramagnetism

in Co_3P ⁶³ and Fe_3P .⁶⁴ In addition, the catalytic properties of the Ni nanoparticles may be severely affected by the unintended P doping. The density of states (DOS) near the Fermi surface affects how a molecule can bind to the material, as the molecular orbitals form bonding and antibonding states with the surface states. According to our DOS calculations, the majority states at 100 meV above the Fermi level are strongly affected by the P presence, which reduces the number of states. Comparing doped (6.25 at. % P) Ni to pure Ni, there is a 40% reduction in the number of states observed at 100 meV (**Fig. 3.7**). This is particularly significant because these nanoparticles are notable for their use in catalytic applications, and properties of catalytic materials are very sensitive to surface states, therefore the excess P content may detrimentally degrade the catalytic properties of these Ni nanoparticles.

Through a combination of characterization techniques, including EXAFS to probe short-range structural order and XRD to determine the long-range crystal structure, as well as DFT, TEM, SQUID, and XANES, we were able to elucidate the structure of Ni nanoparticles and derive conclusions concerning the relation of their synthetic conditions to the resulting structure-property relations. Using TOP to promote stabilization and coordination in Ni nanoparticle synthesis can also lead to undesired phosphorus doping. This phosphorus doping increases as a function of synthetic temperature and reaction time. This is likely relevant to other synthetic systems which employ TOP and similarly strong-binding phosphorus ligands, such as triphenyl phosphine. Even with phosphorus content as high as several percent, the crystalline *fcc* Ni lattice is not significantly disrupted. There is, however, a lattice expansion notable in the XRD pattern as a function of P at. %, which enables

calculation of the P content of the nanoparticles based on XRD peak position alone, a useful technique in fine-tuning the synthesis. We find that the structure consists of a crystalline *fcc* lattice, with P substitutional atoms and distortion only of the Ni atoms surrounding the P substitutional sites. This unintentional P doping significantly impacts the nanoparticle structural behavior, magnetic properties, and catalytic activities, which we have demonstrated through both the experimental and modeled phenomena.

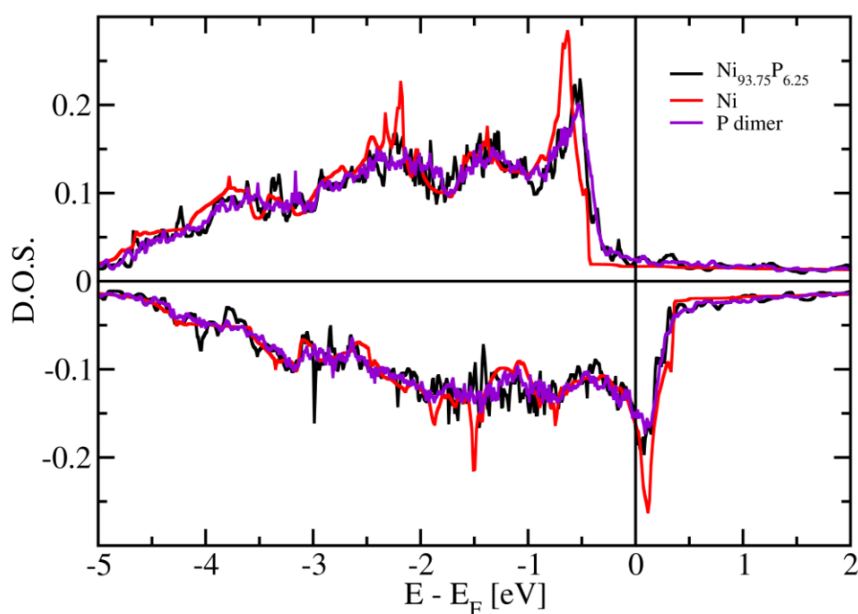


Figure 3.7 Bulk Ni density of states (DOS) near the Fermi surface. The majority states around 100 meV above the Fermi level are strongly affected by the P content. Substitutional P (6.25%) is shown for evenly distributed P (black) and for P dimers (purple). The P presence reduces the number of states in both cases.

3.5 Conclusion

The results of this study suggest that it should be taken into consideration in optimizing nanoparticles for use in applications, that there may be a significant concentration of XRD amorphous species present in the nanoparticles, which may interfere with desired properties. Thus care should be taken when using strong binding surfactant ligands such as TOP in the synthesis of nanoparticles, particularly when they are used in high concentrations.

3.6 References

1. Murray, C. B.; Norris, D. J.; Bawendi, M. G. *J. Am. Chem. Soc.* **1993**, *115*, 8706-8715.
2. Yin, Y.; Alivisatos, A. P. *Nature* **2005**, *437*, 664-670.
3. Murray, C. B.; Kagan, C. R.; Bawendi, M. G. *Annu. Rev. Mater. Sci.* **2000**, *30*, 545-610.
4. Peng, X.; Manna, U.; Yang, W.; Wickham, J.; Scher, E.; Kadavanich, A.; Alivisatos, A. P. *Nature* **2000**, *404*, 59-61.
5. Bealing, C. R.; Baumgardner, W. J.; Choi, J. J.; Hanrath, T.; Hennig, R. G. *ACS Nano* **2012**, *6*, 2118-2127.
6. Liu, H.; Owen, J. S.; Alivisatos, A. P. *J. Am. Chem. Soc.* **2007**, *129*, 305-312.
7. Wang, F.; Tang, R.; Buhro, W. E. *Nano Lett.* **2008**, *8*, 3521-3524.
8. Evans, C. M.; Evans, M. E.; Krauss, T. D. *J. Am. Chem. Soc.* **2010**, *132*, 10973-10975.
9. Owen, J. S.; Park, J.; Trudeau, P.-E.; Alivisatos, A. P. *J. Am. Chem. Soc.* **2008**, *130*, 12279-12281.
10. Zhang, H.; Ha, D.-H.; Hovden, R.; Kourkoutis, L. F.; Robinson, R. D. *Nano Lett.* **2011**, *11*, 188-197.
11. Hanada, N.; Ichikawa, T.; Fujii, H. *J. Phys. Chem. B* **2005**, *109*, 7188-7194.
12. Wu, S.-H.; Chen, D.-H. *J. Colloid Interface Sci.* **2003**, *259*, 282-286.

13. Ozay, O.; Aktas, N.; Inger, E.; Sahiner, N. *Int. J. Hydrogen Energ.* **2011**, *36*, 1998-2006.
14. Mahata, N.; Cunha, A. F.; Orfao, J. J. M.; Figueiredo, J. L. *Appl. Catal.* **2008**, *351*, 204-209.
15. Lin, K. Y.; Tsai, W. T.; Chang, J. K. *Int. J. Hydrogen Energ.* **2010**, *35*, 7555-7562.
16. Lin, K. Y.; Tsai, W. T.; Yang, T. J. *J. Power Sources* **2011**, *196*, 3389-3394.
17. Yang, C. C.; Li, Y. J.; Chen, W. H. *Int. J. Hydrogen Energ.* **2010**, *35*, 2336-2343.
18. Kim, C.; Noh, M.; Choi, M.; Cho, J.; Park, B. *Chem. Mater.* **2005**, *17*, 3297-3301.
19. Park, J.; Kang, E.; Son, S. U.; Park, H. M.; Lee, M. K.; Kim, J.; Kim, K. W.; Noh, H.-J.; Park, J.-H.; Bae, C. J.; Park, J.-G.; Hyeon, T. *Adv. Mater.* **2005**, *17*, 429-434.
20. Park, J.; Joo, J.; Kwon, S. G.; Jang, Y.; Hyeon, T. *Angew. Chem., Int. Ed.* **2007**, *46*, 4630-4660.
21. Muthuswamy, E.; Savithra, G. H. L.; Brock, S. L. *ACS Nano* **2011**, *5*, 2402-2411.
22. Henkes, A. E.; Vasquez, Y.; Schaak, R. E. *J. Am. Chem. Soc.* **2007**, *129*, 1896-1897.

23. Wang, J.; Johnston-Peck, A. C.; Tracy, J. B. *Chem. Mater.* **2009**, *21*, 4462-4467.
24. Chiang, R.-K.; Chiang, R.-T. *Inorg. Chem.* **2007**, *46*, 369-371.
25. Gao, J.; Guan, F.; Zhao, Y.; Yang, W.; Ma, Y.; Lu, X.; Hou, J.; Kang, J. *Mater. Chem. Phys.* **2001**, *71*, 215-219.
26. Peng, T. C.; Xiao, X. H.; Wu, W.; Fan, L. X.; Zhou, X. D.; Ren, F.; Jiang, C. *Z. J. Mater. Sci.* **2012**, *47*, 508-513.
27. Carencio, S.; Boissiere, C.; Nicole, L.; Sanchez, C.; Le, F. P.; Mezailles, N. *Chem. Mater.* **2010**, *22*, 1340-1349.
28. Aruguete, D. M.; Marcus, M. A.; Li, L. S.; Williamson, A.; Fakra, S.; Gygi, F.; Galli, G. A.; Alivisatos, A. P. *J. Phys. Chem. C* **2007**, *111*, 75-79.
29. Marcus, M. A.; Flood, W.; Stiegerwald, M.; Brus, L.; Bawendi, M. *J. Phys. Chem.* **1991**, *95*, 1572-1576.
30. Cheng, G.; Carter, J. D.; Guo, T. *Chem. Phys. Lett.* **2004**, *400*, 122-127.
31. Park, J.-I.; Kim, M. G.; Jun, Y.-W.; Lee, J. S.; Lee, W.-R.; Cheon, J. *J. Am. Chem. Soc.* **2004**, *126*, 9072-9078.
32. Sarma, L. S.; Chen, C.-H.; Kumar, S. M. S.; Wang, G.-R.; Yen, S.-C.; Liu, D.-G.; Sheu, H.-S.; Yu, K.-L.; Tang, M.-T.; Lee, J.-F.; Bock, C.; Chen, K.-H.; Hwang, B.-J. *Langmuir* **2007**, *23*, 5802-5809.
33. Rodriguez, J. A.; Hanson, J. C.; Kim, J.-Y.; Liu, G.; Iglesias-Juez, A.; Fernandez-Garcia, M. *J. Phys. Chem. B* **2003**, *107*, 3535-3543.

34. Rockenberger, J.; Troeger, L.; Kornowski, A.; Vossmeier, T.; Eychmueller, A.; Feldhaus, J.; Weller, H. *J. Phys. Chem. B* **1997**, *101*, 2691-2701.
35. Frenkel, A. I.; Hills, C. W.; Nuzzo, R. G. *J. Phys. Chem. B* **2001**, *105*, 12689-12703.
36. Bunker, G., *Introduction to XAFS: a practical guide to X-ray absorption fine structure spectroscopy*. Cambridge University Press: Cambridge, 2010; p 260.
37. Stern, E. A. *Phys. Rev. B* **1974**, *10*, 3027-3037.
38. Stern, E. A. *Contemp. Phys.* **1978**, *19*, 289-310.
39. Mantina, M.; Wang, Y.; Chen, L. Q.; Liu, Z. K.; Wolverton, C. *Acta Mater.* **2009**, *57*, 4102-4108.
40. Chan, T. L.; Tiago, M. L.; Kaxiras, E.; Chelikowsky, J. R. *Nano Lett.* **2007**, *8*, 596-600.
41. Song, J.; Wei, Z.; Pan, Z.; Xie, Z.; Wei, S. *AIP Conf. Proc.* **2007**, *882*, 453-456.
42. Blanchard, P. E. R.; Grosvenor, A. P.; Cavell, R. G.; Mar, A. *J. Mater. Chem.* **2009**, *19*, 6015-6022.
43. Anspoks, A.; Kuzmin, A. *J. Non-Cryst. Solids* **2011**, *357*, 2604-2610.
44. Arcon, I.; Tuel, A.; Kodre, A.; Martin, G.; Barbier, A. *J. Synchrotron Radiat.* **2001**, *8*, 575-577.
45. Calvin, S.; Miller, M. M.; Goswami, R.; Cheng, S. F.; Mulvaney, S. P.; Whitman, L. J.; Harris, V. G. *J. Appl. Phys.* **2003**, *94*, 778-783.

46. Gurman, S. J. *J. Synchrotron Radiat.* **1995**, *2*, 56-63.
47. Nietubyc, R.; Czerwosz, E.; Diduszko, R.; Dluzewski, P.; Kozlowski, M.; Welter, E. *J. Alloys Compd.* **2009**, *484*, 896-901.
48. Ha, D.-H.; Moreau, L. M.; Bealing, C. R.; Zhang, H.; Hennig, R. G.; Robinson, R. D. *J. Mater. Chem.* **2011**, *21*, 11498-11510.
49. Häglund, J.; Fernández Guillermet, A.; Grimvall, G.; Körling, M. *Phys. Rev. B* **1993**, *48*, 11685.
50. Moreels, I.; Justo, Y.; De, G. B.; Haustraete, K.; Martins, J. C.; Hens, Z. *ACS Nano* **2011**, *5*, 2004-2012.
51. Katari, J. E. B.; Colvin, V. L.; Alivisatos, A. P. *J. Phys. Chem.* **1994**, *98*, 4109-4117.
52. Bader, R. *Atoms in Molecules: A Quantum Theory* **1994**.
53. Oryshchyn, S.; Babizhetskyy, V.; Chykhriy, S.; Aksel'rud, L.; Stoyko, S.; Bauer, J.; Guerin, R.; Kuz'ma, Y. *Inorg. Mater.* **2004**, *40*, 380-385.
54. König, E. K., G., Ni(0), Ni(I). In *SpringerMaterials- The Landolt-Bornstein Database*, Hellwege, K.-H. Hellwege, A. M.
55. Gong, W.; Li, H.; Zhao, Z.; Chen, J. *J. Appl. Phys.* **1991**, *69*, 5119-5121.
56. Zhang, H. T.; Wu, G.; Chen, X. H.; Qiu, X. G. *Mater. Res. Bull.* **2006**, *41*, 495-501.
57. Leslie-Pelecky, D. L.; Rieke, R. D. *Chem. Mater.* **1996**, *8*, 1770-1783.

58. Du, Y.; Xu, M.; Wu, J.; Shi, Y.; Lu, H.; Xue, R. *J. Appl. Phys.* **1991**, *70*, 5903-5905.
59. Jun, Y.-w.; Seo, J.-w.; Cheon, J. *Acc. Chem. Res.* **2008**, *41*, 179-189.
60. Johnson, D.; Perera, P.; O'Shea, M. J. *J. Appl. Phys.* **1996**, *79*, 5299-5301.
61. Roy, S.; Dubenko, I.; Ederh, D. D.; Ali, N. *J. Appl. Phys.* **2004**, *96*, 1202-1208.
62. Blanco-Mantecon, M.; O'Grady, K. *J. Magn. Magn. Mater.* **2006**, *296*, 124-133.
63. Konig, E. K., G., Co(0), Co(I). In *SpringerMaterials- The Landolt-Bornstein Database*, Hellwege, K.-H., Hellwege, A. M.
64. Konig, E., Part 2. In *SpringerMaterials- The Landolt-Bornstein Database*, Hellwege, K.-H. Hellwege, A. M.

APPENDIX B

B SUPPLEMENTARY INFORMATION FOR CHAPTER 3

Experimental Section

General Synthesis Procedures.

Synthesis of the Ni nanoparticle samples was based on thermal decomposition of a Ni-TOP complex as outlined by Muthuswamy et. al.¹ The synthesis was a one-pot strategy using standard Schlenk line and glove box techniques in a dry, oxygen-free di-nitrogen atmosphere. Ethanol ($\geq 99.5\%$), oleylamine (70%), nickel acetylacetonate ($\text{Ni}(\text{acac})_2$, 95%) and dioctyl ether (99%) were purchased from Aldrich. Tri-*n*-octylphosphine (TOP, 97%) was purchased from STREM Chemicals. Briefly, 1.17g (4 mmol) of $\text{Ni}(\text{acac})_2$ and 4.48 mmol of TOP were mixed into a flask containing 10 mL of octyl ether and 4 mL oleylamine. The solution was heated to 230 °C and the particles were allowed to grow for 1 hour. After the reaction had completed, the flask was removed from the heating mantle and the nanoparticle products were isolated by centrifugation with excess ethanol. The centrifugation process was repeated to ensure removal of excess reactant molecules.

Our synthesis recipe for Ni nanoparticles falls within the range of conditions reported by other groups for pure-phase Ni.¹⁻⁴ The literature methods for the synthesis of Ni nanoparticles use TOP/ $\text{Ni}(\text{acac})_2$ ratios from 0.8 to 3, temperatures ranging from 200 °C to 240 °C, and oleylamine ratios from 3-10.¹⁻⁴ Thus, our results, in which we find surprisingly high P concentrations in the Ni nanoparticles, should be applicable to these previous works.

Transmission Electron Microscopy

TEM images of the nanoparticle samples were obtained using a FEI Tecnai F12 microscope operating at 120 keV. At least 200 particles were analyzed per sample to obtain a representative size distribution. High-resolution TEM (HRTEM) was done using a FEI Tecnai F20 microscope operating at 200 keV. HRTEM samples are cleaned by oxygen plasma cleaning before imaging in order to obtain a clearer image. It is possible that this process may oxidize the surface of nanoparticles slightly. The magnetic properties of the samples are analyzed by utilizing superconducting quantum interference device (SQUID, Quantum Design MPMS-XL).

X-ray Diffraction

XRD (X-ray diffraction) spectra were collected using a Scintag theta-theta x-ray diffractometer (Cu K α radiation). Average grain sizes with the nanoparticle samples were determined from the XRD spectra using the Scherrer equation.

Inductively Coupled Plasma

ICP-OES (Inductively coupled plasma optical emission spectroscopy) results were obtained from Columbia Analytical Services. Samples from several Ni syntheses were first characterized with TEM and XRD, and then shipped for ICP analysis. Eight samples in total were tested. One sample was repeat-tested to ensure accurate results. The Ni data was collected using a wavelength of 231.604 nm and P

using a wavelength of 214.914 nm. The RSD % (relative standard deviation) associated with the data collection was 5.7 %.

Ligand Exchange

Ligand exchange was performed on the as-synthesized Ni nanoparticles to study the potential effects of TOP surface ligands on elemental analysis. Synthesized Ni nanoparticles were re-dispersed in 7 mL of oleic acid in a 25 mL flask. The solution was kept at 100 °C under the di-nitrogen atmosphere. After heating for 2.5 hours, the solution was cooled down by removing the heating mantle and Ni nanoparticles were purified by adding excess ethanol and centrifugation. The supernatant was decanted and the nanoparticles were re-dispersed in hexanes. This precipitation/re-dispersion process was performed twice overall to ensure removal of excess organic species.

X-ray Absorption Spectroscopy

XAS spectra of the Ni nanoparticle samples were obtained at the C1 station of the Cornell High Energy Synchrotron Source (CHESS) using a Si(220) monochromator and fluorescence detection to probe the nickel K-edge (8333 eV). Data was obtained over the energy range from 8280 eV to 8780 eV, in order to include both the XANES and EXAFS regions. A cobalt filter was used in order to control signal level. To prevent precipitation and obtain a homogeneously-thick sample such that XAS spectra with a constant intensity signal could be achieved, the Ni samples

were drop-casted between two pieces of Kapton tape. Five to six scans were obtained per sample using 15 minute scans over three regions with varying step size (pre-edge region 5.0 eV, edge region 1.0 eV, and EXAFS region 3.0 eV). Self-absorption was not a concern with the fluorescence detection because the samples were sufficiently dilute in solution. The fluorescence measurements are proportional to the absorption coefficient, $\mu(E)$, which produces a spectrum describing the strength of X-ray absorption as a function of energy.⁵ The scans were then averaged together to enhance the smoothness and ensure data consistency. Transmission detection was simultaneously used to probe the K-edge of a Ni metal foil during each of the scans, to function as a standard for comparison and edge calibration.

The raw spectra were averaged and processed using ATHENA,⁶ part of the IFEFFIT software package. Data processing involved edge determination from the first inflection point in the absorption data, background subtraction using the AUTOBK algorithm, and normalization of the EXAFS modulations (greater than 50 eV above the edge).⁷ The spectra were converted from energy-space to k-space, then underwent a phase shift specific to the absorbing and scattering elements.⁵ A k-weight of 1 was chosen in order to best observe the scattering of phosphorus, a low-Z scattering element.⁸ Nickel is also a lower-scattering element,⁸ and when a k-weight of 1 was used the intensity modulations were evenly distributed through the k-space region of interest (0–10 \AA^{-1}), indicating an appropriate weighting was applied.⁸ The spectra was then Fourier Transformed into R-space.⁵ In R-space each peak appears at the relative spacing of that particular shell from the scattering atom, which enables visualization of the relative contributions as a function of inter-atomic distance.⁷ The

data was then analyzed by the ab-initio method and multiple data set fitting in k-space and R-space using ARTEMIS.⁶ Crystal structures from theory were inputted using ATOMS.⁹ By fitting well-matched theoretical pathways to the experimental spectra through loosening variables to deviate from the theoretical bulk structures, specific structural information could be determined including coordination number, inter-atomic spacing and mean-squared disorder, as outlined in the EXAFS equation.^{7, 10, 11, 12}

$$\chi(k) = \sum_{\Gamma} \left[\frac{N_{\Gamma} S_0^2 F_{\Gamma}(k)}{2kR_{\Gamma}^2} e^{-2k^2\sigma_{\Gamma}^2} e^{-2R_{\Gamma}/\lambda(k)} \times \sin(2kR_{\Gamma} + \phi_{\Gamma}(k)) \right] \quad (1)$$

Γ is the summation over the individual scattering pathways, k is the photoelectron wavevector, $F_{\Gamma}(k)$ is the scattering amplitude, $\lambda(k)$ is the mean free path of inelastically-scattered photoelectrons and $\Phi(k)$ is the phase shift, which is calculated as a function of the absorbing and scattering atom. S_0^2 , the amplitude reduction factor, was set to 0.754 during fitting (the value extracted from fitting the Ni foil). This enables a more accurate determination of the coordination number.¹¹ Degeneracy (N_{Γ}), half-path length (R_{Γ}), energy shift parameter (E_0), and mean-squared disorder (σ_{Γ}^2), which includes contributions from structural and thermal disorder (Debye-Waller factor),⁷ were allowed to float during the fit in order to extract the values specific to each nanoparticle sample. ΔE_0 was fixed to a single variable for all pathways with the same absorbing and scattering element in order to limit the number of variables, as ΔE_0 values should be nearly equal for similar bonds within the structure.¹³

The EXAFS spectra were fit with a theoretical model in R-space and k-space in order to extract accurate parameters for the average radial structure around a central core Ni atom. Each fitting model resulted in an “R-factor” value between 0.005 and 0.012 in R-space and between 0.019 and 0.038 in k-space. The R-factor value is a statistical measurement which is minimized in order to ensure quality of the fit, where a value less than 0.05 is commonly referred as a good fit. The minimization of this statistical factor proves that our best-fit models are well-correlated to the experimental data.

Density Functional Theory

All DFT calculations were carried out using the VASP package.¹⁴⁻¹⁷ Plane wave basis sets were employed, with the projector-augmented wave (PAW) method.^{18,}
¹⁹ The gradient-corrected PBE exchange-correlation functional²⁰ was used for all calculations. Brillouin zone integration was carried out using the smearing method of Methfessel and Paxton²¹ (first-order), with a smearing width of 0.10, except for the reference calculations for P_{black} , where the tetrahedron method with Blöchl corrections was used.²² Special k-point meshes were chosen according to the method of Monkhorst and Pack,²³ and the density of k-points was taken to be ≥ 45 points per inverse Å, along each of the reciprocal lattice vectors. Increasing the k-point density to be > 60 points per inverse Å did not appreciably change the calculated total energies. The kinetic energy cutoff for the wave functions was set to 350.0 eV, and the cutoff for the augmentation functions to 707.9 eV.

Although the use of PBCs (periodic boundary conditions) does not account for nanoscale effects, they are consistent with the results obtained experimentally for the nano-sized system, and can be used as a supplement means to confirm and expand our experimental results. The large size of the nanoparticles employed in this study (~20 nm) suggests that we should expect this approach to be reasonable for much of their interior. Additionally, an ab initio study using P-doped model nanoparticles of a similar size would be prohibitively expensive.

With regard to charge transfer calculations, the calculated charge transfer of $<0.25 e$ is small in comparison to the Bader charge investigated for ionic systems such as KF and MgO, (0.9 e and 1.6 e, close to the nominal values of 1 e and 2 e). This is also consistent with the difference in electronegativity for NiP (0.28), which is roughly an order of magnitude smaller than that for KF (3.16) and MgO (2.13).

Estimating ionic charges in solids or molecules is an ill-defined problem due to the fact that electrons are indistinguishable particles and that the electron density is usually positive definite everywhere inside the solid or molecule. The Bader charge analysis empirically often slightly underestimates charge transfers in most systems in comparison with the nominal charges expected from chemical considerations.

Magnetic measurements

The magnetic properties of the nanoparticle samples were analyzed using a superconducting quantum interference device (SQUID, Quantum Design MPMS – XL).

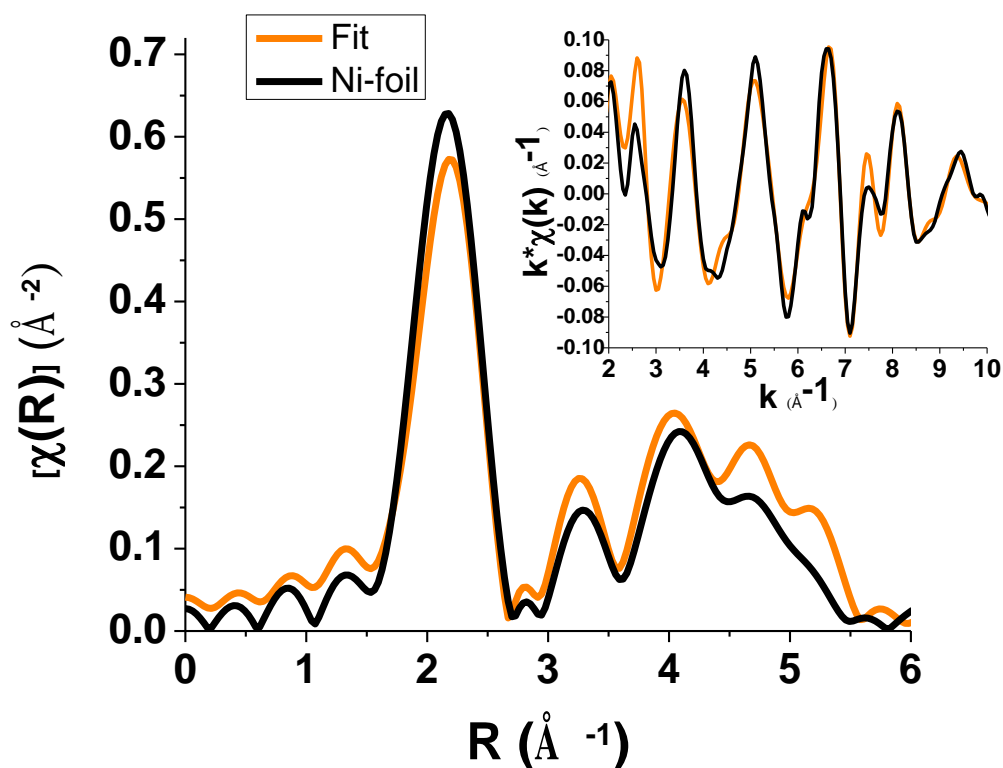


Figure B.1 EXAFS fit to Ni foil. The fitting model using a single set of Ni *fcc* variables resulted in a well matched fit (orange) to the data (black).

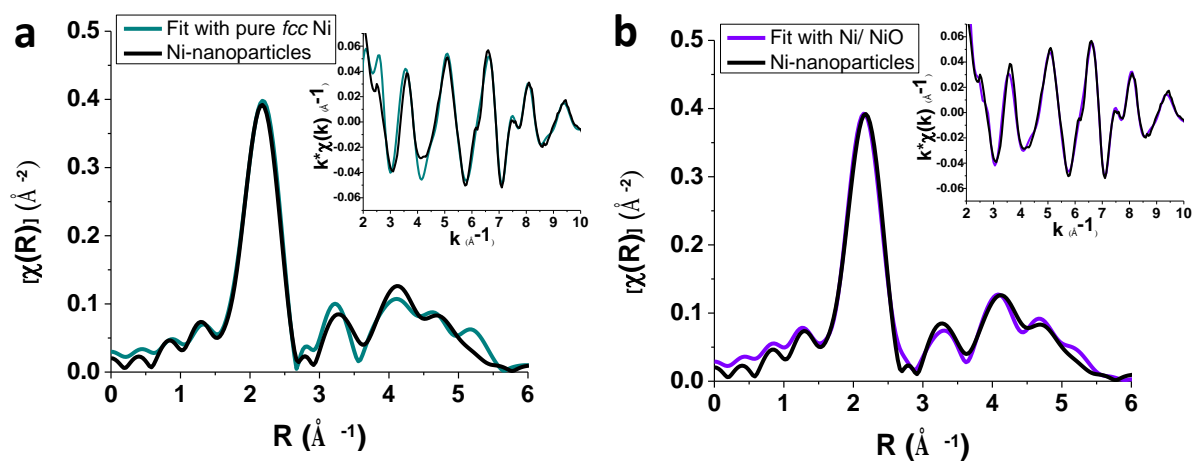


Figure B.2 EXAFS fitting models from *fcc* Ni and NiO. (a) The fitting model using purely Ni *fcc* pathways (cyan) was well-matched to the experimental spectra (black) in both R -space and k -space (inset), yet resulted in unreasonably low degeneracy values. (b) The fitting model using a combination of Ni *fcc* and NiO pathways (violet) matches the experimental spectra (black), yet the fitting parameters were again unreasonable, making neither of these fitting models a viable option to describe the nanoparticle structure.

Fit using only Ni *fcc* pathways

Table B.1 Pathway parameters for fit using only Ni *fcc* pathways. The Ni *fcc* pathway parameters used to construct the best-fit EXAFS model for the Ni nanoparticle sample are listed. The numbers in the multiple scattering pathways represent the coordination shell number involved in the multiple scattering. Note the unreasonably low degeneracy values associated with the fitting model (N(exp.) vs. N(acc.)). These parameters correspond with the fitting results shown in **Fig. B.2a**.

Single Scattering Pathways from Ni							
Pathway	N (acc.)	N (exp.)	R (Å)	ΔR (Å)	R + ΔR (Å)	E ₀ (eV)	σ^2 (Å ²) x 10 ⁻³
Ni – Ni (shell 1)	12	8.82	2.49	-0.003	2.49	6.33	7.77
Ni- Ni (shell 2)	6	4.08	3.52	-0.004	3.52	6.33	9.95
Ni-Ni (shell 3)	24	16.6	4.32	-0.002	4.31	6.33	14.1
Ni – Ni (shell 4)	12	8.30	4.98	-0.002	4.98	6.33	14.1
Ni – Ni (shell 5)	24	16.6	5.57	-0.002	5.57	6.33	14.1
Multiple Scattering Pathways from Ni							
Pathway	N (acc.)	N (exp.)	R (Å)	ΔR (Å)	R + ΔR (Å)	E ₀ (eV)	σ^2 (Å ²) x 10 ⁻³
Ni_1 Ni_1	48	32.3	3.74	-0.006	3.73	6.33	11.0
Ni_2 Ni_1	48	32.3	4.25	-0.006	4.25	6.33	11.0
Ni_1 Ni_1	48	32.3	4.65	-0.006	4.64	6.33	11.0
Ni_3 Ni_1	96	64.7	4.65	-0.006	4.64	6.33	11.0
Ni_1 Ni_1	12	8.09	4.98	-0.006	4.98	6.33	11.0
Ni_1 [+] Ni_1	12	8.09	4.98	-0.006	4.98	6.33	11.0
Ni_4 Ni_1	24	16.2	4.98	-0.006	4.98	6.33	11.0
Ni_1 [+] Ni_1	12	8.09	4.98	-0.006	4.98	6.33	11.0
Ni_1 Ni_4 Ni_1	12	8.09	4.98	-0.006	4.98	6.33	11.0
Ni_1 Ni_1 Ni_1	48	32.3	4.98	-0.006	4.98	6.33	11.0
Ni_1 Ni_3 Ni_1	48	32.3	4.98	-0.006	4.98	6.33	11.0
Ni_1 [+] Ni_1	48	32.3	4.98	-0.006	4.98	6.33	11.0
Ni_3 Ni_1	48	32.3	5.17	-0.006	5.16	6.33	11.0
Ni_3 Ni_2	48	32.3	5.17	-0.006	5.16	6.33	11.0
Ni_3 Ni_1	96	64.7	5.56	-0.006	5.56	6.33	11.0
Ni_3 Ni_2	48	32.3	5.56	-0.006	5.56	6.33	11.0

Fit using Ni *fcc* + NiO pathways

Table B.2 Pathway parameters for fit using Ni *fcc* + NiO pathways. The Ni *fcc* and NiO pathway parameters used to construct the best-fit EXAFS model for the Ni nanoparticle sample are listed. The numbers in the multiple scattering pathways represent the coordination shell number involved in the multiple scattering. Note the unreasonably high degeneracy values for the higher versus lower NiO shells. These parameters correspond with the fitting results shown in **Fig. B.2b**.

Single Scattering Pathways from Ni <i>fcc</i>							
Pathway	N (acc.)	N (exp.)	R (Å)	ΔR (Å)	R + ΔR (Å)	E ₀ (eV)	σ^2 (Å ²) x 10 ⁻³
Ni - Ni (shell 1)	12	9.30	2.49	-0.012	2.48	3.77	8.49
Ni - Ni (shell 2)	6	3.93	3.52	-0.036	3.49	3.77	8.52
Ni - Ni (shell 3)	24	13.3	4.32	-0.007	4.31	3.77	9.86
Ni - Ni (shell 4)	12	6.67	4.98	-0.007	4.98	3.77	9.86
Ni - Ni (shell 5)	24	13.3	5.57	-0.007	5.57	3.77	9.86
Multiple Scattering Pathways from Ni <i>fcc</i>							
Pathway	N (acc.)	N (exp.)	R (Å)	ΔR (Å)	R + ΔR (Å)	E ₀ (eV)	σ^2 (Å ²) x 10 ⁻³
Ni ₁ Ni ₁	48	26.4	3.74	-0.016	3.72	3.77	10.6
Ni ₂ Ni ₁	48	26.4	4.25	-0.016	4.24	3.77	10.6
Ni ₁ Ni ₁	48	26.4	4.65	-0.016	4.63	3.77	10.6
Ni ₃ Ni ₁	96	52.8	4.65	-0.016	4.63	3.77	10.6
Ni ₁ Ni ₁	12	6.60	4.98	-0.016	4.97	3.77	10.6
Ni ₁ [+] Ni ₁	12	6.60	4.98	-0.016	4.97	3.77	10.6
Ni ₄ Ni ₁	24	13.2	4.98	-0.016	4.97	3.77	10.6
Ni ₁ [+] Ni ₁	12	6.60	4.98	-0.016	4.97	3.77	10.6
Ni ₁ Ni ₄ Ni ₁	12	6.60	4.98	-0.016	4.97	3.77	10.6
Ni ₁ Ni ₁ Ni ₁	48	26.4	4.98	-0.016	4.97	3.77	10.6
Ni ₁ Ni ₃ Ni ₁	48	26.4	4.98	-0.016	4.97	3.77	10.6
Ni ₁ [+] Ni ₁	48	26.4	4.98	-0.016	4.97	3.77	10.6
Ni ₃ Ni ₁	48	26.4	5.17	-0.016	5.15	3.77	10.6
Ni ₃ Ni ₂	48	26.4	5.17	-0.016	5.15	3.77	10.6
Ni ₃ Ni ₁	96	52.8	5.56	-0.016	5.55	3.77	10.6
Ni ₃ Ni ₂	48	26.4	5.56	-0.016	5.55	3.77	10.6
Single Scattering Pathways from NiO							
Pathway	N (acc.)	N (exp.)	R (Å)	ΔR (Å)	R + ΔR (Å)	E ₀ (eV)	σ^2 (Å ²) x 10 ⁻³
Ni - O (shell 1)	6	0.97	2.08	-0.009	2.08	7.11	17.0
Ni - Ni (shell 1)	12	1.48	2.95	-0.103	2.84	3.77	7.23
Ni - O (shell 2)	8	2.17	3.61	0.020	3.63	7.11	10.2

Ni – Ni (shell 2)	6	1.56	4.17	-0.015	4.15	3.77	10.8
Ni – O (shell 3)	24	6.51	4.66	0.020	4.68	7.11	10.2
Ni – Ni (shell 3)	24	6.23	5.11	-0.015	5.09	3.77	10.8

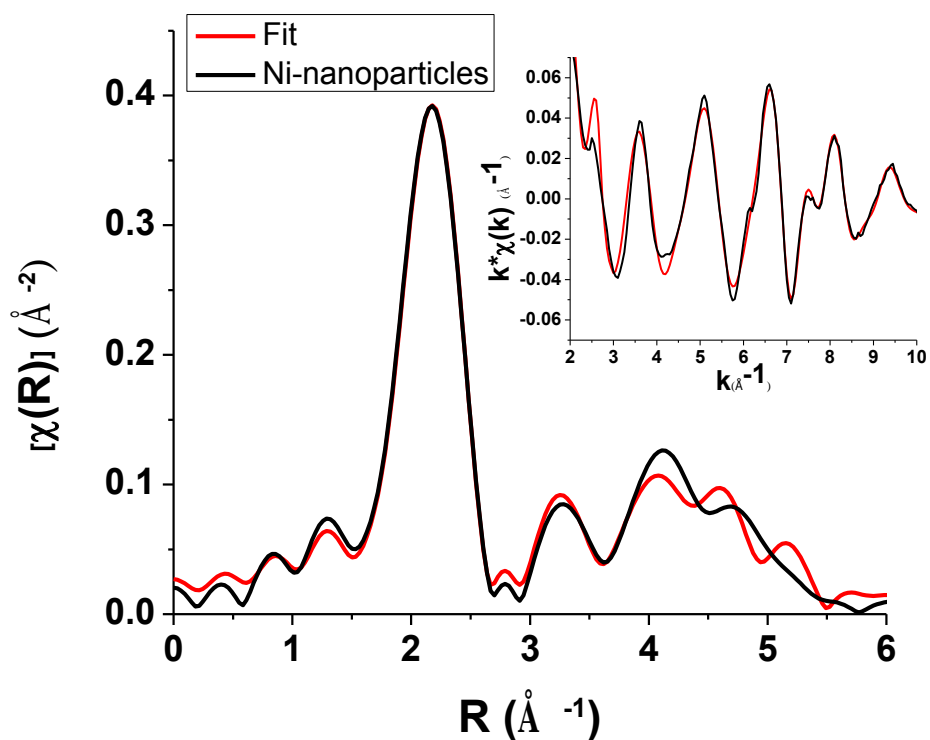


Figure B.3 EXAFS fitting model using Ni *fcc* / Ni₂P pathways. The fitting model using a combination of Ni *fcc* and Ni₂P pathways (red) was well-matched to the experimental spectra (black) in both R-space and k-space (inset). Yet the great distortion in the Ni₂P pathway parameters indicates that the phosphide contributions are not crystalline Ni₂P.

Fit using Ni *fcc* + Ni₂P pathways

Table B.3 Pathway parameters for fit using Ni *fcc* + Ni₂P pathways. The Ni *fcc* and Ni₂P pathway parameters used to construct the best-fit EXAFS model for the Ni nanoparticle sample are listed. The numbers in the multiple scattering pathways represent the coordination shell number involved in the multiple scattering. Notice the well-ordered (low ΔR values) associated with the Ni *fcc* pathways in comparison to the disordered Ni₂P pathways. This is likely why Ni *fcc* was the only phase detectable by XRD. These parameters correspond with the fitting results shown in **Fig.**

B.3.

Single Scattering Pathways from Ni <i>fcc</i>							
Pathway	N (acc.)	N (exp.)	R (Å)	ΔR (Å)	R + ΔR (Å)	E₀ (eV)	σ^2 (Å²) x 10⁻³
Ni – Ni (shell 1)	12	8.26	2.49	0.002	2.49	6.94	6.70
Ni- Ni (shell 2)	6	3.98	3.52	-0.000	3.52	6.94	13.3
Ni-Ni (shell 3)	24	15.9	4.32	-0.000	4.32	6.94	13.3
Ni – Ni (shell 4)	12	7.96	4.98	-0.000	4.98	6.94	13.3
Ni – Ni (shell 5)	24	15.9	5.57	-0.000	5.57	6.94	13.3
Multiple Scattering Pathways from Ni <i>fcc</i>							
Pathway	N (acc.)	N (exp.)	R (Å)	ΔR (Å)	R + ΔR (Å)	E₀ (eV)	σ^2 (Å²) x 10⁻³
Ni_1 Ni_1	48	31.6	3.74	0.001	3.74	6.94	11.5
Ni_2 Ni_1	48	31.6	4.25	0.001	4.26	6.94	11.5
Ni_1 Ni_1	48	31.6	4.65	0.001	4.65	6.94	11.5
Ni_3 Ni_1	96	63.2	4.65	0.001	4.65	6.94	11.5
Ni_1 Ni_1	12	7.91	4.98	0.001	4.99	6.94	11.5
Ni_1 [+] Ni_1	12	7.91	4.98	0.001	4.99	6.94	11.5
Ni_4 Ni_1	24	15.8	4.98	0.001	4.99	6.94	11.5
Ni_1 [+] Ni_1	12	7.91	4.98	0.001	4.99	6.94	11.5
Ni_1 Ni_4 Ni_1	12	7.91	4.98	0.001	4.99	6.94	11.5
Ni_1 Ni_1 Ni_1	48	31.6	4.98	0.001	4.99	6.94	11.5
Ni_1 Ni_3 Ni_1	48	31.6	4.98	0.001	4.99	6.94	11.5
Ni_1 [+] Ni_1	48	31.6	4.98	0.001	4.99	6.94	11.5
Ni_3 Ni_1	48	31.6	5.17	0.001	5.17	6.94	11.5
Ni_3 Ni_2	48	31.6	5.17	0.001	5.17	6.94	11.5
Ni_3 Ni_1	96	63.2	5.56	0.001	5.17	6.94	11.5
Ni_3 Ni_2	48	31.6	5.56	0.001	5.17	6.94	11.5
Single Scattering Pathways from Ni₂P crystal structure							

Pathway	N (acc.)	N (exp.)	R (Å)	ΔR (Å)	R + ΔR (Å)	E ₀ (eV)	σ^2 (Å ²) x 10 ⁻³
Ni ₁ – Ni	5	3.54	2.79	0.226	3.02	6.94	14.7
Ni ₂ – Ni	6	2.71	2.92	0.063	2.98	6.94	6.91
Ni ₁ - P	2	0.63	2.24	-0.050	2.19	-9.66	3.65
Ni ₂ – P	2.5	0.60	2.44	0.016	2.46	-9.66	6.18
Ni ₁ – Ni (shell 2)	2	1.04	3.83	-0.334	3.49	6.94	7.94
Ni ₁ – Ni (shell 3)	5	2.61	4.29	-0.334	3.96	6.94	7.94
Ni ₁ – Ni (shell 4)	2	1.04	4.75	-0.361	4.39	6.94	7.94
Ni ₁ – Ni (shell 5)	4	2.09	5.11	-0.361	4.75	6.94	7.94
Ni ₁ - Ni (shell 6)	5	2.61	5.46	-0.361	5.09	6.94	7.94
Ni ₂ – Ni (shell 2)	1	0.64	4.10	-0.352	3.75	6.94	8.24
Ni ₂ – Ni (shell 3)	3	1.92	4.30	-0.352	3.95	6.94	8.24
Ni ₂ – Ni (shell 4)	6	3.84	4.64	0.329	4.97	6.94	8.24
Ni ₂ – Ni (shell 5)	2	1.28	5.32	0.329	5.65	6.94	8.24
Ni ₂ – Ni (shell 6)	4	2.56	5.45	0.329	5.78	6.94	8.24
Ni ₁ – P (shell 2)	1	0.23	3.70	-0.392	3.31	-9.66	4.64
Ni ₁ – P (shell 3)	2	0.46	4.04	-0.392	3.65	-9.66	4.64
Ni ₁ – P (shell 4)	2	0.46	4.71	-0.316	4.39	-9.66	4.64
Ni ₁ – P (shell 5)	2	0.46	5.02	-0.316	4.70	-9.66	4.64
Ni ₁ – P (shell 6)	1	0.23	5.29	-0.316	4.98	-9.66	4.64
Ni ₁ – P (shell 7)	2	0.46	5.52	-0.316	5.21	-9.66	4.64
Ni ₂ – P (shell 2)	0.5	0.16	3.49	0.137	3.63	-9.66	4.72
Ni ₂ – P (shell 3)	1	0.31	4.13	0.137	4.27	-9.66	4.72
Ni ₂ – P (shell 4)	2	0.63	4.46	-0.123	4.34	-9.66	4.72
Ni ₂ – P (shell 5)	4	1.25	5.06	-0.123	4.94	-9.66	4.72
Ni ₂ – P (shell 6)	2	0.63	5.38	-0.123	5.25	-9.66	4.72

Table B.4 Ni and P atomic positions from Ni₂P pathways used in EXAFS fitting of the Ni nanoparticle structure. According to the interatomic distances ($R + \Delta R$) resulting from EXAFS fitting, the Ni and P atoms from the distorted Ni₂P pathways used resulted in the atoms sitting primarily in Ni *fcc* atomic positions and octahedral interstitial sites.

Atom type from Ni₂P Pathways	Percent in Ni FCC positions	Percent in Octahedral positions	Percent in Other positions
Ni	47 %	51 %	2 %
P	63 %	17 %	20 %

Fit using Ni *fcc* + substitutional P

Table B.5 Pathway parameters for fit using Ni *fcc* + substitutional P. The Ni *fcc* and substitutional P pathway parameters used to construct the best-fit EXAFS model for the Ni nanoparticle sample are listed. Note the the Ni atoms modeled to be part of the Ni₃P *fcc* structure (surrounding the substitutional P atoms) are distorted from their *fcc* positions. The Ni₃P pathways used in the model are shown in **Fig. B.4**.

Single Scattering Pathways from Ni <i>fcc</i>							
Pathway	N (acc.)	N (exp.)	R (Å)	ΔR (Å)	R + ΔR (Å)	E ₀ (eV)	σ ² (Å ²) x 10 ⁻³
Ni – Ni (shell 1)	12	9.49	2.49	-0.003	2.49	6.26	7.73
Ni- Ni (shell 2)	6	4.72	3.52	-0.008	3.52	6.26	12.0
Ni-Ni (shell 3)	24	18.9	4.32	-0.008	4.31	6.26	12.0
Ni – Ni (shell 4)	12	9.41	4.98	0.052	5.04	6.26	18.3
Ni – Ni (shell 5)	24	18.8	5.57	0.052	5.62	6.26	18.3
Multiple Scattering Pathways from Ni <i>fcc</i>							
Pathway	N (acc.)	N (exp.)	R (Å)	ΔR (Å)	R + ΔR (Å)	E ₀ (eV)	σ ² (Å ²) x 10 ⁻³
Ni_1 Ni_1	48	32.1	3.74	0.004	3.74	6.26	12.4
Ni_2 Ni_1	48	32.1	4.25	0.004	4.26	6.26	12.4
Ni_1 Ni_1	48	32.1	4.65	0.004	4.65	6.26	12.4
Ni_3 Ni_1	96	64.1	4.65	0.004	4.65	6.26	12.4
Ni_1 Ni_1	12	8.01	4.98	0.004	4.99	6.26	12.4
Ni_1 [+] Ni_1	12	8.01	4.98	0.004	4.99	6.26	12.4
Ni_4 Ni_1	24	16.1	4.98	0.004	4.99	6.26	12.4
Ni_1 [+] Ni_1	12	8.01	4.98	0.004	4.99	6.26	12.4
Ni_1 Ni_4 Ni_1	12	8.01	4.98	0.004	4.99	6.26	12.4
Ni_1 Ni_1 Ni_1	48	32.1	4.98	0.004	4.99	6.26	12.4
Ni_1 Ni_3 Ni_1	48	32.1	4.98	0.004	4.99	6.26	12.4
Ni_1 [+] Ni_1	48	32.1	4.98	0.004	4.99	6.26	12.4
Ni_3 Ni_1	48	32.1	5.17	0.004	5.17	6.26	12.4
Ni_3 Ni_2	48	32.1	5.17	0.004	5.17	6.26	12.4
Ni_3 Ni_1	96	64.1	5.56	0.004	5.57	6.26	12.4
Ni_3 Ni_2	48	32.1	5.56	0.004	5.57	6.26	12.4
Ni-P pathways (<i>fcc</i> substitutional)							
Pathway	N (acc.)	N (exp.)	R (Å)	ΔR (Å)	R + ΔR (Å)	E ₀ (eV)	σ ² (Å ²) x 10 ⁻³
Ni –P (shell 1)	4	0.83	2.49	-0.194	2.30	-8.70	8.95
Ni- P(shell 2)	8	1.65	4.32	0.094	4.41	-8.70	9.13
Ni – P (shell 3)	8	1.62	5.57	-0.238	5.33	-8.70	9.44
Ni-Ni distorted <i>fcc</i> pathways							
Pathway	N (acc.)	N (exp.)	R (Å)	ΔR (Å)	R + ΔR (Å)	E ₀ (eV)	σ ² (Å ²) x 10 ⁻³
Ni – Ni (shell 1)	8	1.68	2.49	0.277	2.77	6.26	13.8
Ni- Ni (shell 2)	6	1.25	3.52	-0.280	3.24	6.26	14.0
Ni-Ni (shell 3)	16	3.34	4.32	-0.280	4.04	6.26	14.0
Ni – Ni (shell 4)	12	2.48	4.98	0.232	5.22	6.26	14.2
Ni – Ni (shell 5)	16	3.31	5.57	0.232	5.80	6.26	14.2

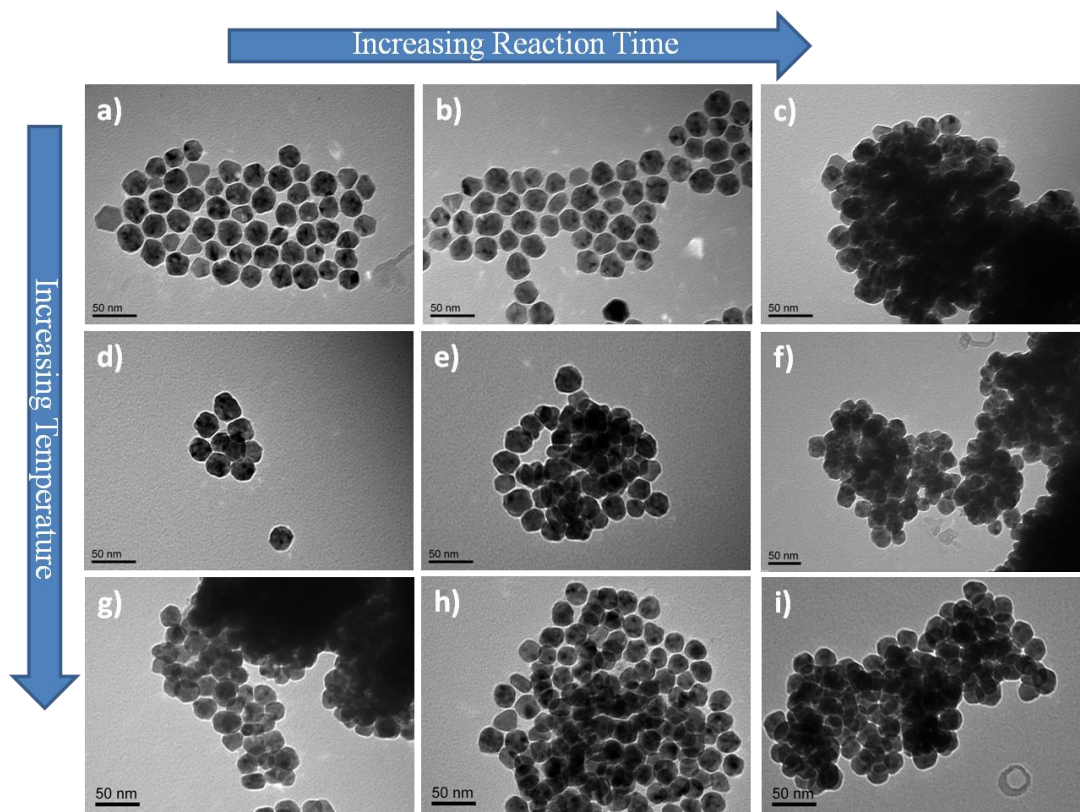


Figure B.5 TEM images of Ni nanoparticles synthesized varying reaction time and temperature. Reaction temperature increases from 210 °C (a-c) to 220 °C (d-f) to 230 °C (g-i). Reaction time varies from 20 minutes (left-hand column) to 40 minutes (center column) to 60 minutes (right-hand column). Note that the particle size and quasi-spherical morphology remains consistent, despite the increased phosphorus content of the nanoparticles as a function of increasing reaction time and temperature.

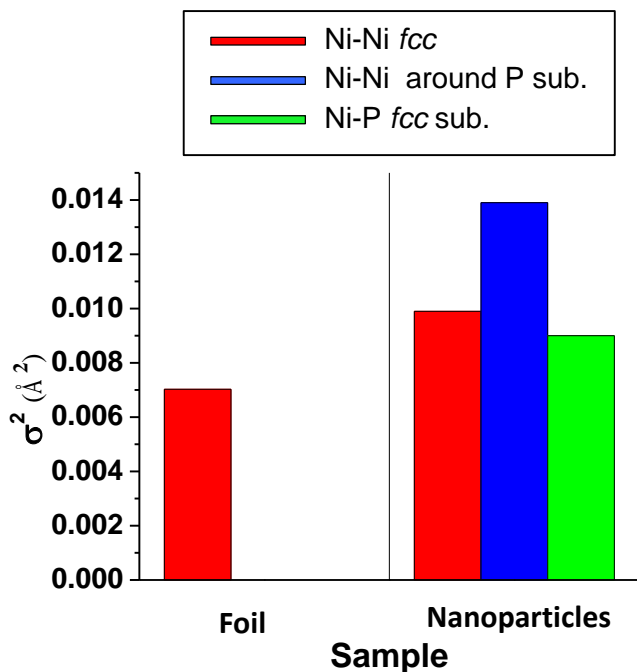


Figure B.6 Mean-squared disorder comparison. Average mean-squared disorder values from the first two shells of each of the structures. Larger mean-squared disorder values are associated with greater structural and thermal disorder. The mean-squared disorder values in the nanoparticle sample exceed those of bulk structure.

Table B.6 Lattice constant and bulk modulus calculations as a function of P atomic percent: Calculated lattice constant and bulk modulus fit using a Birch-Murnaghan equation of state, for pure Ni, and P-doped Ni at 6.25 and 12.5 at.% P. The bulk modulus calculated using this method is overestimated by ~8% for pure Ni, with respect to the experimental value of 180 GPa.

At.% P in Ni-P	Lattice constant [\AA]	Bulk Modulus [GPa]
0	3.523	194.2
6.25	3.517	194.8
12.5	3.509	196.3

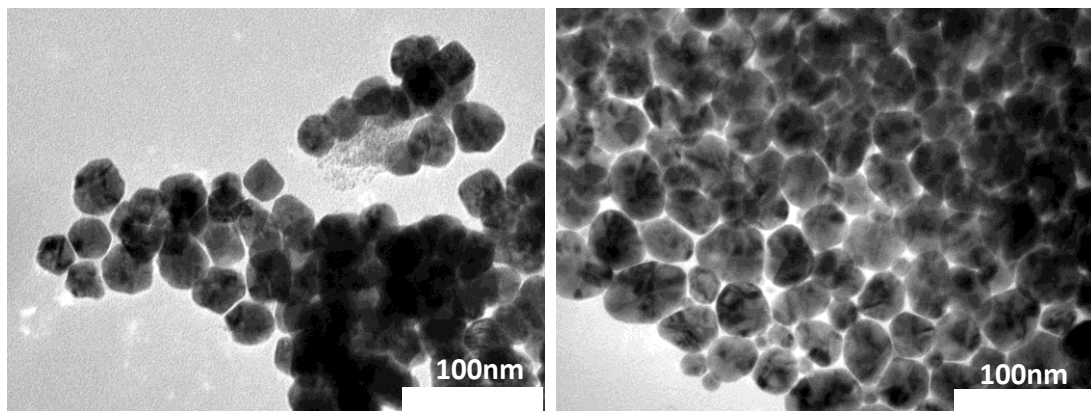


Figure B.7 TEM images of Ni nanoparticles used in magnetic studies. The left-hand figure shows Ni nanoparticles synthesized using less TOP (2.24 mmol compared to 4.48 mmol) and the right-hand figure shows Ni nanoparticles synthesized without the use of TOP. Note the increased polydispersity and size that results as lower amounts of TOP are used in the synthesis compared to our standard reaction conditions.

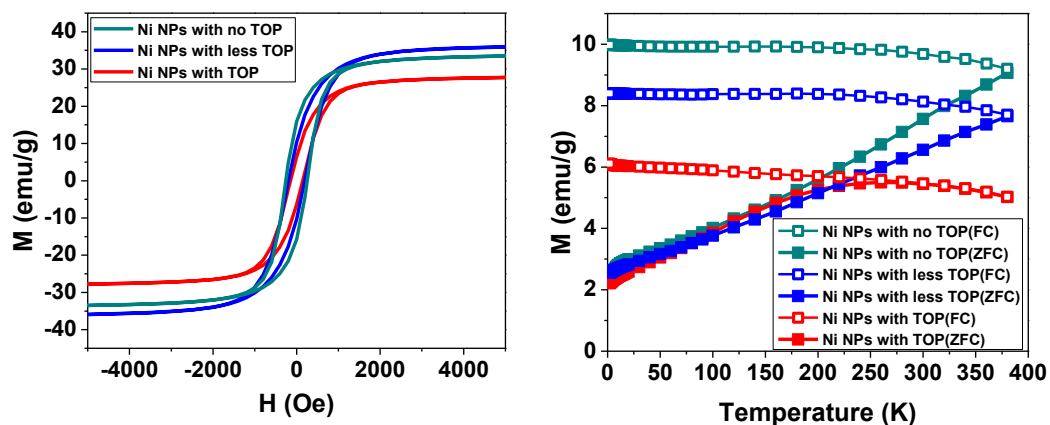


Figure B.8 Magnetization data for Ni samples. (left) Magnetization vs applied field hysteresis loops of the Ni sample synthesized with no TOP, (green) less TOP, (blue) and with TOP (red) measured at 2 K. (right) FC and ZFC magnetization curve for Ni samples. Temperature dependence of the magnetization for samples under a magnetic field of 100 Oe after zero-field- cooling (filled squares) and field-cooling (open squares). Green line, blue line, and red line indicate the Ni samples synthesized with no TOP, less TOP, and standard amount of TOP respectively.

Ni *fcc* + P substitutional model, atomic percentage contribution calculations

We can use the *fcc* Ni + substitutional P model to estimate the amount of P in the nanoparticles by examining the degeneracy of the pathways. The P content is determined by summing the degeneracy values (*i.e.*, N_{exp}) for the Ni–P pathways and dividing by the sum of the degeneracies for all pathways. This effectively counts the number of P atoms and divides by the total number of atoms within a set radius. Since the P is dilute we choose a large radial distance of 5.57 Å as the shell and sum the atoms within this shell to determine the atomic percent contributions. The percentage of Ni atoms well ordered in their *fcc* positions, Ni atoms distorted from their *fcc* positions and P substitutional atoms shown in **Table 3.2** were determined as follows:

From the experimental data shown in **Table B.4**:

$$\begin{aligned} N_{\text{Ni-P, total}} &= 0.827 + 1.652 + 1.615 \\ &= 4.094 \end{aligned}$$

$$\begin{aligned} N_{\text{Ni-Ni, fcc}} &= 9.492 + 4.715 + 18.86 + 9.405 + 18.81 \\ &= 61.282 \end{aligned}$$

$$\begin{aligned} N_{\text{Ni-Ni, distorted}} &= 1.678 + 1.251 + 3.335 + 2.479 + 3.306 \\ &= 12.049 \end{aligned}$$

$$\begin{aligned} N_{\text{Ni-Ni, total}} &= 9.492 + 4.715 + 18.86 + 9.405 + 18.81 + 1.678 + 1.251 + 3.335 + 2.479 \\ &+ 3.306 \\ &= 73.331 \end{aligned}$$

Plugging into the equation to determine atomic percentage phosphorus*:

$$\Sigma(N_{\text{Ni-P, total}})/\Sigma(N_{\text{Ni-P, total}} + N_{\text{Ni-Ni, total}}) = \mathbf{5.3 \text{ at. \% P}}$$

$$N_{\text{Ni-P}} \text{ is a minimum where: } N_{\text{Ni-P, min}} = N_{\text{Ni-P, total}} - 0.1(N_{\text{Ni-P, total}}) = 3.685$$

$$N_{\text{Ni-P}} \text{ is a maximum where: } N_{\text{Ni-P, max}} = N_{\text{Ni-P, total}} + 0.1(N_{\text{Ni-P, total}}) = 4.503$$

$$N_{\text{Ni-Ni}} \text{ is a minimum where: } N_{\text{Ni-Ni, min}} = N_{\text{Ni-Ni, total}} - 0.1(N_{\text{Ni-Ni, total}}) = 65.998$$

$$N_{\text{Ni-Ni}} \text{ is a maximum where: } N_{\text{Ni-Ni, max}} = N_{\text{Ni-Ni, total}} + 0.1(N_{\text{Ni-Ni, total}}) = 80.664$$

Using these values, the maximum and minimum atomic phosphorus percentage can be determined.

$$\text{Minimum possible atomic P \%: } \Sigma(N_{\text{Ni-P, min}})/\Sigma(N_{\text{Ni-P, min}} + N_{\text{Ni-Ni, max}}) = 4.4\%$$

$$\text{Maximum possible atomic P \%: } \Sigma(N_{\text{Ni-P, max}})/\Sigma(N_{\text{Ni-P, max}} + N_{\text{Ni-Ni, min}}) = 6.4\%$$

Thus, using the greater difference as the error magnitude, the atomic % P in the Ni NP sample is: **5.3 % ± 1.1 %**

*The atomic percentages of ordered and distorted Ni *fcc* atoms were calculated from the degeneracy values in the same manner. The atomic P percent was used in order to provide a sample calculation.

References

1. Muthuswamy, E.; Savithra, G. H. L.; Brock, S. L. *ACS Nano* **2011**, *5*, 2402-2411.
2. Carencu, S.; Boissiere, C.; Nicole, L.; Sanchez, C.; Le, F. P.; Mezailles, N. *Chem. Mater.* **2010**, *22*, 1340-1349.
3. Wang, J.; Johnston-Peck, A. C.; Tracy, J. B. *Chem. Mater.* **2009**, *21*, 4462-4467.
4. Park, J.; Kang, E.; Son, S. U.; Park, H. M.; Lee, M. K.; Kim, J.; Kim, K. W.; Noh, H.-J.; Park, J.-H.; Bae, C. J.; Park, J.-G.; Hyeon, T. *Adv. Mater.* **2005**, *17*, 429-434.
5. Bunker, G., *Introduction to XAFS: a practical guide to X-ray absorption fine structure spectroscopy*. Cambridge University Press: Cambridge, 2010; p 260.
6. Ravel, B.; Newville, M. *J. Synchrotron Radiat.* **2005**, *12*, 537-541.
7. Stern, E. A. *Contemp. Phys.* **1978**, *19*, 289-310.
8. Koningsberger, D. C.; Mojet, B. L.; van Dorssen, G. E.; Ramaker, D. E. *Top. Catal.* **2000**, *10*, 143-155.
9. Ravel, B. *J. Synchrotron Radiat.* **2001**, *8*, 314-316.
10. Stern, E. A. *Phys. Rev. B* **1974**, *10*, 3027-3037.
11. Ravel, B.; Kelly, S. D. *AIP Conf. Proc.* **2007**, *882*, 150-152.

12. Scott, R., *Physical Methods in Bioinorganic Chemistry: Spectroscopy and Magnetism*. University Science Books: 2000.
13. Michalowicz, A.; Vlais, G. *J. Synchrotron Radiat.* **1998**, *5*, 1317-1320.
14. Kresse, G.; Hafner, J. *Phys. Rev. B* **1993**, *47*, 558.
15. Kresse, G.; Hafner, J. *Phys. Rev. B* **1994**, *49*, 14251.
16. Kresse, G.; Furthmüller, J. *Phys. Rev. B* **1996**, *54*, 11169.
17. Kresse, G.; Furthmüller, J. *Comput. Mater. Sci.* **1996**, *6*, 15-50.
18. Blöchl, P. E. *Phys. Rev. B* **1994**, *50*, 17953.
19. Kresse, G.; Joubert, D. *Phys. Rev. B* **1999**, *59*, 1758.
20. Perdew, J. P.; Burke, K.; Ernzerhof, M. *Phys. Rev. Lett.* **1996**, *77*, 3865-3868.
21. Methfessel, M.; Paxton, A. T. *Phys. Rev. B* **1989**, *40*, 3616-3621.
22. Blochl, P. E.; Jepsen, O.; Andersen, O. K. *Phys. Rev. B* **1994**, *49*, 16223-16233.
23. Monkhorst, H. J.; Pack, J. D. *Phys. Rev. B* **1976**, *13*, 5188.

CHAPTER 4

4 DEFINING CRYSTALLINE/AMORPHOUS PHASES OF NANOPARTICLES THROUGH X-RAY ABSORPTION SPECTROSCOPY AND X-RAY DIFFRACTION: THE CASE OF NICKEL PHOSPHIDE*

4.1 Abstract

In this study we elucidate the structural distinctions between amorphous and crystalline Ni₂P nanoparticles synthesized using tri-*n*-octylphosphine (TOP), through X-ray absorption spectroscopy (XAS), X-ray diffraction (XRD), and inductively coupled plasma (ICP). We determine the differences in their chemical and atomic structure, which have not been previously reported, yet are essential for understanding their potential as nanocatalysts. These structural characteristics are related to the corresponding nanoparticle magnetic properties analyzed by performing magnetic measurements. XAS results reveal a significant P concentration in the amorphous nanoparticle sample – placing the stoichiometry close to Ni₂P – despite XRD results that show only *fcc* Ni contributions. By comparing the long-range structural order from XRD to the short-range radial structure from EXAFS we conclude that both techniques are necessary to obtain a complete structural picture of amorphous and crystalline nanoparticle phases due to the limitations of XRD amorphous

* Originally Published as: L. M. Moreau,* D.-H. Ha,* H. Zhang, R. Hovden, D. Muller, and R. D. Robinson, "Defining Crystalline/Amorphous Phases of Nanoparticles through X-ray Absorption Spectroscopy and X-ray Diffraction: The Case of Nickel Phosphide," *Chem. Mater.* **25**, 2394 (2013) Reprinted with Permission from American Chemical Society. (* = equally contributed)

characterization. We find that phases are amorphous with respect to XRD when their offsets (deviations) from bulk inter-atomic distances have a standard deviation as high as ~4.82. Phases with lower standard deviation (e.g. $< \sim 1.22$), however, are detectable as crystalline through XRD. The possible presence of amorphous phases should be considered when using XRD alone for nanoparticle characterization. This is particularly important when highly reactive reagents such as TOP are used in synthesis. By characterizing amorphous nickel phosphide nanoparticles that have a comparable stoichiometry to Ni₂P, we confirm that TOP serves as a highly effective phosphorus source, even at temperatures as low as 230 °C. Unintended amorphous structure domains may significantly affect nanoparticle properties, and, in turn, their functionality.

4.2 Introduction

Crystallinity control in nanoparticles holds the key to optimizing their functionality. It has been shown that crystallinity modification can lead to dramatic changes in nanoparticle properties.¹⁻⁴ Although nanoparticles with controlled crystalline and amorphous characteristics are desirable in applications,^{2, 4-6} the characterization of nanoparticle crystallinity is not well established or defined.

Nickel phosphides are under increasing interest as catalysts for hydrotreating in fuels.^{7, 8} Ni₂P has been reported to outperform commercially used catalysts in terms of resistance to poisoning.⁹⁻¹¹ Several new studies have reported synthetic methods for nickel phosphide nanoparticles but little is known about their chemical and structural

attributes. In recent years, tri-*n*-octylphosphine (TOP) has been used in the synthesis of metal phosphide nanoparticles through thermal decomposition of metal-phosphine complexes in the standard nanoparticle synthesis method.¹² Brock et al.,¹³ Hyeon et al.,¹⁴ Schaak et al.,¹⁵ Tracy et al.,¹⁶ and Chiang et al.¹⁷ have used this method to synthesize Ni and Ni-P nanoparticles. For the Ni nanoparticles, TOP was used as a ligand and thought to only act as a stabilizing surfactant on the surface; the particles were characterized, based on XRD, as pure *fcc* nickel.¹⁸ In a previous study we discovered unintended phosphorus doping from these TOP ligands during the nickel nanoparticle synthesis by correlating X-ray absorption spectroscopy (XAS), a technique sensitive to amorphous structure, with traditional characterization tools (e.g., XRD and ICP).¹⁹ The phosphorus doping was high (~6 atomic %) and has significant implications on the structural, magnetic and catalytic properties of the nanoparticles.¹⁹ Amorphous nickel phosphide nanoparticles have been synthesized in literature,^{13, 16, 20} yet little is known about their chemical composition, local ordering, and the implications of their structure on their novel properties. These prior studies reveal the necessity to combine advanced XAS techniques with conventional techniques (e.g., XRD and TEM) to provide a complete structural and chemical characterization of the Ni-P nanoparticles that contain both crystalline and amorphous phases.

Although techniques that enable the structural characterization of bulk material have been well-developed, the characterization of material at the nanoscale still presents significant challenges. The dominance of surface facets, small size, and poor crystalline order makes characterization of nanoparticles difficult. X-ray absorption

spectroscopy (XAS) is a method which has been used to resolve the structure of colloidal nanocrystals.²¹⁻²⁸ With the use of the high energy beam available through synchrotron radiation, XAS spectra can be obtained and used to gain insight into material structural properties.^{29, 30} The structure of both XRD-detectable and XRD-amorphous materials can be determined through analysis of both the lower-energy XANES (X-ray absorption near edge) portion of the spectrum to resolve geometric structure, and the higher-energy quasi-periodic EXAFS (extended X-ray absorption fine structure) modulations to resolve radial structure, including inter-atomic distances, coordination numbers, and mean-squared disorder.³¹ By using XAS in combination with the conventional characterization techniques of XRD to determine crystalline behavior (long-range order) and TEM to determine size, morphology, long range order and phase, with ICP to confirm stoichiometry, and by performing magnetic measurements using a superconducting quantum interference device (SQUID) magnetometer to measure magnetic properties, structure-property relationships of the particles can be resolved. EXAFS and XRD complement each other by providing insight into short-range and long-range (crystalline) order, respectively.

Through this investigation we synthesize nickel phosphide nanoparticles using precursors with identical Ni/P ratios but with different reaction conditions. One reaction results in an amorphous phase and the other in a crystalline Ni₂P phase. Although both phases have been previously reported in literature,¹³ their structural characteristics have not been described. For these reactions we: 1) report the atomic structure of amorphous and crystalline Ni₂P nanoparticle samples (referred to hereafter

as nanoparticle reaction products **I** and **II**, respectively), and particularly the differences in structure despite their similar elemental composition, 2) reveal the tendency for Ni atoms in nanoparticles to retain *fcc* positions even with a phosphorus-rich composition, 3) show how nanoparticle magnetization is highly dependent on the structure of the nanoparticle samples, 4) confirm that TOP can serve as a P source that is effective enough to produce nanoparticles with the stoichiometry of Ni₂P even at temperatures as low as 230 °C, and 5) define the amorphous-limit of XRD in characterizing non-crystalline phases by comparing the XRD structural characterizations with EXAFS analysis. In conjunction with our previous Co-P³² and Ni¹⁹ nanoparticle studies, we propose that a phase is crystalline through XRD (XRD crystalline) when the standard deviation of offsets from bulk interatomic distances is minimal (e.g. <~1.22). When the standard deviation is higher (~4.82), the phase may not be detectable by XRD (is XRD amorphous). This limitation of XRD in defining amorphous structure (which exhibits only short-range ordering) and of EXAFS in recognizing crystalline behavior (which exhibits long-range order), necessitates the use of both techniques in a thorough characterization of the Ni₂P nanoparticle structure. A thorough knowledge of the amorphous and crystalline phases within nanoparticles, as well as their relative contributions and effect on resulting structurally-based properties, will enable optimization of nanoparticles for use in applications such as catalysis.

4.3 Methods

Synthesis of the nickel phosphide nanoparticles was based on thermal decomposition of a Ni-TOP complex as outlined by Muthuswamy et al.¹³ This thermal decomposition is the reduction reaction of the Ni(II) precursor into Ni(0) by the primary amine¹⁸; a recent study has demonstrated this mechanism.³³ Additional descriptions of these methods are outlined in the supplementary materials. The temperature, reaction time, and oleylamine concentration were varied between samples. The specific conditions used in the synthesis of the two samples are outlined in **Table 4.1**. The Ni/P ratio was identical for reaction **I** and **II** but the temperature and time were increased for reaction **II**, and reagent and surfactant concentration were varied.

Table 4.1 Nickel phosphide nanoparticle synthetic conditions. Reaction conditions are listed for the Ni₂P amorphous (I) and crystalline (II) samples. The temperature and time were increased for reaction II. The Ni/P ratio is identical for both samples.

Reaction	Ni(acac)₂	TOP	octyl ether	oleylamine	Temp.	Time
I	1.17 g (4 mmol)	22.4 mmol	10 mL	4 mL	230 °C	1 hr
II	0.585 g (2 mmol)	11.2 mmol	10 mL	11.5 mL	350 °C	2 hr

The XAS data acquisition and analysis methods are outlined as follows. A more detailed description and all other methods can be found in the supplementary

materials. XAS spectra of the nickel phosphide nanoparticle samples were obtained at the C1 station of the Cornell High Energy Synchrotron Source (CHESS) using a fluorescence detection to probe the nickel K-edge (8333 eV). Transmission detection was simultaneously used to probe the K-edge of a Ni metal foil during each of the scans, to function as a standard for comparison and edge calibration.

The raw spectra were averaged and processed using ATHENA,³⁴ part of the IFEFFIT software package. Data processing involved edge determination from the first inflection point in the absorption data, background subtraction using the AUTOBK algorithm, and normalization of the EXAFS modulations (greater than 50 eV above the edge).³¹ The data was then analyzed by the ab-initio method and multiple data set fitting in k-space and R-space using ARTEMIS.³⁴ By fitting well-matched theoretical pathways to the experimental spectra through loosening variables to deviate from the theoretical bulk structures, specific structural information could be determined including coordination number, inter-atomic spacing and mean-squared disorder.^{30, 31, 35, 36}

4.4 Results

TEM images of the nickel phosphide nanoparticles (**Fig. 4.1a,b**) show monodisperse particles with a narrow size distribution, as typically observed in reactions involving TOP as a surfactant.¹⁸ The nanoparticle products of **I** are small (9.0 nm, std. dev. 8.9%) and spherical (**Fig. 4.1a**). Nanoparticles from **II** are larger (14.6 nm, std. dev. 8.3%) and show structural hollowing as a result of the nanoscale Kirkendall effect that is typically observed for these nanoparticles, indicating that they

may have transformed from Ni to Ni₂P (**Fig. 4.1b**).^{16, 37} The hollow voids (3.6 nm, std. dev. 18%) are visible as the lighter regions in the center of the Ni₂P particles. Nanoparticles from **II** are not perfectly spherical but quasi-faceted, as more clearly observed in high-angle annular dark-field (HAADF) STEM images (**Fig. 4.2**).

HRTEM images of the samples show clear differences in the crystallinity (**Fig. 4.3**). The nanoparticle from **I** exhibits randomly distributed atoms with limited ordering while sample **II** is single crystalline with lattice spacing that well-matches the Ni₂P hexagonal structure.

XRD was also utilized to identify the long range (crystalline) order of the samples. The samples were deposited on a quartz slide that has no background noise (see supplementary online materials for the XRD measurement details). XRD results show only *fcc* Ni contributions from the nanoparticles from **I** (**Fig. 4.1c**, JCPDS #65-2865). The XRD diffraction pattern of nanoparticles from **I** shows poor crystalline order: a very broad peak at ~44.5°, which corresponds to the main characteristic peak for *fcc* Ni, suggests a disordered, non-crystalline structure. This product, under similar synthetic conditions and having a similar resulting XRD pattern, was previously characterized as amorphous Ni_xP_y.^{13, 16} Prior studies have shown that amorphous Ni-P nanoparticles with this XRD pattern will crystallize to Ni₂P upon heating without any additional P added.³⁸ The grain size of nanoparticles from **I** using the Scherrer equation (fit to the first *fcc* Ni peak using a Gaussian function) is ~1.88 nm (much smaller than the nanoparticle size), as may be expected for an XRD amorphous structure.^{39, 40} The XRD diffraction pattern of **II** (**Fig. 4.1d**) shows sharp peaks that match the Ni₂P crystal structure (JCPDS #65-1989) and small contributions from

peaks with low intensity at $\sim 50^\circ$ that suggest a small presence of impurities in the sample. These additional peaks, however, did not correspond to any crystal structure included in the JCPDS database composed of Ni, Ni-P, P, Ni-O, C-H-O-P, Ni-O-P, P-O, or Ni(acac)₂, which represent expected impurity phases. Although a previous study demonstrated the presence of nickel carbide structure using similar synthetic methods⁴¹ these additional peaks also do not match any Ni-C phase, indicating that these phases are not present in our as-synthesized structure. Overall, the intensity of the Ni₂P peaks, and the fact that the XRD pattern of the reaction **II** nanoparticles is not shifted or distorted from reference Ni₂P peaks, suggests that the particles from **II** contain crystalline Ni₂P as their major phase. The calculated grain size for the nanoparticles from **II** based on XRD is ~ 13.8 nm. This large grain size is close to the size observed by TEM (14.6 nm), which suggests that the nanoparticles from **II** are single-crystalline. The single-crystalline nature is confirmed by HRTEM (**Fig. 4.3**). The nanoparticles from **I** show extremely broad features in comparison to those observed for the reaction **II** nanoparticles, and exhibit an amorphous-like structure. This is further confirmed with electron diffraction patterns of the samples, which reveal that sample **I** has an amorphous structure with a broad contribution from fcc Ni and that sample **II** is crystalline Ni₂P (**Fig. 4.1e,f**).

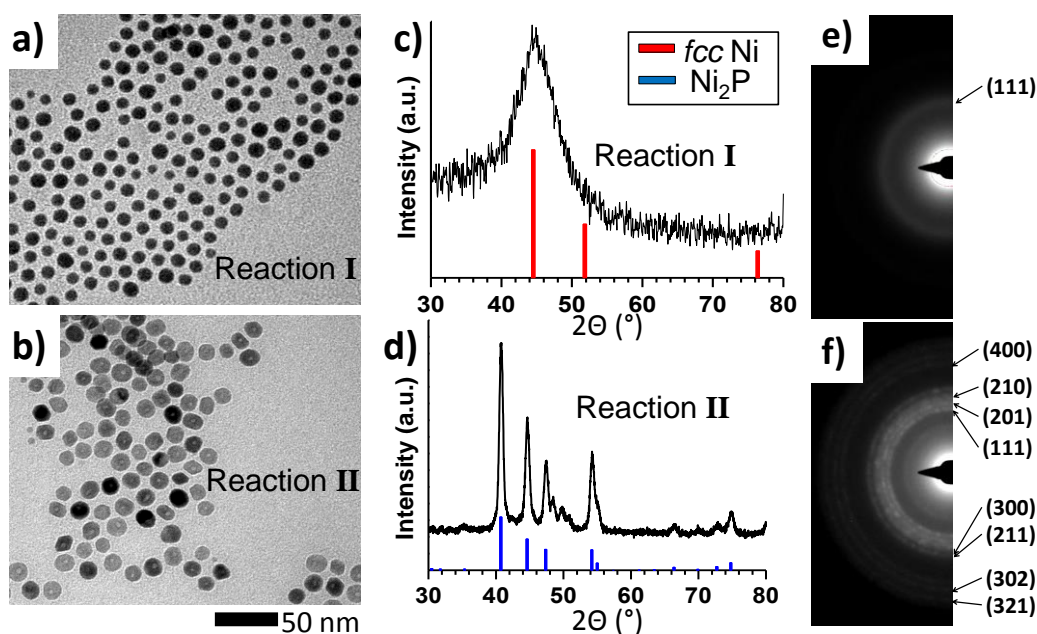


Figure 4.1 TEM images and XRD spectra of the nanoparticles. TEM images with the corresponding XRD pattern shown for the nanoparticles from reaction I (a,c) and II (b,d). The red lines correspond to *fcc* Ni peak positions (JCPDS #65-2865) and the blue lines to Ni₂P peak positions (JCPDS #65-1989). The particles from reaction I are small (~9.0 nm) spherical particles with a broad XRD peak in the primary *fcc* Ni position. The particles from reaction II exhibit structural Kirkendall hollowing and quasi-faceted morphology. The corresponding XRD pattern from nanoparticles of II shows primarily Ni₂P with minute impurity contributions. Electron diffractions also indicate the amorphous pattern (e) from *fcc* Ni for the sample I and crystalline Ni₂P structure for the sample II, which confirms these results.

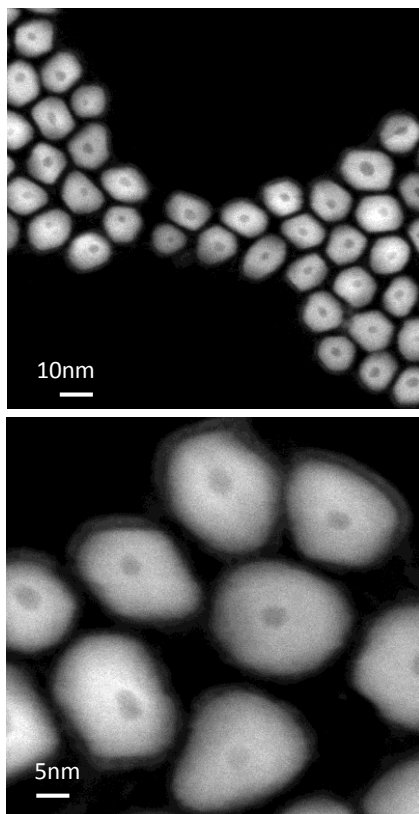


Figure 4.2 HAADF STEM images of nanoparticles from reaction II. Dark-field STEM images of the nanoparticles display their quasi-faceted morphology with distinct hollow voids. The apparent thin shell may be due to surface oxidation as a result of plasma treatment.

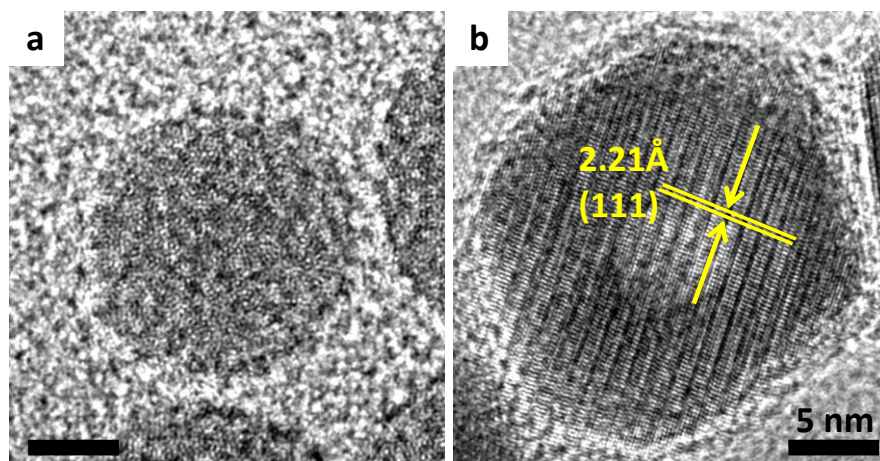


Figure 4.3 HRTEM images of the samples. (a) Sample I shows amorphous atomic arrangements with no well-defined crystalline lattice. (b) Sample II, in contrast, is single crystalline and the lattice distances are well matched with Ni₂P structure. Scale bars are 5 nm.

XAS data in energy-space, k -space and R -space from the nanoparticle samples and a bulk Ni foil standard are shown in **Fig. 4.4**. The energy-space spectrum from reaction **I** (**Fig. 4.4a**, blue) shows a blue-shift in the edge value from pure *fcc* Ni to 8343 eV (+9 eV from Ni), which suggests dominance of the Ni k -edge, or $1s-3p$ transition atomic line.⁴² This alteration from the bulk standard *fcc* Ni spectrum indicates a change in geometric structure. A notable feature of the XAS spectrum from **I** that is different from the *fcc* Ni spectrum is a pronounced white line peak, which is indicative of charge transfer from Ni to P atoms.⁴³ Such charge transfer has also been observed in X-ray photoelectron spectroscopy (XPS) experiments.^{44,45} The oscillatory structure of the EXAFS modulations is also severely damped in

comparison to a pure-phase, crystalline structure, such as the Ni metal foil (red)¹⁹, an effect characteristic of samples which lack crystalline order.⁴³ The oscillatory nature of the EXAFS modulations from sample **II**, in contrast, is more well-defined, with notably less damping. It is interesting that the XRD spectra from **I** only shows structural contributions from *fcc* Ni, while its XAS spectrum is clearly far different from the *fcc* Ni spectrum, and shows a greater similarity to one observed in bulk Ni-P amorphous alloys with phosphorus concentrations of 26%.⁴³

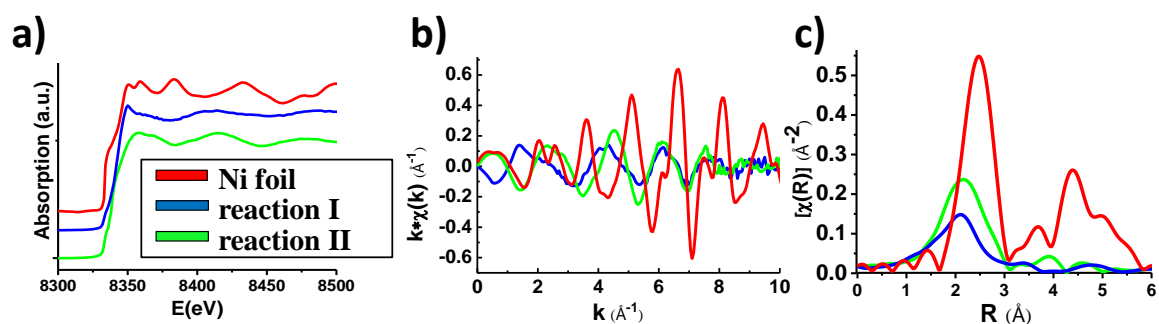


Figure 4.4 XAS spectra of Ni₂P nanoparticles from Ni foil standard (red), reaction I (blue) and reaction II (green). (a) The Energy-space spectrum of I (blue) reveals a sharp white-line peak. The spectrum of reaction II (green) visibly differs from the reaction I spectrum. (b) The *k*-space XAS spectra show a decrease in amplitude and change in phase for I in comparison to II. (c) The *R*-space spectrum shows less accumulation for the first shell peak of I, with higher order shells that are smeared together and diminished. The aforementioned features of I are characteristic of an amorphous structure. In a, b, and c, the reaction I and reaction II spectra vary significantly from the Ni foil.

Analyzing the k -space and R -space spectra (**Fig. 4.4b** and **4.4c**, blue) of nanoparticles from **I**, there is little second shell behavior in comparison to that observed for bulk fcc Ni,¹⁹ or even nanoparticle Ni doped with small amounts of P.¹⁹ The higher shell features are smeared together and diminished, producing poorly defined peaks, unlike what is characteristic of a crystalline structure.²⁹ Because of these smeared features it is not surprising that XRD results in no clear crystalline phase. This lack of long-range order results from a large distribution of inter-atomic distances characteristic to amorphous structures.⁴⁶ The spectrum of **I** is more similar to crystalline Ni₂P than to fcc Ni.¹⁹ Observable in the R -space spectrum from nanoparticles of **I** and **II** is a similar left-shift in the first coordination shell compared to the fcc Ni bulk reference spectrum¹⁹ (**Fig. 4.4c**), due to Ni-P contributions in these samples, which have shorter bonding lengths compared to the 2.5 Å of Ni-Ni in fcc Ni.⁴⁷ Also, it is notable that there is a shorter-distance accumulation of the primary peak, which accumulates with a maximum at ~2.1 Å in the nanoparticles from **I** in comparison to the 2.5 Å associated with Ni-Ni bonds in the fcc Ni crystal structure.⁴⁸ Despite some XAS spectral similarities to the nanoparticles from **II**, the decreased order, diminished oscillations, and lack of higher-order coordination shells reveal that the nanoparticles from **I** display structurally amorphous characteristics.

The energy-space spectrum of nanoparticles from **II** (**Fig. 4.4a**, green) differs from that of **I**. The white line peak is significantly broadened, attributable to a decrease in occupancy of 4d states.⁴⁹ There is a blue-shift from the fcc Ni edge value to 8338 eV (+4 eV). As a result, the edge is positioned below the energy of the 1s–4p atomic line with mixing from 3p P orbitals.^{42, 50} This transition is often observed in

structures which possess tetrahedral coordination,⁴² which occurs for Ni 3f site atoms in the Ni₂P crystal structure⁵¹ [see supplementary online materials for placement of 3f and 3g site Ni atoms in the Ni₂P crystal structure]. The *k*-space and *R*-space spectra of **II** (**Fig. 4.4b** and **4.4c**, green) show increased peak amplitude in comparison to the spectrum of **I**, particularly in the higher order shells of the *R*-space spectrum (**Fig. 4.4c**), which is indicative of a structure that exhibits crystalline behavior.²² Yet this amplitude is much lower than that observed for the bulk *fcc* Ni foil,¹⁹ revealing the structural disorder still present within the structure, despite being XRD-crystalline. Also, while the *fcc* Ni crystal structure has the Ni-Ni bonds clustered at ~2.5 Å, the reference Ni₂P crystal structure has both Ni-P and Ni-Ni bonding distances which vary considerably, even within a 2-3 Å radius, causing the first peak in the *R*-space XAS spectrum to accumulate over a wide range of distances in comparison to *fcc* Ni.^{19, 47, 48} The edge shift and peak features observed in the spectra from **II** provide additional confirmation that this sample, characterized as Ni₂P based on XRD, is indeed primarily Ni₂P. In addition, the differences between the near-edge spectra of **I** and **II** suggest that particles from **I** do not exhibit the crystalline Ni₂P structure. However, the nanoparticles from **I** also differ from *fcc* Ni. Therefore, the structure of nanoparticles from **I**, as we will confirm with EXAFS analysis and ICP results, must be amorphous Ni₂P (as confirmed by ICP and EXAFS modeling). This amorphous Ni₂P retains some *fcc* Ni character (Ni-Ni local bonding characteristics), which is also apparent from XRD *fcc* Ni peaks, despite the P-rich composition. In other words, the *fcc* Ni lattice is so phosphorus-rich that the composition resembles Ni₂P, yet without complete disruption of the *fcc* Ni lattice.

Table 4.2 First shell path parameters from EXAFS fitting models. The *fcc* Ni and Ni₂P pathway parameters used to construct the best-fit EXAFS model for the I (top) and II (bottom) nanoparticles. The names “Ni_(3f)” and “Ni_(3g)” represent the Ni 3f site and Ni 3g site atoms within the Ni₂P crystal structure. The listed parameters include the theoretical degeneracy value found in bulk structure (N(theory)), the degeneracy value extracted from the experimental spectra (N(exp.)), the theoretical pathlength from bulk structure (R), the deviation from the theoretical pathlength (ΔR), the energy shift parameter (E_0) and the mean-squared disorder (σ^2).

Reaction I Fitting Parameters							
	Pathway	N (theory)	N (exp.)	R (Å)	ΔR (Å)	E_0 (eV)	σ^2 (x 10⁻³ Å²)
<i>fcc</i> Ni Pathways	Ni – Ni	12	1.16	2.492	-0.114	-9.93	8.45
Pathways from Ni₂P crystal structure	Ni _(3f) – Ni	5	4.07	2.792	-0.037	-9.93	7.23
	Ni _(3g) – Ni	6	7.36	2.920	-0.189	-9.93	7.08
	Ni _(3f) – P	2	1.24	2.238	-0.031	-9.98	4.25
	Ni _(3g) – P	2.5	4.16	2.439	-0.137	-9.98	4.62
Reaction II Fitting Parameters							
Pathways from Ni₂P crystal structure	Pathway	N (theory)	N (exp.)	R (Å)	ΔR (Å)	E_0 (eV)	σ^2 (x 10⁻³ Å²)
	Ni _(3f) – Ni	5	5.12	2.792	-0.115	-3.63	8.10
	Ni _(3g) – Ni	6	5.99	2.920	-0.044	-3.63	7.22
	Ni _(3f) – P	2	1.96	2.238	-0.047	-1.94	3.49
	Ni _(3g) – P	2.5	2.35	2.439	-0.086	-1.94	4.85

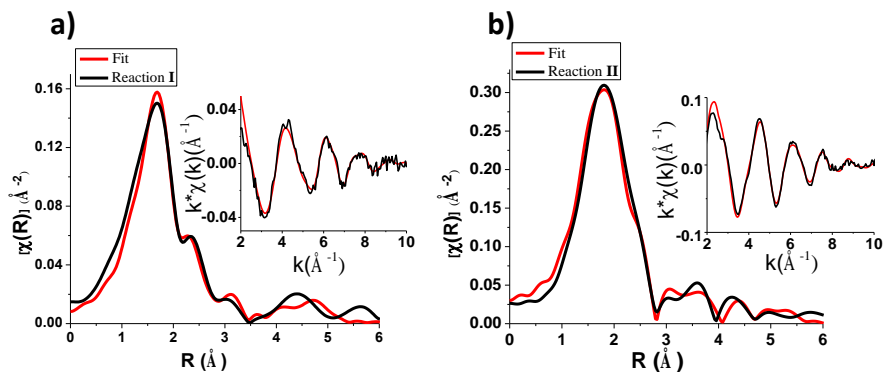


Figure 4.5 EXAFS models of the nickel phosphide nanoparticle spectra. R-space and k-space (inset) fitting models (red) are well matched to the experimental nanoparticle spectra results (black) for I (a) and II (b).

In order to extract accurate parameters for the atoms surrounding the central Ni core atom the nanoparticle XAS spectra were fit using theoretical models in both R -space (**Fig. 4.5**) and k -space (**Fig. 4.5**, inset). A combination of scattering pathways from *fcc* Ni and Ni₂P crystal structures were used to create the theoretical models. **Table 4.2** contains the parameters used to construct the theoretical fitting models for the nanoparticles from **I** and **II**. The parameters included in the table are: the degeneracy value from the bulk reference structure (N_{theory}),^{47, 48} which can be compared to the degeneracy value determined by the fit to the experimental spectra ($N_{\text{exp.}}$), the bulk reference structure's inter-atomic distance from the scattering atom (R),^{47, 48} the deviation found in the experimental results from the bulk reference inter-atomic distance (ΔR), the energy shift parameter (E_0), which was fixed for bonds of the same type, and the mean-squared disorder (σ^2), which includes contributions from both structural and thermal disorder.³¹ Only first coordination shell pathways are

included in the tables for simplification. The higher shell pathway parameters are included in the supplementary materials.

Table 4.3 Ni and P contributions and associated error within the nanoparticles from EXAFS modeling and ICP. The first column lists the nanoparticle reaction.

The Ni (*fcc* positions), Ni (Ni₂P positions), Ni (combined *fcc* and Ni₂P positions) and P (Ni₂P positions) atomic percentages calculated from the EXAFS fitting model are listed in the next four columns. The phosphorus content of the nanoparticles from I closely mimics Ni₂P despite the differences in structure and XRD crystalline characterization. The final two columns show the elemental analysis results from ICP measurements, which are in agreement with our EXAFS results within the realm of error.

Sample	Atomic % (EXAFS modeling)				Atomic % (ICP-OES)	
	Ni from <i>fcc</i> Ni	Ni from Ni ₂ P	Ni Combined	P from Ni ₂ P	Ni	P
I	10.3 ± 0.7	57.2 ± 4.0	67.5 ± 4.7	32.5 ± 4.7	70.3 ± 3.5	29.7 ± 1.5
II	0	67.8 ± 4.9	67.8 ± 4.9	32.2 ± 4.9	64.1 ± 3.2	35.9 ± 1.8

Table 4.3 shows the atomic percentages of Ni atoms (in either the *fcc* Ni position or the Ni₂P positions) and P atoms (in Ni₂P positions) along with their standard deviations based on the EXAFS fitting models of the spectra from

nanoparticles of **I** and **II**. These percentages were estimated from the sum of the degeneracy values for the first three shells of the relevant pathway in the fitting model divided by the total number of atoms included in these shells (see supplementary materials for sample calculation and previous paper showing more detail of this method¹⁹). In this way, the phosphorus atomic percentages could be estimated, as well as the relative Ni contributions from the *fcc* Ni and Ni₂P structures (for the nanoparticles from reaction **I**, both *fcc* Ni and Ni₂P phases were necessary to include in the fitting model for a good fit, thus the total amount of Ni-Ni is included in **Table 4.3** column 4, for a combined representation). ICP-OES (inductively coupled plasma optical emission spectroscopy) was used to confirm the elemental composition. Results from ICP analysis are included in the two right-most columns of **Table 4.3**.

All pathways for the nanoparticles from **I** displayed large deviations in inter-atomic distance, which are consistent with results from XRD and near-edge XAS features that suggest a disordered structure. Modeling of the atomic structure from reaction **I** was accomplished using a combination of *fcc* Ni and Ni₂P pathways that deviate significantly from the bulk reference inter-atomic distances, even within the first coordination shell, a feature not characteristic of a crystalline structure, which is expected to have near-bulk values. The spectra from reaction **I** nanoparticles were best modeled using ΔR and σ^2 values which are considerably larger than those expected in a crystalline bulk structure by as much as a full order of magnitude, consistent with an amorphous structure lacking well-ordered pathways. This deviation is indicative of structural disorder.²³ The 32.5 atomic % phosphorus determined for nanoparticle from **I** (29.7 % by ICP) closely resembles the stoichiometry of Ni₂P. The

high atomic % of phosphorus within the reaction **I** nanoparticles despite XRD results that show only a broad peak from *fcc* Ni indicates that some of the Ni *fcc* positions are retained (local structure Ni-Ni bonds still retain *fcc* Ni character), and an amorphous structure is stabilized despite phosphorus atomic percentages as high as Ni₂P.

XAS spectra of nanoparticles from **II** were well-fit using only well-ordered Ni₂P pathways. Including additional Ni-C, Ni-O, and Ni-P phases worsened the quality of the EXAFS fit. The phosphorus composition is close to the pure phase Ni₂P based on both ICP and EXAFS modeling results (35.9 ± 1.8 P atomic % by ICP and 32.2 ± 4.9 P atomic % by EXAFS, compared to the 33.3 atomic % expected for pure Ni₂P). The goodness of fit achieved using only Ni₂P pathways in the theoretical model suggests that the pathways associated with the nanoparticles from **II** are primarily crystalline Ni₂P, in agreement with XRD results. The deviations in inter-atomic distance (ΔR) are lower than those observed in nanoparticles from **I** (within the 5 % error associated with this parameter), and each of the values is negative.

Comparing the samples from reactions **I** and **II**, it may be that increased reaction time and temperature results in the phosphorus-rich nature of the reaction **II** nanoparticles than reaction **I** (by ICP 29.7 at% vs 35.9 at%, respectively). This mechanism is probable: we have previously reported a similar trend of P incorporation into *fcc* Ni from TOP ligands, that shows higher P incorporation for longer reaction times and higher temperatures.¹⁹

For better understanding of the contribution from the surfactant ligands, we tuned the chemistry of the surface of the nanoparticles from **I** and **II** through

controlling the cleaning process and through ligand exchange. Three series of samples were prepared for the nanoparticles from **I** and **II**. The nanoparticles were: 1) cleaned once by adding ethanol to the as-synthesized raw solution, 2) cleaned three times with a hexane/ethanol wash, and 3) subjected to a ligand exchange with oleic acid (see supplementary online materials for the detailed process). Nanoparticles from **I** that were cleaned once resulted in a high percentage of C (70.46 at%). The number of C atoms to account for this is higher than the number of TOP molecules that can fully passivate the surface of the sample **I** nanoparticles (see the calculations in supplementary online materials). After two additional washings the C content decreases significantly (17.2 at%). If we assume that these carbons are all due to TOP molecules, this implies that the TOP molecules are bound to only 10.6 % of the Ni atoms on the surface of nanoparticles from **I** (see the calculations in supplementary online materials). The Ni/P ratio also slightly increased by 3.8 % due to the removal of TOP molecules during the two additional purification washes. However, the oleic acid ligand exchange did not further increase the Ni/P ratio from the 3× wash sample, but these ligand exchange samples did contain a higher C percentage (43.6 at%). This increased C with the same Ni/P ratio indicates that the P contribution from TOP is negligible for sample **I** since the Ni/P ratio is constant even after the ligands are replaced. For sample **II**, the ICP data shows the same amount of Ni, P, and C for the sample after all three washes and ligand exchange treatments. This implies that most of the unbound TOP ligands were washed off during the first cleaning process for sample **II** and the surface is not well covered with surfactant ligands (the surface coverage by ligands <30%, see supplementary online materials). By calculating the P

contribution from TOP based on the C content we also find that the P contribution from TOP is not a significant portion of the total P content, for both sample **I** and **II** (P from TOP/total P amount: 3.2 % for **I** and 3.95 % for **II**, see supplementary online materials)

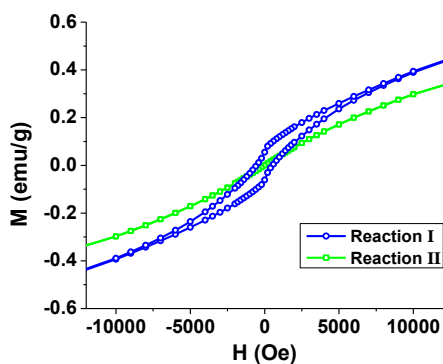


Figure 4.6 Magnetization vs. applied field hysteresis loops measured at 2 K. Blue and green lines correspond to nanoparticles from I and II, respectively. Nanoparticles from II have decreased magnetization from I, and both have significantly decreased magnetization compared to nanoparticle Ni.¹⁹

The magnetic properties of the nanoparticle samples were analyzed by performing magnetic measurements with a superconducting quantum interference device (SQUID, Quantum Design MPMS-XL) magnetometer. **Fig. 4.6** shows the magnetization versus applied-field (M vs. H) hysteresis loops for the nanoparticles from **I** and **II** at 2 K. The nanoparticles from **I** exhibit very low remnant magnetization (M_r , 0.055 emu/g) while the nanoparticles from **II** exhibit almost a zero

M_r value. Zero field cooling (ZFC) – field cooling (FC) measurements show that the blocking temperature of the nanoparticles from reaction **I** is about 7 K (**Fig. 4.7a**), while nanoparticles from reaction **II** show no blocking temperature down to 2 K (**Fig. 4.7b**). The suppressed ferromagnetic behavior of this sample (**I**) in comparison to *fcc* Ni is likely due to small grain size (~1.88 nm from Scherrer analysis) and phosphorus content. The remnant magnetization, however, is higher in **I** than in **II**, despite EXAFS modeling that shows similar stoichiometry between the samples. Nanoparticles from **II** show paramagnetic behavior based both on field dependence of the magnetization and ZFC-FC measurements. Bulk Ni₂P is known as a Pauli-paramagnetic material,⁵² however, sample **II** shows temperature dependent behavior at low temperatures (< ~250 K). To further understand the magnetic behavior of the nanoparticles from **II**, the molar susceptibility of Ni ions is plotted (**Fig. 4.7b** inset). The molar susceptibility of Ni (χ) as a function of temperature can be fit as

$$\chi(T) = \chi_o + \frac{C}{T-\theta}, \quad (1)$$

where χ_o , C , and θ are the temperature-independent susceptibility, Curie constant, and Curie-Weiss temperature, respectively. The temperature-independent susceptibility (χ_o) is associated with Pauli-paramagnetism and the second term in eq. (1) is the Curie-Weiss type susceptibility. For sample **II** the fitting parameters are: $\chi_o = 5.62 \times 10^{-5} \text{ emu} \cdot (\text{Oe} \cdot \text{mol of Ni})^{-1}$, $C = 0.0175 \text{ emu} \cdot \text{K} \cdot (\text{Oe} \cdot \text{mol of Ni})^{-1}$, and $\theta = -2.18 \text{ K}$. The effective magnetic moment per Ni ion, μ_{eff} , can be obtained from the Curie constant (C) by

$$\mu_{eff} = \left(\frac{3 k_b C}{N} \right)^{1/2}, \quad (2)$$

where k_b is the Boltzmann's constant and N is the Avogadro's number. This equation results in $\mu_{eff} = 0.374\mu_B$, where μ_B is the Bohr magneton. These residual moments are most likely due to paramagnetic impurities and/or surface states.^{52, 53} If we consider that the magnetic moments originate solely from the surface Ni atoms (only ~ 5.4 % of the total Ni atoms in sample **II** are on the surface) the effective magnetic moment per surface Ni atom is found to be: $\mu_{eff} \approx 1.61\mu_B$ (see supplementary online materials). Using this same core-surface strategy, the core Ni atoms (~ 94.6 % of the total Ni atoms) have a temperature-independent susceptibility of 5.94×10^{-5} emu \cdot (Oe \cdot mol of Ni)⁻¹. It is complicated, however, to fully resolve the origin of non-Pauli paramagnetic behaviors due to the inhomogeneous composition and unidentified impurities. Comparing two samples **I** and **II**, it may be that the nanoparticle properties may be more severely affected by the crystal structure than by the presence of phosphorus within the structure since both samples contain significant P composition despite the difference in magnetism. The exact reason for the difference in magnetic behavior between samples, however, is unclear - the positioning of the P atoms within **I** is not precisely defined. It is possible that the nanoparticles from **I** may contain small *fcc* Ni domains, which may contribute to the enhanced magnetization compared with the nanoparticles from reaction **II**. In addition, the nanoparticles from **II** contain P in slight excess.

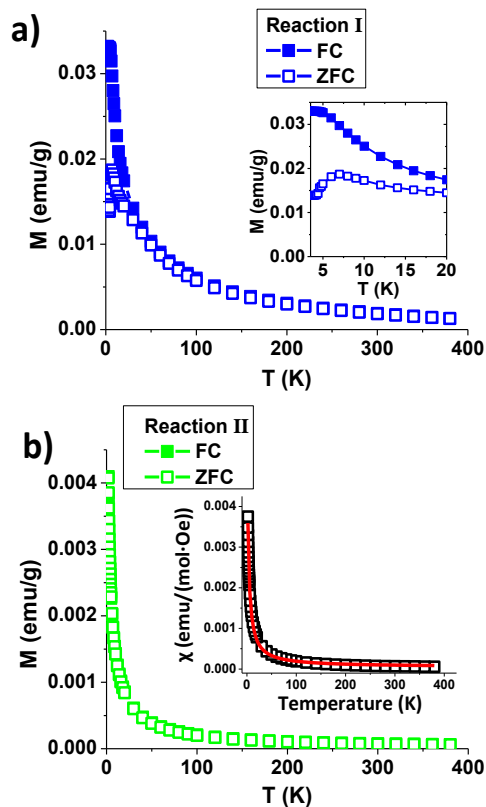


Figure 4.7 FC and ZFC magnetization curves and susceptibility plot. Temperature dependence of the magnetization for samples under a magnetic field of 100 Oe after field-cooling (filled square) and zero-field-cooling (open square) are shown for the nanoparticles from reaction (a) I and (b) II. The (b) inset is the molar susceptibility (χ) of sample II as a function of temperature. In the (b) inset, black open squares are results converted from FC measurements and the red line presents the fitted model.

4.5 Discussion

The structural offsets and disorder terms can be used to understand and classify ordering of the atoms in relation to their crystalline phases determined by XRD. **Fig. 4.8** shows the first and second shell percent deviation in distance from bulk reference values ($\Delta R/R$) for the reaction **I** and **II** nanoparticles, as well as an *fcc* Ni bulk foil.¹⁹ A decrease in inter-atomic distance is associated with nanoscale effects, however this effect is only observed in small, angstrom-sized clusters and should not be relevant to our system.⁵⁴ This means that offsets in inter-atomic distance can be interpreted as structural differences from the bulk standard phases.

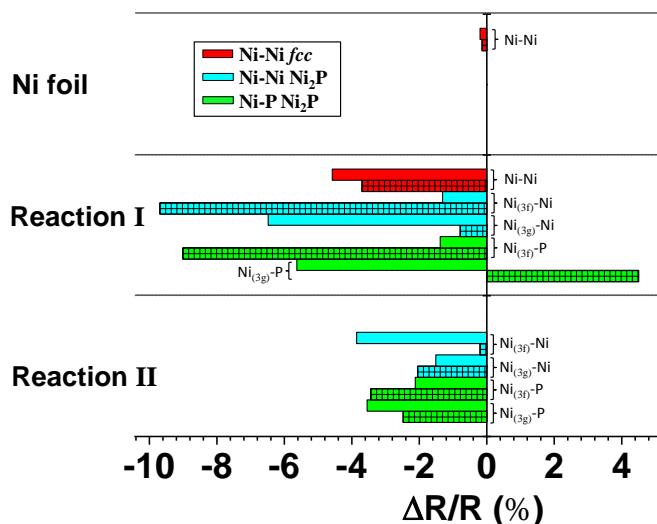


Figure 4.8 Offsets in inter-atomic distance for the modeled pathways versus bulk reference distances. First and second shell data are included; second shell data are indicated by mesh pattern. The names “Ni_(3f)” and “Ni_(3g)” represent the Ni 3f site and Ni 3g site atoms within the Ni₂P crystal structure. In particular, note the larger differences in deviations associated with the Ni₂P pathways in reaction **I**.

The nanoparticles from reaction **I** have large $\Delta R/R$ values for both *fcc* Ni (**Fig. 4.8**, red) and Ni₂P (**Fig. 4.8**, blue and green) pathways, and large σ^2 values for the *fcc* Ni pathways (see supporting information). More significantly, the standard deviation from their average (-3.72) in the Ni₂P pathway ($\Delta R/R$) values is 4.82 for reaction **I** (see **Table 4.4**) which is substantially higher than that of *fcc* Ni pathways in reaction **I** (0.62) and the *fcc* Ni pathways in the bulk foil (0.04). The standard deviation in the ($\Delta R/R$) values provides a more accurate determination of crystalline behavior since uniform ($\Delta R/R$) values would result from isotropic lattice contraction or expansion. The difference in standard deviation values may explain why there is no XRD contribution at all from Ni₂P in **I**: the standard deviation is high in comparison to the XRD-detectable phases (Reaction **I**, *fcc* Ni and Reaction **II**, Ni₂P) (**Table 4.4**). Although the *fcc* Ni pathways from **I** have a low standard deviation in $\Delta R/R$ (0.62), the mean-squared disorder values for the second shell (see supporting information) are high compared to the other Ni-Ni pathways. Greater disorder in higher-order shells is associated with amorphous structures that lack long-range order.^{43, 55} In addition, the *fcc* Ni degeneracy values (1.16) are much lower than bulk (12), meaning that the *fcc* Ni contributions within the structure are minimal. The existence of the XRD *fcc* Ni peak and its finite size domains of 1.88 nm combined with the very low degeneracy value (1.16) imply that a small percentage of the Ni atoms are arranged as *fcc* Ni. Since the majority of the Ni-Ni bonding is represented by the Ni₂P structure (as determined by XAS fitting), the average *fcc* Ni Ni-Ni degeneracy is lower than the Ni₂P Ni-Ni degeneracy. In addition, the average Ni₂P pathways for **I** have shorter Ni-Ni bonding lengths than in the bulk reference Ni₂P structure, making these bonds

intermediate between the *fcc* Ni and Ni₂P bulk structure distances, which may account for the missing *fcc* Ni degeneracies.

Table 4.4 Average $\Delta R/R$ % and standard deviation for EXAFS fitting models. For each crystal structure used in the EXAFS fitting models for reaction I and reaction II, the average and standard deviation values of $\Delta R/R$ % are reported. Note that the XRD-crystalline phases (Reaction I, *fcc* Ni and Reaction II, Ni₂P) have lower standard deviation values than the Ni₂P pathways from Reaction I. Ni foil data is included as a bulk standard of comparison.

	Ni foil	Reaction I		Reaction II
Pathway :	<i>fcc</i> Ni	<i>fcc</i> Ni	Ni ₂ P	Ni ₂ P
Average $\Delta R/R$ % :	-0.17	-4.14	-3.72	-2.40
Std. Dev. of $\Delta R/R$ % Avg. :	0.04	0.62	4.82	1.22

The nanoparticles from **II** show well-developed crystallinity based on XRD, which agrees with the offsets in interatomic distance that are observed from EXAFS modeling (**Fig. 4.8**). These offsets are all within the 5 % error associated with EXAFS interatomic distance determination. The offsets in inter-atomic distance from bulk values have a standard deviation 1.22, which is much smaller (by 4×) compared to the Ni₂P pathways from **I** (**Table 4.4**). Thus with increased heating and time, the

nanoparticles form a crystalline Ni₂P structure that is XRD detectable, and contributions from *fcc* Ni are no longer observed.

To propose the conditions under which a phase is characterized as XRD amorphous, we compare our samples' offsets in inter-atomic distance from bulk reference crystal structure values for the phases that are detectable in the Ni-P nanoparticle samples. These results, as well as those from our previous studies of the Co-P³² and Ni¹⁹ nanoparticle systems, suggest that phases within nanoparticles are detectable by XRD when standard deviations in offsets from bulk inter-atomic distances are minimized. Phases with lower standard deviations (e.g., 0.62 - 1.22) are detected as crystalline by XRD, whereas higher standard deviations (~4.82) prevent a phase from being XRD-crystalline. There must exist a threshold between these values for which a phase is no longer detected by XRD: this will be the subject of future study.

The limitations of XRD (a crystalline characterization technique) in determining amorphous phases that may be present within nanoparticle structure are apparent from our EXAFS results that display contributions not detected by XRD, such as the phosphorus present within the reaction **I** nanoparticle structure. Yet EXAFS too, has its own limitations in determining long-range crystalline order. Although we have shown that EXAFS is a method to determine crystalline behavior based on standard deviations in interatomic distance offsets, EXAFS does not display the long-range order apparent from XRD. Thus, as we demonstrate in our characterization of the amorphous and crystalline nickel phosphide nanoparticles,

these two techniques should be paired in order to obtain a complete characterization of both long-range and radial structure.

The large amount of P within the structure despite relatively low temperature synthesis conditions confirms recent synthetic protocols that show that it is still feasible for TOP to act as a phosphorus source at temperatures as low as 230 °C.¹³ Although in previous work we demonstrated that dilute P doping increases directly with reaction time and temperature,¹⁹ it is still interesting that TOP can act as a surprisingly effective phosphorus source even at these low temperatures; through our thorough characterization of the reaction I nanoparticles we show that Ni/P ratios comparable to Ni₂P can be achieved. This contrasts previous beliefs that TOP does not act as a phosphorus source below 250 °C.^{56, 57} Without higher temperatures, however, the structure cannot form into crystalline Ni₂P. It is interesting that some of the *fcc* Ni structure is retained, despite the significant phosphorus content. Clearly this result speaks to the stability of the *fcc* Ni lattice within the nanoparticle structure.

4.6 Conclusion

X-ray absorption spectra reveal that even at concentrations of phosphorus comparable to that of Ni₂P, contributions from *fcc* Ni are still detectable in amorphous samples, demonstrating the unique stability of the Ni *fcc* crystal lattice. Magnetic properties of the nanoparticles are severely affected by the nanoparticle structure, despite similar EXAFS-determined phosphorus content (local ordering) between samples. Therefore, a complete structural characterization using both long-range

techniques such as XRD, and radial structure determination from EXAFS is necessary in optimizing nanoparticles for use in magnetic and catalytic applications. Knowledge obtained from this study can be used to tune synthetic methods to obtain nanoparticles with finely controlled composition and resulting properties based on both amorphous and crystalline phases contained in nanoparticle phosphide systems.

Neither XRD nor EXAFS alone is a sufficient technique for nanoparticle characterization. Results from this Ni-P study suggest that a nanoparticle phase will not be characterizable by XRD as a crystalline phase if the $\Delta R/R$ values have standard deviations as high as ~ 4.82 . With lower standard deviations, however, (e.g. $< \sim 1.22$), phases are XRD crystalline. It should therefore be taken into consideration that there may be a significant amount of XRD amorphous structure present in nanoparticles, which is undetectable based on conventional techniques and may interfere with desired nanoparticle properties. In addition, thorough compositional characterization of the reaction **I** nanoparticles with high phosphorus content proves that TOP may serve as an effective phosphorus source even at temperatures as low as 230 °C.

4.7 References

1. Portales, H.; Goubet, N.; Saviot, L.; Adichtchev, S.; Murray, D. B.; Mermet, A.; Duval, E.; Pileni, M. P. *Proc. Natl. Acad. Sci. U. S. A.* **2008**, 105, 14784-14789.
2. Anthony, R.; Kortshagen, U. *Phys. Rev. B* **2009**, 80, 115407.
3. Guo, Y.; Zhang, J.; Yang, L.; Wang, H.; Wang, F.; Zheng, Z. *Chem. Commun.* **2010**, 46, 3493-3495.
4. Tang, Y.; Ouyang, M. *Nat. Mater.* **2007**, 6, 754-759.
5. Barnes, C. A.; Elsaesser, A.; Arkusz, J.; Smok, A.; Palus, J.; Leśniak, A.; Salvati, A.; Hanrahan, J. P.; Jong, W. H. d.; Dziubałtowska, E. b.; Stępnik, M.; Rydzyński, K.; McKerr, G.; Lynch, I.; Dawson, K. A.; Howard, C. V. *Nano Lett.* **2008**, 8, 3069-3074.
6. Portalès, H.; Goubet, N.; Saviot, L.; Yang, P.; Sirotkin, S.; Duval, E. n.; Mermet, A.; Pileni, M.-P. *ACS Nano* **2010**, 4, 3489-3497.
7. Shu, Y.; Oyama, S. T. *Chem. Commun.* **2005**, 1143-5.
8. Senevirathne, K.; Burns, A. W.; Bussell, M. E.; Brock, S. L. *Adv. Funct. Mater.* **2007**, 17, 3933-3939.
9. Wang, X.; Clark, P.; Oyama, S. T. *J. Catal.* **2002**, 208, 321-331.
10. Oyama, S. T. *J. Catal.* **2003**, 216, 343-352.
11. Oyama, S. T.; Gott, T.; Zhao, H.; Lee, Y.-K. *Catal. Today* **2009**, 143, 94-107.

12. Murray, C. B.; Norris, D. J.; Bawendi, M. G. *J. Am. Chem. Soc.* **1993**, 115, 8706-8715.
13. Muthuswamy, E.; Savithra, G. H. L.; Brock, S. L. *ACS Nano* **2011**, 5, 2402-2411.
14. Park, J.; Kang, E.; Son, S. U.; Park, H. M.; Lee, M. K.; Kim, J.; Kim, K. W.; Noh, H.-J.; Park, J.-H.; Bae, C. J.; Park, J.-G.; Hyeon, T. *Adv. Mater.* **2005**, 17, 429-434.
15. Henkes, A. E.; Vasquez, Y.; Schaak, R. E. *J. Am. Chem. Soc.* **2007**, 129, 1896-1897.
16. Wang, J.; Johnston-Peck, A. C.; Tracy, J. B. *Chem. Mater.* **2009**, 21, 4462-4467.
17. Chiang, R.-K.; Chiang, R.-T. *Inorg. Chem.* **2007**, 46, 369-371.
18. Carenco, S.; Boissiere, C.; Nicole, L.; Sanchez, C.; Le, F. P.; Mezailles, N. *Chem. Mater.* **2010**, 22, 1340-1349.
19. Moreau, L. M.; Ha, D.-H.; Bealing, C. R.; Zhang, H.; Hennig, R. G.; Robinson, R. D. *Nano Lett.* **2012**, 12, 4530-4539.
20. Carenco, S.; Le Goff, X. F.; Shi, J.; Roiban, L.; Ersen, O.; Boissière, C.; Sanchez, C.; Mézailles, N. *Chem. Mater.* **2011**, 23, 2270-2277.
21. Arugute, D. M.; Marcus, M. A.; Li, L. S.; Williamson, A.; Fakra, S.; Gygi, F.; Galli, G. A.; Alivisatos, A. P. *J. Phys. Chem. C* **2007**, 111, 75-79.

22. Marcus, M. A.; Flood, W.; Stiegerwald, M.; Brus, L.; Bawendi, M. *J. Phys. Chem.* **1991**, *95*, 1572-1576.
23. Cheng, G.; Carter, J. D.; Guo, T. *Chem. Phys. Lett.* **2004**, *400*, 122-127.
24. Park, J.-I.; Kim, M. G.; Jun, Y.-W.; Lee, J. S.; Lee, W.-R.; Cheon, J. *J. Am. Chem. Soc.* **2004**, *126*, 9072-9078.
25. Sarma, L. S.; Chen, C.-H.; Kumar, S. M. S.; Wang, G.-R.; Yen, S.-C.; Liu, D.-G.; Sheu, H.-S.; Yu, K.-L.; Tang, M.-T.; Lee, J.-F.; Bock, C.; Chen, K.-H.; Hwang, B.-J. *Langmuir* **2007**, *23*, 5802-5809.
26. Rodriguez, J. A.; Hanson, J. C.; Kim, J.-Y.; Liu, G.; Iglesias-Juez, A.; Fernandez-Garcia, M. *J. Phys. Chem. B* **2003**, *107*, 3535-3543.
27. Rockenberger, J.; Troeger, L.; Kornowski, A.; Vossmeier, T.; Eychmueller, A.; Feldhaus, J.; Weller, H. *J. Phys. Chem. B* **1997**, *101*, 2691-2701.
28. Frenkel, A. I.; Hills, C. W.; Nuzzo, R. G. *J. Phys. Chem. B* **2001**, *105*, 12689-12703.
29. Bunker, G., *Introduction to XAFS: a practical guide to X-ray absorption fine structure spectroscopy*. Cambridge University Press: Cambridge, 2010; p 260.
30. Stern, E. A. *Phys. Rev. B* **1974**, *10*, 3027-37.
31. Stern, E. A. *Contemp. Phys.* **1978**, *19*, 289-310.
32. Ha, D.-H.; Moreau, L. M.; Bealing, C. R.; Zhang, H.; Hennig, R. G.; Robinson, R. D. *J. Mater. Chem.* **2011**, *21*, 11498-11510.

33. Carenco, S.; Labouille, S.; Bouchonnet, S.; Boissière, C.; Le Goff, X.-F.; Sanchez, C.; Mézailles, N. *Chem. Eur. J.* **2012**, 18, 14165-14173.
34. Ravel, B.; Newville, M. *J. Synchrotron Radiat.* **2005**, 12, 537-541.
35. Ravel, B.; Kelly, S. D. *AIP Conf. Proc.* **2007**, 882, 150-152.
36. Scott, R., *Physical Methods in Bioinorganic Chemistry: Spectroscopy and Magnetism*. University Science Books: 2000.
37. Yin, Y. D.; Rioux, R. M.; Erdonmez, C. K.; Hughes, S.; Somorjai, G. A.; Alivisatos, A. P. *Science* **2004**, 304, 711-714.
38. Carenco, S.; Resa, I.; Le, G. X.; Le, F. P.; Mezailles, N. *Chem. Commun.* **2008**, 2568-2570.
39. Voevodin, A. A.; O'Neill, J. P.; Zabinski, J. S. *Thin Solid Films* **1999**, 342, 194-200.
40. Schrunner, M.; Polzer, F.; Mei, Y.; Lu, Y.; Haupt, B.; Ballauff, M.; Gödel, A.; Drechsler, M.; Preussner, J.; Glatzel, U. *Macromol. Chem. Phys.* **2007**, 208, 1542-1547.
41. Goto, Y.; Taniguchi, K.; Omata, T.; Otsuka-Yao-Matsuo, S.; Ohashi, N.; Ueda, S.; Yoshikawa, H.; Yamashita, Y.; Oohashi, H.; Kobayashi, K. *Chem. Mater.* **2008**, 20, 4156-4160.
42. Blanchard, P. E. R.; Grosvenor, A. P.; Cavell, R. G.; Mar, A. *J. Mater. Chem.* **2009**, 19, 6015-6022.

43. Song, J.; Wei, Z.; Pan, Z.; Xie, Z.; Wei, S. *AIP Conf. Proc.* **2007**, 882, 453-456.
44. Li, H.; Wang, W.; Li, H.; Deng, J.-F. *J. Catal.* **2000**, 194, 211-221.
45. Okamoto, Y.; Nitta, Y.; Imanaka, T.; Teranishi, S. *J. Chem. Soc., Faraday Trans. 1* **1979**, 75, 2027-39.
46. Cezar, J.; uacute;lio, C.; Tolentino, H.; eacute;lio, C. N.; Knobel, M. *Phys. Rev. B* **2003**, 68, 054404.
47. Rundqvist, S. *Acta Chem. Scand.* **1962**, 16, 992-998.
48. Häglund, J.; Fernández Guillermet, A.; Grimvall, G.; Körling, M. *Phys. Rev. B* **1993**, 48, 11685.
49. Colpas, G. J.; Maroney, M. J.; Bagyinka, C.; Kumar, M.; Willis, W. S.; Suib, S. L.; Mascharak, P. K.; Baidya, N. *Inorg. Chem.* **1991**, 30, 920-8.
50. Hatsui, T.; Takata, Y.; Kosugi, N. *J. Synchrotron Radiat.* **1999**, 6, 376-378.
51. Seo, H.-R.; Cho, K.-S.; Kim, S.-H.; Lee, Y.-K. *J. Korean Phys. Soc.* **2010**, 56, 2083-2087.
52. Zeppenfeld, K.; Jeitschko, W. *J. Phys. Chem. Solids* **1993**, 54, 1527-1531.
53. Park, J.; Koo, B.; Yoon, K. Y.; Hwang, Y.; Kang, M.; Park, J.-G.; Hyeon, T. *J. Am. Chem. Soc.* **2005**, 127, 8433-8440.
54. Arcon, I.; Tuel, A.; Kodre, A.; Martin, G.; Barbier, A. *J. Synchrotron Radiat.* **2001**, 8, 575-577.

55. Sprouster, D. J.; Giulian, R.; Araujo, L. L.; Kluth, P.; Johannessen, B.; Cookson, D. J.; Foran, G. J.; Ridgway, M. C. *J. Appl. Phys.* **2010**, 107, 014313-10.
56. Brock, S. L.; Senevirathne, K. *J. Solid State Chem.* **2008**, 181, 1552-1559.
57. Seo, H.-R.; Cho, K.-S.; Lee, Y.-K. *Mater. Sci. Eng., B* **2011**, 176, 132-140.

APPENDIX C

C SUPPLEMENTARY INFORMATION FOR CHAPTER 4

Experimental Section

General Synthesis Procedures.

Synthesis of the nickel phosphide nanoparticles (NPs) was based on thermal decomposition of a Ni-TOP complex as outlined by Muthuswamy et. al.¹ The reaction was run in a one-pot strategy using standard Schlenk line and glove box techniques in a dry, oxygen-free di-nitrogen atmosphere. Ethanol ($\geq 99.5\%$), oleylamine (70%), nickel acetylacetonate ($\text{Ni}(\text{acac})_2$, 95%) and dioctyl ether (99%) were purchased from Aldrich. Tri-*n*-octylphosphine (TOP, 97%) was purchased from STREM Chemicals. Ni and P precursors ($\text{Ni}(\text{acac})_2$ and TOP, respectively) were combined with 10 mL of octyl ether (solvent) and oleylamine (surfactant). The resulting solution was heated using a heating mantle with temperature controller and attached thermocouple to ensure temperature stability. Ni:P precursor ratios, temperature, reaction time, and oleylamine concentration were varied between samples. The specific conditions used in the synthesis of the two samples are outlined in **Table C.1**. The Ni/P ratio is identical for reaction **I** and **II** but the temperature and time were increased for reaction **II** and solvent and surfactant concentration were varied.

At the end of the reaction the flask containing the reaction solution was removed from the heating mantle and the nanoparticle products were isolated by centrifugation with

excess ethanol. The centrifugation process was repeated to ensure removal of excess reactant molecules.

Transmission Electron Microscopy

TEM images of the nanoparticle samples were obtained using a FEI Tecnai T12 microscope operating at 120 keV. At least 200 particles were analyzed per sample to obtain a representative size distribution.

High-Angle Annular Dark-field Scanning Transmission Electron Microscopy

STEM images of the nanoparticles were obtained using a FEI Tecnai F20 microscope operating at 200 keV. Elastically scattered electrons were collected using a high-angle annular dark field detector with a 150 mm camera length.

X-ray Diffraction

XRD (X-ray diffraction) diffraction patterns were collected using a Scintag theta-theta x-ray diffractometer (Cu K α radiation). The step size of the XRD scans was 0.02 degrees and the scan rate was 0.3 degrees/min. Average grain sizes with the nanoparticle samples were determined from the XRD spectra using the Scherrer equation.

Inductively Coupled Plasma

ICP-OES (Inductively coupled plasma optical emission spectroscopy) results were obtained from Columbia Analytical Services. Samples from reactions **I** and **II** were first characterized with TEM and XRD, and then shipped for ICP analysis. The Ni

data was collected using a wavelength of 231.604 nm and P using a wavelength of 214.914 nm. The RSD % (relative standard deviation) associated with the data collection was 5.7 %.

X-ray Absorption Spectroscopy

XAS spectra of the nickel phosphide nanoparticle samples were obtained at the C1 station of the Cornell High Energy Synchrotron Source (CHESS) using a Si (220) monochromator and fluorescence detection to probe the nickel K-edge (8333 eV). Data was obtained over the energy range from 8280 eV to 8780 eV, in order to include both the XANES and EXAFS regions. A cobalt filter was used in order to control signal level. To prevent precipitation and obtain a homogeneously-thick sample such that XAS spectra with a constant intensity signal could be achieved, the nanoparticle samples were drop-casted between two pieces of Kapton tape. Five to six scans were obtained per sample using 15 minute scans over three regions with varying step size (pre-edge region 5.0 eV, edge region 1.0 eV, and EXAFS region 3.0 eV). Self-absorption was not a concern with the fluorescence detection because the samples were sufficiently dilute in solution. The fluorescence measurements are proportional to the absorption coefficient, $\mu(E)$, which produces a spectrum describing the strength of X-ray absorption as a function of energy.² The scans were then averaged together to enhance the smoothness and ensure data consistency. Transmission detection was simultaneously used to probe the K-edge of a Ni metal foil during each of the scans, to function as a standard for comparison and edge calibration.

The raw spectra were averaged and processed using ATHENA,³ part of the IFEFFIT software package. Data processing involved edge determination from the first inflection point in the absorption data, background subtraction using the AUTOBK algorithm, and normalization of the EXAFS modulations (greater than 50 eV above the edge).⁴ The spectra were converted from energy-space to k-space, then underwent a phase shift specific to the absorbing and scattering elements.² A k-weight of 1 was chosen in order to best observe the scattering of phosphorus, a low-Z scattering element.⁵ Nickel is also a lower-scattering element,⁵ and when a k-weight of 1 was used the intensity modulations were evenly distributed through the k-space region of interest (0–10 Å⁻¹), indicating an appropriate weighting was applied.⁵ The spectra was then Fourier Transformed into R-space.² In R-space each peak appears at the relative spacing of that particular shell from the scattering atom, which enables visualization of the relative contributions as a function of inter-atomic distance.⁴ The data was then analyzed by the ab-initio method and multiple data set fitting in k-space and R-space using ARTEMIS.³ Crystal structures from theory were inputted using ATOMS.⁶ By fitting well-matched theoretical pathways to the experimental spectra through loosening variables to deviate from the theoretical bulk structures, specific structural information could be determined including coordination number, inter-atomic spacing and mean-squared disorder, as outlined in the EXAFS equation.^{4, 7, 8, 9}

$$\chi(k) = \sum_{\Gamma} \left[\frac{N_{\Gamma} S_{\Gamma}^2 F_{\Gamma}(k)}{2kR_{\Gamma}^2} e^{-2k^2\sigma_{\Gamma}^2} e^{-2R_{\Gamma}/\lambda(k)} \times \sin(2kR_{\Gamma} + \phi_{\Gamma}(k)) \right] \quad (1)$$

Γ is the summation over the individual scattering pathways, k is the photoelectron wavevector, $F_{\Gamma}(k)$ is the scattering amplitude, $\lambda(k)$ is the mean free path of inelastically-scattered photoelectrons and $\Phi(k)$ is the phase shift, which is calculated as a function of the absorbing and scattering atom. S_0^2 , the amplitude reduction factor, was set to 0.754 during fitting (the value extracted from fitting the Ni foil). This enables a more accurate determination of the coordination number.⁸ Degeneracy (N_{Γ}), half-path length (R_{Γ}), energy shift parameter (E_0), and mean-squared disorder (σ_{Γ}^2), which includes contributions from structural and thermal disorder (Debye-Waller factor),⁴ were allowed to float during the fit in order to extract the values specific to each nanoparticle sample. ΔE_0 was fixed to a single variable for all pathways with the same absorbing and scattering element in order to limit the number of variables, as ΔE_0 values should be nearly equal for similar bonds within the structure.¹⁰

The EXAFS spectra were fit with a theoretical model in R-space and k-space in order to extract accurate parameters for the average radial structure around a central core Ni atom. Each fitting model resulted in an “R-factor” value between 0.005 and 0.012 in R-space and between 0.02 and 0.04 in k-space. The R-factor value is a statistical measurement which is minimized in order to ensure quality of the fit, where a value less than 0.05 is commonly referred to as a good fit. The minimization of this statistical factor proves that our best-fit models are well-correlated to the experimental data.

Ligand Exchange

The ligand exchange method is similar to the standard procedures.¹¹ Ligand exchange was performed on the as-synthesized sample **II** (crystalline Ni₂P nanoparticles) to study the potential effects of TOP surface ligands on elemental analysis. Synthesized Ni nanoparticles were re-dispersed in 8 mL of oleic acid in a 25 mL flask. The solution was kept at 100 °C under di-nitrogen atmosphere. After heating for 2 hours, the solution was cooled down by removing the heating mantle and sample **II** nanoparticles were purified by centrifugation with excess ethanol. The supernatant was decanted and the nanoparticles were re-dispersed in hexanes. This precipitation/re-dispersion process was performed twice overall to ensure removal of excess organic species.

Magnetic measurements

The magnetic properties of the nanoparticle samples were analyzed by performing magnetic measurements using a superconducting quantum interference device (SQUID, Quantum Design MPMS – XL) magnetometer.

EXAFS models

Fit using Ni *fcc* pathways and Ni₂P pathways for reaction I

Table C.1: Pathway parameters for reaction I fitting model. The Ni *fcc* and Ni₂P pathway parameters used to construct the best-fit EXAFS model for reaction I are listed. These parameters correspond with the fitting results shown in **Fig. 5.5a**.

Single Scattering Pathways from Ni							
Pathway	N (acc.)	N (exp.)	R (Å)	ΔR (Å)	R + ΔR (Å)	E ₀ (eV)	σ ² (Å ²) x 10 ⁻³
Ni - Ni (shell 1)	12	1.16	2.49	-0.114	2.38	-9.93	8.45
Ni - Ni (shell 2)	6	0.57	3.52	-0.130	3.39	-9.93	17.5
Ni - Ni (shell 3)	24	2.28	4.32	-0.130	4.19	-9.93	17.5
Ni - Ni (shell 4)	12	1.14	4.98	-0.130	4.85	-9.93	17.5
Ni - Ni (shell 5)	24	2.28	5.57	-0.130	5.44	-9.93	17.5
Single Scattering Pathways from Ni ₂ P crystal structure							
Pathway	N (acc.)	N (exp.)	R (Å)	ΔR (Å)	R + ΔR (Å)	E ₀ (eV)	σ ² (Å ²) x 10 ⁻³
Ni _(3f) - Ni	5	4.07	2.79	-0.037	2.76	-9.93	7.23
Ni _(3g) - Ni	6	7.36	2.92	-0.189	2.73	-9.93	7.08
Ni _(3f) - P	2	1.24	2.24	-0.031	2.21	-9.98	4.25
Ni _(3g) - P	2.5	4.16	2.44	-0.137	2.30	-9.98	4.62
Ni _(3f) - Ni (shell 2)	2	1.85	3.83	-0.371	3.46	-9.93	1.18
Ni _(3f) - Ni (shell 3)	5	4.63	4.29	-0.371	3.92	-9.93	1.18
Ni _(3f) - Ni (shell 4)	2	1.85	4.75	-0.371	4.38	-9.93	1.18
Ni _(3f) - Ni (shell 5)	4	5.45	5.11	-0.003	5.10	-9.93	1.01
Ni _(3f) - Ni (shell 6)	5	6.19	5.46	-0.003	4.55	-9.93	1.01
Ni _(3g) - Ni (shell 2)	1	1.12	4.10	-0.033	4.07	-9.93	7.30
Ni _(3g) - Ni (shell 3)	3	3.36	4.30	-0.033	4.27	-9.93	7.30
Ni _(3g) - Ni (shell 4)	6	6.72	4.64	-0.033	4.60	-9.93	7.30
Ni _(3g) - Ni (shell 5)	2	1.24	5.32	0.187	5.51	-9.93	11.0
Ni _(3g) - Ni (shell 6)	4	2.48	5.45	0.187	5.64	-9.93	11.0
Ni _(3f) - P (shell 2)	1	0.99	3.70	-0.334	3.37	-9.98	10.2
Ni _(3f) - P (shell 3)	2	1.99	4.04	-0.334	3.71	-9.98	10.2
Ni _(3f) - P (shell 4)	2	1.99	4.71	-0.334	4.37	-9.98	10.2
Ni _(3f) - P (shell 5)	2	1.06	5.02	0.306	5.32	-9.98	9.24
Ni _(3f) - P (shell 6)	1	0.53	5.29	0.306	5.60	-9.98	9.24
Ni _(3f) - P (shell 7)	2	1.06	5.52	0.306	5.83	-9.98	9.24
Ni _(3g) - P (shell 2)	0.5	0.62	3.49	0.157	3.65	-9.98	11.0
Ni _(3g) - P (shell 3)	1	1.24	4.13	0.157	4.29	-9.98	11.0
Ni _(3g) - P (shell 4)	2	2.48	4.46	0.157	4.62	-9.98	11.0

Ni _(3g) - P (shell 5)	4	6.87	5.06	0.094	5.16	-9.98	9.43
Ni _(3g) - P (shell 6)	2	3.43	5.38	0.094	5.47	-9.98	9.43

Fit using Ni₂P pathways for reaction II

Table C.2: Pathway parameters for reaction II fitting model. The Ni₂P pathway parameters used to construct the best-fit EXAFS model for reaction II are listed.

These parameters correspond with the fitting results shown in **Fig. 5.5b**.

Single Scattering Pathways from Ni ₂ P crystal structure							
Pathway	N (acc.)	N (exp.)	R (Å)	ΔR (Å)	R + ΔR (Å)	E ₀ (eV)	σ ² (Å ²) x 10 ⁻³
Ni _I - Ni	5	5.12	2.79	-0.115	2.68	-3.63	8.10
Ni _{II} - Ni	6	5.99	2.92	-0.044	2.88	-3.63	7.22
Ni _I - P	2	1.96	2.24	-0.047	2.19	-1.94	3.49
Ni _{II} - P	3	2.82	2.61	-0.086	2.53	-1.94	4.85
Ni _I - Ni (shell 2)	2	2.04	3.83	-0.008	3.82	-3.63	9.90
Ni _I - Ni (shell 3)	5	5.10	4.29	-0.008	4.28	-3.63	9.90
Ni _I - Ni (shell 4)	2	2.04	4.75	-0.008	4.74	-3.63	9.90
Ni _I - Ni (shell 5)	4	4.08	5.11	-0.008	5.10	-3.63	9.90
Ni _I - Ni (shell 6)	5	5.10	5.46	-0.008	5.45	-3.63	9.90
Ni _{II} - Ni (shell 2)	1	1.00	4.10	-0.084	4.02	-3.63	10.8
Ni _{II} - Ni (shell 3)	3	2.99	4.30	-0.084	4.22	-3.63	10.8
Ni _{II} - Ni (shell 4)	6	5.99	4.64	-0.084	4.55	-3.63	10.8
Ni _{II} - Ni (shell 5)	2	2.00	5.32	-0.084	5.23	-3.63	10.8
Ni _{II} - Ni (shell 6)	4	3.99	5.45	-0.084	5.36	-3.63	10.8
Ni _I - P (shell 2)	1	0.98	3.70	-0.128	3.58	-1.94	9.02
Ni _I - P (shell 3)	2	1.96	4.04	-0.128	3.91	-1.94	9.02
Ni _I - P (shell 4)	2	1.96	4.71	-0.128	4.58	-1.94	9.02
Ni _I - P (shell 5)	2	1.96	5.02	-0.128	4.89	-1.94	9.02
Ni _I - P (shell 6)	1	0.98	5.30	-0.128	5.17	-1.94	9.02
Ni _I - P (shell 7)	2	1.96	5.52	-0.128	5.39	-1.94	9.02
Ni _{II} - P (shell 2)	1	0.95	4.13	0.133	4.26	-1.94	9.43
Ni _{II} - P (shell 3)	2	1.89	4.46	0.133	4.60	-1.94	9.43
Ni _{II} - P (shell 4)	4	3.79	5.06	0.133	5.20	-1.94	9.43
Ni _{II} - P (shell 5)	2	1.89	5.38	0.133	5.51	-1.94	9.43

Atomic percentage contribution calculations

Atomic percentage contribution is calculated based on the degeneracy values extracted from the experimental spectra. The specific degeneracy value (*e.g.*, Ni contribution in the Ni₂P structure) is divided by the total degeneracy values to determine the atomic percentage contribution.

The percentage P atoms in Ni₂P positions from reaction **I** shown in **Table 4.3** were determined as follows:

From the experimental data shown in **Table C.1** (using first 3 shells):

$$N_{\text{Ni-P}} \text{ (Total degeneracy of Ni-P)} = 1.24415 + 4.163 + 0.9932 + 1.9863 + 0.6208 + \\ 1.2416 + 2.4833 = 12.7324$$

$$N_{\text{Ni-Ni}} \text{ (Total degeneracy of Ni-Ni)} = 1.1584 + 0.571 + 2.284 + 4.072 + 7.3598 + \\ 1.8506 + 4.6266 + 1.1196 + 3.3588 = 26.4008$$

Now, plugging into the equation to determine atomic percentage:

$$\Sigma(N_{\text{Ni-P}}) / \Sigma(N_{\text{Ni-P}} + N_{\text{Ni-Ni}}) = \mathbf{32.5} \text{ at. \% P (ICP results were 29.7\%)}$$

The error magnitude of the atomic percentage contribution can be calculated based on $\pm 10\%$ error bar of degeneracy values.¹²

$$N_{\text{Ni-P}} \text{ is a minimum where: } N_{\text{Ni-P, min}} = N_{\text{Ni-P}} - 0.1(N_{\text{Ni-P}}) = 11.45916$$

$$N_{\text{Ni-P}} \text{ is a maximum where: } N_{\text{Ni-P, max}} = N_{\text{Ni-P}} + 0.1(N_{\text{Ni-P}}) = 14.0056$$

$$N_{\text{Ni-Ni}} \text{ is a minimum where: } N_{\text{Ni-Ni, min}} = N_{\text{Ni-Ni}} - 0.1(N_{\text{Ni-Ni}}) = 23.76072$$

$$N_{\text{Ni-Ni}} \text{ is a maximum where: } N_{\text{Ni-Ni, max}} = N_{\text{Ni-Ni}} + 0.1(N_{\text{Ni-Ni}}) = 29.04088$$

Using these values, the maximum and minimum atomic phosphorus percentage can be determined.

$$\text{Minimum possible atomic P \%: } \Sigma(N_{\text{Ni-P, min}}) / \Sigma(N_{\text{Ni-P, min}} + N_{\text{Ni-Ni, max}}) = 28.3\%$$

$$\text{Maximum possible atomic P \%: } \Sigma(N_{\text{Ni-P, max}}) / \Sigma(N_{\text{Ni-P, max}} + N_{\text{Ni-Ni, min}}) = 37.1\%$$

Thus, the atomic % P in the Ni NP sample is: **32.5 % \pm 4.7 %**

The atomic percentages of Ni atoms in *fcc* positions and Ni atoms in Ni₂P positions were calculated from the degeneracy values in the same manner. The atomic P percent was used in order to provide a sample calculation. The atomic percentages present from reaction **II** were also calculated by this method.

The calculation for the ligand coverage of nanoparticles (NPs)

The number of surface atoms is calculated based on the ratio of the atomic shell volume to the core volume. The number of ligands also can be estimated by the Carbon atomic % measured by ICP. Then the ligand coverage is calculated by comparing the number of the surface atoms and the number of the ligands.

Nickel has *fcc* crystal structure with 0.352 nm lattice parameter. The size of our nanoparticle sample **I** is 9 nm (radius: 4.5 nm).

Volume of the Core:

$$V_{core} = \frac{4}{3}\pi(4.5 - 0.176)^3 = 3.386 \times 10^2 \text{ nm}^3$$

Volume of the total NP:

$$V_{tot} = \frac{4}{3}\pi(4.5)^3 = 3.817 \times 10^2 \text{ nm}^3$$

Volume of the Shell:

$$V_{shell} = V_{tot} - V_{core} = 3.817 \times 10^2 - 3.386 \times 10^2 = 43.05 \text{ nm}^3$$

Volume of unit cell: $V_{unit\ cell} = (0.352)^3 = 4.3614 \times 10^{-2} \text{ nm}^3$

Number of unit cells in shell: $Unitcells_{shell} = \frac{V_{shell}}{V_{unit}} = \frac{43.05}{4.3614 \times 10^{-2}} = 987.2$

Atoms in shell: $987.2 \times 4 = 3948$

Number of unit cells in total: $Unitcells_{total} = \frac{V_{tot}}{V_{unit}} = \frac{381.7}{4.3614 \times 10^{-2}} = 8751.8$

Atoms in total: $8751.8 \times 4 = 35,007$

Fraction on the surface: $= 3948/35007 = 0.1128 = 11.28 \%$

If we consider Ni_2P structure instead of *fcc* Ni, the fraction on the surface would be 10.9 %.

Table C.3. ICP results of the sample I, washed once.

Ni at%	P at%	C at%
21.4	8.09	70.46

Among Ni and P atoms, 72.6% ($= \frac{21.4}{21.4+8.09}$) are Ni atoms

Therefore, total number of Ni atoms on the shell is $0.726 \times 3948 = 2867$

When we assume that each Ni atom on the surface bind to one TOP molecule, there are 68,807 ($=2867 \times 24$) Carbon atoms since one TOP molecule has 24 Carbon atoms.

The C/(Ni+P) ratio from ICP results is 2.386 so the number of Carbon atoms is 83,517 ($=35007 \times 2.386$) which is $\sim 21\%$ higher than the sample I NP fully passivated by TOP molecules. Therefore, the sample washed once has unbound TOP molecules and/or other organic species.

Table C.4. ICP results of the sample I, washed three times.

Ni at%	P at%	C at%
60.7	22.1	17.2

The C/(Ni+P) ratio is 0.208, then the number of Carbon atoms are 7283 ($=35,007 \times 0.208$).

If we assume that 7283 atoms are from TOP molecules, the number of TOP molecules is 303 ($=7283/24$).

This is only ~10.6% of the number of Ni atoms on the surface (2867) implying the coverage of surfactant ligand by the surface of NP is ~10.6%.

This indicates that two additional washing processes wash off the significant amount of TOP molecules. Due to this removal of TOP molecules, the P/Ni ICP ratio dropped from 0.377 (washed once) to 0.365 (washed three times) during additional cleaning.

Table C.5. ICP results of the sample I, ligand exchanged with Oleic acid.

Ni at%	P at%	C at%
41.3	15.1	43.6

The C/(Ni+P) ratio is 0.774, then the number of Carbon atoms are 27109 ($=35,007 \times 0.774$).

If we assume that all the TOP molecules are replaced by oleic acids, the number of Oleic acid molecules is 1506 ($=27109/18$).

Then the coverage by Oleic acid would be ~52.5%.

The P/Ni ratio was not changed significantly after ligand exchanged (~ 0.365).

Calculations of the P contribution originated from TOP contribution

Sample I

Based on the ICP results (**Table C.4**), the atomic % of P and C are 22.1 at % and 17.2 at %, respectively. If we assume that the C atoms are all originate from TOP, the atomic percentage of P from TOP is calculated as 0.71 at % ($= \frac{17.2 \text{ at \%}}{24}$) since each TOP molecule has 24 Carbons and one P atom. Therefore, the P contribution originating from TOP for the total P content in the sample is calculated as 3.24 % ($0.0324 = \frac{0.71 \text{ at \%}}{22.1 \text{ at \%}}$).

Sample II

Based on the ICP results, the atomic % of P and C are 27.5 at % and 26.1 at %, respectively. If we assume that the C atoms are all originate from TOP, the atomic percentage of P from TOP is calculated as 1.09 at % ($= \frac{26.1 \text{ at \%}}{24}$) since each TOP molecule has 24 Carbons and one P atom. Therefore, the P contribution originating from TOP for the total P content in the sample is calculated as 3.95 % ($0.0395 = \frac{1.09 \text{ at \%}}{27.5 \text{ at \%}}$).

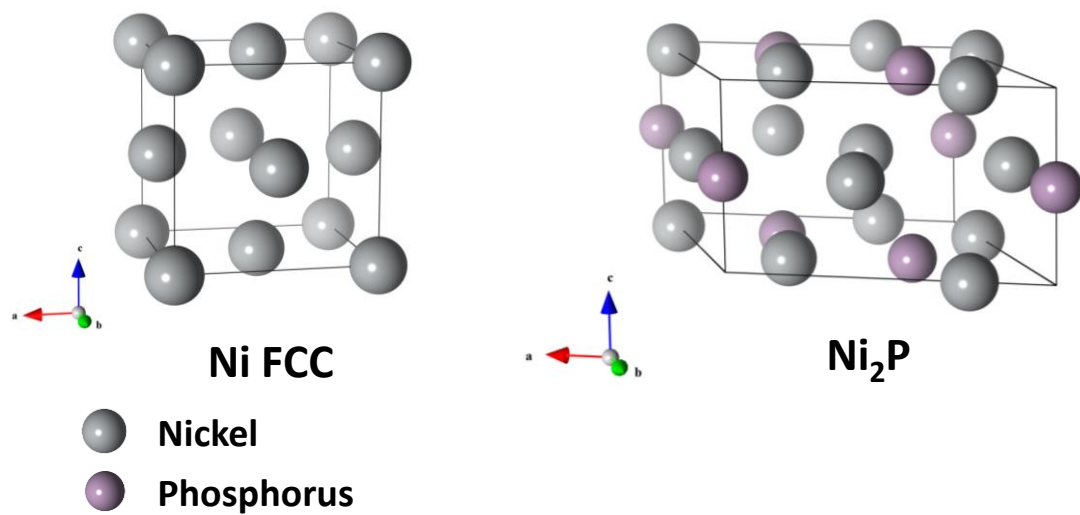


Fig. C.1: Unit cell of crystal structures used in EXAFS modeling. (left) Crystal structure of *fcc* Ni. (right) Crystal structure of Ni₂P. Grey ball and purple ball indicate Ni and P atoms respectively.

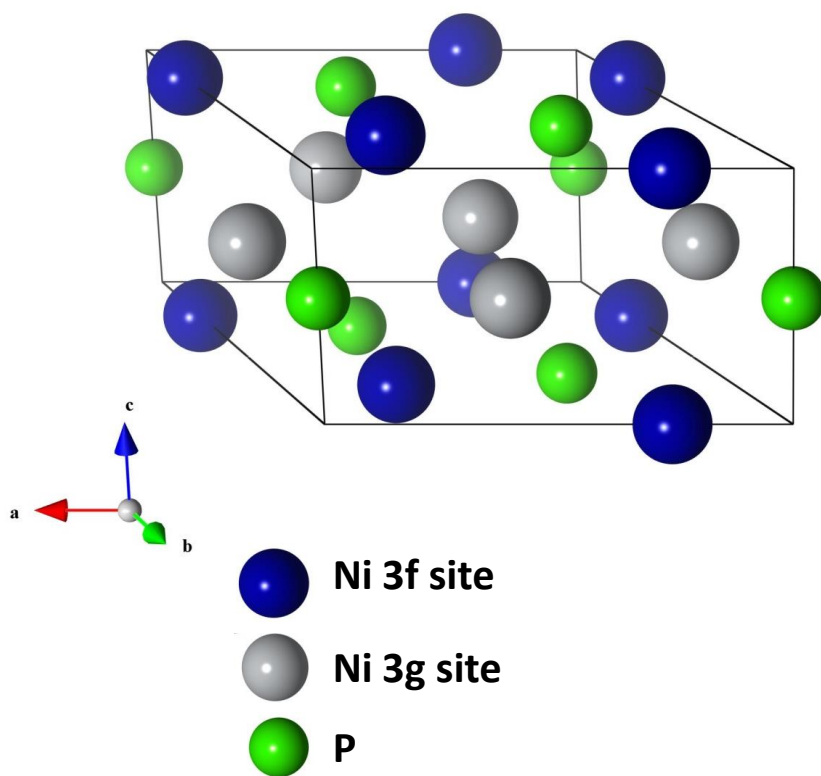


Fig. C.2: Placement of Ni 3f site and Ni 3g site atoms in the Ni_2P crystal structure. Phosphorus atoms are indicated in green, and the blue and gray spheres correspond to Ni 3f site and Ni 3g site atom positions, respectively.

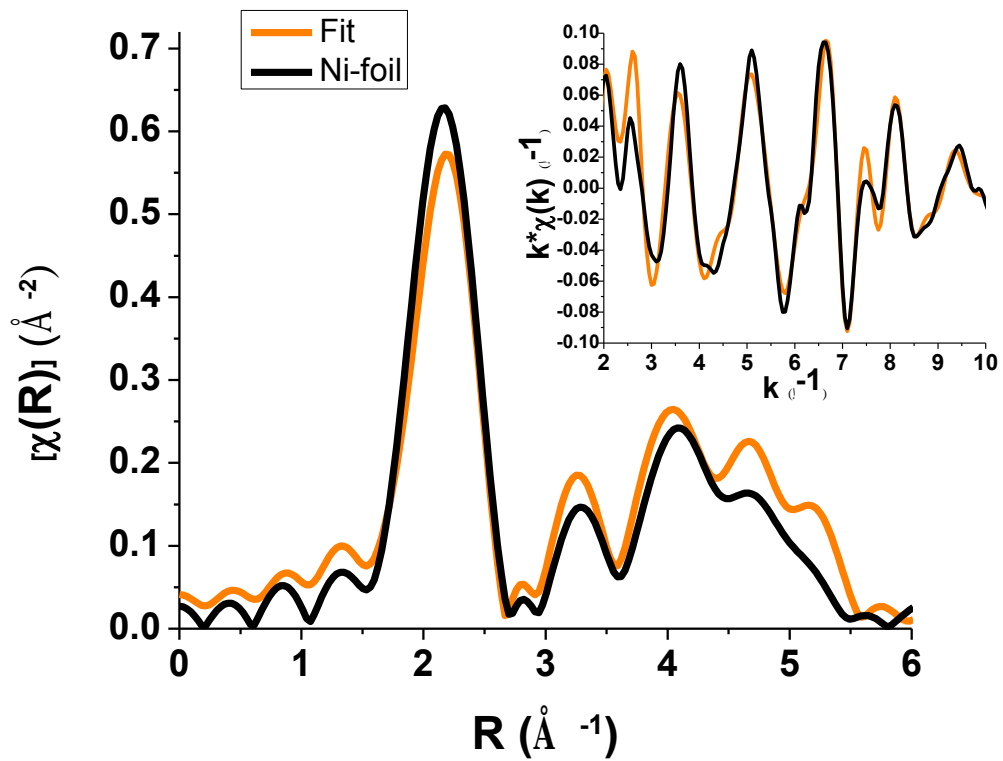


Fig. C.3: EXAFS fit to Ni foil. The fitting model using a single set of Ni *fcc* variables resulted in a well matched fit (orange) to the data (black).

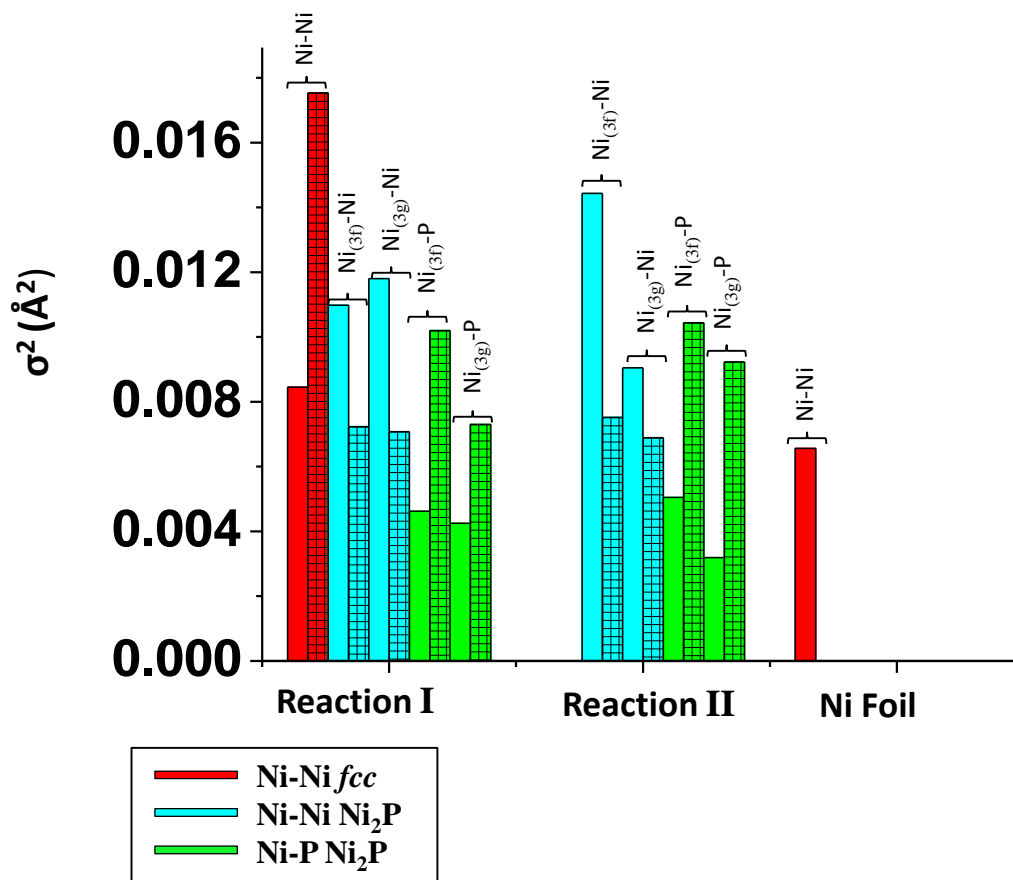


Fig. C.4: Mean-squared disorder comparison. Mean-squared disorder values from the first two shells of each of the structural pathways. Second shell pathways are distinguished with a mesh pattern. Ni_(3f) and Ni_(3g) refer to the Ni 3f site and Ni 3g site atoms from the Ni₂P crystal structure. Larger mean-squared disorder values are associated with greater structural and thermal disorder. The mean-squared disorder values associated with the *fcc* Ni structure in **I** are notably higher than the other pathways. Ni foil values are included as a bulk reference of comparison.

Calculations on magnetic properties of sample II

If we assume that the Curie-Weiss behavior solely originates from the surface Ni atoms, we can fit the susceptibility curve as $\chi(T) = \chi_o + \frac{C}{T-\theta}$ without weight or mole normalization. χ_o can then be normalized by the number of core Ni atoms expressed in moles (core Ni atoms are roughly $\sim 94.6\%$ of total Ni atoms) which results in $5.94 \times 10^{-5} \text{ emu} \cdot (\text{Oe} \cdot \text{mol of Ni})^{-1}$. The Curie-Weiss susceptibility term, $\frac{C}{T-\theta}$, is then normalized by the moles of the surface Ni atoms (only $\sim 5.4\%$ of the total Ni atoms in sample II are on the surface). The effective moment of the Ni atoms on the NP surface is $1.61 \mu_B$, extracted from the Curie constant using the following equation,

$$\mu_{eff} = \left(\frac{3 k_b C}{N}\right)^{1/2}.$$

References

1. Muthuswamy, E.; Savithra, G. H. L.; Brock, S. L. *ACS Nano* **2011**, *5*, 2402-2411.
2. Bunker, G., *Introduction to XAFS: a practical guide to X-ray absorption fine structure spectroscopy*. Cambridge University Press: Cambridge, 2010; p 260.
3. Ravel, B.; Newville, M. *J. Synchrotron Radiat.* **2005**, *12*, 537-541.
4. Stern, E. A. *Contemp. Phys.* **1978**, *19*, 289-310.
5. Koningsberger, D. C.; Mojet, B. L.; van Dorssen, G. E.; Ramaker, D. E. *Top. Catal.* **2000**, *10*, 143-155.
6. Ravel, B. *J. Synchrotron Radiat.* **2001**, *8*, 314-316.
7. Stern, E. A. *Phys. Rev. B* **1974**, *10*, 3027-37.
8. Ravel, B.; Kelly, S. D. *AIP Conf. Proc.* **2007**, *882*, 150-152.
9. Scott, R., *Physical Methods in Bioinorganic Chemistry: Spectroscopy and Magnetism*. University Science Books: 2000.
10. Michalowicz, A.; Vlaic, G. *J. Synchrotron Radiat.* **1998**, *5*, 1317-1320.
11. Murray, C. B.; Norris, D. J.; Bawendi, M. G. *J. Am. Chem. Soc.* **1993**, *115*, 8706-8715.
12. Nietubyc, R.; Czerwosz, E.; Diduszko, R.; Dluzewski, P.; Kozlowski, M.; Welter, E. *J. Alloys Compd.* **2009**, *484*, 896-901.

CHAPTER 5

5 THE OXIDATION OF COBALT NANOPARTICLES INTO KIRKENDALL-HOLLOWED COO AND CO₃O₄: THE DIFFUSION MECHANISMS AND ATOMIC STRUCTURAL TRANSFORMATIONS*

5.1 *Abstract*

We report on the atomic structural changes and diffusion processes during the chemical transformation of ϵ -Co nanoparticles (NPs) through oxidation in air into hollow CoO NPs and then Co₃O₄ NPs. Through XAS, XRD, TEM and DFT calculations the mechanisms of the transformation from ϵ -Co to CoO to Co₃O₄ are investigated. Our DFT calculations and experimental results suggest that a two-step diffusion process is responsible for the Kirkendall hollowing of ϵ -Co into CoO NPs. The first step is O in-diffusion by an indirect exchange-mechanism through interstitial O and vacancies of type I Co sites of the ϵ -Co phase. This indirect exchange mechanism of O has a lower energy barrier than a vacancy-mediated diffusion of O through type I sites. When the CoO phase is established the Co then diffuses outward faster than the O diffuses inward, resulting in a hollow NP. The lattice orientations during the transformation show preferential orderings after the single crystalline ϵ -Co NPs are transformed to polycrystalline CoO and Co₃O₄ NPs. Our Co₃O₄ NPs possess

* Originally Published as: D.-H. Ha, L. M. Moreau, S. Honrao, R. G. Hennig, and R. D. Robinson, "The Oxidation of Cobalt Nanoparticles into Kirkendall-Hollowed CoO and Co₃O₄: the Diffusion Mechanisms and Atomic Structural Transformations," *J. Phys. Chem. C* **117**, 14303 (2013) Reprinted with Permission from American Chemical Society.

a high ratio of {110} surface planes, which are known to have favorable catalytic activity. The Co_3O_4 NPs can be redispersed in an organic solvent by adding surfactants, thus rendering a method to create solution-processable colloidal, monodisperse Co_3O_4 NPs.

5.2 Introduction

There have been years of tremendous efforts in nano-synthetic chemistry to develop methods to control the size, shape, and composition of nanoparticles (NPs), which, in turn, can tune their unique properties.¹⁻⁵ Chemical transformations of NPs, such as by cation exchange⁶ or galvanic replacement,⁷ provide a new route to manipulate the crystal phase, composition, and morphology of NPs. Moreover, chemical transformations can lead to new nanomaterials and unusual patterns or shapes, which are not easily obtained through direct synthesis.⁸⁻¹⁴ However, the mechanisms and kinetics of these chemical transformations are not well understood or established for NPs. It is essential to understand these reaction processes and diffusion mechanisms in order to optimize nanomaterial properties and access new NP material compositions and morphologies.

Most metals are easily oxidized in air, making it simple to exploit this naturally occurring oxidation process to synthesize metal oxides. This conversion has been extensively explored in bulk due to the dramatic change of properties as a metal transforms into a ceramic. The oxidation process is widely studied for bulk metal oxides, but it is not well investigated for nanomaterials. Unlike bulk materials,

nanoparticles generally show size and shape dependent kinetics and thermodynamics.¹⁵⁻¹⁷ Previous work on the oxidation of metal NPs – such as Ni-NiO,¹⁸⁻²⁰ Fe-Fe_xO_y,^{5,21} Cu-Cu₂O,²² and Co-CoO^{10,23-25}/Co₃O₄²⁶– have yielded important insights, however, the atomic structural evolutions and diffusion processes that occur during NP oxidation are not yet well understood. Cobalt oxide nanomaterials have attracted great attention due to their exceptional and wide-ranging functionality. Particularly, Co₃O₄ nanomaterials have been considered as a promising material for applications including electrocatalysis,²⁷⁻²⁹ batteries,³⁰⁻³² supercapacitors,³³ and gas sensors.³¹ A thorough understanding of the diffusion processes and mechanisms of oxidation is an important step towards tailoring the properties of Co₃O₄ NPs for use in applications.

These metal oxidation reactions in NPs result in hollow structures due to the nanoscale Kirkendall effect, which arises from the difference in diffusion rates between the anion and cation. This hollowing behavior is observed in many NP systems including metal to metal chalcogenides^{10,34-36} and metal phosphides³⁷⁻³⁹ conversions. Several research projects have focused on understanding the mechanism by studying the size-dependent hollow void formations,¹⁸ defining the reaction regimes,³⁴ and by studying the influence of surface diffusion.⁴⁰ These investigations revealed several important aspects to elucidate underlying mechanisms but the atomic diffusion and structural developments for the nanoscale Kirkendall effect have yet to be extensively investigated and resolved.

X-ray absorption spectroscopy (XAS) is a powerful tool to probe the atomic structure of a material with short-range order, and has been widely used to

characterize NPs with amorphous and complicated atomic structure.⁴¹⁻⁴⁶ XAS is an ideal characterization method for NPs that are undergoing chemical transformation since they usually contain a significant amount of intermediate or disordered structure.³⁷ Therefore XAS and X-ray diffraction (XRD) can complement each other by identifying both short-range and long-range order, respectively. Additionally morphological and atomic evolutions during NP transformations can be observed by transmission electron microscopy (TEM) and high-resolution transmission electron microscopy (HRTEM). The combination of all these techniques allows us to obtain a more detailed and complete picture of the chemical transformation of NPs.

These experimental characterizations provide information about the structure, composition, bond distances etc., however they are unable to provide insights into the thermodynamics behind the reaction in the transformation. Therefore, it is very useful to combine characterization methods with computational simulations. This combination gives us the ability to predict the most likely mechanism for a reaction. Theoretical calculations can provide information about the atomistic structures and energetics of point defects, surfaces, and diffusion pathways. Density-functional theory (DFT), in particular, is a powerful approach for the description of ground state properties of metals, semiconductors, and insulators, and has been shown to provide accurate structural and energetic results.^{47,48} Using DFT we can calculate the defect formation energies and atomic migration barriers, and hence predict the diffusion activation barriers for the transformation. Combining these values with XRD and XAS data helps us identify the diffusing species and thus elucidate the reaction pathways of the NPs during their chemically transformation.

In this study we introduce a simple approach to convert colloidal NPs of ϵ -Co into CoO and Co₃O₄ NPs through oxidation in air. Through the investigation by XAS, XRD, TEM and HRTEM we find that the as-synthesized ϵ -Co NPs have a native oxide layer that grows during heating in air and leads to CoO NPs with a hollow morphology due to the nanoscale Kirkendall effect. Further heating in air results in the Co₃O₄ phase. Our theoretical calculations and experimental results indicate a two-step diffusion mechanism for the transformation from ϵ -Co to CoO with an indirect exchange-mechanism for the diffusion of oxygen into ϵ -Co. We find that the type I Co sites in ϵ -Co are much more reactive than the type II sites for the oxidation reaction. In terms of structure, the CoO and Co₃O₄ NPs are polycrystalline and the orientation of the grains show that several specific lattice planes are preferentially exposed at the surface of the NPs. Since the {110} planes of Co₃O₄ are very catalytically active^{49,50} our Co₃O₄ NPs with frequent {110} facets would be ideal for use in catalysis.

5.3 *Methods*

Synthesis

ϵ -Co NPs were synthesized using standard procedures.² Tri-*n*-octylphosphine oxide (0.1 g) and oleic acid (0.09 g) in 1,2-dichlorobenzene (DCB, 12 mL) was heated to 180 °C and 0.52 g of Co₂(CO)₈ dissolved in 4 mL of DCB was quickly injected. After the solution was kept for 5 minutes at 180 °C and the flask was quenched by water bath. The NPs were collected through centrifugation with ethanol/hexane at

least two times. The ϵ -Co NPs dispersed in hexane were kept in a glove box to prevent sample oxidation.

The oxidation process was carried out in a furnace. The furnace was pre-heated to 200 °C for at least 1 hour in order to obtain a homogeneous temperature. The ϵ -Co NP film was formed by depositing NPs on a quartz slide and subsequently placed in the furnace.

XAS measurement

XAS data was obtained at the C-line station of the Cornell High Energy Synchrotron Source (CHESS), using fluorescence detection. The cobalt k-edge was probed from 7680 eV to 8140 eV, in order to include both the lower and higher energy portions of the spectrum (XANES and EXAFS respectively). A Co foil was simultaneously probed using transmission detection, to ensure determination of the exact value of the edge, to offset potential shifts in the equipment which may occur during detection. The samples were each suspended in hexane, in 1 mm diameter cylindrical quartz capillaries. The 90 minutes sample was not evenly dispersed in solution and would have resulted in an uneven concentration, and therefore an XAS spectrum of inconsistent intensity signal. This sample was instead dropped between two pieces of Kapton tape, and a region of uniform concentration found by utilizing z- and x-position intensity scans at iso-energy, so that the slight beam-shift as a function of energy would not affect the resultant spectra. Five samples in total were analyzed. These included the ϵ -Co NP templates, and these NPs heated in the presence of oxygen at 200 °C for 5 mins, 10 mins, 30 mins and 1.5 hours.

Calculation of atomic contributions based on EXAFS

The atomic contribution percentage is calculated from the EXAFS fitting results as reported previously (see Supporting Information for EXAFS analysis methods).⁴⁴ The content of atoms contributing to a certain phase is determined by summing the degeneracy values (*i.e.*, N_{exp}) for the pathways of the specific phase (*e.g.* $N_{(\text{Co-O})}$ from the CoO phase) and dividing by the sum of the degeneracies for all pathways within the structure. This effectively counts the number of atoms from the specific phase and divides by the total number of atoms within a set radius.

Density-functional method

Density-functional calculations were performed with the Vienna Ab-initio Software Package (VASP)⁵¹⁻⁵⁴ using the PBE exchange-correlation functional⁵⁵ and the projector augmented wave method.^{56,57} The Brillouin zone integration was performed using a Monkhorst and Pack k -point mesh.⁵⁸ For ϵ -Co, CoO and Co₃O₄, a $8 \times 8 \times 8$ and $6 \times 6 \times 6$ k -point mesh was employed for structural relaxations and nudged-elastic band (NEB) calculations,⁵⁹ respectively. The kinetic energy cutoff for the plane wave basis was set to 360 eV for the structural relaxations and 270 eV for the NEB calculations of the diffusion barriers. The corresponding cutoff energies for the augmentation functions were set to 650 eV and 480 eV, respectively. For the defect formation energies involving changes in the composition, the DFT energies of ϵ -Co, CoO, Co₃O₄, and molecular O₂, are used as reference chemical potential as appropriate and described below.

Calculation of diffusion activation barriers

For a defect mediated-diffusion mechanism, the activation energy of diffusion, $E_{\text{def}}^{\text{act}}$, is given by the sum of the defect formation energy, $E_{\text{def}}^{\text{f}}$, and the defect migration energy barrier, $E_{\text{def}}^{\text{m}}$. The different diffusion mechanisms are investigated by calculating the formation energies of various vacancies and interstitial defects and their energy barriers for diffusion.

The vacancy formation energies for sites I and II in ϵ -Co are calculated by removing a type I or II Co atom, respectively, from a 20-atom ϵ -Co cell. The vacancy formation energies are $E_{\epsilon\text{-Co}19\text{V(I)}}^{\text{f}} = 1.39$ eV and $E_{\epsilon\text{-Co}19\text{V(II)}}^{\text{f}} = 1.84$ eV, indicating that vacancies in ϵ -Co preferentially occupy type I sites. The type I sublattice forms a network of nearest neighbor sites such that it is possible for an atom to diffuse through ϵ -Co on the type I site sublattice. The migration energy barrier for a Co atom to move from a type I site to a neighboring vacant type I site, $E_{\text{Co(I)-V(I)}}^{\text{m}}$ is calculated using the nudged-elastic band (NEB) method.⁵⁹ The initial path is obtained by a linear interpolation between the endpoints configurations. The resulting migration energy barrier is only 0.08 eV, yielding an activation energy for Co atoms diffusing by vacancies on the type I sublattice $E_{\text{Co(I)-V(I)}}^{\text{act}} = 1.47$ eV. This value is smaller than the vacancy formation energy on the type II sublattice of 1.84 eV, indicating that in pure ϵ -Co diffusion on type I sublattice dominates.

O atoms in ϵ -Co can occupy either substitutional or interstitial lattice sites. Considering first substitutional defects, the formation energy for an ϵ -Co cell including a substitutional O atom on a Co site is calculated as $E_{\text{O(I)}}^{\text{f}} = -0.18$ eV for

type I and $E_{\text{O(II)}}^{\text{f}} = 0.35$ eV for type II sites, using molecular O_2 to define the reference chemical potential. The significantly lower formation energy for oxygen on type I sites compared to type II, indicates that oxygen atoms, just like vacancies, would preferentially occupy type I lattice sites. To determine if oxygen can diffuse by Co vacancies, we calculate the formation energy for the defect pair of a substitutional O atom and a vacancy on neighboring type I sites and find it to be $E_{\text{V(I)O(I)}}^{\text{f}} = 1.02$ eV, indicating a small binding energy between O and vacancies. The NEB value for the migration energy barrier is 0.21 eV, resulting in a diffusion activation barrier for O atoms through vacancies on type I sites of $E_{\text{O(I)-V(I)}}^{\text{act}} = 1.23$ eV.

To determine if O occupies interstitial sites in ϵ -Co, several interstitial sites were investigated. The most favorable site for an interstitial O atom in the 20-atom ϵ -Co cell is given by the fractional coordinates (0.375, 0.375, 0.375) and has an energy of -0.81 eV. Using the NEB method, the migration energy barrier between adjacent interstitial sites in ϵ -Co is found to be quite large with 2.53 eV. The resulting diffusion activation barrier for interstitial diffusion of O is $E_{\text{O(int)-O(int)}}^{\text{act}} = 1.72$ eV.

For CoO, vacancy mediated diffusion of Co and O was investigated. The formation energy of a Co vacancy in a Co_8O_8 cell is 0.96 eV, using the energies of CoO and Co_3O_4 to define the Co reference chemical potential. The barrier to migration of the Co atom was calculated using the NEB method as 0.18 eV; the total diffusion activation barrier for Co was found to be $E_{\text{Co-V}}^{\text{act}} = 1.14$ eV.

The diffusion activation barrier for O in CoO was calculated in a similar way using a Co_8O_8 cell with the energies of ϵ -Co and CoO to define the O reference

chemical potential. The formation of a vacancy of the O sublattice is 1.14 eV. Using NEB, the migration energy barrier for O to move to a neighboring vacant O sublattice site was found to be quite large with a value of 2.05 eV. The diffusion activation barrier for O in CoO was found to be 3.19 eV.

5.4 Results and Discussion

The morphology evolution of the NPs during their oxidation at 200 °C was characterized by TEM (**Figure 5.1**). The samples for TEM were prepared by drop casting the Cobalt NPs on a carbon coated copper TEM grid and these samples were heated in a furnace at 200 °C. The initial cobalt NPs are spherical with uniform size (size: 10.8 nm, std dev: 8 %). The initial cobalt sample shows a core-shell (cobalt + cobalt oxide) structure due to immediate surface oxidation after exposure to air, as previously reported.^{23,37} Five minutes of oxidation lead to a smaller cobalt dark core and thicker oxide shell (**Figure 5.1b**). After 10 minutes of oxidation some of the NPs (~20 %) begin to show small voids and the overall spherical shape becomes irregular compared to the initially spherical Co NPs. These particles then become hollow after 30 total minutes of oxidation (NP size: 13.7 nm, std dev: 9.5 %, void size: ~5 nm). This hollow morphology is maintained in the sample after 90 total minutes of oxidation. At this stage the NPs are slightly larger in size (NP size: 14.4 nm, std dev: 9 %, void size: ~5 nm) than the initial Co NPs. The final particles are ~30 % bigger than the initial Co NPs and the shape is faceted with a void in the center.

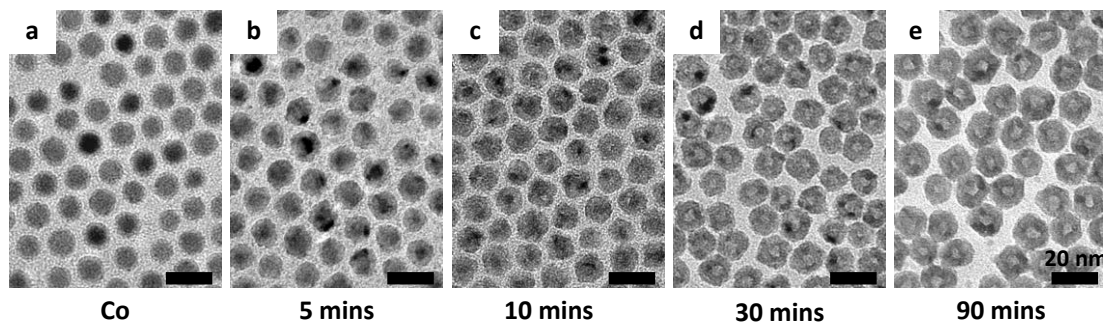


Figure 5.1 TEM images of the samples during the oxidation at 200 °C in air. (a) The initial ϵ -Co NPs are spherical with an oxide shell. The samples are oxidized for 5 mins (b), 10 mins (c), 30 mins (d), and 90 mins (e) and transform to a hollow structure with irregular faceted morphology.

XRD was used to determine the long-range order structure and identify the phases (**Figure 5.2a**). The XRD samples are prepared by depositing the Co NPs on a quartz slide which has no background noise and placed in a furnace with the TEM samples at 200 °C for a specified time. The XRD pattern of the initial cobalt NPs is well matched with the ϵ -Co phase (**Figure 5.2a** pink bars). ϵ -Co has a metastable complex cubic structure and is the common phase for nanocrystals of cobalt.^{2,60-62} The cobalt oxide phase is not detected from XRD patterns even though the oxide shell is observed in TEM, which is consistent with previous reports.^{23,37} After the sample is oxidized for 5 mins the XRD pattern exhibits broad peaks corresponding to the CoO phase (**Figure 5.2a** blue bars, JCPDS 48-1719) and has suppressed contributions from ϵ -Co indicating that the first phase during the oxidation process of cobalt is CoO. According to the phase diagram of the Co-O system, the stable phase is Co_3O_4 at 200

°C in air for both bulk and nanomaterials,¹⁵ but Co should transform to CoO before Co₃O₄ since the transformation to Co₃O₄ is much slower than that to CoO.⁶³ The reverse process (Co₃O₄ to CoO to Co-metal) has been observed in the systems under reduction conditions^{64,65} with varying temperature.⁶⁶ The XRD pattern of the sample calcinated for 10 mins corresponds well to the rock-salt CoO phase and ϵ -Co phase is no longer detected. The sample oxidized for 30 mins shows an increased peak around 37° in the XRD pattern. This peak corresponds to the strongest pattern from the Co₃O₄ phase reference (**Figure 5.2a** black bars, JCPDS 42-1467) and the second strongest pattern from CoO phase reference (**Figure 5.2a** blue bars). This implies that the sample is beginning to transform from the CoO to the Co₃O₄ structure. The final NP sample oxidized for 90 mins displays only Co₃O₄ phase from XRD confirming that the sample is fully converted to Co₃O₄ (**Figure 5.2a** black curve). The organic surfactant ligands which were initially on the surface of the as-synthesized ϵ -Co are burned off after the 90 mins of oxidation.³⁰ This oxidation in air is a very efficient means to obtain the Co₃O₄ phase; as comparison the solution-phase process does not result in Co₃O₄ even when reacted at 200 °C for up to 3 hours (see Supporting Information, **Figure D.1**).

The short-range order of the samples is probed through EXAFS of the Co K-edge. **Figure 5.2b** shows the Fourier transformed (FT) k-weighted EXAFS spectra of the samples during oxidation of cobalt NPs. The structural contributions (atomic %) of the phases for our samples' EXAFS fittings are listed in **Table 5.1**, which roughly shows the phase evolutions during the oxidation process. In the FT EXAFS spectra the first peak around 1.45 Å and the second peak around 2.4 Å in R-space correspond

roughly to the 1st shell of Co-O and Co-Co scattering pathways, respectively. The general trend of the oxidation process is apparent from the increasing peak intensities with increasing oxidation time in the lower values of R where cobalt-oxygen bonds are anticipated. The pink line in **Figure 5.2b** represents the EXAFS data of the cobalt NP sample that is identified as ϵ -Co from XRD. However, to fit the data with EXAFS modeling the CoO phase is required, indicating that the sample contains not only ϵ -Co but also bond-contributions which resemble the CoO phase (~19%, **Table 5.1**). This matches well with previous reports of a native oxide forming on the surface of cobalt NPs.^{37,60} This oxide shell layer is also observed in the TEM image (**Figure 5.1a**). The 5 mins sample is well-fit with the combination of ϵ -Co (48.2%) and the CoO phase (51.8%), which is consistent with our XRD result. The EXAFS pattern from the 10 mins oxidation sample still shows bond contributions from the ϵ -Co phase (35%) and ~65 % of the CoO phase is present, despite the fact that the CoO phase is the only phase detected from XRD. The NP calcinated for 30 mins is well-fit with CoO and a small portion of Co₃O₄ phase (~27.5 %), which corresponds to the XRD results. The FT EXAFS spectrum from the 30 mins sample shows the narrowest peaks at low R of the FT EXAFS spectra from the samples (see **Table D.1**) suggesting that this sample might contain a high percentage of CoO due to its simple crystal structure: CoO has rock-salt structure containing more narrowly spread bonding distances within the first shell than the ϵ -Co or Co₃O₄ structures. Increases in EXAFS amplitudes generally signify increased order of atomic structure,⁶⁷ therefore the more ordered CoO structure should show these narrow intense peaks inherently. The EXAFS spectrum of the final sample (90 mins) is well-fit with only the Co₃O₄ phase spinel structure. The high ratio

of first peak to second intensity of this 90 mins sample supports the idea that this sample has significant Co-O orderings.

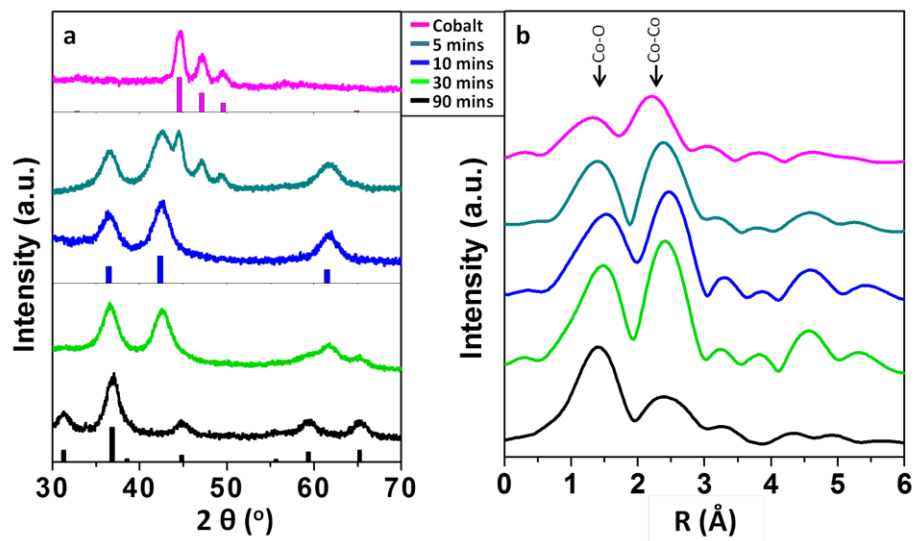


Figure 5.2 (a) XRD and (b) EXAFS results of the NP samples. The pink, turquoise, blue, light green, and black lines represent the starting cobalt NPs, oxidized for 5 mins, 10 mins, 30 mins, and 90 mins samples, respectively. The XRD patterns of the samples (left) during the oxidation show gradual transition from ϵ -Co phase (pink bars)⁴² to CoO (blue bars, JCPDS 48-1719) and Co₃O₄ (black bars, JCPDS 42-1467). Fourier-transformed k-weighted EXAFS data (right) of the samples show the increased intensities from Co-O scattering pathways ~ 1.5 Å and suppressed Co-Co scattering pathways ~ 2.5 Å through the oxidation of cobalt NP.

Table 5.1 The structural contributions (atomic %) from the EXAFS fitting models for the samples

	Co (ϵ -Co)	O (CoO)	Co (CoO)	O (Co ₃ O ₄)	Co (Co ₃ O ₄)
0 minutes	81.2 %	10.17 %	8.58 %	-	-
5 minutes	48.2 %	25.4 %	26.5 %	-	-
10 minutes	34.5 %	30.0 %	35.5 %	-	-
30 minutes	-	31.1 %	41.3 %	13.6 %	13.9 %
1.5 hours	-	-	-	53.2 %	46.8 %

The signature of structures that are identified through EXAFS modeling but not by XRD (*i.e.*, the cobalt oxide found by EXAFS in the ϵ -Co sample, and the ϵ -Co found by EXAFS in the 10 minutes sample) can occur for several reasons, including: 1) the structure is amorphous/disordered, 2) the size of crystal is sub-nm, and/or 3) the structure may be partially or fully interdiffused (solid solution) into a dominant crystalline phase, making it a “hidden” substructure of the dominant crystal, resulting in a hidden phase radial structure that is severely affected by the dominant phase, which manifests itself in the coordination and interatomic spacing values. Our EXAFS models, which are using the end-points of the transformation (*i.e.*, ϵ -Co, CoO, and Co₃O₄), reveal important information about the arrangement of the atoms through the transformation, but to precisely determine which structural forms are present more complicated models which incorporate intermediate atomic structures (*e.g.*, atomic

arrangements that can occur between CoO and Co₃O₄) could be used.⁴⁴ Modeling of these intermediate arrangements are, however, too complex to include in the present EXAFS fitting models and will be treated in future research. The value of the analyses presented here is the ability to differentiate between amorphous/interdiffused arrangements and pure crystalline structure. For the 10 minutes oxidized sample, our analysis shows that ~35% of the structure resembles ϵ -Co, but given that 1) the XRD does not show the presence of ϵ -Co and, 2) this transformation occurs *via* the diffusion of Co through ϵ -Co and CoO, the most likely arrangement of this ~35% Co is in a solid solution or amorphous phase with the CoO. For the native oxide on the initial ϵ -Co NPs, given that this oxide is observable in the TEM, our results point to this oxide as amorphous or partially interdiffused with the Co metal surface.

Figure 5.3a shows the concentration of oxygen incorporated within the NP as a function of time based on EXAFS analysis. This plot provides insight for understanding the kinetics of oxygen diffusion. The rate of oxygen incorporation increases logarithmically with increasing oxidation time. (The initial oxidation is extremely fast and then it slows down.) This oxygen concentration change as a function of the oxidation time can be fitted by the logarithmic functions ((oxygen%)=8.5+10*ln(oxidation time), R²=0.97) shown as the red line in **Figure 5.3a**. This oxidation rate behavior of our NPs follows the general trend observed from bulk materials.^{68,69}

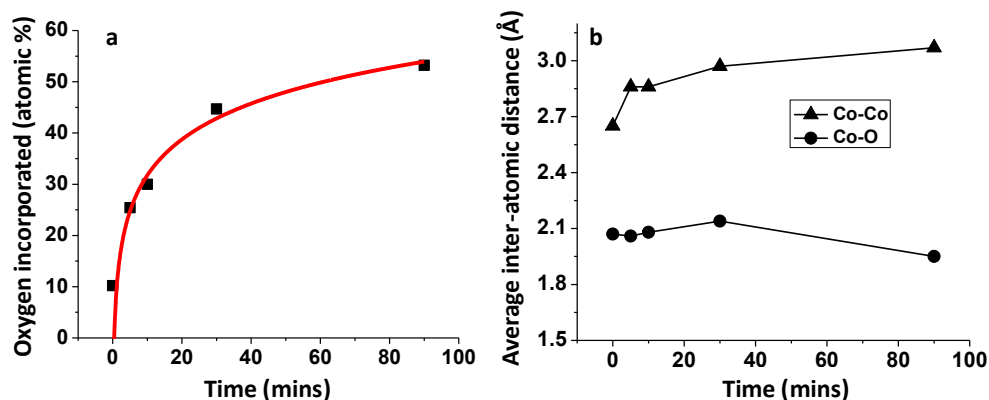


Figure 5.3 The oxygen concentrations and the average inter-atomic distances of the samples during the oxidation process. (a) The oxygen concentrations based on the EXAFS fitting model increase logarithmically and are well fit with the logarithmic function ($(\text{oxygen \%})=8.5+10*\ln(\text{oxidation time})$, $R^2=0.97$). (b) The filled triangles and filled circles represent the Co-Co inter-atomic distances and Co-O inter-atomic distances, respectively.

The changes in inter-atomic distances during the transition from cobalt to two phases of cobalt oxide are plotted in **Figure 5.3b** as a function of the oxidation time. This plot shows the evolution of inter-atomic distances of Co-O (filled circle) and Co-Co (filled triangle) represented by the average distances for their first shells as extracted from EXAFS analysis. The Co-O inter-atomic distance is relatively constant from the beginning of the bond formation while Co-Co inter-atomic distance increases roughly parabolically as a function of oxidation time. This trend is similar to previous Co-P study in terms of constant bond lengths between cation and anion and increasing distances between Co and Co, as the metal is transformed into a phosphide/oxide.³⁷

We define the average bonding distance as the average of interatomic distances within the first primitive shell of the radial structure ($< \sim 3.1 \text{ \AA}$). The ideal average bonding distances of Co-Co and Co-O from the CoO crystal structure are 3.02 \AA and 2.13 \AA , respectively (**Table D.5**). The average distance values found in our 30 mins sample, which displays a structure very close to CoO, were 2.97 \AA and 2.14 \AA , respectively, indicating that the Co-O bonding distances are well established while Co-Co distances are slightly shorter ($\sim 1.7\%$) than ideal distances. The 90 mins sample also exhibits a slightly shortened Co-Co average distance (3.07 \AA) compared to the ideal distance (3.21 \AA) while the Co-O distance (1.95 \AA) is closer to the ideal distance (1.91 \AA) (**Table D.6**). This indicates that Co-O bondings are more rigid, form earlier, and are well defined during the transformation compared to the Co-Co bondings.

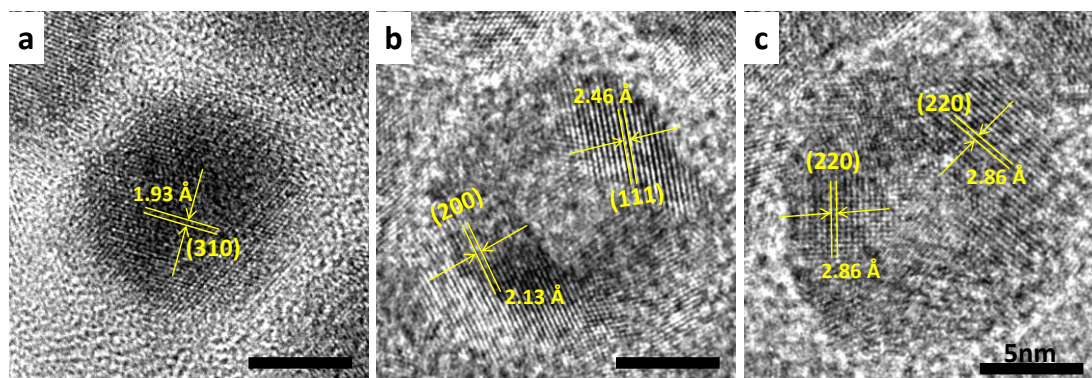


Figure 5.4 The high-resolution TEM images of the samples. (a) The starting ϵ -Co NP is single crystalline and the lattice distances are well matched with ϵ -Co crystal structure. (b) The CoO sample is polycrystalline and matched lattice distances are from CoO structure. (c) Co_3O_4 NP is polycrystalline and identified as Co_3O_4 by lattice distances. All the scale bars in the figures are 5 nm.

HRTEM images of the samples show that the initial ϵ -Co NP is single crystalline and exhibits spherical morphology (**Figure 5.4a**). Once the NPs transform to CoO they become polycrystalline with a larger overall size and develop a void inside (**Figure 5.1** and **5.4b**). This polycrystalline CoO converts to Co_3O_4 with a similar polycrystalline and hollow morphology (**Figure 5.4c**).

One of the keys to fully utilizing cobalt oxide in electrochemistry or catalysis is control of the surface structure since their properties are significantly affected by the type of the lattice planes exposed at the surface.^{49,70} The lattice planes of the CoO and Co_3O_4 NP samples were investigated through HRTEM on ~50 NPs to observe the orientations of the grains (**Figure 5.4b,c**). For the CoO NP sample, ~42% and ~55% of the exposed lattice planes were {111} and {100}, respectively. The other planes (*e.g.*, {110} and {311}) constituted less than 3% of the total surface planes. In general the crystals tend to minimize the total surface energy by reducing the surfaces that have high surface energies.⁷¹ However, interestingly, the {111} surface of the rock-salt metal oxides (a majority exposed facet in our CoO) is known to have very high surface energy due to their polar surface, which causes increased surface Gibbs energy.⁷²⁻⁷⁴ In the Co_3O_4 NPs the {110} planes were frequently (~55%) observed as the surface plane while other planes (*e.g.*, {111}, {100}, and {311}) appeared only 15% each or less. This is also not consistent with the calculated surface energy (γ) of the spinel Co_3O_4 structure that follows the order: $\gamma(100) < \gamma(111) < \gamma(110)$.⁷⁵ Since the planes with the low surface energies do not make up a majority of the exposed surfaces in our CoO and Co_3O_4 NPs, other factors might play a large role to induce such orientations of the grains during the transformation. Previous studies have

reported that the {110} planes are the most catalytically active facets⁵⁰ due to the high population of the active Co^{3+} sites.⁴⁹ Since our Co_3O_4 NPs have large portion of exposed {110} surfaces, unlike the common isotropic spherical NPs, our Co_3O_4 NPs are promising for catalysis applications.

CoO and Co_3O_4 NPs oxidized using our methodology can be converted to solution-phase colloidal NPs by a simple procedure. Our previous study shows that most of the organic surfactants attached on the initial ϵ -Co are burned off during oxidation resulting in aggregated NPs that are not soluble in non-polar organic solvents.³⁰ It is known that the oleic acid is removed at ~ 250 °C.⁷⁶ This indicates that the oleic acids from our initial Co NP ligands might be removed at 200 °C if they are held for more than 1.5 hours at 200 °C. However, these NPs can be made soluble again by dispersing them in a non-polar organic solvent with addition of excess of surfactant ligands such as oleylamine (see Supporting Information). After this ligand attachment process the NPs become dispersible in non-polar solvents such as hexane. **Figure 5.5a** shows the good solubility of the NPs re-dispersed in a solvent, showing a black solution even after the cleaning process with hexane and acetone after the attachment of the ligands. The TEM image also confirms that the NPs are well dispersed after the attachment process and not sintered during oxidation process (**Figure 5.5c**). The NPs ultrasonicated without additional ligands show poor solubility (**Figure 5.5b**) confirming that most of the organic surfactant ligands are burned off during oxidation. This solution processability of our cobalt oxide NPs would be beneficial for making devices.

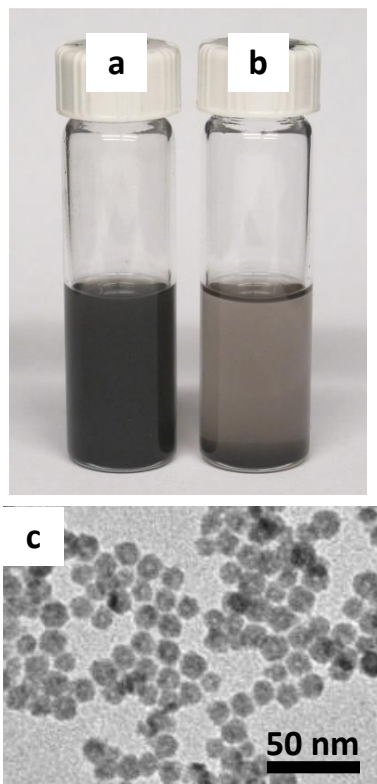


Figure 5.5 The photograph and TEM image of the Co_3O_4 NP samples re-dispersed in an organic solvent after oxidation process. (a) This sample is the Co_3O_4 NPs dispersed in hexane after the ligand attachment process and washed twice with hexane/acetone. The NPs become solution-phase colloidal NPs after the attachment of the ligands by ultrasonication with addition of ligands. (b) Most of the NPs dispersed in hexane without additional ligands precipitate immediately even after ultrasonication for 10 mins. (c) The TEM image shows well-dispersed Co_3O_4 NPs after the ligand attachment process.

In order to understand the atomic diffusion processes during the oxidation, diffusion activation barriers were calculated for the Co and O atoms diffusing through

the ϵ -Co phase, to infer the likely mechanism for the transformation from ϵ -Co to CoO. The formation energy of our starting ϵ -Co phase is calculated as 0.10 eV/atom higher than the *fcc* Co phase. From our results we find that for the vacancy-mediated diffusion both Co and O atoms are more likely to diffuse through type I sites than type II sites of ϵ -Co (see the **Figure D.2** for the ϵ -Co crystal structure), due to the lower formation energies on type I sites: $E_{\epsilon\text{-Co}19\text{V(I)}}^{\text{f}} = 1.39$ eV vs. $E_{\epsilon\text{-Co}19\text{V(II)}}^{\text{f}} = 1.84$ eV for Co, and $E_{\text{O(I)}}^{\text{f}} = -0.18$ eV vs. $E_{\text{O(II)}}^{\text{f}} = 0.35$ eV for O. **Table 5.2** presents the formation energies, migration barriers and diffusion activation barriers for the diffusion of Co and O through type I sites in the ϵ -Co structure (**Table 5.2**, first two rows, **Figure D.3** for the schematics). Activation barriers are also calculated for the interstitial diffusion of O atoms through the ϵ -Co crystal (**Table 5.2**, third row). The formation energy of an interstitial O atom is favorable, but its high barrier towards migration prevents interstitial O diffusion.

We investigated a number of complex diffusion processes involving Co and O to infer the most likely mechanism for the transformation from ϵ -Co to CoO. We discovered a complex diffusion mechanism for O in ϵ -Co that is best described as an indirect exchange-mechanism illustrated in **Figure 5.6**. First, a substitutional O atom on a type I site moves to an adjacent interstitial site with a small migration energy barrier. This step is followed by the migration of a neighboring Co atom into the now vacant type I site. Finally, the O atom migrates to the type I site abandoned by the moved Co atom. The barrier to migration for this three-step mechanism can be estimated as the energy required to overcome the highest energy barrier in the mechanism (**Fig. 5.7**), and this comes out to be 1.06 eV. Adding the formation energy

for the initial defect of -0.18 eV to the migration barrier gives us a diffusion activation barrier of 0.88 eV. This value is considerably lower than for the vacancy-mediated diffusion of O through type I sites (1.23 eV). In addition, this diffusion mechanism does not require any additional motion of Co vacancies, which is necessary for the simple vacancy-mediated diffusion mechanism of O on the type I sublattice. This result indicates that O diffusion in ϵ -Co occurs *via* an indirect exchange mechanism of Co and O atoms. This result also shows that O diffusion is faster than Co diffusion.

Table 5.2 The formation energy, migration barrier and diffusion activation

barrier for Co and O diffusing through ϵ -Co. For the indirect exchange, the

formation energy is based on the structure with O in a Co vacant site (Figure 6a) and

the barrier energy to migration refers to the highest barrier energy in the diffusion

steps shown in **Figure 5.6 b,c,d**.

Diffusion type	Formation energy (eV)	Barrier to migration (eV)	Diffusion activation barrier (eV)
Co _(I) - V _(I)	1.39	0.08	1.47
O _(I) - V _(I)	1.02	0.21	1.23
O _(int) - O _(int)	-0.81	2.53	1.72
Indirect exchange	-0.18	1.06	0.88

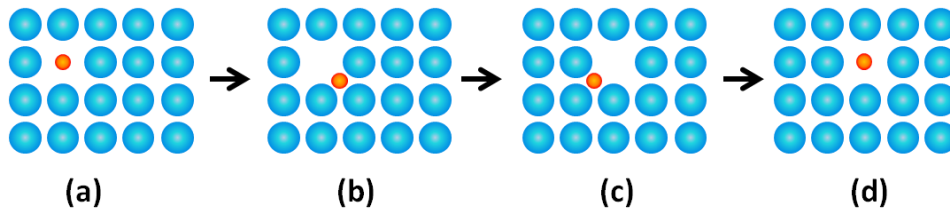


Figure 5.6 The proposed indirect exchange-mechanism of O diffusion in the ϵ -Co phase takes place over four steps (a) – (d). (a) O atom in the vacant type I site; (b) O atom diffuses to an adjacent interstitial site; (c) neighboring type I Co atom diffuses to site vacated by O; (d) O hops back into the empty type I site.

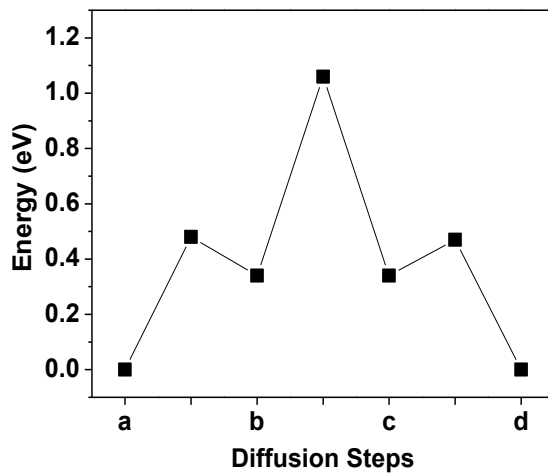


Figure 5.7 The migration energy diagram of the indirect-exchange mechanism.

This figure shows the migration energy barrier through the steps shown in **Figure 5.6**.

The highest energy barrier point is the point between the b and c steps, which is 1.06

eV.

Diffusion activation barriers were also calculated for the Co and O atoms diffusing by a vacancy mechanism in the CoO phase. **Table 5.3** provides the formation energies, migration barriers and diffusion activation barriers for the diffusion of Co and O atoms through the CoO crystal. The much lower activation barrier for Co diffusion through CoO compared to O ($E_{\text{Co-V}}^{\text{act}} = 1.14$ eV vs. $E_{\text{O-V}}^{\text{act}} = 3.19$ eV) indicates that Co diffuses significantly faster than O in CoO.

Table 5.3 The formation energy, migration barrier and diffusion activation barrier for Co and O diffusing through CoO.

Diffusion type	Formation energy (eV)	Barrier to migration (eV)	Diffusion activation barrier (eV)
Co - V	0.96	0.18	1.14
O - V	1.14	2.05	3.19

The mechanism of the transformation from Co to CoO can be described by combining the analyses and results from both experiments and calculations. The computational results suggest that the diffusional transformation from Co to CoO occurs in two steps. First, O diffuses faster than Co in the ϵ -Co structure allowing O to enter the ϵ -Co NPs by the indirect exchange mechanism through type I sites and interstitial sites. Once enough O is present, CoO is formed. Then, the fast diffusing species switches from O to Co: the Co diffuses faster in the CoO phase than the O. TEM, EXAFS and XRD results also confirm this two-step mechanism: No hollow

structures were observed until 5 mins of the reaction meaning that O is still diffusing inward faster than the Co diffusion outward but once the major phase becomes CoO through 10 mins of the reaction (pure CoO phase based on XRD results and 75% of CoO phase based on EXAFS analysis), the voids began to appear in the NP centers. This indicates that the Co diffusion is more rapid than the O diffusion, resulting in hollow structures. Therefore the critical switching point for the diffusion rate of Co and O atoms is between 5 and 10 mins of the reaction. This insight into the nanoscale Kirkendall effect mirrors our previous results in the Co-P system that showed a similar two-step process.³⁷

Further, DFT was used to calculate the formation energies of amorphous phases with the stoichiometry of CoO. Averaging the formation energy over 5 different amorphous structures gave us a value which was only 0.06 eV/atom higher than that of crystalline CoO. This suggests that the transformation from Co to CoO might occur through the formation of an amorphous CoO region, which then converts to crystalline CoO. Evidence for this amorphous CoO may be observed in the EXAFS analysis of the initial ϵ -Co sample that show CoO bonding but no evidence of this phase in the XRD patterns. The sample oxidized for 10 mins also shows a high content of ϵ -Co (~35%) based on the EXAFS analysis while CoO was the only phase from XRD result indicating that Co atoms exist in the form of amorphous or interdiffused.

The mechanism of the transition from CoO to Co₃O₄ is different from that of Co to CoO. Co atoms are the mobile species while the O anion sublattice is expected to remain rigid due to the low diffusion activation energy of Co atoms in the CoO

phase (see **Table 5.3**). This mechanism is well confirmed by the TEM images showing no further hollowing process from CoO to Co₃O₄ samples with a similar size of the voids. The slight increase in the overall size of the NPs during the transformation from CoO to Co₃O₄ might be due to the lower density of the Co₃O₄ phase (6.06 g/cm³) compared to CoO (6.44 g/cm³).⁷⁷ The increase in size might also be due to the formation of more cobalt oxide on the surface from the change in stoichiometry between CoO and Co₃O₄, that is, the excess Co from the CoO migrates from the CoO to the outer surface and forms the more O-rich Co₃O₄ phase after exposure to O atoms in air. This also indicates that the CoO sample does not contain the Co-rich phase inside of the CoO NPs which may cause further hollowing that Co-P samples showed in the previous study.³⁷

5.5 Conclusion

We have demonstrated a simple synthesis of hollow CoO and Co₃O₄ NPs through the chemical transformation of ϵ -Co NPs. The phase transition of NPs occurs through oxidation in air at 200 °C. During this chemical transformation from ϵ -Co to CoO, the single-crystal spherical ϵ -Co NPs convert to polycrystalline hollow CoO NPs due to the nanoscale Kirkendall effect. This morphology remains as the NPs transform during further heating in air to the Co₃O₄ phase. After a ligand attachment process the Co₃O₄ NPs are re-dispersible in organic solvents.

Through the thorough investigation with XRD, EXAFS, TEM, and DFT calculation, we elucidate the atomic structural change and diffusion mechanisms during the oxidation from ϵ -Co to two phases (CoO and Co₃O₄) of cobalt oxide NPs.

The initial ϵ -Co NPs likely form an amorphous CoO layer on the surface and this oxide layer grows (O diffusion inward) into the ϵ -Co NPs *via* an indirect exchange-mechanism. Once the crystalline CoO phase establishes the Co atoms become the more mobile species, which leads to fast Co out-diffusion and the formation of a void inside the cobalt oxide NPs. The morphology of the NPs does not change significantly during the further oxidation from CoO to Co₃O₄. We also observed preferential grain orientations within the polycrystalline cobalt oxide NPs. The high density of exposed catalytically active {110} surface planes may make our Co₃O₄ NPs excellent candidates for catalysis applications.

5.6 References

1. Yin, Y.; Alivisatos, A. P. *Nature* **2005**, 437, (7059), 664-670.
2. Puentes, V. F.; Krishnan, K. M.; Alivisatos, A. P. *Science* **2001**, 291, (5511), 2115-2117.
3. Murray, C. B.; Norris, D. J.; Bawendi, M. G. *J. Am. Chem. Soc.* **1993**, 115, (19), 8706-8715.
4. Manna, L.; Scher, E. C.; Alivisatos, A. P. *J. Am. Chem. Soc.* **2000**, 122, (51), 12700-12706.
5. Cabot, A.; Puentes, V. F.; Shevchenko, E.; Yin, Y.; Balcells, L.; Marcus, M. A.; Hughes, S. M.; Alivisatos, A. P. *J. Am. Chem. Soc.* **2007**, 129, (34), 10358-10360.
6. Son, D. H.; Hughes, S. M.; Yin, Y. D.; Alivisatos, A. P. *Science* **2004**, 306, 1009-1012.
7. Sun, Y.; Xia, Y. *Science* **2002**, 298, (5601), 2176-2179.
8. Robinson, R. D.; Sadtler, B.; Demchenko, D. O.; Erdonmez, C. K.; Wang, L. W.; Alivisatos, A. P. *Science* **2007**, 317, (5836), 355-358.
9. González, E.; Arbiol, J.; Puentes, V. F. *Science* **2011**, 334, (6061), 1377-1380.
10. Yin, Y. D.; Rioux, R. M.; Erdonmez, C. K.; Hughes, S.; Somorjai, G. A.; Alivisatos, A. P. *Science* **2004**, 304, (5671), 711-714.
11. Miszta, K.; Dorfs, D.; Genovese, A.; Kim, M. R.; Manna, L. *ACS Nano* **2011**, 5, (9), 7176-7183.

12. Demchenko, D. O.; Robinson, R. D.; Sadtler, B.; Erdonmez, C. K.; Alivisatos, A. P.; Wang, L. W. *ACS Nano* **2008**, 2, (4), 627-636.
13. Sadtler, B.; Demchenko, D. O.; Zheng, H.; Hughes, S. M.; Merkle, M. G.; Dahmen, U.; Wang, L.-W.; Alivisatos, A. P. *J. Am. Chem. Soc.* **2009**, 131, (14), 5285-5293.
14. Li, H.; Zanella, M.; Genovese, A.; Povia, M.; Falqui, A.; Giannini, C.; Manna, L. *Nano Lett.* **2011**, 11, (11), 4964-4970.
15. Navrotsky, A.; Ma, C.; Lilova, K.; Birkner, N. *Science* **2010**, 330, (6001), 199-201.
16. Barnard, A. S. *Acc. Chem. Res.* **2012**, 45, (10), 1688-1697.
17. Guisbiers, G. *J. Phys. Chem. C* **2011**, 115, (6), 2616-2621.
18. Railsback, J. G.; Johnston-Peck, A. C.; Wang, J.; Tracy, J. B. *ACS Nano* **2010**, 4, (4), 1913-1920.
19. Nakamura, R.; Lee, J. G.; Mori, H.; Nakajima, H. *Philos. Mag.* **2008**, 88, (2), 257-264.
20. Medford, J. A.; Johnston-Peck, A. C.; Tracy, J. B. *Nanoscale* **2013**, 5, (1), 155-159.
21. Wang, C. M.; Baer, D. R.; Thomas, L. E.; Amonette, J. E.; Antony, J.; Qiang, Y.; Duscher, G. *J. Appl. Phys.* **2005**, 98, (9), 094308-7.
22. Nakamura, R.; Tokozakura, D.; Nakajima, H.; Lee, J. G.; Mori, H. *J. Appl. Phys.* **2007**, 101, (7), 074303-7.

23. Jia, S.; Hsia, C.-H.; Son, D. H. *J. Phys. Chem. C* **2011**, 115, (1), 92-96.
24. Chernavskii, P. A.; Pankina, G. V.; Zaikovskii, V. I.; Peskov, N. V.; Afanasiev, P. *J. Phys. Chem. C* **2008**, 112, (26), 9573-9578.
25. Varon, M.; Ojea-Jimenez, I.; Arbiol, J.; Balcells, L.; Martinez, B.; Puntès, V. *Nanoscale* **2013**, 5, (6), 2429-2436.
26. Keng, P. Y.; Kim, B. Y.; Shim, I.-B.; Sahoo, R.; Veneman, P. E.; Armstrong, N. R.; Yoo, H.; Pemberton, J. E.; Bull, M. M.; Griebel, J. J.; Ratcliff, E. L.; Nebesny, K. G.; Pyun, J. *ACS Nano* **2009**, 3, (10), 3143-3157.
27. Liang, Y. Y.; Li, Y. G.; Wang, H. L.; Zhou, J. G.; Wang, J.; Regier, T.; Dai, H. *Nat. Mater.* **2011**, 10, (10), 780-786.
28. Xu, J.; Gao, P.; Zhao, T. S. *Energy Environ. Sci.* **2012**, 5, (1), 5333-5339.
29. Esswein, A. J.; McMurdo, M. J.; Ross, P. N.; Bell, A. T.; Tilley, T. D. *J. Phys. Chem. C* **2009**, 113, (33), 15068-15072.
30. Ha, D.-H.; Islam, M. A.; Robinson, R. D. *Nano Lett.* **2012**, 12, (10), 5122-5130.
31. Li, W. Y.; Xu, L. N.; Chen, J. *Adv. Funct. Mater.* **2005**, 15, 851-857.
32. Poizot, P.; Laruelle, S.; Grugeon, S.; Dupont, L.; Tarascon, J. M. *Nature* **2000**, 407, (6803), 496-499.
33. Xia, X.-h.; Tu, J.-p.; Zhang, Y.-q.; Mai, Y.-j.; Wang, X.-l.; Gu, C.-d.; Zhao, X.-b. *RSC Adv.* **2012**, 2, (5), 1835-1841.

34. Cabot, A.; Ibáñez, M.; Guardia, P.; Alivisatos, A. P. *J. Am. Chem. Soc.* **2009**, 131, (32), 11326-11328.
35. Ibáñez, M.; Fan, J.; Li, W.; Cadavid, D.; Nafria, R.; Carrete, A.; Cabot, A. *Chem. Mater.* **2011**, 23, (12), 3095-3104.
36. Cabot, A.; Smith, R. K.; Yin, Y.; Zheng, H.; Reinhard, B. r. M.; Liu, H.; Alivisatos, A. P. *ACS Nano* **2008**, 2, (7), 1452-1458.
37. Ha, D.-H.; Moreau, L. M.; Bealing, C. R.; Zhang, H.; Hennig, R. G.; Robinson, R. D. *J. Mater. Chem.* **2011**, 21, (31), 11498-11510.
38. Chiang, R.-K.; Chiang, R.-T. *Inorg. Chem.* **2007**, 46, (Copyright (C) 2011 American Chemical Society (ACS). All Rights Reserved.), 369-371.
39. Muthuswamy, E.; Savithra, G. H. L.; Brock, S. L. *ACS Nano* **2011**, 5, (Copyright (C) 2011 American Chemical Society (ACS). All Rights Reserved.), 2402-2411.
40. Fan, H. J.; Knez, M.; Scholz, R.; Hesse, D.; Nielsch, K.; Zacharias, M.; Gösele, U. *Nano Lett.* **2007**, 7, (4), 993-997.
41. Aruguete, D. M.; Marcus, M. A.; Li, L. S.; Williamson, A.; Fakra, S.; Gygi, F.; Galli, G. A.; Alivisatos, A. P. *J. Phys. Chem. C* **2007**, 111, (1), 75-79.
42. Menard, L. D.; Wang, Q.; Kang, J. H.; Sealey, A. J.; Girolami, G. S.; Teng, X.; Frenkel, A. I.; Nuzzo, R. G. *Phys. Rev. B* **2009**, 80, (6), 064111.
43. Marcus, M. A.; Flood, W.; Stiegerwald, M.; Brus, L.; Bawendi, M. *J. Phys. Chem.* **1991**, 95, (4), 1572-1576.

44. Moreau, L. M.; Ha, D.-H.; Bealing, C. R.; Zhang, H.; Hennig, R. G.; Robinson, R. D. *Nano Lett.* **2012**, 12, (9), 4530-4539.
45. Park, J.-I.; Kim, M. G.; Jun, Y.-W.; Lee, J. S.; Lee, W.-R.; Cheon, J. *J. Am. Chem. Soc.* **2004**, 126, (29), 9072-9078.
46. Moreau, L. M.; Ha, D.-H.; Zhang, H.; Hovden, R.; Muller, D. A.; Robinson, R. D. *Submitted*.
47. Parr, R. G.; Yang, W., *Density-Functional Theory of Atoms and Molecules*. Oxford University Press, USA: 1989.
48. Dreizler, R. M.; Gross, E. K. U., *Density Functional Theory, An Approach to the Quantum Many-Body Problem*. Springer-Verlag, Berlin: 1990.
49. Xie, X. W.; Li, Y.; Liu, Z. Q.; Haruta, M.; Shen, W. J. *Nature* **2009**, 458, (7239), 746-749.
50. Ma, C. Y.; Mu, Z.; Li, J. J.; Jin, Y. G.; Cheng, J.; Lu, G. Q.; Hao, Z. P.; Qiao, S. Z. *J. Am. Chem. Soc.* **2010**, 132, (8), 2608-2613.
51. Kresse, G.; Hafner, J. *Phys. Rev. B* **1993**, 47, (1), 558.
52. Kresse, G.; Hafner, J. *Phys. Rev. B* **1994**, 49, (20), 14251.
53. Kresse, G.; Furthmüller, J. *Comput. Mater. Sci.* **1996**, 6, (1), 15-50.
54. Kresse, G.; Furthmüller, J. *Phys. Rev. B* **1996**, 54, (16), 11169.
55. Perdew, J. P.; Burke, K.; Ernzerhof, M. *Phys. Rev. Lett.* **1996**, 77, (18), 3865.
56. Blöchl, P. E. *Phys. Rev. B* **1994**, 50, (24), 17953.

57. Kresse, G.; Joubert, D. *Phys. Rev. B* **1999**, 59, (3), 1758.
58. Monkhorst, H. J.; Pack, J. D. *Phys. Rev. B* **1976**, 13, (12), 5188.
59. Jónsson, H.; Mills, G.; Jacobsen, K. W., Nudged elastic band method for finding minimum energy paths of transition. In *Classical and quantum dynamics in condensed phase simulations*, World Scientific: 1998; pp 385-404.
60. Dinega, D. P.; Bawendi, M. G. *Angew. Chem. Int. Ed.* **1999**, 38, (12), 1788-1791.
61. Osorio-Cantillo, C.; Perales-Perez, O.; Guinel, M. J. *J. Appl. Phys.* **2011**, 109, (7), 07B531-3.
62. Nie, X.; Jiang, J. C.; Meletis, E. I.; Tung, L. D.; Spinu, L. *J. Appl. Phys.* **2003**, 93, (8), 4750-4755.
63. Martin, M.; Koops, U.; Lakshmi, N. *Solid State Ionics* **2004**, 172, (1-4), 357-363.
64. Jacobs, G.; Ji, Y.; Davis, B. H.; Cronauer, D.; Kropf, A. J.; Marshall, C. L. *Appl. Catal., A* **2007**, 333, (2), 177-191.
65. Connor, P. A.; Irvine, J. T. S. *Electrochim. Acta* **2002**, 47, (18), 2885-2892.
66. Ernst, B.; Bensaddik, A.; Hilaire, L.; Chaumette, P.; Kiennemann, A. *Catal. Today* **1998**, 39, (4), 329-341.
67. Cheng, G.; Carter, J. D.; Guo, T. *Chem. Phys. Lett.* **2004**, 400, (1-3), 122-127.
68. Petitto, S. C.; Marsh, E. M.; Carson, G. A.; Langell, M. A. *J. Mol. Catal. A: Chem.* **2008**, 281, (1-2), 49-58.

69. Tompkins, H. G.; Augis, J. A. *Oxid. Met.* **1981**, 16, (5), 355-369.
70. Xiao, X.; Liu, X.; Zhao, H.; Chen, D.; Liu, F.; Xiang, J.; Hu, Z.; Li, Y. *Adv. Mater.* **2012**, 24, (42), 5762-5766.
71. Adamson, A. W.; Gast, A. P., *Physical chemistry of surfaces*. Wiley: 1997.
72. Wolf, D. *Phys. Rev. Lett.* **1992**, 68, (22), 3315-3318.
73. Henrich, V. E.; Cox, P. A., *The Surface Science of Metal Oxides*. Cambridge University Press: 1994.
74. Al-Abadleh, H. A.; Grassian, V. H. *Surf. Sci. Rep.* **2003**, 52, (3-4), 63-161.
75. Zasada, F.; Piskorz, W.; Stelmachowski, P.; Kotarba, A.; Paul, J.-F. o.; Płociński, T.; Kurzydłowski, K. J.; Sojka, Z. *J. Phys. Chem. C* **2011**, 115, (14), 6423-6432.
76. Zhang, H.; Hu, B.; Sun, L.; Hovden, R.; Wise, F. W.; Muller, D. A.; Robinson, R. D. *Nano Lett.* **2011**, 11, (12), 5356-5361.
77. Nam, K. M.; Shim, J. H.; Han, D. W.; Kwon, H. S.; Kang, Y. M.; Li, Y.; Song, H.; Seo, W. S.; Park, J. T. *Chem. Mater.* **2010**, 22, (15), 4446-4454.

APPENDIX D

D SUPPLEMENTARY INFORMATION FOR CHAPTER 4

Transmission Electron Microscopy

TEM images of the nanoparticle samples were obtained using a FEI Tecnai T12 microscope operating at 120 keV. At least 200 particles were analyzed per sample to obtain a representative size distribution. High-resolution TEM (HRTEM) was performed on a FEI Tecnai F20 microscope operating at 200 keV.

X-ray Diffraction

XRD (X-ray diffraction) diffraction patterns were collected using a Scintag theta-theta x-ray diffractometer (Cu K α radiation).

X-ray Absorption Spectroscopy

The raw spectra were averaged and processed using ATHENA,¹ part of the IFEFFIT software package. Data processing involved edge determination from the first inflection point in the absorption spectrum, background subtraction using the AUTOBK algorithm, and normalization of the EXAFS modulations (greater than 50 eV above the edge).² The spectra were converted from energy-space to k-space, then underwent a phase shift specific to the absorbing and scattering elements.³ A k-weight of 1 was chosen in order to best observe the scattering of oxygen, a low-Z scattering element.⁴ Cobalt is also a lower-scattering element,⁴ and when a k-weight of 1 was used the intensity modulations were evenly distributed through

the k-space region of interest (0–10 Å⁻¹), indicating an appropriate weighting was applied.⁴ The spectra was then Fourier Transformed into R-space.³ In R-space each peak appears at the relative spacing of that particular shell from the scattering atom, which enables visualization of the relative contributions as a function of inter-atomic distance.² The data was then analyzed by the ab-initio method and multiple data set fitting in k-space and R-space using ARTEMIS.¹ Crystal structures from theory were inputted using ATOMS.⁵ By fitting well-matched theoretical pathways to the experimental spectra through loosening variables to deviate from the theoretical bulk structures, specific structural information could be determined including coordination number, inter-atomic spacing and mean-squared disorder, as outlined in the EXAFS equation.^{2,6,7,8}

$$\chi(k) = \sum_{\Gamma} \left[\frac{N_{\Gamma} S_0^2 F_{\Gamma}(k)}{2kR_{\Gamma}^2} e^{-2k^2 \sigma_{\Gamma}^2} e^{-2R_{\Gamma}/\lambda(k)} \times \sin(2kR_{\Gamma} + \phi_{\Gamma}(k)) \right] \quad (1)$$

Γ is the summation over the individual scattering pathways, k is the photoelectron wavevector, $F_{\Gamma}(k)$ is the scattering amplitude, $\lambda(k)$ is the mean free path of inelastically-scattered photoelectrons and $\Phi(k)$ is the phase shift, which is calculated as a function of the absorbing and scattering atom. S_0^2 , the amplitude reduction factor, was set to 0.754 during fitting (the value extracted from fitting the Co foil). This enables a more accurate determination of the coordination number.⁷ Degeneracy (N_{Γ}), half-path length (R_{Γ}), energy shift parameter (E_0), and mean-squared disorder (σ_{Γ}^2), which includes contributions from structural and thermal disorder (Debye-Waller factor),² were allowed to float during the fit in order to extract the values specific to each nanoparticle sample. ΔE_0 was fixed to a single variable for all pathways with the same absorbing and scattering element in order to limit the number of variables, as ΔE_0 values should be nearly equal for similar bonds within the structure.⁹

The EXAFS spectra were fit with a theoretical model in R-space and k-space in order to extract accurate parameters for the average radial structure around a central core Co atom. Each fitting model resulted in an “R-factor” value between 0.015 and 0.027 in R-space and between 0.045 and 0.049 in k-space. The R-factor value is a statistical measurement which is minimized in order to ensure quality of the fit, where a value less than 0.05 is commonly referred as a good fit. The minimization of this statistical factor proves that our best-fit models are well-correlated to the experimental data.

Oxidation in solution

The as-synthesized ϵ -Co NPs (~100mg) dispersed in hexane (4ml) were injected into the flask filled with TOPO (tri-*n*-octylphosphine oxide, 8g). The flask is vacuumed at 70°C in order to remove hexane and heat up to 200°C. When the temperature is stabilized, air is bubbled into the solution through a needle. After the reaction progressed for 3 hours, the solution was quenched by water bath. The aliquot was taken from the solution after 2 hours of the reaction. The sample was isolated by centrifugation with excess acetone.

Ligand attachment of Co₃O₄ NPs

After the standard oxidation process at 200 °C for 90 mins, the Co₃O₄ NPs (20 mg) were redispersed in a mixture of hexane (2 mL) and oleylamine (2 mL) and ultrasonicated for 10 mins. The solution became black after the ultrasonication. The

NPs were cleaned by adding acetone and centrifuge. This cleaning process was repeated one more time. The final NPs were well suspended in hexane even after the cleaning process as shown in **Figure 5.5**.

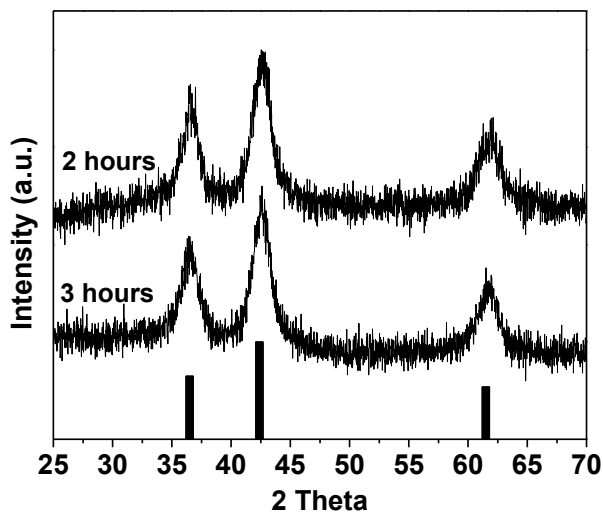


Figure D.1 XRD patterns of the NPs oxidized in a solution phase at 200°C. The samples oxidized for 2 and 3 hours in a solution are well matched with CoO phase (black bar, JCPDS 48-1719). No Co_3O_4 or $\epsilon\text{-Co}$ phase is observed.

Table D.1 Full width at half maximum (FWHM) of two peaks (Co-O and Co-Co) from EXAFS spectra in Figure 5.2b.

Sample	FWHM of Co-O peak (\AA)	FWHM of Co-Co peak (\AA)
$\epsilon\text{-Co}$	0.97	0.74
5 mins	0.8	0.71
10 mins	0.95	0.73
30 mins	0.8	0.7
90 mins	0.778	0.95

EXAFS data fitting parameters.

Table D.2 EXAFS fitting parameters for the ϵ -Co NP sample

Single Scattering Pathways from ϵ -Co crystal structure							
Pathway	N (acc.)	N (exp.)	R (Å)	ΔR (Å)	R + ΔR (Å)	E_0 (eV)	σ^2 (Å ²)
Co ₁ – Co ₁	1.2	1.254	2.282	-0.148	2.134	6.4823	0.0118
	0.4	0.418	2.996	-0.148	2.848	6.4823	0.0118
	2.4	2.448	3.881	0.0583	3.939	6.4823	0.00704
	0.4	0.408	3.984	0.0583	4.042	6.4823	0.00704
	0.4	0.408	4.154	0.0583	4.212	6.4823	0.00704
	2.4	2.395	4.878	-0.150	4.728	6.4823	0.0159
	2.4	2.395	4.952	-0.150	4.802	6.4823	0.0159
	1.2	1.197	5.000	-0.150	4.850	6.4823	0.0159
	3.2	3.193	5.280	-0.150	5.130	6.2823	0.0159
Co ₁ – Co ₂ / Co ₂ – Co ₁	2.4	2.201	2.487	-0.0426	2.444	6.4823	0.00942
	2.4	2.201	2.543	-0.0426	2.500	6.4823	0.00942
	2.4	2.201	2.587	-0.0426	2.544	6.4823	0.00942
	2.4	2.172	3.840	-0.2017	3.638	6.4823	0.0128
	2.4	2.172	4.061	-0.2017	3.859	6.4823	0.0128
	2.4	2.172	4.231	-0.2017	4.029	6.4823	0.0128
	2.4	2.172	4.368	-0.2017	4.166	6.4823	0.0128
	2.4	2.254	4.551	-0.2683	4.283	6.4823	0.00925
	2.4	2.254	4.740	-0.2683	4.472	6.4823	0.00925
	2.4	2.254	4.863	-0.2683	4.595	6.2823	0.00925
	2.4	2.254	4.909	-0.2683	4.641	6.4823	0.00925
	Co ₂ – Co ₂	2.4	2.202	2.555	0.1181	2.673	6.4823
1.2		1.101	2.580	0.1181	2.698	6.4823	0.00762
1.2		1.101	3.158	0.1181	3.040	6.4823	0.00762
0.6		0.542	3.531	-0.2373	3.294	6.4823	0.01285
1.2		1.084	3.765	-0.2373	3.528	6.4823	0.01285
0.6		0.542	4.127	-0.2373	3.890	6.4823	0.01285
2.4		2.167	4.207	-0.2373	3.970	6.4823	0.01285
1.2		1.084	4.259	-0.2373	4.022	6.4823	0.01285
2.4		2.167	4.401	-0.2373	4.164	6.2823	0.01285
2.4		2.167	4.463	-0.2373	4.226	6.4823	0.01285
0.6		0.544	4.610	0.0578	4.668	6.4823	0.0137
0.6		0.544	4.772	0.0578	4.830	6.4823	0.0137
2.4		2.175	4.979	0.0578	5.037	6.4823	0.0137
2.4		2.175	5.011	0.0578	5.069	6.4823	0.0137
1.2		1.088	5.066	0.0578	5.124	6.4823	0.0137
0.6		0.544	5.229	0.0578	5.287	6.4823	0.0137
Single Scattering Pathways from CoO							

Pathway	N (acc.)	N (exp.)	R (Å)	ΔR (Å)	R + ΔR (Å)	E ₀ (eV)	σ^2 (Å ²)
Co - O	6	1.165	2.133	-0.0643	2.069	0.5488	0.00278
	8	1.576	3.695	0.0506	3.746	0.5488	0.00358
	24	4.727	4.770	0.0506	4.821	0.5488	0.00358
Co - Co	12	2.334	3.017	0.0921	3.109	6.4823	0.00608
	6	0.793	4.267	0.1616	4.429	6.4823	0.00709
	24	3.173	5.226	0.1616	5.388	6.4823	0.00709

Table D.3 EXAFS fitting parameters for the 5 mins oxidation sample

Single Scattering Pathways from ϵ -Co crystal structure							
Pathway	N (acc.)	N (exp.)	R (Å)	ΔR (Å)	R + ΔR (Å)	E ₀ (eV)	σ^2 (Å ²)
Co ₁ - Co ₁	1.2	0.645	2.282	0.1776	2.460	0.077	0.0113
	0.4	0.215	2.996	0.1776	3.174	0.077	0.0113
	2.4	1.287	3.881	-0.0202	3.861	0.077	0.0103
	0.4	0.214	3.984	-0.0202	3.964	0.077	0.0103
	0.4	0.214	4.154	-0.0202	4.134	0.077	0.0103
	2.4	1.286	4.878	-0.2702	4.608	0.077	0.0116
	2.4	1.286	4.952	-0.2702	4.682	0.077	0.0116
	1.2	0.643	5.000	-0.2702	4.730	0.077	0.0116
	3.2	1.715	5.280	-0.2702	5.010	0.077	0.0116
Co ₁ - Co ₂ / Co ₂ - Co ₁	2.4	1.244	2.487	-0.0282	2.459	0.077	0.00993
	2.4	1.244	2.543	-0.0282	2.515	0.077	0.00993
	2.4	1.244	2.587	-0.0282	2.559	0.077	0.00993
	2.4	1.247	3.840	0.0379	3.878	0.077	0.0109
	2.4	1.247	4.061	0.0379	4.099	0.077	0.0109
	2.4	1.247	4.231	0.0379	4.269	0.077	0.0109
	2.4	1.247	4.368	0.0379	4.406	0.077	0.0109
	2.4	1.246	4.551	-0.2566	4.295	0.077	0.0111
	2.4	1.246	4.740	-0.2566	4.483	0.077	0.0111
	2.4	1.246	4.863	-0.2566	4.606	0.077	0.0111
	2.4	1.246	4.909	-0.2566	4.652	0.077	0.0111
Co ₂ - Co ₂	2.4	1.271	2.555	0.1718	2.727	0.077	0.00930
	1.2	0.635	2.580	0.1718	2.752	0.077	0.00930
	1.2	0.635	3.158	0.1718	3.330	0.077	0.00930
	0.6	0.315	3.531	0.009065	3.540	0.077	0.00987
	1.2	0.629	3.765	0.009065	3.774	0.077	0.00987
	0.6	0.315	4.127	0.009065	4.136	0.077	0.00987
	2.4	1.259	4.207	0.009065	4.216	0.077	0.00987
	1.2	0.629	4.259	0.009065	4.268	0.077	0.00987

	2.4	1.259	4.401	0.009065	4.410	0.077	0.00987
	2.4	1.259	4.463	0.009065	4.472	0.077	0.00987
	0.6	0.312	4.610	-0.0192	4.591	0.077	0.0111
	0.6	0.312	4.772	-0.0192	4.753	0.077	0.0111
	2.4	1.249	4.979	-0.0192	4.960	0.077	0.0111
	2.4	1.249	5.011	-0.0192	4.992	0.077	0.0111
	1.2	0.625	5.066	-0.0192	5.047	0.077	0.0111
	0.6	0.312	5.229	-0.0192	5.210	0.077	0.0111
Single Scattering Pathways from CoO							
Pathway	N (acc.)	N (exp.)	R (Å)	ΔR (Å)	R + ΔR (Å)	E₀ (eV)	σ² (Å²)
Co - O	6	2.796	2.133	-0.0773	2.056	-3.935	0.00691
	8	3.707	3.695	-0.1401	3.555	-3.935	0.00674
	24	11.109	4.770	- 0.00847	4.762	-3.935	0.0113
Co - Co	12	5.271	3.017	0.0214	3.038	0.077	0.00893
	6	2.633	4.267	-0.1786	4.088	0.077	0.0112
	24	10.485	5.226	0.0556	5.282	0.077	0.0107

Table D.4 EXAFS fitting parameters for the 10 mins oxidation sample

Single Scattering Pathways from ϵ-Co crystal structure							
Pathway	N (acc.)	N (exp.)	R (Å)	ΔR (Å)	R + ΔR (Å)	E₀ (eV)	σ^2 (Å²)
Co ₁ – Co ₁	1.2	0.492	2.282	0.0535	2.336	-3.738	0.0064
	0.4	0.164	2.996	0.0535	3.046	-3.738	0.0064
	2.4	0.982	3.881	-0.0861	3.795	-3.738	0.00804
	0.4	0.164	3.984	-0.0861	3.898	-3.738	0.00804
	0.4	0.164	4.154	-0.0861	4.068	-3.738	0.00804
	2.4	0.980	4.878	-0.0532	4.825	-3.738	0.01096
	2.4	0.980	4.952	-0.0532	4.899	-3.738	0.01096
	1.2	0.490	5.000	-0.0532	4.947	-3.738	0.01096
	3.2	1.306	5.280	-0.0532	5.227	-3.738	0.01096
Co ₁ – Co ₂ / Co ₂ – Co ₁	2.4	0.901	2.487	-0.0430	2.444	-3.738	0.00971
	2.4	0.901	2.543	-0.0430	2.500	-3.738	0.00971
	2.4	0.901	2.587	-0.0430	2.544	-3.738	0.00971
	2.4	0.949	3.840	-0.0577	3.782	-3.738	0.00904
	2.4	0.949	4.061	-0.0577	4.003	-3.738	0.00904
	2.4	0.949	4.231	-0.0577	4.173	-3.738	0.00904
	2.4	0.949	4.368	-0.0577	4.310	-3.738	0.00904
	2.4	0.947	4.551	0.0101	4.561	-3.738	0.01031
	2.4	0.947	4.740	0.0101	4.750	-3.738	0.01031
	2.4	0.947	4.863	0.0101	4.873	-3.738	0.01031
	2.4	0.947	4.909	0.0101	4.919	-3.738	0.01031
Co ₂ – Co ₂	2.4	0.981	2.555	0.0962	2.651	-3.738	0.00613
	1.2	0.490	2.580	0.0962	2.676	-3.738	0.00613
	1.2	0.490	3.158	0.0962	3.254	-3.738	0.00613
	0.6	0.240	3.531	-0.2801	3.251	-3.738	0.00820
	1.2	0.480	3.765	-0.2801	3.485	-3.738	0.00820
	0.6	0.240	4.127	-0.2801	3.847	-3.738	0.00820
	2.4	0.960	4.207	-0.2801	3.927	-3.738	0.00820
	1.2	0.480	4.259	-0.2801	3.979	-3.738	0.00820
	2.4	0.960	4.401	-0.2801	4.121	-3.738	0.00820
	2.4	0.960	4.463	-0.2801	4.183	-3.738	0.00820
	0.6	0.241	4.610	-0.3260	4.284	-3.738	0.01022
	0.6	0.241	4.772	-0.3260	4.446	-3.738	0.01022
	2.4	0.965	4.979	-0.3260	4.653	-3.738	0.01022
	2.4	0.965	5.011	-0.3260	4.685	-3.738	0.01022
	1.2	0.483	5.066	-0.3260	4.740	-3.738	0.01022
	0.6	0.241	5.229	-0.3260	4.903	-3.738	0.01022
Single Scattering Pathways from CoO							
Pathway	N (acc.)	N (exp.)	R (Å)	ΔR (Å)	R + ΔR (Å)	E₀ (eV)	σ^2 (Å²)

Co - O	6	3.507	2.133	-0.0570	2.076	-2.064	0.00739
	8	4.670	3.695	-0.1967	3.498	-2.064	0.00743
	24	13.950	4.770	-0.1820	4.588	-2.064	0.01224
Co - Co	12	7.490	3.017	-0.0456	2.971	-3.738	0.01093
	6	3.742	4.267	0.0989	4.356	-3.738	0.01096
	24	14.954	5.226	-0.0435	5.183	-3.738	0.01101

Table D.5 EXAFS fitting parameters for the 30 mins oxidation sample

Single Scattering Pathways from CoO							
Pathway	N (acc.)	N (exp.)	R (Å)	ΔR (Å)	R + ΔR (Å)	E₀ (eV)	σ² (Å²)
Co - O	6	3.72	2.133	-0.00912	2.124	-3.399	0.00678
	8	4.96	3.695	-0.16698	3.528	-3.399	0.00683
	24	14.34	4.770	-0.12971	4.640	-3.399	0.01099
Co - Co	12	8.74	3.017	-0.03379	2.983	-3.420	0.00721
	6	4.37	4.267	0.13732	4.404	-3.420	0.00804
	24	17.44	5.226	-0.00916	5.217	-3.420	0.01109
Single Scattering Pathways from Co₃O₄							
Pathway	N (acc.)	N (exp.)	R (Å)	ΔR (Å)	R + ΔR (Å)	E₀ (eV)	σ² (Å²)
Co ₁ - O	1.33	0.37	1.985	-0.06643	1.919	-3.399	0.00644
	4	1.11	3.396	-0.07462	3.321	-3.399	0.00732
	4	1.11	4.245	0.01563	4.261	-3.399	0.00870
	4	1.11	5.060	-0.18108	4.879	-3.399	0.00990
Co ₁ - Co ₁	1.33	0.44	3.495	-0.25044	3.245	-3.420	0.01004
Co ₁ - Co ₂ / Co ₂ - Co ₁	8	2.57	3.347	-0.26409	3.083	-3.420	0.00847
	10.7	3.43	5.243	-0.08975	5.153	-3.420	0.01037
Co ₂ - O	4	1.01	1.891	0.05348	1.944	-3.399	0.00579
	1.33	0.34	3.258	-0.16319	3.095	-3.399	0.00799
	4	1.01	3.582	-0.16319	3.419	-3.399	0.00799
	8	2.01	4.457	-0.30384	4.153	-3.399	0.00905
	8	2.01	4.699	-0.30384	4.395	-3.399	0.00905
Co ₂ - Co ₂	4	1.31	2.854	-0.29889	2.555	-3.420	0.00883
	8	2.56	4.943	0.01259	4.956	-3.420	0.01468

Table D.6 EXAFS fitting parameters for the 90 mins oxidation sample

Single Scattering Pathways from Co_3O_4							
Pathway	N (acc.)	N (exp.)	R (Å)	ΔR (Å)	R + ΔR (Å)	E_0 (eV)	σ^2 (Å ²)
Co ₁ - O	1.33	1.34	1.985	0.13906	2.124	2.250	0.00407
	4	4.03	3.396	-0.08576	3.310	2.250	0.00598
	4	4.03	4.245	0.05140	4.296	2.250	0.00702
	4	4.02	5.060	-0.10769	4.952	2.250	0.00788
Co ₁ - Co ₁	1.33	1.39	3.495	-0.17337	3.322	-9.989	0.00730
Co ₁ - Co ₂ / Co ₂ - Co ₁	8	7.65	3.347	-0.20093	3.146	-9.989	0.00968
	10.7	9.98	5.243	-0.04813	5.195	-9.989	0.01032
Co ₂ - O	4	3.42	1.891	-0.01177	1.879	2.250	0.00770
	1.33	1.13	3.258	-0.05597	3.202	2.250	0.01095
	4	3.41	3.582	-0.05597	3.526	2.250	0.01095
	8	6.82	4.457	0.04282	4.500	2.250	0.01297
	8	6.82	4.699	0.04282	4.742	2.250	0.01297
Co ₂ - Co ₂	4	4.19	2.854	0.00630	2.860	-9.989	0.00824
	8	7.63	4.943	0.06375	5.007	-9.989	0.01498

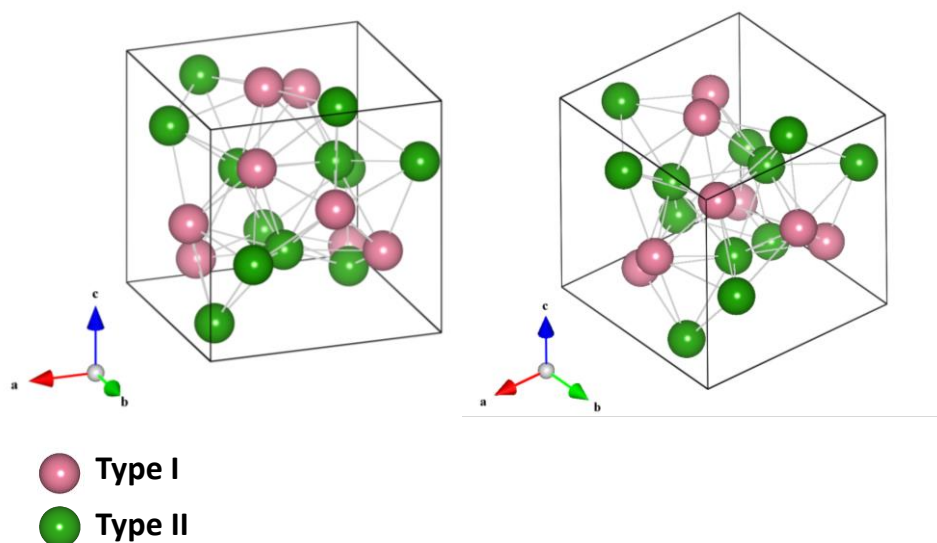


Figure D.2 The crystal structure of ϵ -cobalt. The pink and green atoms represent the type I and II cobalt atomic positions, respectively.

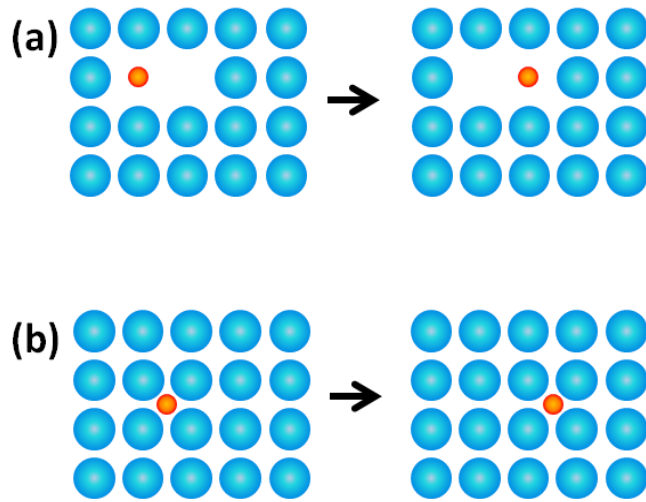


Figure D.3 The schematics of the diffusion mechanisms. The oxygen atom (red ball) can diffuse through the cobalt lattices (blue balls) by (a) the vacancy diffusion and (b) interstitial diffusion.

REFERENCES

1. Ravel, B.; Newville, M. *J. Synchrotron Radiat.* **2005**, 12, (4), 537-541.
2. Stern, E. A. *Contemp. Phys.* **1978**, 19, (4), 289-310.
3. Bunker, G., *Introduction to XAFS: a practical guide to X-ray absorption fine structure spectroscopy*. Cambridge University Press: Cambridge, 2010; p 260.
4. Koningsberger, D. C.; Mojet, B. L.; van Dorssen, G. E.; Ramaker, D. E. *Top. Catal.* **2000**, 10, (3), 143-155.
5. Ravel, B. *J. Synchrotron Radiat.* **2001**, 8, (2), 314-316.
6. Stern, E. A. *Phys. Rev. B* **1974**, 10, (8), 3027-37.
7. Ravel, B.; Kelly, S. D. *AIP Conf. Proc.* **2007**, 882, (1), 150-152.
8. Scott, R., *Physical Methods in Bioinorganic Chemistry: Spectroscopy and Magnetism*. University Science Books: 2000.
9. Michalowicz, A.; Vlais, G. *J. Synchrotron Radiat.* **1998**, 5, (5), 1317-1320.

CHAPTER 6

6 THE INTERPLAY BETWEEN CATION DIFFUSION AND STRAIN TO INDUCE SOLID-SOLID PHASE TRANSFORMATIONS IN 2D HETEROSTRUCTURED NANOCRYSTALS *

6.1 *Abstract*

Mechanisms of solid-solid phase transformations in heterostructured nanocrystals (NCs) are not well understood, but can be a tool to modulate new phases and optimize NC properties. Here, we demonstrate dual interface formation in NCs through cation exchange, creating epitaxial heterostructures within spherical NCs. The thickness of the inner-disk layer can be tuned to form two-dimensional (2D), single atomic layers (<1 nm). This unconventional heterostructure will open new routes to creating confined 2D layers in NCs, which should enable the study of special phenomena in NCs, such as a 2D hole gas or 2D quantum well. During the cation exchange reaction from copper sulfide to zinc sulfide (ZnS), we observe a solid-solid phase transformation of the copper sulfide phase in heterostructured NCs. As the cation exchange reaction is initiated, Cu ions replaced by Zn ions at the interfaces are accommodated in intrinsic Cu vacancy sites present in the initial roxbyite ($\text{Cu}_{1.81}\text{S}$) phase of copper sulfide, inducing a phase transition to djurleite ($\text{Cu}_{1.94}\text{S}$)/low

* Originally Submitted as: D.-H. Ha, A.H. Caldwell, M.J. Ward, S. Honrao, K. Mathew, R. Hovden, M.K.A. Koker, D.A. Muller, R.G. Hennig, and R.D. Robinson, "The interplay between cation diffusion and strain to induce solid-solid phase transformations in 2D heterostructured nanocrystals," *Submitted*

chalcocite (Cu_2S), which is a more thermodynamically stable phase than roxbyite. This result demonstrates that ion diffusion generated by a cation exchange reaction can initiate a solid-solid phase transition, and tune the phase of NCs. Further reaction leads to a thinner copper sulfide layer, and the epitaxial strain at the interfaces between copper sulfide and ZnS increases. This strain energy reaches a maximum when the thickness of the copper sulfide disk is ~ 5 nm and induces another phase transformation back to roxbyite. This second phase transition occurs to minimize strain energy, as the roxbyite structure shares a similar sulfur sublattice with wurtzite ZnS. The observation of a solid-solid phase transformation in our unique heterostructured NCs provides a new pathway to control desired phases and an insight into the influence of cation exchange on nanoscale phase transitions in heterostructured materials.

6.2 Introduction

Cation exchange is a powerful method to post-synthetically manipulate the composition of as-synthesized nanocrystals (NCs).¹ Cation exchange can induce novel NC structural changes, including doping,^{2, 3} heterostructure formation^{4, 5, 6, 7} and core-shell formation.⁸ The exact mechanistic pathways still remain unknown for nanoscale cation exchange reactions, but certain aspects of the transformation have been empirically determined and qualitative models from minerals and thin-films have been applied to the NC system.^{1, 9, 10, 11}

Cation exchange reactions can act as useful templates to study solid-solid phase transformations in nanoparticles to determine how such processes differ from

those in bulk solids. When cations are exchanged from the starting material (parent NC) into the fully exchanged material (child NC), a new phase is often created that is the lowest-energy phase of the fully exchanged material (e.g., wurtzite CdS into orthorhombic Ag₂S).^{1, 5} This process is a compositional conversion, not a conventional phase transformation governed by the phase diagram. However, it has recently been shown that the child NC can exist as a stabilized, metastable material either through a partial exchange, such as the formation of a CdS and Ag₂S superlattice,⁵ or through a full exchange, such as the formation of Cu₂Se nanocrystals in a metastable hexagonal phase from wurtzite CdSe.¹² Previous research on solid-solid phase transformations in NCs has shown that NCs transform as a single-domain nucleation event,^{13, 14} that metastable structures can exist in ambient conditions,¹⁵ and that thermodynamic considerations are responsible for the structural metastability rather than the size-dependence of the kinetics.¹⁵ In these solid-solid phase transformation experiments, pressure has been induced in free-standing NCs with exposed surfaces,¹³ and these exposed surfaces may influence the transformation: if low index surfaces are dominant then the phase change results in high index, high energy surfaces under high pressure that then act to destabilize the high pressure phase and initiate nucleation of a phase transition. However, if one or more of the surfaces in the nanocrystal are confined, say through an epitaxial junction with another crystal, it is unclear how the surface energies of the free surfaces, the energy of the surface interface, and the effects of diffusion in the crystal will affect the transformation. Little is known about solid-solid transformations in NC heterostructures, specifically

how an epitaxial alignment of heterostructures will influence the phase and size of the domain.

Copper sulfide (Cu_{2-x}S , $0 \leq x \leq 1$) is a p-type semiconductor with potential applications in photovoltaic devices,¹⁶ superionic materials,^{17, 18} battery electrodes,¹⁹ and photocatalysis.²⁰ As the properties of copper sulfides are sensitive to both the Cu-S stoichiometry and crystal structures, it is critical to finely tune their phases for use in applications. In addition, copper sulfide is an ideal template material to investigate solid-solid phase transformations because copper sulfide shows unique transformation behaviors such as transient structural transformations under electron-beam irradiation²¹ and size dependent solid–solid phase transitions.²² Heterostructure architectures in NCs enable modulation of electrical and optical properties.²³ In particular, interfacial strain in heterostructures is a key mechanism for controlling electronic band structure,²⁴ morphology,^{5, 25} and catalytic activity.²⁶ Alteration of lattice parameters through lattice mismatch in heterostructures has been widely utilized.^{23, 24} However, the phase transition induced by lattice strain in free standing NCs is not well established yet.

In this report we describe a method to create a dual-interface heterostructure through cation exchange in copper sulfide NCs. We find that cation exchange initially prompts a solid-solid phase transformation in the parent NC copper sulfide phase, transforming it to a lower-energy phase. As the copper sulfide layer becomes thinner it transforms back to the original parent phase due to epitaxial alignment with the child NC material. This is a system in which not only does strain induce a phase

transformation in the NC during cation exchange, but also the cation exchange reaction itself initiates a solid-solid phase transformation in the parent NC.

6.3 Results

Transmission electron microscopy (TEM) images show the morphology evolution during the transformation (**Fig. 6.1**, t = thickness of copper sulfide disk). The initial copper sulfide NCs are spherical with a uniform size (**Fig. 6.1a**, 22 nm, std dev: 3.4%). After the cation exchange reaction is initiated, small ZnS grains symmetrically nucleate on opposite sides of the spherical NCs (**Fig. 6.1b**). At the onset of ZnS grain growth, the ZnS interfaces curve inward toward the center of the NC (convex ZnS interface). The radius of the interface curvature is ~20 nm at the early stage of the cation exchange reaction when the copper sulfide layer is ~15 nm in thickness (**Fig. 6.1b**, t = 15 nm). This interface curvature gradually decreases as the cation exchange progresses, with the copper sulfide region in the center of the NCs eventually becoming a disk-like 2-dimensional (2D) layer (**Fig. 6.1c-e**), the thickness of which can be tuned by controlling the reaction time (**Table E.1**). These interfaces are stable; the heterostructured NCs retain their interface structure even after a week (**Fig. E.1**). When the thickness of the copper sulfide layer is ~8 nm (**Fig. 6.1c**, t = 8 nm) the NCs become slightly elongated perpendicular to the interfaces, up to ~10%. At the end of the reaction most NCs are fully converted to ZnS, with the spherical shape and size of the initial copper sulfide NCs preserved; however, approximately 30% of the final NCs maintain a thin copper sulfide layer or show evidence of

superimposed lattices from Moire patterns in TEM images of the NCs. The thin copper sulfide layer seen in the center of these NCs disappears during tilting of the TEM specimen holder, suggesting that the value of 30% could be an underestimate of ZnS with copper sulfide disks percentage (see **Fig. E.2**). High-angle annular dark-field (HAADF) imaging with electron energy loss spectroscopic (EELS) mapping confirms that the heterostructured NCs have Zn, Cu, and S elements (**Fig. 6.1f**). In these “sandwich-like” samples the electron microscopy study confirms that the two symmetrically-growing grains at opposite ends of the NCs are ZnS and that the centrally-located “disk” is copper sulfide (**Fig. 6.1f**).

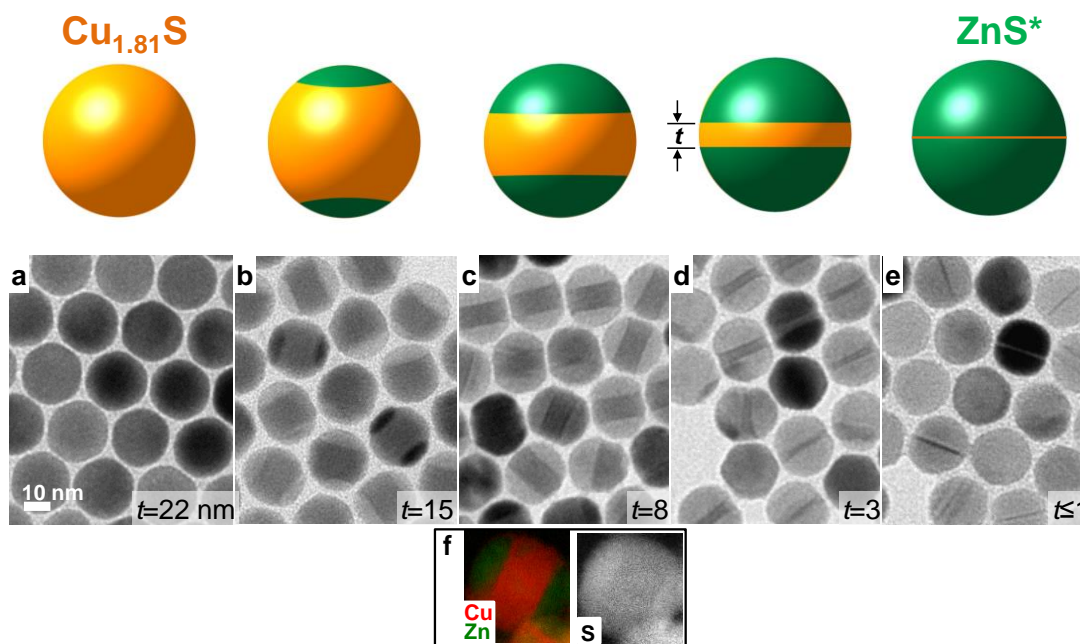


Figure 6.1 Cation exchange transformation of copper sulfide nanoparticles into dual-interface heterostructured particles with zinc sulfide caps. Schematic (top) and TEM images (bottom) show the composition change from the initial copper sulfide particle (a, leftmost) into a ZnS (e, rightmost) with a copper sulfide thin disk. The final product is denoted ZnS* because a thin 2D copper sulfide disk is present in the TEM images for ~30% of the nanoparticles. The copper sulfide disk thickness (“ t ”) is indicated. (f) HAADF EELS image showing the presence of Cu and Zn (left) and S (right) in the heterostructured particles.

The final NC sample either resolves into fully crystalline ZnS NCs (estimated at around 70% of the NCs), or NCs with a thin ($t < 1$ nm) 2D copper sulfide layer between ZnS grains. For the fully converted ZnS NCs, high-resolution TEM (HRTEM) images indicate good crystallinity with relatively few defects (**Fig. 6.2a**) and approximately 20% show stacking faults (**Fig. 6.2b**). The predominance of final ZnS crystals with low-defects suggests that the dual ZnS growth fronts are well-aligned to the anion sublattice and planar. For the final NCs containing a 2D layer of material, HAADF analysis confirms that the atomically thin layer is composed of Cu and S and that the surrounding material consists of Zn and S (**Fig. 6.2c**). The HAADF and EELS analysis shows that the Cu-S layer primarily occupies a single atomic plane in regions, but may also extend to adjacent layers. The regions where the Cu concentration width extends two layers may be the result of a planar step viewed in projection or two adjacent Cu-S layers. That copper sulfide remains in the final NCs for ~30 % of the samples indicates there is a stabilization force for the copper sulfide phase even in an aggressive reaction environment. Even Cu-S NCs reacted at higher temperatures for longer times (100 °C for 30 minutes) also result in ~30 % of the final NCs with thin layers (see **Fig. E.3**). This HAADF analysis also suggests that Cu-Zn-S alloy formation does not occur and that a sharp heterostructure interface is maintained in the final NCs. Core-shell structures formed through cation has been studied extensively^{9, 27} but an atomically thin 2D planar structure centered in a spherical NC has not been achieved previously, to our knowledge. This heterostructure formation is not limited to a specific size or shape of copper sulfide NCs. Large (~40 nm) roxbyite NCs of hexagonal bipyramid shape also transform to 2D heterostructures through this

cation exchange reaction (see **Fig. E.4**). The ability to create an atomically thin copper sulfide layer in a NC could be useful for examining unique phenomena such as a 2D hole gas, 2D quantum well, or quantized plasmons.²⁸

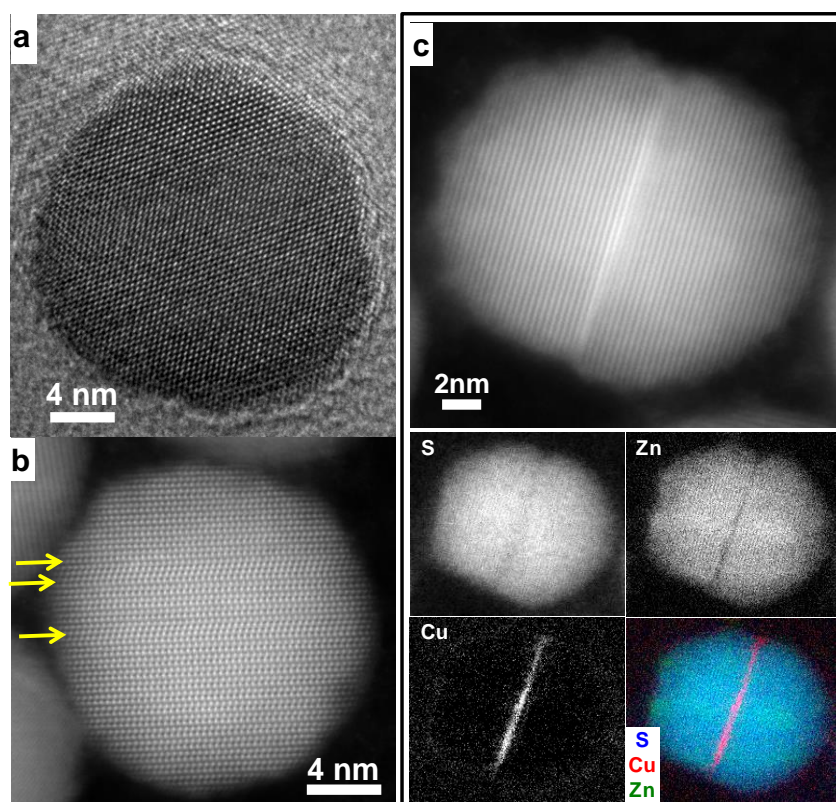


Figure 6.2 HRTEM and HAADF images of the cation exchange reaction final sample. (a) HRTEM images show most ZnS* final sample nanocrystals as perfect crystals without defects. (b) HAADF HRTEM image showing stacking faults as indicated by yellow arrows. Approximately 20% of ZnS* final nanocrystals have stacking faults. (c) HAADF EELS of the final samples with thin 2D disks show Cu and S in the internal disk region and Zn and S in the surrounding regions. About 30% of the disks show apparent copper sulfide thin disks in the center of nanocrystals indicating that a Cu-Zn-S alloy does not occur.

Compared to conventional film deposition techniques such as molecular beam epitaxy (MBE), colloidal nanoparticles present several advantages as a route toward 2D quantum well structures. The relative cost and simplicity of solution-phase syntheses make them attractive from a resources perspective. Solution-phase processing of colloids makes their handling more versatile and enables the industrial-levels of throughput necessary for device fabrication. Colloidal heterostructure NCs exhibit greater flexibility with regards to particle geometry and heterostructure arrangement²⁹: traditional thin film fabrication requires the clever manipulation of interfacial strain and surface energies to achieve confined structures beyond large-area planar layers. MBE quantum dots are often limited to shapes such as square pyramidal^{29, 30, 31, 32} while colloidal nanocrystal heterostructures can have multiple morphologies such as spherical dots, nanorods,^{5, 33} and branched structures⁵. Moreover, the nature of thin film techniques requires that the nanostructures be attached to a substrate, barring use in *in-situ* biological applications such as sensors and labelling.

X-ray diffraction (XRD) patterns of NC samples confirm the chemical transformation from $\text{Cu}_{1.81}\text{S}$ to ZnS (**Fig. 6.3a,b**). The XRD pattern of the initial copper sulfide NCs (**Fig. 6.3a**, orange plot) is well-matched with the roxbyite phase (**Fig. 6.3a**, orange bars, JCPDS 23-0958), which has ~ 1.81 ($\text{Cu}_{58}\text{S}_{32}$) stoichiometry between Cu and S atoms.^{34, 35} Roxbyite has a triclinic crystal structure and is readily synthesized in nanomaterials but is uncommon for bulk syntheses.^{34, 35, 36} Scherrer analysis of an XRD pattern of the initial copper sulfide NCs gives a ~ 22.5 nm grain size, which is consistent with the NC diameter measured from TEM images (~ 22 nm).

As the extent of cation exchange increases, the XRD contribution from the roxbyite phase gradually decreases, and the ZnS XRD contribution dominates. The peaks corresponding to copper sulfide and ZnS remain distinct during the transformation, suggesting the absence of Cu-Zn-S alloy formation. Interestingly, the XRD peaks corresponding to the initial roxbyite phase show significant shifts toward smaller 2θ angles at the onset of the cation exchange reaction between the initial copper sulfide NCs ($t = 22\text{nm}$) and NCs with small ZnS caps ($t = \sim 20\text{ nm}$) (**Fig. 6.3b**). The maximum shift toward smaller angles is $\sim 0.5^\circ$ for the diffraction peaks at 48.9° and 49.2° for the 5 minute sample, the NCs of which have small ZnS grains ($\sim 1\text{ nm}$ thick, $t = \sim 20\text{ nm}$) as measured from TEM images. A shift of this magnitude toward smaller 2θ angles implies that either a phase transition occurs in the copper sulfide phase or the crystal lattice expands ($\sim 1.1\%$ lattice expansion). The shifted peak positions match the reference peak positions of higher Cu-content copper sulfide phases, such as djurleite $\text{Cu}_{1.94}\text{S}$ (**Fig. 6.3b**) or low-chalcocite Cu_2S . After the initial shift to smaller 2θ angles, the XRD peaks shift towards larger 2θ angles, indicating that the lattice parameters of the copper sulfide phase are decreasing during cation exchange. The peak at 48.9° for the initial copper sulfide NCs shifts to 49° for the $t = 13\text{ nm}$ NC sample and to 49.1° for the $t = 7\text{ nm}$ NC sample. This peak shifts toward larger 2θ angles indicate that a $\sim 0.4\%$ lattice contraction occurs for the $t = 7\text{ nm}$ NCs relative to the initial copper sulfide NCs. When $t < 7\text{ nm}$, the XRD signal from ZnS dominates the XRD pattern. The XRD pattern of the final sample is well-matched with that of the wurtzite ZnS phase (**Fig. 6.3a**, green bars, JCPDS 36-1450), showing no discernable impurity peaks or copper sulfide contributions. The final sample shows a $\sim 23\text{ nm}$

grain size, as determined from a Scherrer analysis (see Method section), which is similar to the NC size measured from TEM images (~22 nm, std. dev: 4%), indicating that the majority of the NCs in the final sample are single crystalline ZnS or have two ZnS grains that are crystallographically well matched as previously seen in stacked nanosheets.³⁷

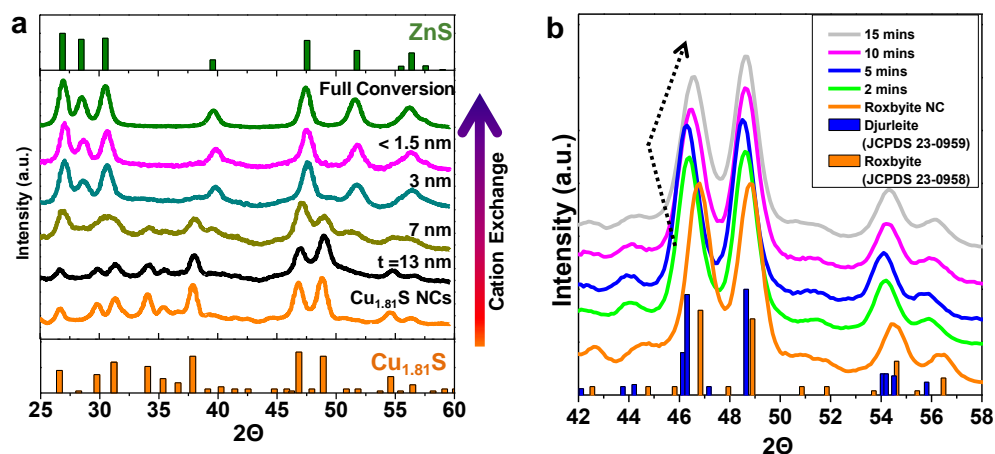


Figure 6.3 XRD structural evolution of heterostructured particles. (a) XRD

patterns show the initial particles are well matched to roxbyite phase (a, orange plot and bars) and the phase evolves to ZnS at the conclusion of the reaction (a, green plot and bars). The copper sulfide disk thickness “*t*” maps the progression. (b) Multiple scans for samples at the early stage of cation exchange reaction from the initial Cu_{1.81}S nanocrystals up to a *t* = 19 nm sample. Samples are labeled in terms of the reaction time because the ZnS grains are small up to 15 minutes of the reaction. The 15 minutes sample corresponds to approximately *t* = 19 nm (ZnS caps grain thickness = ~1.5 nm). The diffraction peaks of the initial roxbyite NC shift to lower 2θ values during the early stages of the reaction (b, 0 to 15 mins) and then shift back to higher 2θ values.

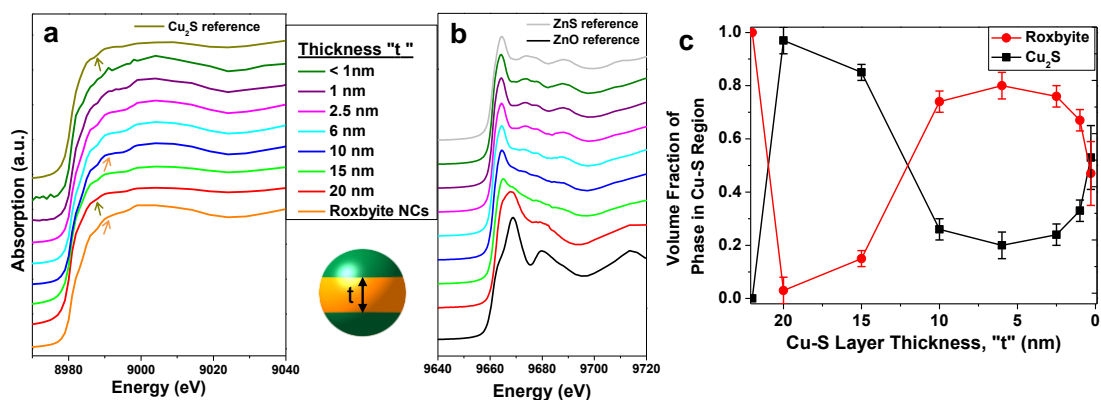


Figure 6.4 XANES structural evolution of heterostructured NCs. XANES

measured at Cu (a) and Zn (b) K-edges. As the transformation occurs the thickness of the copper sulfide region decreases, which is indicated in the legend (" t "). The initial copper sulfide roxbyite nanocrystals are shown at the bottom in orange (a). (Note: XANES of the Zn edge results in no spectra (b)). Arrows in (a) point out key spectral features of initial roxbyite phase (orange, and orange arrows) and final Cu_2S phase (top spectra in army green, and army green arrows) which indicate an immediate change in XANES spectra from initial sample to $t=20$ sample (red) and then back to roxbyite ($t=10$ sample, blue). The reference spectrum for Cu_2S is shown in (a, army green) and the reference spectra for ZnS and ZnO are shown in (b). During cation exchange, the early nanocrystal samples ($t = 20$ and 15 nm) exhibit XANES features consistent with Cu_2S but not of the initial $\text{Cu}_{1.81}\text{S}$ roxbyite phase. (c) Copper sulfide phase volume fraction as a function of Cu-S layer thickness derived from linear combination fitting of the Cu K-edge XANES using $\text{Cu}_{1.81}\text{S}$ roxbyite (red circles) and Cu_2S low chalcocite (black squares) phases as reference standards.

X-ray absorption spectroscopy (XAS) provides a complementary approach to XRD for investigating phase transitions in the NCs (**Fig. 6.4**).^{38, 39, 40} The high sensitivity and elemental specificity of XAS makes it an ideal method for probing the local chemical environment of complex systems such as our copper sulfide-zinc sulfide heterostructured NCs. In contrast to XRD, which requires long range order and a reasonably large scattering volume for identification of a minor phase (which may be required to be as large as ~5% of the total volume in order to be detected, depending on the density of scattering atoms and the sample volume), XAS is sensitive to the local chemical environment around an absorber, does not require long range order (can be measured on amorphous and disordered phases), and is routinely used for chemical speciation and/or phase identification at parts per million (ppm) concentration levels using X-ray fluorescence (XRF) detection methods. Copper and zinc K-edge (1s) X-ray absorption near edge structure (XANES) measurements, which probe the local chemical environment of the Cu or Zn absorber through $1s \rightarrow np$ ($n \geq 4$ for Cu and Zn) dipole allowed ($\Delta l \pm 1$) transitions, were performed on the roxbyite ($\text{Cu}_{1.81}\text{S}$) NC starting material, NC samples taken from various times during the transformation, and copper (Cu_2S and CuS) and zinc (ZnS and ZnO) bulk reference standards.

The Cu K-edge XANES of NC samples with various copper sulfide layer thicknesses, t , from the initial roxbyite starting material to the final NC sample, as well as that for the Cu_2S bulk reference standard are displayed in **Fig. 6.4a**. A shift in the Cu K-edge towards a XANES spectrum exhibiting spectral features of the Cu_2S reference standard (**Fig. 6.4a and Fig. E.5,6**) was observed immediately (5 minutes)

after the chemical transformation begins. The copper K-edge XANES of NC samples with $t = 20$ and 15 nm exhibit XANES profiles of Cu_2S (djurleite/low chalcocite) in the near-edge region.^{41, 42} After 50 mins (when the thickness of the copper sulfide band in the NC, t , is 10 nm) the Cu K-edge XANES shifts back to that of the initial roxbyite NC starting material (see **Fig. 6.4a** and **Fig. E.5,7**). All NC samples with $t \leq 10$ nm exhibit the XANES profile of the initial roxbyite phase (note: initial roxbyite NC size is $t=22$ nm). The Cu K-edge XANES of the final NC sample ($t < 1$ nm), although noisy due to the very low concentration of copper remaining in the sample, appears to have the same spectral profile of the $\text{Cu}_{1.81}\text{S}$ roxbyite phase. Due to the broad spectral features observed from copper K-edge XANES profiles of all NC samples and reference standards it is clear that fitting is required to assign spectral contributions.

In order to quantify $\text{Cu}_{1.81}\text{S}$ and Cu_2S contributions to the copper K-edge XANES of the heterostructure NCs, we fit the absorption coefficient, $\mu(E)$, with a linear combination of $\text{Cu}_{1.81}\text{S}$ (roxbyite) and Cu_2S (djurleite/low chalcocite) reference spectra (see **Fig. E.8** and **Table E.2** and discussion that follows in Supplementary Information). Linear combination XANES (LC-XANES) fitting is a common method for determining phase fraction from XAS, and has been used to study mechanisms of gold bioaccumulation⁴³, iron-monosulfide oxidation⁴⁴, secondary phases in kesterite $\text{Cu}_2\text{ZnSnS}_4$ thin films⁴⁵, electrochemical delithiation of LiFePO_4 ⁴⁶, (de)lithiation mechanisms in Li/SeS_x ($x = 0-7$)⁴⁷, and palladium phase fraction of palladium nanoparticle electrocatalysts in lithium-oxygen batteries⁴⁸. LC-XANES fitting of Cu K-edge XANES profiles from the NC samples indicate that upon initial formation of

ZnS grains (initial ZnS-Cu_{1.81}S-ZnS heterostructure, $t = 20$ nm) the copper sulfide phase undergoes a rapid, and nearly complete, transformation from Cu_{1.81}S (roxbyite) to a Cu₂S (low chalcocite/djurleite) phase (see **Fig. 6.4c** and **Table E.2**). The solid-solid copper sulfide phase transformation indicated by the XANES analysis corroborates XRD results which show a peak shift toward smaller 2Θ angles observed in the initial transformed NC samples ($22 > t > 13$ nm) (**Fig. 6.3b**), and thus, confirms the solid-solid phase transformation of copper sulfide during the cation exchange reaction. As the cation exchange proceeds and the relative volume fraction of copper sulfide to ZnS in the NCs decreases, the phase fraction of Cu_{1.81}S increases until it reaches a maximum for the sample $t = 6$ nm (**Fig. 6.4c** and **Table E.2**). The position of E_0 (absorption edge) for the heterostructured NC samples, the Cu_{1.81}S roxbyite NC starting materials, and the Cu₂S bulk sample was ~ 8980 eV (**Table E.3**), which is consistent with copper in the 1+ oxidation state (E_0 for Cu metal is 8979 eV).

Zinc K-edge XANES of the heterostructured NC samples as well as those of the ZnS and ZnO reference standards are shown in **Fig. 6.4b**. The $t = 20$ nm NC sample has strong contributions from both ZnS and ZnO. The ZnO contribution can be attributed to air-oxidation of ZnS after the NCs have been synthesized. Since there is only a very thin ZnS capping layer (~ 1 nm) at the poles of the NC is in the initially-transformed sample ($t = 20$ nm sample in **Fig. 6.4b**) the amorphous ZnO layer on the surface dominates the absorption spectrum. As the volume fraction of ZnS in the NCs increases, contributions to the Zn K-edge XANES spectrum from the ZnO surface oxide layer rapidly decrease. For NC samples with $t < 2.5$ nm the spectral features of the near edge region become increasingly sharp as the crystallinity of ZnS increases.

The position of E_0 for the samples with $t < 15$ nm, the bulk ZnS and the bulk ZnO is ~ 9661 eV (**Table E.4**), which is consistent with zinc in the 2+ oxidation state (E_0 for Zn metal is 9659 eV). The position of E_0 for the sample with $t = 20$ nm is 9662.3 ± 0.1 eV, but this increase is most likely the result of the superposition of $\mu(E)$ contributions from ZnO and ZnS, and does not reflect a change in the oxidation state of Zn. This slight shift of E_0 to higher energy decreases with an increase in the ZnS contribution to $\mu(E)$ as the cation exchange proceeds, which is consistent with the preceding argument.

To understand the solid-solid phase transformation in the copper sulfide layer it is necessary to examine the interface between ZnS and copper sulfide. HAADF and HRTEM characterization reveals that the copper sulfide – zinc sulfide heterostructure interface is atomically sharp (**Fig. 6.5a,b**), implying that Cu ions and Zn ions do not inter-diffuse and that cation exchange only occurs at the interface. The crystallographic planes along the interface were identified as $(100/\bar{1}00)$ for copper sulfide and $(001/00\bar{1})$ for ZnS, based on the spacing of the planes and the Fourier transform of the lattices at the interface, as shown in the HAADF and HRTEM images (**Fig. 6.5a,b**). These epitaxial interfaces form due to the well-matched sulfur sublattices shared by $\text{Cu}_{1.81}\text{S}$ and ZnS (**Fig. 6.5c,d**). Although roxbyite copper sulfide has a low symmetry crystal structure, its sulfur sublattice for $(001/00\bar{1})$ is hexagonal with maximum deviations of ± 0.35 Å from the sulfur sublattice spacing in wurtzite ZnS $(001/00\bar{1})$. In addition dual interface formation in our $\text{Cu}_{1.81}\text{S}/\text{ZnS}$ heterostructured NCs may be due to similar atomic arrangements of the (100) and $(\bar{1}00)$ plane of the roxbyite phase, which provides a similar chemical environment for

the cation exchange and interface formation (see **Fig. E.9**). However, other planes are poorly matched between low symmetry roxbyite and wurtzite ZnS (see **Fig. E.10**). This favorable epitaxial matching with only a few atomic planes is likely the reason that Cu_{1.81}S/ZnS heterostructured NCs do not form a core-shell structure. This dual interface formation is different from previous reports of CdS-Cu₂S that cite the two atomically-distinct crystal planes of (001) and (00 $\bar{1}$) as leading to different reactivity's at either ends of the CdS nanorod for forming either one or two interfaces.⁴ The lattice constant of the sulfur sublattice in ZnS (001/00 $\bar{1}$) is 1.1% smaller than that of the sulfur sublattice in roxbyite (100/ $\bar{1}00$). This lattice mismatch results in the formation of curved interfaces between copper sulfide and ZnS (**Fig. 6.5e**); strain relaxation occurs by the development of atomic steps along the interfaces (**Fig. 6.5a**, yellow dotted lines show the atomic steps between copper sulfide and ZnS). This curvature can be engineered by reversing the stress at the interface materials, the use of Cd, rather than Zn, in the cation exchange reaction forms wurtzite CdS which has a sulfur sublattice spacing that is 6.8 % larger than that of the sulfur sublattice in roxbyite copper sulfide. This lattice mismatch induces interface formation with an outward curvature which is opposite to that of the interface between copper sulfide and ZnS (**Fig. 6.5f**). HRTEM images of the interface confirm that the roxbyite phase is stabilized epitaxially at the ZnS surface; however, further into the copper sulfide region there are stacking faults that may indicate the presence of different Cu-S phases (**Fig. 6.5b**).

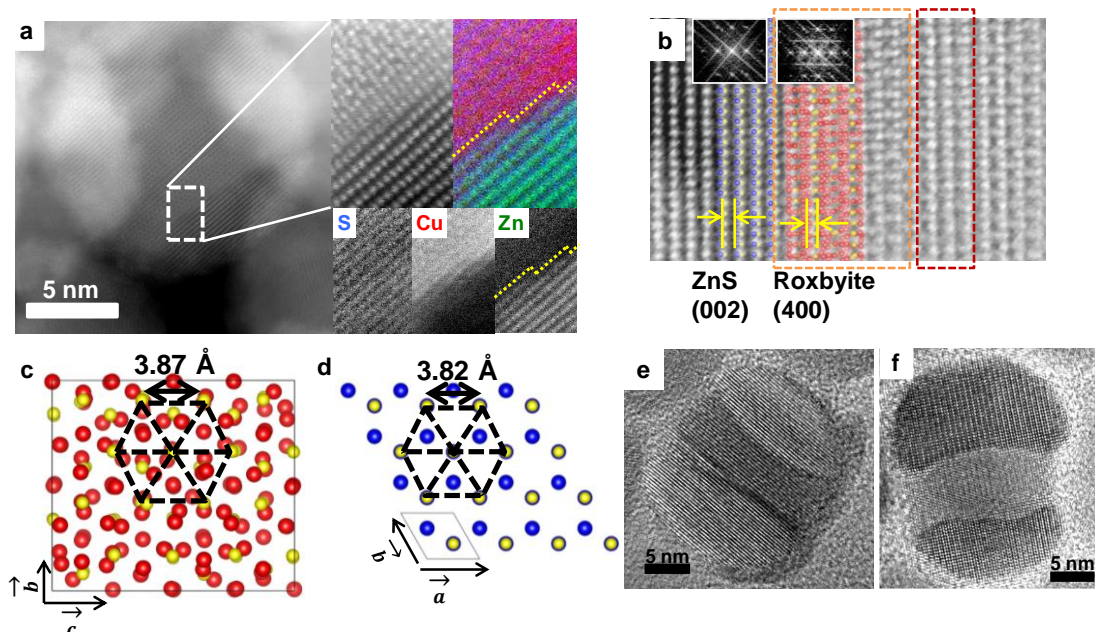


Figure 6.5 Characterization of the heterointerface. (a) HAADF images of the interface showing the elemental composition and atomic steps (yellow dotted line). (b) HRTEM image of a nanocrystal with a thick copper sulfide layer (~12 nm) showing the epitaxial interface of the roxbyite to the ZnS, and stacking faults in the copper sulfide further away from the interface. (c,d) Atomic models of the roxbyite (c) and ZnS (d) lattices. The sulfur atoms are shown in yellow. The sulfur sublattice has a good epitaxial match between the two structures with only 1.1% mismatch for the (100) and (001) planes in the roxbyite and ZnS, respectively. (e,f) HRTEM images showing the convex curvature of ZnS caps (e) and concave curvature of CdS caps (f) on the copper sulfide layer. The opposite curvature is due to the reversal of interfacial strain for the ZnS (copper sulfide is in compression) versus the CdS (copper sulfide is in tension) caps.

Table 6.1 Diffusion activation barrier for Cu, Zn, and Cd

Diffusing atom	Diffusion activation barrier (eV)		
	In roxbyite	In ZnS	In CdS
Cu	0.08	1.21	0.37
Zn	0.54	0.35	
Cd	0.86		0.22

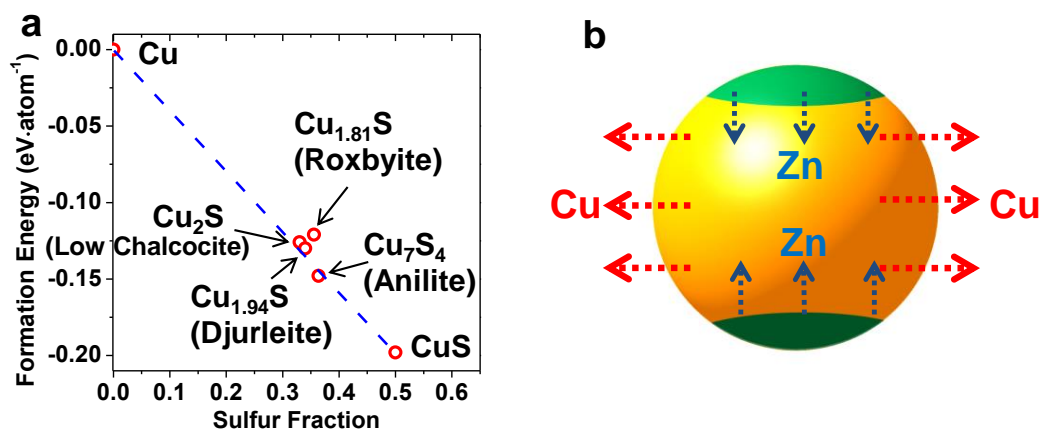


Figure 6.6 Phase stability calculation and diffusion pathways. (a) Formation energy calculations of copper sulfide phases. (b) The diffusion pathways of Cu and Zn atoms during the cation exchange reaction in heterostructured nanocrystals. Based on calculated diffusion activation barriers, during the cation exchange the Zn diffuses inward from the ZnS regions (green) and the Cu diffuses in the Cu-S region (orange).

The excess Cu in the Cu-S region could be the cause for the solid-solid phase transformation.

Density functional theory (DFT) has been extensively used to study the thermodynamic stability of different phases and predict the lowest energy structures.^{39, 49, 50} DFT calculations predict that the phase transition from roxbyite to copper-rich phases such as djurleite and low chalcocite, during the chemical transformation, is thermodynamically favorable (**Fig. 6.6a**). Our calculation of diffusion activation barriers indicate that Cu ions diffuse much faster in the roxbyite phase than in ZnS or CdS (see **Table 6.1**). In addition, the diffusion activation barriers for Zn and Cd are smaller in ZnS and CdS, respectively, than in roxbyite. Taking into consideration these calculated diffusion activation barriers, an accurate picture of the cation exchange process can be formed. Zn ions participating in the cation exchange reaction at the $\text{Cu}_{1.81}\text{S}/\text{ZnS}$ interface are supplied from the Zn ion solution and diffuse through the ZnS phase, whereas the Cu ions replaced by the Zn ions are released into the solution via diffusion through the copper sulfide region as shown in the **Fig. 6.6b**. During this diffusion of Cu outward into the solution, a fraction of the Cu ions are accommodated in intrinsic Cu vacancy sites present in the roxbyite phase, inducing a phase transition to the more Cu-rich copper sulfide phases such as djurleite or low chalcocite. Djurleite and low chalcocite are more thermodynamically stable phases than roxbyite (**Fig. 6.6a**): roxbyite has a formation energy of -0.12 eV per atom, while djurleite ($\text{Cu}_{1.94}\text{S}$) and low chalcocite (Cu_2S) have lower formation energies (-0.126 eV for djurleite and -0.13 eV for low chalcocite) and share a similar crystal structure with a slightly higher Cu to S ratio. The anion sublattice framework should be preserved during this phase transition between copper sulfide phases as well as between the zinc and copper sulfide cation exchange; the concept of anion sublattice

preservation during cation exchange has been previously documented.⁵¹ Thus, it is a thermodynamic driving force which induces the copper sulfide phase transition in the early stages of the cation exchange reaction as confirmed by XRD and XANES (**Fig. 6.3b, Fig. 6.4c**).

The findings from continuum modeling calculations of the strain distributions in the heterostructured NCs corroborate the NC morphology evolution seen during cation exchange (**Fig. 6.7**).⁵² The calculated direction of the interfacial curvature between ZnS/CdS and Cu_{1.81}S agrees with the experimentally observed interfacial curvature (ZnS-Cu_{1.81}S: curved inward to the center copper sulfide layer, CdS-Cu_{1.81}S: curved outward from the center copper sulfide layer). The strain along the axis perpendicular to the interfaces (z direction, **Fig. 6.7a**, bottom) determines the curvature. The z-direction strain arises from the mismatched interfacial strain along the x direction (the y direction has the same degree of strain as the x direction due to isotropic strain along the xy plane). The difference (~1.1 %) in the z-direction strain between the center of the NC and outer surface of the copper sulfide layer leads to an inward curvature of the interface towards the center (compressive strain in the center and tensile strain at the sides of the copper sulfide layer).

The calculated strain energy density in a NC during cation exchange increases as the copper sulfide layer thickness decreases (**Fig. 6.7b**, blue points, right hand y-axis). The strain energy density increases as the cation exchange reaction progresses, and is a maximum (1.52×10^{-5} Bar·nm⁻³) when $t = 4.8$ nm. The strain energy gradually decreases as the copper sulfide layer thickness decreases further ($t < 4.8$ nm).

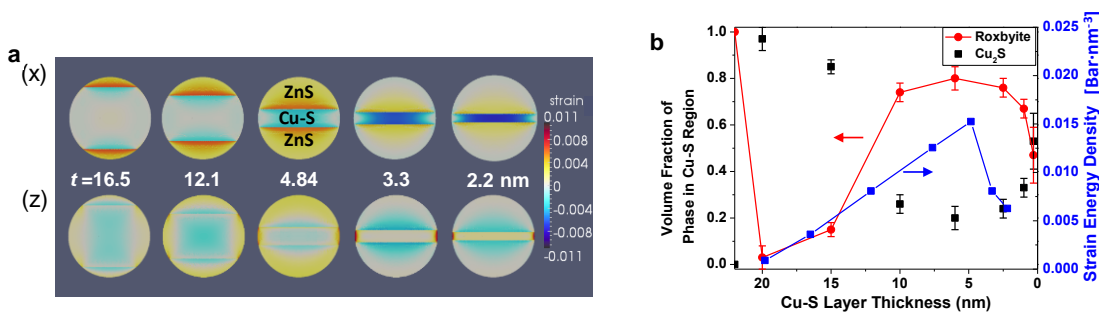


Figure 6.7 Modeled strain in the heterostructured nanocrystals. (a, top) Strain for the x-y direction, parallel to the interface. (a, bottom) Strain for the z direction, perpendicular to the interface. The color scale spans from 1.1% compression (red) to 1.1% tension (dark blue). (b) Strain energy density (blue squares, right y-axis) found from strain model and plotted against phase fraction in the copper sulfide. As the total strain in the nanocrystal increases the majority of the copper sulfide phase reverts to roxbyite, which has a good epitaxial match to the ZnS interface.

It is likely that the evolution of the strain energy density in our heterostructured NCs is directly linked to the copper sulfide phase transitions characterized through XAS. Since the lattice of the roxbyite phase is better-matched to the sulfur sublattice of ZnS than that of djurleite/low chalcocite (**Fig. E.11,12**), the roxbyite phase is strain-stabilized at the interfaces. As the thickness of the copper sulfide layer decreases, the djurleite phase that is present in the NC interior, away from the interfaces, transforms to roxbyite to minimize lattice strain, even though djurleite/low chalcocite in bulk is thermodynamically more stable than roxbyite. The evolution of the calculated strain energy mirrors the phase transitions determined from the XANES fitting. XANES

analysis shows that the initial NC is entirely of the roxbyite phase of copper sulfide, and that, at the onset of the cation exchange reaction, the majority (97%) of the copper sulfide volume immediately transforms to the low chalcocite/djurleite phase (**Fig. 6.7b**, red & black points). As the reaction proceeds, the volume fraction of the roxbyite phase gradually increases until the thickness of the copper sulfide layer is 6 nm ($t = 6$ nm); this trend is well-matched with the strain energy calculation, which shows that the strain energy reaches a maximum at $t = 5$ nm. During the transformation the roxbyite phase is stabilized at the ZnS interface as a consequence of minimizing interfacial strain. HAADF images confirm that the copper sulfide phase at the interface with ZnS is $\text{Cu}_{1.81}\text{S}$ (roxbyite), while stacking faults observed in the middle of the copper sulfide region indicate the presence of different copper sulfide compositions (**Fig. 6.5b**). The strain controlled phase transition in copper sulfide NCs suggests that this roxbyite phase should appear at the interface with other wurtzite metal sulfides where the properties of heterostructures are controlled.

This result is interesting in light of previous research on solid-solid phase transformations in NCs. Previous work has demonstrated that the entire NC acts as a single domain for phase transitions under high pressure.⁵³ Other work has attempted to identify the critical nucleus for phase transformations through a 1D nucleation seed.⁵⁴ These results are based on free-standing NCs with pressure induced transformations. Our result shows a coexistence of two phases within the Cu-S layer of the NC. Although a clear trend in the initial transformation indicates that the NC would prefer to transform as a single domain (NC transforms to djurleite/low chalcocite upon initiation of the cation exchange). However, the second phase

transition induced by lattice strain does not appear to prefer a single domain even though the thickness of the Cu-S region is only between 1 and 10 nm. This may imply that the critical nucleus for the phase transition mediated by cation exchange is different from that mediated by interfacial strain. In addition, the phase transformations back and forth between roxbyite and djurleite/low chalcocite is energetically similar to the transient transformations between the low chalcocite and high chalcocite phase observed by TEM.²¹ The calculated formation energies per formula unit between roxbyite and djurleite/low chalcocite are 42 meV/38 meV, which are comparable with that between low chalcocite and high chalcocite (40 meV^{21, 55}), however, in the roxbyite and djurleite/low chalcocite case one would expect a progression to the lower energy phase (djurleite/low chalcocite) and a larger barrier for a reverse transform.

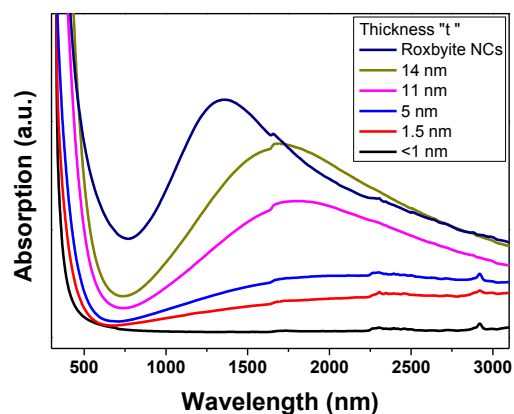


Figure 6.8 Absorption spectra of nanocrystal samples. The initial roxbyite $\text{Cu}_{1.81}\text{S}$ nanocrystals (dark blue line) show LSPR peak at ~ 1300 nm. The LSPR peak shifts toward longer wavelength with decreasing thickness (t) of the copper sulfide layer confined between ZnS caps. The final nanocrystal sample (black line) does not exhibit an LSPR peak.

The heterostructured NCs exhibit localized surface plasmon resonance (LSPR) peaks due to the intrinsically high carrier concentration of copper sulfide (**Fig. 6.8**). Cu_{2-x}S is a well-known p-type semiconductor exhibiting a stoichiometry-dependent bandgap.^{56, 57} By controlling the extent of cation exchange between copper sulfide and ZnS the resonance wavelength of the surface plasmons in the copper sulfide phase of our NCs can be tuned over a broad range of wavelengths from ~1300 nm for the initial copper sulfide NCs to ~2300 nm for the NCs with a thin ($t = 2$ nm) copper sulfide layer. Several mechanisms may account for the LSPR red-shift resulting from the cation exchange reaction. Firstly, the copper sulfide hole concentration is dependent on the stoichiometry, and thus transitions from roxbyite to more copper-rich phases will decrease the carrier concentration, resulting in a red-shift in the plasmon resonance.⁵⁸ Secondly, changes in the copper sulfide structure due to a phase change or strain in the lattice may alter the dielectric constant or free hole effective mass, both of which would cause a plasmon resonance wavelength shift; however both parameters have to change by more than 3 times their original values to result in the LSPR red-shifts measured for our samples (3 times higher effective mass or 3 times lower dielectric constant than the initial copper sulfide NCs). Such large changes in the free hole effective mass or dielectric constant are not possible for this system even if one considers the effects of lattice strain, as DFT calculations show that the NC lattice strains will only induce only a few percent change in the dielectric constant and effective mass. Lastly, as the volume fraction of copper sulfide decreases, the dielectric constant of ZnS becomes increasingly influential regarding the electronic properties of the NC. The LSPR-red-shift could therefore result from increasing the

dielectric constant of the local medium surrounding the copper sulfide phase via the growth of the ZnS grains. Overall, the plasmon resonance red-shift is most likely the result of a decrease in the carrier concentration and an enlargement in the surrounding dielectric material, but these conclusions warrant further study.

6.4 Discussion

In this study we demonstrate the synthesis of dual-interface, heterostructured NCs through cation exchange. The heterostructure consists of a copper sulfide layer capped with zinc sulfide grains in spherical NCs and can be tuned by controlling the extent of the cation exchange reaction. The reaction can produce an atomic layer of 2D copper sulfide within a ZnS NC, with epitaxial connections between the two materials, which provides a template to investigate unique phenomena in NCs, such as a 2D hole gas or 2D quantum well. In the early stage of the reaction, we observe a solid-solid phase transition of the copper sulfide phase from roxbyite to a more thermodynamically stable, copper-rich phase (djurleite/low chalcocite). This first phase transformation occurs as a result of copper ions, displaced by Zn ions, occupying the intrinsic vacancy sites of the roxbyite phase. The minimization strain energy induces a second phase transition back to roxbyite, which forms a better-matched epitaxial interface with zinc sulfide than does djurleite or low chalcocite. The strain controlled phase transformation in free-standing copper sulfide NCs implies that this roxbyite phase may appear at the interface with other wurtzite metal sulfides where the properties of heterostructures are determined. This solid-solid phase

transition provides insights to understand and control the nucleation of phase transformations in nanoscale systems with two different types (cation exchange and interfacial strain) of origins triggering a phase transition.

6.5 Methods

Synthesis

Chemicals

All synthesis was carried out in a dry, oxygen-free, nitrogen gas atmosphere by employing standard Schlenk line and glove box techniques. Acetone ($\geq 99.5\%$), hexanes ($\geq 98.5\%$), ethanol ($\geq 99.5\%$), toluene ($\geq 99.9\%$), oleylamine (70%), 1-Octadecene (ODE, 90%) tri-*n*-octylphosphine (TOP, 97%), ZnCl₂ (99.999%), di-tert-butyl disulfide (97%), and CdCl₂ (99.99%) were purchased from Aldrich. CuCl₂·2H₂O (99.999%) was purchased from Alfa Aesar.

Roxbyite nanocrystal synthesis

The synthesis of roxbyite nanocrystals (NCs) is slightly modified from the standard procedure.⁵⁹ A mixture of CuCl₂·2H₂O (340.8 mg) and oleylamine (59 mL) was vacuumed for 30 minutes at room temperature and another 30 minutes at 100 °C to remove water and impurities. The solution was then heated to 200 °C under a nitrogen flow. The solution was maintained at 200 °C for one hour after it becomes transparent yellow color. The di-tert-butyl disulfide solution (8 mL) was injected into the solution at 180 °C and the reaction was allowed to proceed for 40 minutes. The solution was quenched with a water bath and the NCs were collected by centrifugation and washed twice with hexane/acetone. The roxbyite NCs were kept in hexane.

Nanocrystal cation exchange (Copper sulfide to zinc sulfide)

Concentrated Zn ion solution was prepared by dissolving ZnCl₂ in oleylamine. A mixture of ZnCl₂ (500 mg) and oleylamine (20 mL) was vacuumed at 100 °C for 30 minutes and heated to 180 °C. The solution was kept at 180 °C for 30 minutes under a nitrogen flow. The solution was then kept at 100 °C under nitrogen.

The roxbyite NC solution was prepared by dispersing dry roxbyite NCs (35 mg) in 7 mL of TOP. This solution was kept at room temperature in a glove box for 3 hours before the cation exchange reaction.

A separate flask was prepared for the cation exchange reaction. A mixture of toluene (30 mL) and pre-prepared concentrated Zn solution (9.33 mL) was heated to 50 °C. When the temperature was stabilized, the roxbyite NC/TOP solution was injected into the Zn solution. Aliquots at different reaction times were taken and immediately quenched by injecting into cold acetone. The copper sulfide layer thickness as a function of reaction time is shown in **Table E.1**. For the final sample, the solution was heated to 100 °C and kept for 10 minutes to facilitate the reaction.

Nanocrystal cation exchange (Copper sulfide to cadmium sulfide)

A roxbyite NC solution was prepared by dispersing dry roxbyite NCs (5 mg) in 5 mL of TOP. This solution was kept at room temperature in a glove box for 3 hours before the cation exchange reaction.

A mixture of CdCl₂ (44.68 mg), ODE (8.75 mL), and oleylamine (8.75 mL) was vacuumed at 100 °C for 30 minutes. Then the solution was cooled down to 50 °C. When the temperature was stable, the roxbyite NC/TOP solution was injected into the Cd solution. The aliquots at different reaction times were taken and immediately quenched by injecting into cold acetone. The cation exchange reaction with Cd is much faster than that with Zn. 2 minutes of the reaction results in a copper sulfide layer thickness of 5 nm (**Fig. E.13**). The reaction was completed in 30 minutes (final sample). XRD results show that NCs are fully converted to wurtzite CdS (**Fig. E.14**). Fast kinetics of the cation exchange reaction between copper sulfide and Cd and the large interfacial strains (~6.8 %) between copper sulfide and CdS result in a less-controlled morphology than that produced by the transformation from copper sulfide to ZnS (**Fig. E.13**). The cation exchange reaction from copper sulfide to CdS occurs in 20 minutes while that to ZnS takes five hours at 50 °C. Additionally, the Cu to Cd ion ratio for the cation reaction is much lower than the Cu to Zn ratio (Cu:Cd≈1:4 vs. Cu:Zn≈1:20).

Transmission Electron Microscopy

TEM images of the nanoparticle samples were obtained using a FEI Tecnai F12 microscope operating at 120 keV. At least 100 particles were analyzed per sample to obtain a representative size distribution. High-resolution TEM (HRTEM) was done using a FEI Tecnai F20 microscope operating at 200 keV.

X-ray Diffraction

XRD (X-ray diffraction) spectra were collected using a Bruker General Area Detector Diffraction System (GADDS). Average grain sizes within the nanoparticle samples were determined from the XRD spectra using the Scherrer equation. The correction for instrumental broadening was conducted using the standard Al₂O₃ sample.

X-ray Absorption Spectroscopy

Copper and zinc K-edge x-ray absorption near edge structure (XANES) measurements were carried out at the bending magnet-based F3 beamline of the Cornell High Energy Synchrotron Source (CHESS) at Cornell University, Ithaca, NY. CHESS is a 5.3 GeV light source which operates in top-up mode (positrons) at a ring current of 200 mA. A silicon (220) double-crystal monochromator (DCM) with an energy resolution ($\frac{\Delta E}{E}$) of $\sim 10^{-4}$ was used to scan x-ray energy across the copper and zinc K-edges. Uniform thin-film nanoparticle samples were prepared by dispersing the nanoparticles in a small volume of toluene and drop casting the nanoparticles onto Kapton tape. Cu₂S (low chalcocite) and CuS reference standards were prepared by

dilution with boron nitride powder (100/1, w/w) and subsequent mixing and grinding with a mortar and pestle, the powders were then pressed into pellets. The Cu K-edge XANES of Cu₂S and CuS reference standards were measured at the bending magnet-based C1 beamline of CHESS using a silicon (111) DCM. The detection mode at both F3 and C1 was fluorescent x-ray yield recorded using a Hitachi 4-element silicon vortex detector with an XIA DXP XMAP processor. The detector count rate was kept below 140,000 counts to insure a linear dead-time response. All spectra were normalized to dead-time corrected I_0 , measured using an ion chamber upstream of the sample filled with 100% N₂. Copper and zinc reference foil standards used for energy calibration were measured in transmission mode downstream of the sample between two ion chambers filled with 100% N₂. All XANES data were calibrated and normalized using the Demeter Athena XAS software package.⁶⁰ Linear combination fitting of XANES data was also performed in Athena.

Scanning Transmission Electron Microscopy

High-angle annular dark-field (HAADF) and electron energy loss spectroscopic (EELS) data were acquired on a 5th-order aberration-corrected scanning transmission electron microscope (Nion UltraSTEM) operated at 100 kV with a probe forming semi-angle of roughly 30 mrad and a collection semi-angle around 80-240 mrad and 0-60 mrad for HAADF and EELS respectively. A Gatan Enfina spectrometer was mounted above (beyond) the collection optics of the microscope for simultaneous HAADF and EELS acquisition. Resolution just below ~1 Angstrom is

roughly the information transfer limit for this microscope optimally operating under these conditions.

Continuum model

The force balance equation in any continuum is given by

$$\vec{\nabla} \cdot \boldsymbol{\sigma} + \vec{f} = 0$$

where $\boldsymbol{\sigma}$ is the cauchy stress tensor and \vec{f} is the body force. Assuming a linear model, the stress tensor can be written as,

$$\sigma_{ij} = C_{ijkl} \epsilon_{kl}$$

where C_{ijkl} is the stiffness tensor and ϵ_{kl} is the strain tensor which under small displacement assumption can be written as

$$\epsilon_{ij} = \frac{1}{2}(u_{i,j} + u_{j,i})$$

where u_{ij} is the derivative along the direction j of the component i of displacement \vec{u} .

Assuming the material to be isotropic, the stiffness tensor can be written as,

$$C_{ijkl} = \lambda \delta_{ij} \delta_{kl} + \mu (\delta_{ik} \delta_{jl} + \delta_{il} \delta_{jk})$$

where λ and μ are the Lamé parameters and δ_{ij} is the Kronecker delta function.

The above equations were solved for the spherical nanoparticle using the Finite

Element Method (FEM) with the values of Lamé parameters obtained from the DFT calculations.

The elastic energy is given by

$$\frac{1}{2} \int_V \sigma_{ij} \epsilon_{ij} dV$$

Density-functional calculation Method

Density-functional calculations were performed with the Vienna Ab-initio Software Package (VASP)^{61, 62, 63, 64} using the PBE exchange-correlation functional⁶⁵ and the projector augmented wave method.^{66, 67} The Brillouin zone integration was performed using a Monkhorst and Pack k -point mesh.⁶⁸ $3 \times 3 \times 3$ k -point meshes were employed for structural relaxations and nudged-elastic band (NEB) calculations⁶⁹ of the 180-atoms roxbyite structure, 144-atoms low chalcocite structure and the CdS/ZnS structures. The kinetic energy cutoff for the plane wave basis was set to 400 eV and the corresponding cutoff energies for the augmentation functions were set to 650 eV for all our calculations. The POSCAR file for roxbyite was created from the Canadian Mineral database structure for $\text{Cu}_{1.81}\text{S}$ ³⁵ whereas the Materials Project Website⁷⁰ was used to get all other POSCAR files. Band gap and dielectric constant calculations were performed on elongated and compressed lattices to study how these properties vary with strain.

6.6 References

1. Son, D. H.; Hughes, S. M.; Yin, Y. D.; Alivisatos, A. P. *Science* **2004**, 306, 1009-1012.
2. Sahu, A.; Kang, M. S.; Kompch, A.; Notthoff, C.; Wills, A. W.; Deng, D.; Winterer, M.; Frisbie, C. D.; Norris, D. J. *Nano Lett.* **2012**, 12, (5), 2587-2594.
3. Vlaskin, V. A.; Barrows, C. J.; Erickson, C. S.; Gamelin, D. R. *J. Am. Chem. Soc.* **2013**, 135, (38), 14380-14389.
4. Sadtler, B.; Demchenko, D. O.; Zheng, H.; Hughes, S. M.; Merkle, M. G.; Dahmen, U.; Wang, L.-W.; Alivisatos, A. P. *J. Am. Chem. Soc.* **2009**, 131, (14), 5285-5293.
5. Robinson, R. D.; Sadtler, B.; Demchenko, D. O.; Erdonmez, C. K.; Wang, L. W.; Alivisatos, A. P. *Science* **2007**, 317, (5836), 355-358.
6. Demchenko, D. O.; Robinson, R. D.; Sadtler, B.; Erdonmez, C. K.; Alivisatos, A. P.; Wang, L. W. *ACS Nano* **2008**, 2, (4), 627-636.
7. Manna, L.; Scher, E. C.; Alivisatos, A. P. *J. Am. Chem. Soc.* **2000**, 122, (51), 12700-12706.
8. Sytnyk, M.; Kirchschrager, R.; Bodnarchuk, M. I.; Primetzhofer, D.; Kriegner, D.; Enser, H.; Stangl, J.; Bauer, P.; Voith, M.; Hassel, A. W.; Krumeich, F.; Ludwig, F.; Meingast, A.; Kothleitner, G.; Kovalenko, M. V.; Heiss, W. *Nano Lett.* **2013**, 13, (2), 586-593.

9. Beberwyck, B. J.; Surendranath, Y.; Alivisatos, A. P. *J. Phys. Chem. C* **2013**, 117, (39), 19759-19770.
10. Putnis, A. *Mineral. Mag.* **2002**, 66, (5), 689-708.
11. Fedorov, V. A.; Ganshin, V. A.; Korkishko, Y. N. *Phys. Status Solidi A* **1993**, 139, (1), 9-65.
12. Li, H.; Zanella, M.; Genovese, A.; Povia, M.; Falqui, A.; Giannini, C.; Manna, L. *Nano Lett.* **2011**, 11, (11), 4964-4970.
13. Tolbert, S. H.; Alivisatos, A. P. *Science* **1994**, 265, (5170), 373-376.
14. Jacobs, K.; Zaziski, D.; Scher, E. C.; Herhold, A. B.; Paul Alivisatos, A. *Science* **2001**, 293, (5536), 1803-1806.
15. Jacobs, K.; Wickham, J.; Alivisatos, A. P. *J. Phys. Chem. B* **2002**, 106, (15), 3759-3762.
16. Wu, Y.; Wadia, C.; Ma, W.; Sadtler, B.; Alivisatos, A. P. *Nano Lett.* **2008**, 8, (8), 2551-2555.
17. Wakamura, K. *Solid State Ionics* **2002**, 149, (1-2), 73-80.
18. Miller, T.; Wittenberg, J.; Wen, H.; Connor, S.; Cui, Y.; Lindenberg, A. *Nat. Commun.* **2013**, 4, 1369.
19. Lai, C.-H.; Huang, K.-W.; Cheng, J.-H.; Lee, C.-Y.; Hwang, B.-J.; Chen, L.-J. *J. Mater. Chem.* **2010**, 20, (32), 6638-6645.
20. Cheng, Z.; Wang, S.; Wang, Q.; Geng, B. *CrystEngComm* **2010**, 12, (1), 144-149.

21. Zheng, H.; Rivest, J. B.; Miller, T. A.; Sadtler, B.; Lindenberg, A.; Toney, M. F.; Wang, L.-W.; Kisielowski, C.; Alivisatos, A. P. *Science* **2011**, 333, (6039), 206-209.
22. Rivest, J. B.; Fong, L.-K.; Jain, P. K.; Toney, M. F.; Alivisatos, A. P. *J. Phys. Chem. Lett.* **2011**, 2, (19), 2402-2406.
23. Donega, C. d. M. *Chem. Soc. Rev.* **2011**, 40, (3), 1512-1546.
24. Smith, A. M.; Mohs, A. M.; Nie, S. *Nat. Nanotechnol.* **2009**, 4, (1), 56-63.
25. McDaniel, H.; Zuo, J.-M.; Shim, M. *J. Am. Chem. Soc.* **2010**, 132, (10), 3286-3288.
26. Wu, J.; Li, P.; Pan, Y.-T.; Warren, S.; Yin, X.; Yang, H. *Chem. Soc. Rev.* **2012**, 41, (24), 8066-8074.
27. Rivest, J. B.; Jain, P. K. *Chem. Soc. Rev.* **2013**, 42, (1), 89-96.
28. Scholl, J. A.; Koh, A. L.; Dionne, J. A. *Nature* **2012**, 483, (7390), 421-427.
29. Leon, R.; Petroff, P. M.; Leonard, D.; Fafard, S. *Science* **1995**, 267, (5206), 1966-1968.
30. Grundmann, M.; Christen, J.; Ledentsov, N. N.; Böhrer, J.; Bimberg, D.; Ruvimov, S. S.; Werner, P.; Richter, U.; Gösele, U.; Heydenreich, J.; Ustinov, V. M.; Egorov, A. Y.; Zhukov, A. E.; Kop'ev, P. S.; Alferov, Z. I. *Phys. Rev. Lett.* **1995**, 74, (20), 4043-4046.
31. Leonard, D.; Krishnamurthy, M.; Reaves, C. M.; Denbaars, S. P.; Petroff, P. *M. Appl. Phys. Lett.* **1993**, 63, (23), 3203-3205.

32. Tersoff, J.; Tromp, R. M. *Phys. Rev. Lett.* **1993**, 70, (18), 2782-2785.
33. Milliron, D. J.; Hughes, S. M.; Cui, Y.; Manna, L.; Li, J.; Wang, L.-W.; Paul Alivisatos, A. *Nature* **2004**, 430, (6996), 190-195.
34. Mumme, W.; Sparrow, G.; Walker, G. *Mineral. Mag.* **1988**, 52, (366), 323-330.
35. Mumme, W. G.; Gable, R. W.; Petříček, V. *Can. Mineral.* **2012**, 50, (2), 423-430.
36. Saldanha, P. L.; Brescia, R.; Prato, M.; Li, H.; Povia, M.; Manna, L.; Lesnyak, V. *Chem. Mater.* **2014**, 26, (3), 1442-1449.
37. Aksit, M.; Toledo, D. P.; Robinson, R. D. *J. Mater. Chem.* **2012**, 22, (13), 5936-5944.
38. Ward, M. J.; Han, W.-Q.; Sham, T.-K. *J. Phys. Chem. C* **2013**, 117, (39), 20332-20342.
39. Ha, D.-H.; Moreau, L. M.; Bealing, C. R.; Zhang, H.; Hennig, R. G.; Robinson, R. D. *J. Mater. Chem.* **2011**, 21, (31), 11498-11510.
40. Moreau, L. M.; Ha, D.-H.; Zhang, H.; Hovden, R.; Muller, D. A.; Robinson, R. D. *Chem. Mater.* **2013**, 25, (12), 2394-2403.
41. Patrick, R. A. D.; Mosselmanns, J. F. W.; Charnock, J. M.; England, K. E. R.; Helz, G. R.; Garner, C. D.; Vaughan, D. J. *Geochim. Cosmochim. Acta* **1997**, 61, (10), 2023-2036.

42. Etschmann, B.; Liu, W.; Testemale, D.; Mueller, H.; Rae, N.; Proux, O.; Hazemann, J.-L.; Brugger, J. *Geochim. Cosmochim. Acta* **2010**, 74, (16), 4723-4739.
43. Lengke, M. F.; Ravel, B.; Fleet, M. E.; Wanger, G.; Gordon, R. A.; Southam, G. *Environ. Sci. Technol.* **2006**, 40, (20), 6304-6309.
44. Burton, E. D.; Bush, R. T.; Sullivan, L. A.; Hocking, R. K.; Mitchell, D. R. G.; Johnston, S. G.; Fitzpatrick, R. W.; Raven, M.; McClure, S.; Jang, L. Y. *Environ. Sci. Technol.* **2009**, 43, (9), 3128-3134.
45. Just, J.; Lützenkirchen-Hecht, D.; Frahm, R.; Schorr, S.; Unold, T. *Appl. Phys. Lett.* **2011**, 99, (26), -.
46. Yu, X.; Wang, Q.; Zhou, Y.; Li, H.; Yang, X.-Q.; Nam, K.-W.; Ehrlich, S. N.; Khalid, S.; Meng, Y. S. *Chem. Commun.* **2012**, 48, (94), 11537-11539.
47. Cui, Y.; Abouimrane, A.; Lu, J.; Bolin, T.; Ren, Y.; Weng, W.; Sun, C.; Maroni, V. A.; Heald, S. M.; Amine, K. *J. Am. Chem. Soc.* **2013**, 135, (21), 8047-8056.
48. Lu, J.; Lei, Y.; Lau, K. C.; Luo, X.; Du, P.; Wen, J.; Assary, R. S.; Das, U.; Miller, D. J.; Elam, J. W.; Albishri, H. M.; El-Hady, D. A.; Sun, Y.-K.; Curtiss, L. A.; Amine, K. *Nat Commun* **2013**, 4.
49. Ogata, K.; Salager, E.; Kerr, C. J.; Fraser, A. E.; Ducati, C.; Morris, A. J.; Hofmann, S.; Grey, C. P. *Nat Commun* **2014**, 5.
50. Kim, J. C.; Moore, C. J.; Kang, B.; Hautier, G.; Jain, A.; Ceder, G. *J. Electrochem. Soc.* **2011**, 158, (3), A309-A315.

51. Jain, P. K.; Amirav, L.; Aloni, S.; Alivisatos, A. P. *J. Am. Chem. Soc.* **2010**, 132, (29), 9997-9999.
52. Bangerth, W.; Hartmann, R.; Kanschat, G. *ACM Trans. Math. Softw.* **2007**, 33, (4), 24.
53. Wickham, J. N.; Herhold, A. B.; Alivisatos, A. P. *Phys. Rev. Lett.* **2000**, 84, (5), 923-926.
54. Grünwald, M.; Dellago, C. *Nano Lett.* **2009**, 9, (5), 2099-2102.
55. Xu, Q.; Huang, B.; Zhao, Y.; Yan, Y.; Noufi, R.; Wei, S.-H. *Appl. Phys. Lett.* **2012**, 100, (6), -.
56. Zhao, Y.; Pan, H.; Lou, Y.; Qiu, X.; Zhu, J.; Burda, C. *J. Am. Chem. Soc.* **2009**, 131, (12), 4253-4261.
57. Xie, Y.; Riedinger, A.; Prato, M.; Casu, A.; Genovese, A.; Guardia, P.; Sottini, S.; Sangregorio, C.; Miszta, K.; Ghosh, S.; Pellegrino, T.; Manna, L. *J. Am. Chem. Soc.* **2013**, 135, (46), 17630-17637.
58. Luther, J. M.; Jain, P. K.; Ewers, T.; Alivisatos, A. P. *Nat. Mater.* **2011**, 10, (5), 361-366.
59. Li, W.; Shavel, A.; Guzman, R.; Rubio-Garcia, J.; Flox, C.; Fan, J.; Cadavid, D.; Ibanez, M.; Arbiol, J.; Morante, J. R.; Cabot, A. *Chem. Commun.* **2011**, 47, (37), 10332-10334.
60. Ravel, B.; Newville, M. *J. Synchrotron Radiat.* **2005**, 12, (4), 537-541.
61. Kresse, G.; Hafner, J. *Phys. Rev. B* **1993**, 47, (1), 558.

62. Kresse, G.; Hafner, J. *Phys. Rev. B* **1994**, 49, (20), 14251.
63. Kresse, G.; Furthmüller, J. *Comput. Mater. Sci.* **1996**, 6, (1), 15-50.
64. Kresse, G.; Furthmüller, J. *Phys. Rev. B* **1996**, 54, (16), 11169.
65. Perdew, J. P.; Burke, K.; Ernzerhof, M. *Phys. Rev. Lett.* **1996**, 77, (18), 3865.
66. Blöchl, P. E. *Phys. Rev. B* **1994**, 50, (24), 17953.
67. Kresse, G.; Joubert, D. *Phys. Rev. B* **1999**, 59, (3), 1758.
68. Monkhorst, H. J.; Pack, J. D. *Phys. Rev. B* **1976**, 13, (12), 5188.
69. Jónsson, H.; Mills, G.; Jacobsen, K. W., Nudged elastic band method for finding minimum energy paths of transition. In *Classical and quantum dynamics in condensed phase simulations*, World Scientific: 1998; pp 385-404.
70. Ong, S. P.; Jain, A.; Hautier, G.; Kocher, M.; Cholia, S.; Gunter, D.; Bailey, D.; Skinner, D.; Persson, K.; Ceder, G. <https://materialsproject.org>.

APPENDIX E

E SUPPLEMENTARY INFORMATION FOR CHAPTER 6

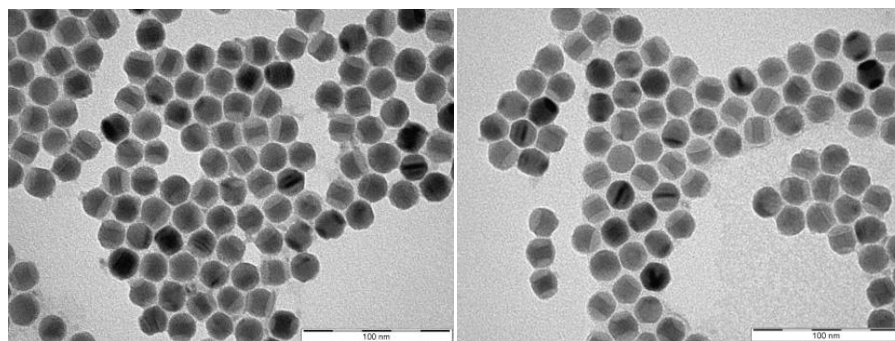


Figure E.1 TEM images of as-synthesized heterostructured NCs (left) and of the same sample after one week (right). Heterostructured NCs (left) retain their interface structure even after one week of air exposure in a vial (right). Dried NCs are stored in a vial after cation exchange and kept in air for a week. NCs are then re-dispersed in hexane for TEM imaging.

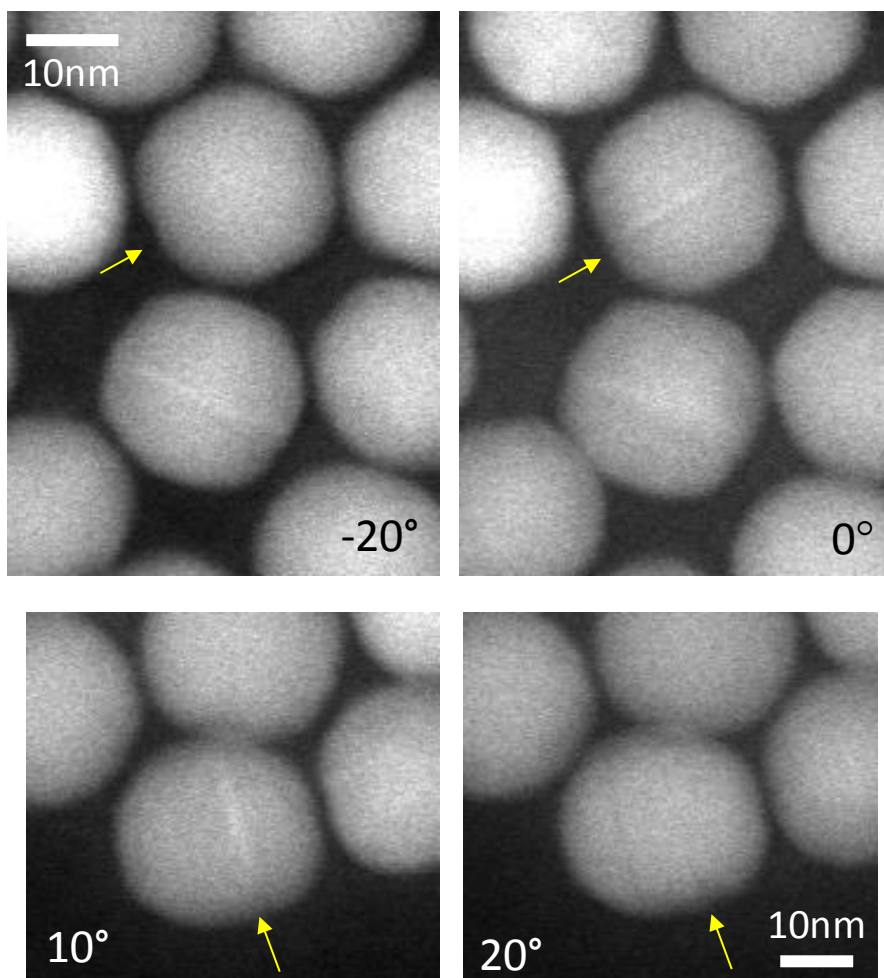


Figure E.2 HAADF images for the final sample (Cu-S/ZnS, Fig. 6.1e). Only copper layers oriented parallel or near-parallel to the electron beam will be clearly visible. The lack of a visible copper layers, does not imply that a layer is not present. When the specimen is tilted relative to the beam direction, copper layers appear and disappear.

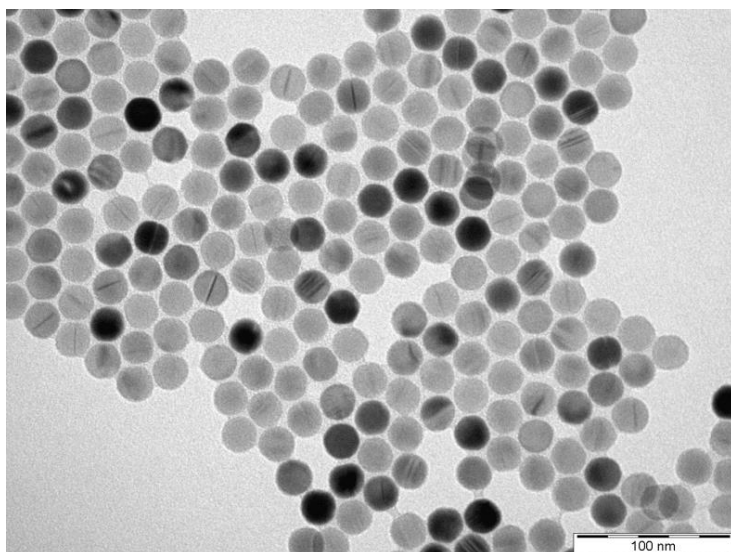


Figure E.3 TEM image of the NCs reacted under an aggressive environment.

After roxbyite NCs are reacted for 4 hours at 50 °C, the temperature is increased to 100 °C and kept for 30 minutes. Approximately 30 % of the NCs show a thin layer.

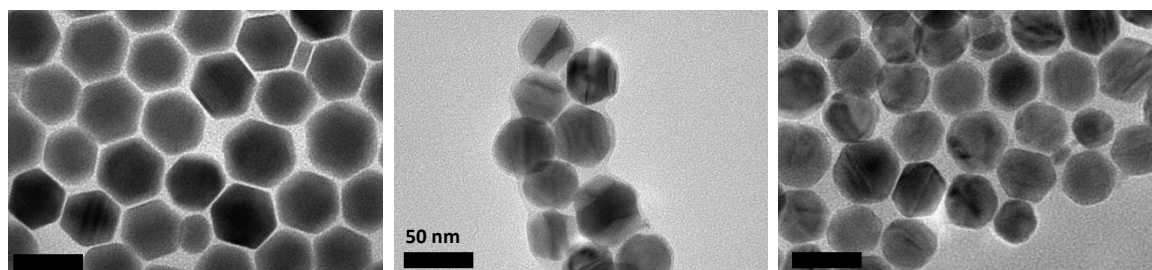


Figure E.4 TEM images of ~40 nm sized NCs during cation exchange reaction.

Starting roxbyite NCs (left) show ~40 nm size.¹ 7 minutes of reaction with Zn solution leads to heterostructured NCs (center). The final NCs (right) show Moiré pattern and thin layer in the center of the NCs.

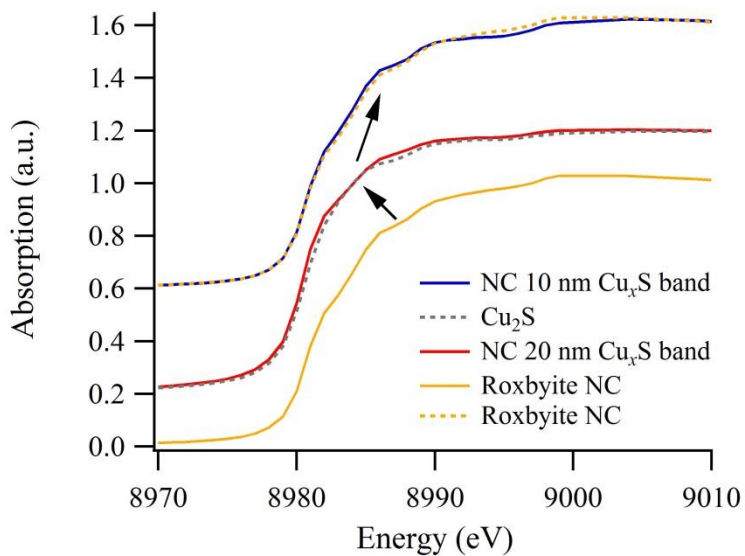


Figure E.5 Cu K-edge XANES of roxbyite NCs, Cu₂S, and NC samples with $t = 20$ nm and 15 nm. Shift observed in the copper K-edge XANES from roxbyite phase to Cu₂S phase at the beginning of the chemical transformation, when the thickness of the Cu_xS band, t , is 20 nm. XANES shifts back toward the roxbyite phase when $t \leq 10$ nm.

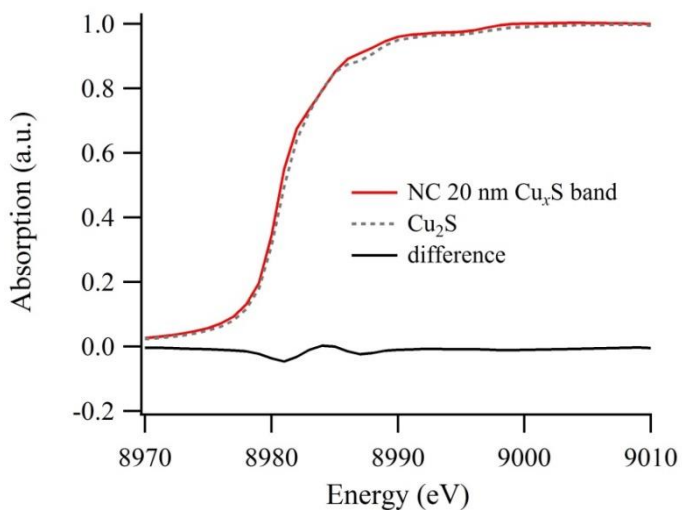


Figure E.6 Difference spectrum from Cu K-edge XANES of NC sample with $t = 20$ nm and Cu_2S .

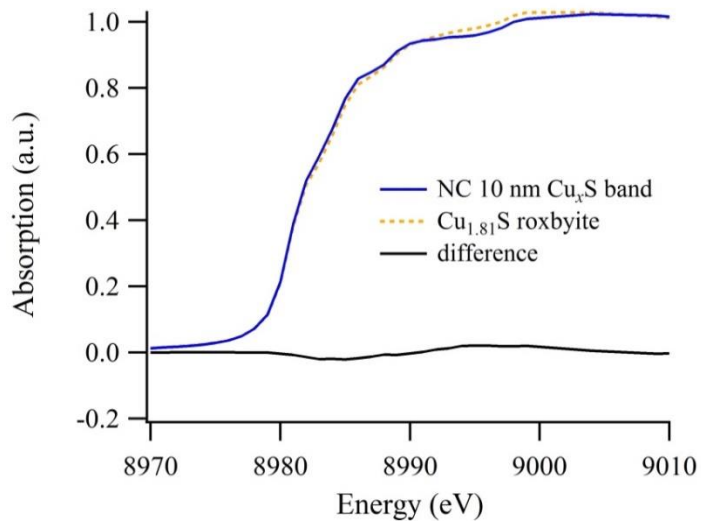


Figure E.7 Difference spectrum from Cu K-edge XANES of NC sample with $t = 10$ nm and $\text{Cu}_{1.81}\text{S}$ roxbyite.

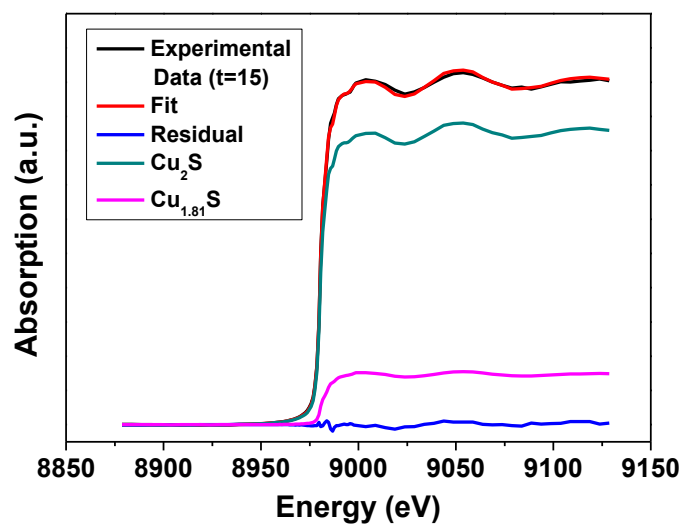


Figure E.8 Linear Combination-XANES fit of NC sample with $t = 15$ nm using $\text{Cu}_{1.81}\text{S}$ (roxbyite) and Cu_2S (djurleite / low chalcocite) as reference standards.

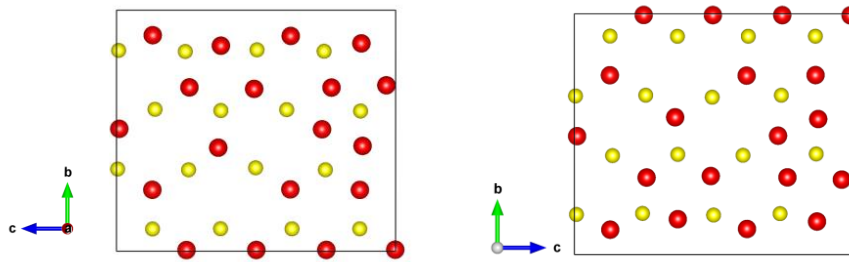


Figure E.9 The (100) plane (left) and $(\bar{1}00)$ plane (right) of roxbyite phase. They share a very similar atomic arrangement.

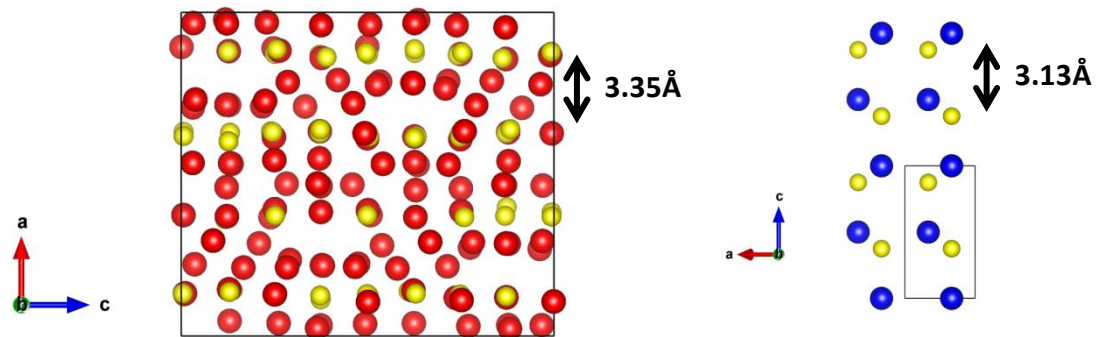


Figure E.10 Distances between S-S sub-layers perpendicular to the epitaxial plane of roxbyite (left) and ZnS (right). They show ~8 % different S-S sub-layer distance which is much higher than the lattice mismatch along the epitaxial plane (~1.1%).

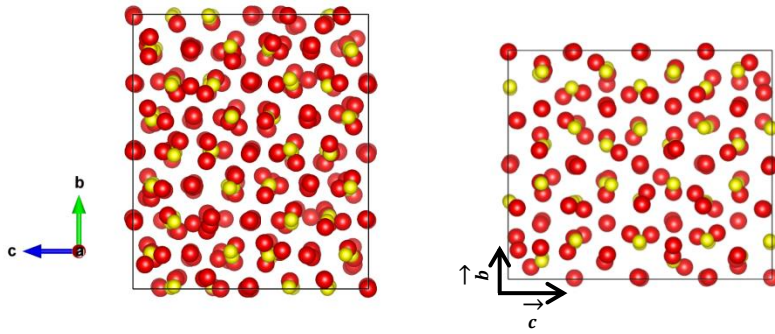


Figure E.11 The epitaxial plane for djurleite (left) and roxbyite (right) for ZnS.

Djurleite and roxbyite share a similar sulfur sub-lattice (S-S distances for djurleite and roxbyite are 3.91\AA and 3.87\AA , respectively). However, S-S distance in djurleite has much higher standard deviation than that in roxbyite (0.13\AA for djurleite vs. 0.08\AA for roxbyite).

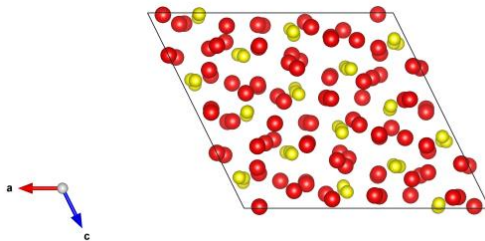


Figure E.12 Epitaxial plane for low chalcocite. The epitaxial plane for low chalcocite are poorly matched with hexagonal lattice.

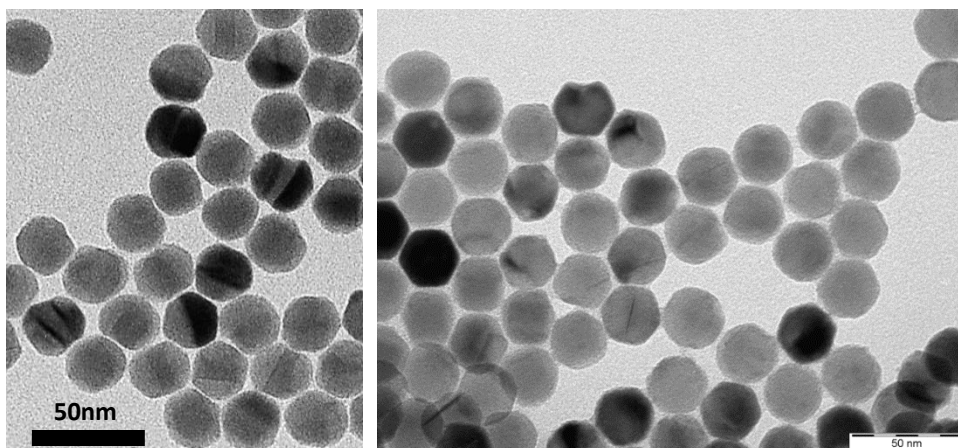


Figure E.13 TEM images of NCs reacted for 2 minutes with Cd solution (left) and the final sample (right).

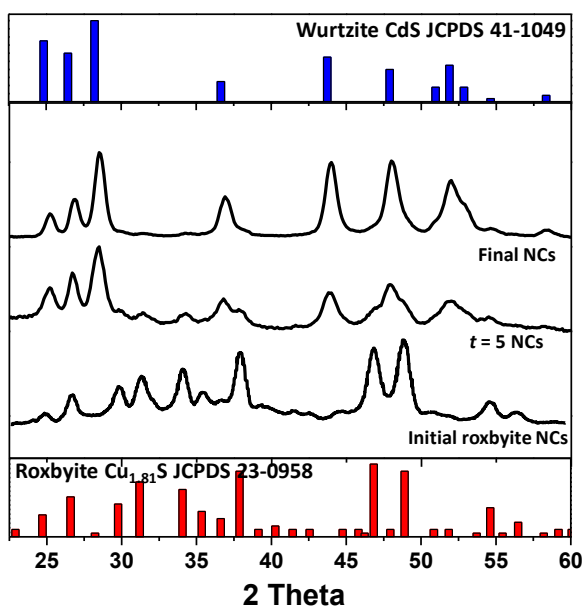


Figure E.14 XRD results of samples from copper sulfide to cadmium sulfide

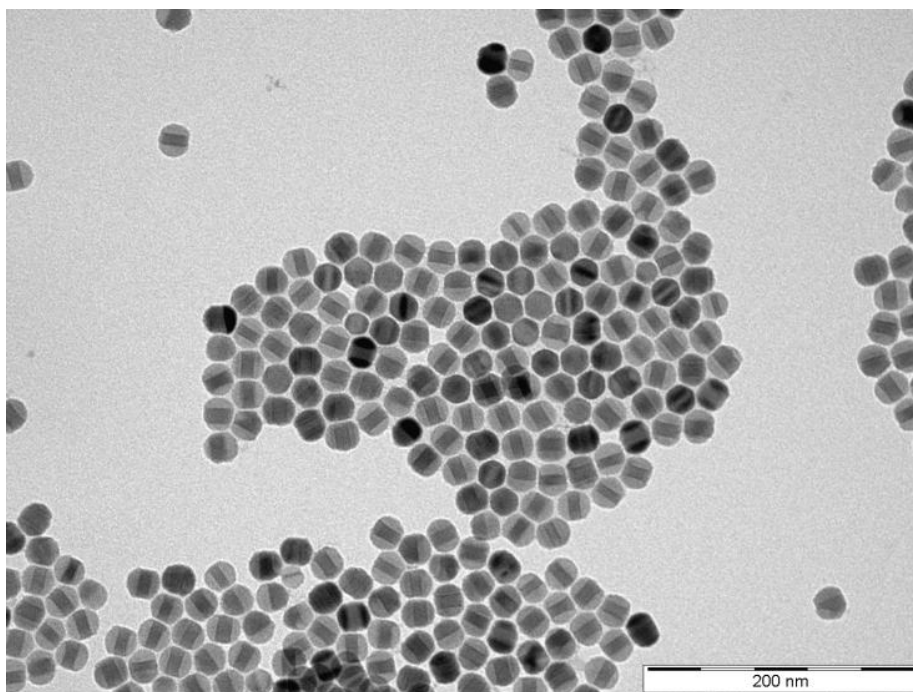


Figure E.15 TEM image with low magnification of the heterostructured (Cu-S/ZnS) NC sample (Fig. 6.1c)

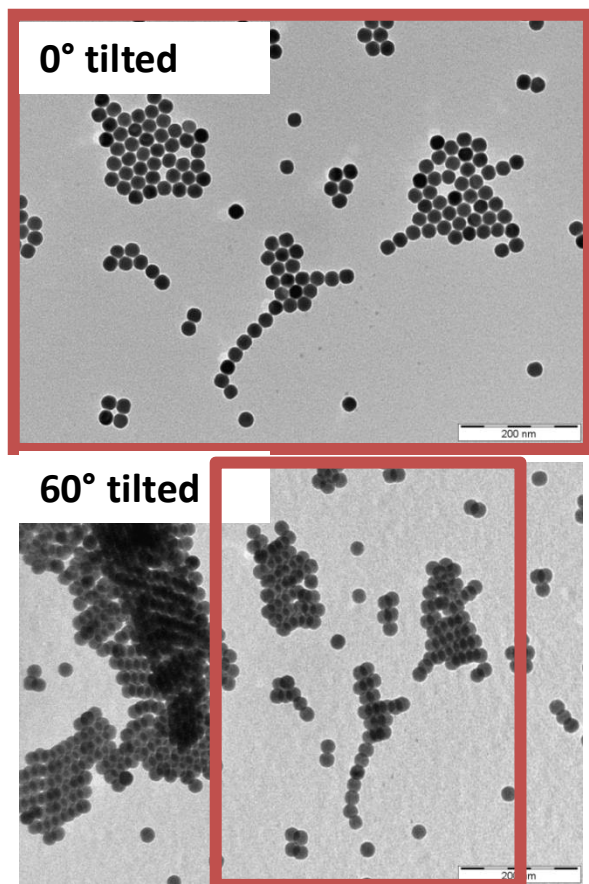


Figure E.16 TEM images of roxbyite NCs. 60° tilted TEM image (bottom) confirms that the starting roxbyite NCs are spherical. Red box displays the sample area before and after the TEM stage tilting experiment.

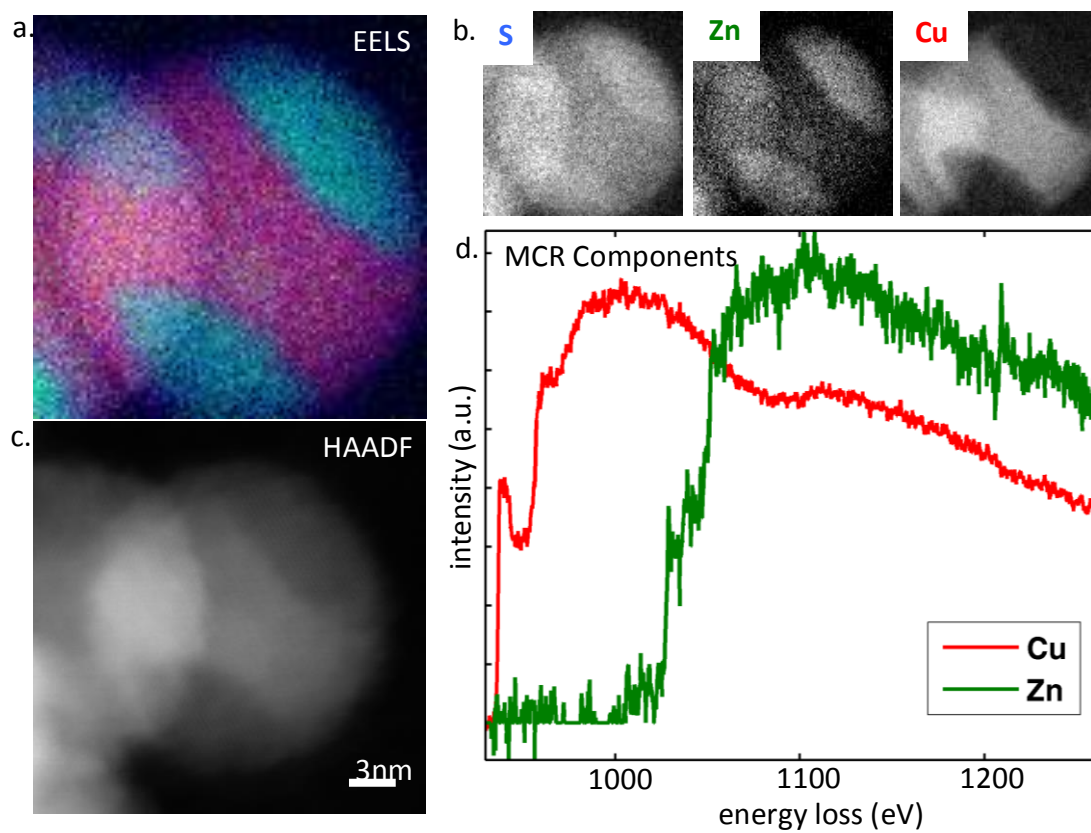


Figure E.17 Multivariate curve resolution (MCR) analysis for Cu and Zn EELS map of an intermediate product nanocrystal. a.) RGB composite image made from three chemical maps (b.), S, Zn, and Cu. c.) a HAADF image of the nanoparticle. d.) the MCR spectral components extracted after 20 iterations. MCR allows better estimation of the convoluted Zn and Cu edges.

Table E.1 Thickness of copper sulfide layer in heterostructured NCs as a function of cation exchange reaction time (a diameter of initial copper sulfide NCs is 22 nm)

Reaction time at 50 °C (minutes)	Copper sulfide layer thickness “ <i>t</i> ” (nm)
5	20 (std. dev. 8%)
15	19 (std. dev. 6%)
30	12 (std. dev. 6%)
75	8 (std. dev. 8%)
150	3 (std. dev. 29%)
240	1.5 (std. dev. 35%)
Final	<1

Table E.2 Linear combination fitting results for the heterostructured NC samples

Sample (Copper sulfide layer thickness, <i>t</i>)	a_{μ} (Cu _{1.81} S)	b_{μ} (Cu ₂ S)
*22 nm	1	0
20 nm	0.03 (±0.05)	0.97 (±0.05)
15 nm	0.15 (±0.03)	0.85 (±0.03)
10 nm	0.74 (±0.04)	0.26 (±0.04)
6 nm	0.80 (±0.05)	0.20 (±0.05)
2.5 nm	0.76 (±0.04)	0.24 (±0.04)
1 nm	0.67 (±0.04)	0.33 (±0.04)
<1 nm	0.47 (±0.12)	0.53 (±0.12)

* roxbyite NC starting material

Table E.2 shows the copper K-edge XANES linear combination fitting results as a function of copper sulfide layer thickness in the NC heterostructures during the chemical transformation from roxbyite to zinc sulfide.

Table E.3 Cu K-edge E_0 for the heterostructured NC samples, $\text{Cu}_{1.81}\text{S}$, and Cu_2S

Sample (Copper sulfide layer thickness, t)	E_0 (eV)
20 nm	8980.1 (± 0.1)
15 nm	8980.3 (± 0.1)
10 nm	8980.4 (± 0.1)
6 nm	8980.4 (± 0.1)
2.5 nm	8980.5 (± 0.1)
1 nm	8980.6 (± 0.1)
< 1 nm	8980.5 (± 0.1)
$\text{Cu}_{1.81}\text{S}$	8980.4 (± 0.1)
Cu_2S	8980.3 (± 0.1)

Table E.3 shows the binding energy threshold for the copper K-edge (1s electron) in the heterostructured NC samples, $\text{Cu}_{1.81}\text{S}$, and Cu_2S . All energies were calibrated using a copper reference foil measured downstream of the sample, the XANES spectra of all samples were aligned on the same energy grid after calibration. The oxidation state of copper in all the heterostructured samples, $\text{Cu}_{1.81}\text{S}$, and Cu_2S is 1+, as expected.²

Table E.4 Zn K-edge E_0 for the heterostructured NC samples, ZnS, and ZnO

Sample (Copper sulfide layer thickness, t)	E_0 (eV)
20 nm	9662.3 (± 0.1)
15 nm	9661.8 (± 0.1)
10 nm	9661.4 (± 0.1)
6 nm	9661.2 (± 0.1)
2.5 nm	9661.3 (± 0.1)
1 nm	9661.2 (± 0.1)
< 1 nm	9661.1 (± 0.1)
ZnS	9661.0 (± 0.1)
ZnO	9661.2 (± 0.1)

Table E.4 shows the binding energy threshold for the zinc K-edge (1s electron) in heterostructured NC samples, ZnS, and ZnO. All energies were calibrated using a zinc reference foil measured downstream of the sample, the XANES spectra of all samples were aligned on the same energy grid after calibration. The oxidation state of zinc in the heterostructured NCs, ZnS, and ZnO is 2+, as expected. The larger value of E_0 for sample A can be attributed to the superposition of $\mu(E)$ contributions from ZnO and ZnS and is not indicative of a change in oxidation state of Zn.

Table E.5 Calculated total strain energy and strain energy density

Copper sulfide layer thickness (<i>t</i>)	Total Strain Energy (kBar)	Strain Energy Density (Bar·nm ³)
2.2	0.035	6.27771E-06
3.3	0.045	8.07134E-06
4.84	0.085	1.52459E-05
7.634	0.07	1.25554E-05
12.1	0.045	8.07134E-06
16.5	0.02	3.58726E-06
19.8	0.005	8.96816E-07

X-ray Absorption Absorption Near Edge Fine Structure (XANES)³

XANES describes the modulation of the linear X-ray absorption coefficient, $\mu(E)$, just above the absorption edge of an element, in this case the Cu or Zn, by neighboring atoms. When a photon strikes a material with an energy greater than the excitation energy of a core level electron (E_0) there is a sharp rise (edge) in the absorption coefficient, $\mu(E)$, this “edge” arises from dipole allowed transitions ($\Delta l \pm 1$, where l is angular momentum) of core level electrons into previously unoccupied electronic states⁴. In the XANES region (from 0 to ~50 eV above the edge) the kinetic energy of the outgoing photoelectron is low, and thus, multiple scattering dominates (for a more rigorous discussion of XANES and multiple scattering see Supplementary Information) which adds a fine structure component to the smooth, step-like, absorption profile (known as the atomic absorption coefficient, $\mu_0(E)$) which would be observed from a lone absorbing atom. Therefore, XANES can be thought of as a chemical fingerprint, containing information about the oxidation state (position of the excitation threshold, E_0) and the local chemical environment (number of neighboring atoms and local coordination geometry) of the absorbing atom (in this case either Cu or Zn). Thus, Cu (Zn) K-edge XANES directly probe the oxidation state and local chemical environment of the Cu (Zn) absorber *via* $1s \rightarrow np$ ($n \geq 4$) dipole allowed transitions.

In the XANES region the incident X-ray photon energy is equal to or just above (~10's of eV) the absorption threshold E_0 resulting in transitions of the core-level electron into previously bound and quasi-bound states. In a multi-atom system there are scattering contributions to the absorption coefficient μ from all the

neighbouring atoms resulting in multiple scattering pathways. The total absorption coefficient μ can be written as a function of energy as

$$\mu(E) = \mu_0 \left[1 + \sum_{n \geq 2} \chi_n(E) \right] \quad (1)$$

where μ_0 is the atomic absorption coefficient, n is the number of atoms, and $\chi_n(E)$ contains contributions to the absorption coefficient from all scattering pathways of $n - 1$ neighbouring atoms. Thus there is a strong effect on the amplitude and spectral shape of the XANES spectrum by the local symmetry, crystal structure, and type of the absorbing atoms.

The absorption coefficient, $\mu(E)$, is in theory proportional to the probability that an X-ray photon will be absorbed by an electron in the absorbing atom producing a transition between initial and final quantum states as described by Fermi's Golden Rule

$$\mu(E) \approx |\langle \psi_i | H | \psi_f \rangle|^2; H = (\hat{\varepsilon} \cdot \vec{r}) e^{i(\hat{k} \cdot \vec{r})} \quad (2)$$

where ψ_i is the initial state function which describes a core-level electron, X-ray photon, and no photoelectron; ψ_f is the final state function which describes a photoelectron, *core-hole*, and no X-ray; and H is the interaction Hamiltonian between the electromagnetic field of the X-ray and the electron. The Hamiltonian expression includes the electric field vector of the X-ray ε , the forward scattering vector k , and the electron coordinate vector r . If we further expand the Hamiltonian we get

$$H = (\hat{\epsilon} \cdot \vec{r}) + (\hat{\epsilon} \cdot \vec{r})(\hat{k} \cdot \vec{r}) + \dots \quad (3)$$

XANES is dominated by the first term in Equation 2-10 which is the dipole component, giving rise to transitions of core-level electrons from 1s to p final states (*K*-edge) and 2p to s + d final states (*L*_{3,2}-edges), etc. which follow the dipole selection rule ($\Delta l = \pm 1$ and $\Delta j = 0$). Although the quadrupole component (the second term of Equation 2-10) is several orders of magnitude weaker it is highly sensitive to metal d-electron–ligand hybridization and gives a strong contribution to the *K*-edge XANES of transition metals which are observed as weak pre-edge features before the main absorption edge^{5, 6}.

An alternative description of XANES is given by the band structure theory approach described by Muller and Wilkins⁷, where the X-ray energy dependence of the absorption coefficient μ can be described as

$$\mu(E) = \frac{4\pi^2\alpha}{\Omega/\nu} F(E) \quad (4)$$

where α is the inverse fine structure constant ($\alpha^{-1} = 137.036$), Ω is the primitive cell volume, ν is the number of atoms that contribute to the primitive cell, and $F(E)$ is the spectral distribution of the oscillator strength. $F(E)$ contains contributions from both atomic and solid state terms. The observed magnitude and shape of the XANES spectrum is determined by the atomic transition of a core-level electron and fine structure in the spectrum is determined by the solid state term which is proportional to the projected density of states.

LC(Linear combination)-XANES Fitting

In order to quantify the $\text{Cu}_{1.81}\text{S}$ and Cu_2S contributions to the copper K-edge XANES of the heterostructure NCs, we fit the absorption coefficient $\mu(E)$ with a linear combination of $\text{Cu}_{1.81}\text{S}$ (roxbyite) and Cu_2S (djurleite / low chalcocite) reference spectra according to (5),

$$\mu(E) = a_\mu \cdot \mu(E)_{\text{Cu}_{1.81}\text{S}} + b_\mu \cdot \mu(E)_{\text{Cu}_2\text{S}} \quad (5)$$

where E is the X-ray excitation energy and a_μ and b_μ are the weighting factors of $\text{Cu}_{1.81}\text{S}$ and Cu_2S , respectively. Fitting of the absorption coefficient $\mu(E)$ of the heterostructured NCs was also attempted using a linear combination of $\text{Cu}_{1.81}\text{S}$, Cu_2S (djurleite / low chalcocite), and CuS reference spectra; however, it was determined that there are no CuS contributions in the near edge region. The position of E_0 for the heterostructured NC samples, the $\text{Cu}_{1.81}\text{S}$ roxbyite NC starting materials, and the Cu_2S bulk sample was ~ 8980 eV, which is consistent with copper in the 1+ oxidation state (E_0 for Cu metal is 8979 eV). The fitting results are shown in **Table E.2**. LC-XANES fitting of NC sample with $t = 20$ nm is shown in **Fig. E.6**.

Scanning Transmission Electron Microscopy

The background EELS spectrum was modeled using a linear combination of power laws and a conservative local background average ranging from 1.5 to 2 pixels FWHM (smaller than the probe width). This provided a marginal improvement over traditional power law background modeling. These techniques were implemented using the open-source Cornell Spectrum Imager software and are described in more detail by P. Cueva et al.⁸

The sulfur EELS signal was obtained by integration over the $L_{2,3}$ core loss edge after background subtraction. The copper and zinc $L_{2,3}$ core loss edges start at 931 and 1020 eV respectively, with the Zn signal resting atop part of the Cu edge. To decompose the convoluted spectrum, reference spectrum obtained from an average of spectra in Cu or Zn regions were obtained and non-negative least square regression was performed.⁹ Better quantification of the Zn and Cu concentrations in the intermediate stage NC—where the Cu SNR was higher—was obtained (**Fig. E.17a,b**) through multivariate curve resolution (MCR) methods.^{10, 11, 12, 13} MCR was performed over 20 iterations to extract the spectral components—**Fig. E.17d** shows typical Cu and Zn MCR components.

References

1. Li, W.; Shavel, A.; Guzman, R.; Rubio-Garcia, J.; Flox, C.; Fan, J.; Cadavid, D.; Ibanez, M.; Arbiol, J.; Morante, J. R.; Cabot, A. *Chem. Commun.* **2011**, 47, (37), 10332-10334.
2. Xie, Y.; Riedinger, A.; Prato, M.; Casu, A.; Genovese, A.; Guardia, P.; Sottini, S.; Sangregorio, C.; Miszta, K.; Ghosh, S.; Pellegrino, T.; Manna, L. *J. Am. Chem. Soc.* **2013**, 135, (46), 17630-17637.
3. Ward, M. J. X-ray Absorption Fine Structure and X-ray Excited Optical Luminescence Studies of Gallium Nitride-Zinc Oxide Solid Solution Nanostructures. The University of Western Ontario, 2013.
4. Ward, M. J.; Rugar, P. A.; Murphy, M. W.; Yiu, Y.-M.; Baines, K. M.; Sham, T. *Chem. Commun.* **2010**, 46, (37), 7016-7018.
5. De Groot, F. *Chem. Rev.* **2001**, 101, (6), 1779-1808.
6. De Groot, F.; Kotani, A., *Core level spectroscopy of solids*. CRC press: 2008.
7. Müller, J. E.; Wilkins, J. W. *Phys. Rev. B* **1984**, 29, (8), 4331.
8. Cueva, P.; Hovden, R.; Mundy, J. A.; Xin, H. L.; Muller, D. A. *Microsc. Microanal.* **2012**, 18, (04), 667-675.
9. Bro, R.; De Jong, S. *J. Chemom.* **1997**, 11, (5), 393-401.
10. Sylvestre, E.; Lawton, W.; Maggio, M. *Technometrics* **1974**, 16, (3), 353-368.
11. Tauler, R.; Izquierdo-Ridorsa, A.; Casassas, E. *Chemometr. Intell. Lab.* **1993**, 18, (3), 293-300.

12. Kotula, P. G.; Keenan, M. R. *Microsc. Microanal.* **2006**, 12, (06), 538-544.
13. Kotula, P. G.; Keenan, M. R.; Grant, R. P.; Hlava, P. F. *Microsc. Microanal.* **2004**, 10, (S02), 118-119.

CHAPTER 7

7 BINDER-FREE AND CARBON-FREE NANOPARTICLE BATTERIES: A METHOD FOR NANOPARTICLE ELECTRODES WITHOUT POLYMERIC BINDERS OR CARBON BLACK *

7.1 *Abstract*

In this work we have developed a new fabrication method for nanoparticle (NP) assemblies for Li-ion battery electrodes that require no additional support or conductive materials such as polymeric binders or carbon black. By eliminating these additives we are able to improve the battery capacity/weight ratio. The NP film is formed by using electrophoretic deposition (EPD) of colloidally synthesized, monodisperse cobalt NPs that are transformed through the nanoscale Kirkendall effect into hollow Co_3O_4 . EPD forms a network of NPs that are mechanically very robust and electrically-connected, enabling them to act as the Li-ion battery anode. The morphology change through cycles indicates stable 5 – 10 nm NPs form after the first lithiation remained throughout the cycling process. This NP-film battery made without binders and conductive additives shows high gravimetric ($>830 \text{ mAh/g}$) and volumetric capacities ($>2100 \text{ mAh/cm}^3$) even after 50 cycles. Because similar films made from drop-casting do not perform well under equal conditions, EPD is seen as the critical step to create good contacts between the particles and electrodes resulting

* Originally Published as: D.-H. Ha, M.A. Islam, and R.D. Robinson, “Binder-free and Carbon-free Nanoparticle Batteries: A Method for Nanoparticle Electrodes without Polymeric Binders or Carbon Black,” *Nano Letters* 12, 5122 (2012) Reprinted with Permission from American Chemical Society.

in this significant improvement in battery electrode assembly. This is a promising system for colloidal nanoparticles and a template for investigating the mechanism of lithiation and delithiation of NPs.

7.2 Introduction

Nanoscale materials are extensively investigated and implemented for Li-ion battery electrodes due to their high surface-to-volume ratio and reduced Li-ion diffusion length, which results in faster charge/discharge.¹⁻³ Nanomaterials also show the ability to accommodate strain through volume expansion without pulverization or capacity fading.² In particular, nanoscale transition metal oxides have been studied as alternative anode materials due to their high capacity, as demonstrated by Tarascon et al.¹ The mechanism for lithiation/delithiation in these particles is through the formation and decomposition of Li_2O .^{1,3} Similar schemes have been expanded to various other transition metal oxides such as Fe_3O_4 , Fe_2O_3 , Co_3O_4 , SnO_2 and Mn_3O_4 leading to improved energy densities and high power density beyond bulk values.^{1,4,5}

However, understanding the physical mechanisms of these advances is obfuscated by inhomogeneities routinely introduced in battery construction, such as the addition of carbon-based conductive materials and polymeric binders, and the polydisperse size distribution of the particles. The commonly used carbon or acetylene black and polymeric binders are included for electrical conduction and better physical contacts between particles and current collector, respectively.⁶⁻⁹ These additives generate a weight increase (10 to 40 percent) for the battery electrode and

extra steps to mix and combine those materials into a film form. And because this mixture is an inhomogeneous blend of carbon black, binders, and nanoparticles, the diffusion paths of the ions and electrons are unclear, and it is difficult to model and characterize. Moreover, the mixture impedes specific testing of the active materials' properties since the choice of additive significantly affects the overall electrochemical performance of a cell.^{10, 11} Another unrefined parameter of conventional batteries is the lack of well-defined sizes and shapes of the nanoparticles. It is generally known that a homogeneous composition and a monodisperse morphology is crucial to maximize the nanoscale advantages.¹² However, controlling the size distribution and morphology of nanoparticles used in Li-ion battery electrodes is not common. Polydispersed nanoparticles complicate the understanding of the reaction mechanisms since each particle has a different Li-ion diffusion length. Many studies have shown that the sizes and shapes of nanoparticles influence the electrochemical performance and, remarkably, indicate that controlling the size and shapes is the key in order to fully understand the nanomaterial systems for Li-ion batteries.^{13, 14}

Previously, binder-free (binderless) and carbon-free electrodes from nanomaterials, such as “nanowires” or “nanotubes”, have been developed.^{2, 15-18} However, the use of nanoparticles has not yet been established for additive-free electrode films. Several reports demonstrate binderless battery electrodes with nanoparticles,¹⁹⁻²² however their films contain carbon-based conductive materials such as carbon nanotubes,^{19, 20} or form a hybrid with carbon, creating a conductive matrix.^{21, 22} These additive carbon materials do not contribute to the actual battery performance or show only limited capacity. A few reports exhibit electrodes without

binders and conductive materials free^{23,24} but their materials are not “nano” sized, and thus don’t benefit from any possible nano-size advantages.^{13,25} There are only a few reports that show additive-free “nanoparticle” electrodes for lithium ion battery. Lee et al. showed binderless and carbonless nanoparticle-like films for Li-ion battery electrode however the particles are polydisperse and require a high temperature (~1400 °C) and a special instrument, hot-wire chemical vapor deposition, in order to build the nanoparticle electrode film.²⁶ Finke et al. demonstrated electrochemical deposition of Bi from an acidic bath of Bi solution, forming a nanoparticle film without additives, however the particles are not monodisperse and the battery does not show cyclability.²⁷ Additive-free, electrode films of nanoparticles (NPs) have not been well-developed, especially for colloiddally synthesized NPs.

To harness the technologically important properties of nanoparticles, the particles need to be assembled in high-density films, devoid of their stabilizing organic ligands; the latter is essential if the film’s charge conductivity is important like in battery electrodes, flat panel displays, and in solar cells. Conventional self-assembly methods, e.g., drop cast and slow solvent evaporation, result in incoherent films with voids and cracks that lack in mechanical strength and do not permit strong interparticle charge transfer.²⁸ An alternative is to use electric field assisted deposition or electrophoretic deposition (EPD). In the simplest scheme of EPD a DC voltage is applied between two electrodes in a parallel plate capacitor configuration submerged in a nanoparticle solution. The particles are attracted to the electrodes simply by the Coulomb force, since many nanoparticle systems have surface facets and defects, and are liable to be electrically charged.

EPD is a widely used technique to make coatings and thin films, and has gained world-wide acceptance for a variety of applications such as automotive, appliance, and general industrial coatings. Advantages of EPD are high adherence and high density of the coating, homogeneity, and throw power. Complex shaped objects, e.g., taps, fasteners, and metal cones have been EPD coated for industrial applications due to EPD's high throw power.²⁹⁻³¹ Wires of kilometer length have been coated for use in superconductivity.³²

Application of EPD for assembling nanoparticles is relatively new. Giersig et al. have prepared ordered two-dimensional gold colloid lattices on carbon coated copper TEM grids by EPD.³³ Yeh et al. have deposited ordered colloidal aggregates of 2 micron diameter polystyrene beads.³⁴ Wong et al. have used the method to deposit 3-5 nm diameter ZnO nanocrystals on ITO electrodes.³⁵ Islam et al. have shown that EPD results in smooth, large area, almost defect-less CdSe nanoparticle films of high density, and that the inter-particle interaction between the neighboring particles and between the electrode (current collector) and the particles in the EPD films is different than that of drop cast films.^{36, 37} Islam et al. have argued that by removing a controlled fraction of the organic ligands from the (inorganic) nanoparticle surface it's possible to simultaneously ensure the stabilization of the particles in the organic solvents and their chemical bonding to a metal electrode during EPD.^{37, 38} This last point was our impetus in fabricating Li-ion battery electrodes using EPD since high-quality dense nanoparticle films with built-in charge transfer pathways is the key to high battery rate capacity, cyclability and longevity.

In this paper we show how to construct a nanoparticle Li-ion battery electrode by using electrophoretic deposition of monodisperse nanoparticles, without the use of binders or carbon black. To obtain monodisperse particles we synthesize cobalt nanoparticles through organic-phase colloidal nanocrystal synthesis methods, which are known to provide well-controlled shapes and sizes through the use of surfactant ligands.³⁹ The cobalt nanoparticles are assembled into films through EPD and then oxidized in air, leading to a hollow Co_3O_4 nanoparticle film (**Figure 7.1**), which is mechanically very robust. We have found that use of EPD to form the binderless, carbon-free films results in good electrical connectivity, while the commonly used drop-casted films of the same particles, calcinated under identical conditions have poor electrical contact and poor battery performance. This EPD film also shows better mechanical stability and comparable electrochemical performance to the slurry coating film prepared by conventional methods. These additive-free Co_3O_4 nanoparticle films show high gravimetric capacity compared to the theoretical capacity value and low degradation over many charge/discharge cycles. Additionally the volumetric capacity ($>2100 \text{ mAh/cm}^3$), based on the volume of Co_3O_4 nanoparticle films, is 2.5 times higher than graphite ($\sim 800 \text{ mAh/cm}^3$) and higher than other nanomaterials previously reported. To our knowledge, this is the first nanoparticle-film battery electrode made without using binders and carbon black additives to show very high gravimetric ($>830 \text{ mAh/g}$) and volumetric capacities ($>2100 \text{ mAh/cm}^3$) even after 50 cycles.

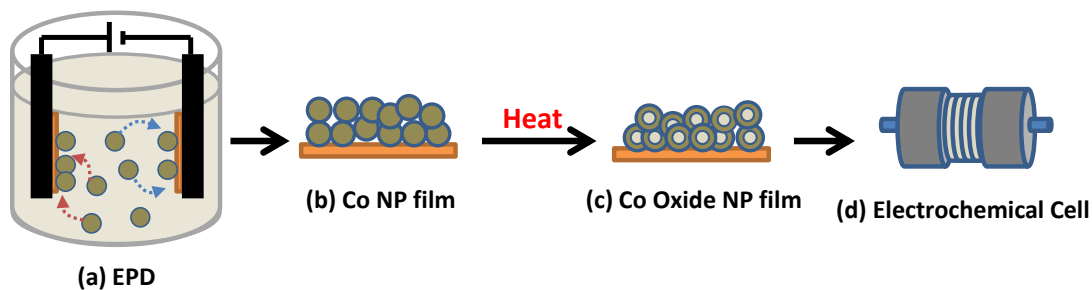


Figure 7.1 Schematic of process for fabrication of binderless, carbon-free nanoparticle film battery electrodes: (a) electrophoretic deposition (EPD) apparatus for making cobalt nanoparticle (NP) films. A beaker with cobalt nanoparticles dispersed in a solvent. On each electrode, there is a copper collector, which acts as the substrate for the NP electrode. After the plates are immersed in the NP solution a voltage is applied to the plates. The voltage induces cobalt NP deposition on both electrodes. (b) The Co NP film formed on copper current collector is calcinated at 200 °C in air and become (c) cobalt oxide NP film. (d) Finally, this film is assembled into an electrochemical cell.

7.3 Results and Discussion

The ϵ -Co nanoparticle (NP) synthesis follows standard procedures.⁴⁰ A N_2 flushed flask is filled with TOPO (0.1 g). After adding 0.09 g (0.32 mmol) of oleic acid dissolved in 12 mL of 1,2-dichlorobenzene, the solution is heated. When the temperature of the solution reaches 180 °C, 0.52 g (1.52 mmol) of $Co_2(CO)_8$ dissolved in 4 mL of 1,2-dichlorobenzene is quickly injected. After the reaction progresses for 5 mins, the heating mantle is removed and the reaction solution is quenched in a water bath. The cobalt NPs are purified by adding ethanol and centrifuged. The supernatant is removed, and the NPs are re-dispersed in hexanes. This precipitation/re-dispersion process is performed twice overall. Generally, additional washing leads to more charges on the NPs, which is important for the electric deposition process.⁴¹ Colloidal ϵ -Co NPs are assembled onto a film through electrophoretic deposition (EPD). As shown in **Figure 7.1**, a copper current collector plate is attached to a stainless steel electrode plate, for each polarity (+ and -). These two copper plates are facing each other and separated by 2 mm. The electrodes are immersed in a solution of concentrated NP (0.1 – 1 mg/ml), dispersed in a solvent. A DC voltage (~150 to 600 V) is then applied to these electrodes. Once the voltage is applied a NP film forms on the electrodes and the NP solution turns from dark to clear. Deposition proceeds until the NP solution is very clear (~ 10 to 30 mins depending on concentration and voltage). A film is formed on both the positive electrode and negative electrode. **Figure 7.2a** clearly shows the black NP film after the deposition of NPs. The film on the positive electrode is generally slightly thicker than that of the negative electrode (~20% – 80%), which indicates that more particles are negatively charged in the

solvent. The thickness of the films can be made to be a few hundreds of nanometers to a few microns by controlling the concentration and deposition time. Generally, the polarities of these two electrodes are reversed several times during deposition in order to get a similar thickness on both electrodes.

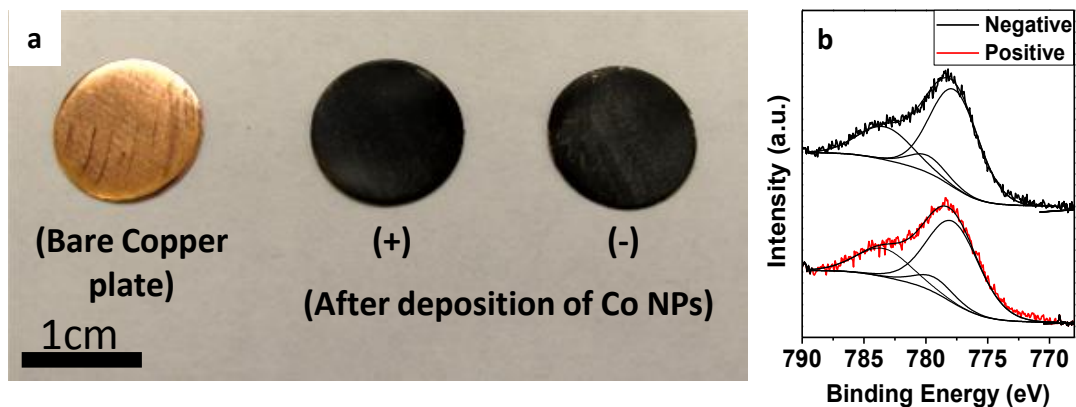


Figure 7.2 EPD-formed nanoparticle film: (a) Photograph of bare copper plate before NP deposition (left) and after deposition on (center) positive electrode and (right) negative electrode which show a thick, black NP film. (b) High-resolution Co $2p_{3/2}$ XPS spectra of Co EPD film formed on positive (red line) and negative (black line) electrode.

To compare the chemistry of the nanoparticle films formed on the opposite electrodes during EPD, XPS (X-ray photoelectron spectroscopy) with monochromated aluminum K-alpha X-rays (1486.6 eV) is utilized. **Figure 7.2b** shows Co $2p_{3/2}$ XPS spectra of the samples fabricated on positive electrode (red line) and negative electrode (black line). Both spectra exhibit the strong Co $2p_{3/2}$ peak around 778.4 eV

confirming that both samples contain Co^0 for major component. Each spectrum is deconvoluted to three Gaussian peaks that correspond to Co^0 at 778.1 eV and Co^{2+} at 780.2 and 783.9 eV (shakeup satellites)^{42, 43} indicating the surface oxidation of CoO phase. Both samples show the identical amount of surface oxidation and energy shifts, confirming that the opposite polarity of e-field during EPD does not influence the chemistry of the NPs.

To form the cobalt oxide used as an electrode in Li-ion batteries the ϵ -cobalt NP films are oxidized in air (see **Figure 7.1**). XRD data show that the NPs transform from ϵ -cobalt to two phases of cobalt oxide through the calcination process in air (**Figure 7.3a**). The Co_3O_4 phase is the useful phase for lithium ion battery anodes since it has one of the highest theoretical capacities among metal oxides.^{1, 8, 44} The XRD peaks of the initial cobalt NPs match well with the reference standard peaks (**Figure 7.3a**, green bars) of the ϵ -cobalt phase, which is the common phase for cobalt metal in NPs.^{40, 45, 46} After heating the Co NP film in the furnace at 200 °C for 10 mins, Co NPs oxidize and the major phase becomes CoO. The XRD spectrum of the sample calcinated for 10 mins shows broader peaks than those of ϵ -Co NPs, which indicates the decreased grain size and reduced long range order from the oxidation. Through further heating, the CoO NPs begin to transform to the Co_3O_4 phase. The XRD pattern of the sample that is calcinated for 30 mins at 200 °C shows two peaks around 37° and 43°, which correspond to the strongest diffraction planes for Co_3O_4 and CoO phase respectively. After heating this intermediate stage (CoO + Co_3O_4) for 1.5 hours the CoO strongest peak is no longer detected and the NPs have transformed

into Co_3O_4 phase. Longer oxidation times do not lead to other oxygen rich phases, such as Co_2O_3 (see **Figure F.1**).

Comparing the air oxidation of cobalt to solution-phase oxidation we note that, unsurprisingly, the air calcination process more effectively converts the metal to the oxide phases. In the solution-phase method, the Co NPs react with an O_2/Ar mixture gas for 3 hours at 455 K and result in only the CoO phase.⁴⁷

TEM characterization of the morphological evolution during the transformation from cobalt to cobalt oxides show monodisperse ϵ -Co NPs that transform into hollow final products. The studies were conducted by depositing ϵ -Co NPs on a carbon-coated TEM grid and heating the grid to 200 °C in air. The initial ϵ -Co NPs are a monodisperse spherical shape and monodisperse size (size: 9.5 nm, std. dev 8 %) (**Figure 7.3b**). After 30 minutes heating at 200 °C, the NPs (**Figure 7.3c**) have a dark center that is commonly seen at the onset of the nanoscale Kirkendall effect as the transformation is initiated and a shell begins to develop.^{45, 47} The nanoscale Kirkendall effect is due to the asymmetric diffusion rates of atoms and ions in a material and results in hollow nanoparticles. After heating for 1.5 hours the sample converts to Co_3O_4 and the NPs exhibit the Kirkendall hollowing with bigger NP size (size: 13.4 nm, std. dev 9 %) (**Figure 7.3d**). Through this transition progression, the single crystalline cobalt NPs transforms to polycrystalline hollow NPs, as confirmed by HRTEM (**Figure 7.3e,f**). Scherrer analysis of the grains also shows a decrease in crystal size from ~10 nm in initial cobalt NP to ~4.3 nm in Co_3O_4 NP (**Figure 7.3a**).

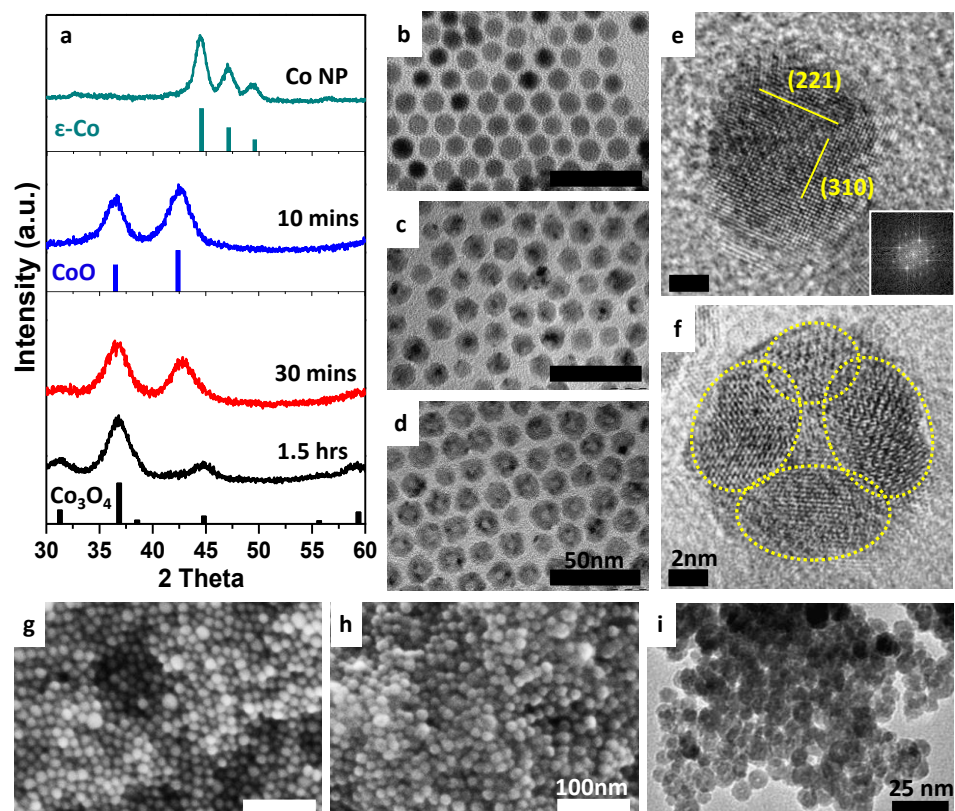


Figure 7.3 Materials characterization of EPD-formed nanoparticle electrodes: (a) XRD spectra of the samples from as-synthesized Co NPs to two phases of cobalt oxide through calcination at 200°C in air. The green, blue, and black vertical bars correspond to references of ϵ -Co⁴⁶, CoO (JCPDS No. 48-1719), and Co₃O₄ (JCPDS No. 42-1467) phases, respectively. The 30 minute oxidation sample is mixed phases of CoO and Co₃O₄. The 1.5 hour sample is fully converted to Co₃O₄. TEM images of (b) as synthesized ϵ -Co NPs, (c) NPs calcinated for 30mins at 200 °C, and (d) NPs calcinated for 1.5 hours at 200 °C. XRD indicates the phase of samples shown in d is the desired Co₃O₄. (e) HRTEM image and FFT (inset) of samples shown in b (ϵ -Co NP) and (f) HRTEM image of samples shown in d. (Co₃O₄) Yellow dotted circles in (f) indicate each crystalline regions of polycrystalline shell. Scale bar is 50 nm in b, c, and d, and 2 nm in e and f. (g and h) SEM images of EPD film: (g) before and (h) after oxidation shows dense network of NPs which should provide good electrical conducting pathways. (i) TEM image of NPs scraped off from oxidized EPD film. Hollow particles are evident in these films. Scale bar is 100 nm for g and h and 25 nm for i.

SEM images of the films show a random network of deposited particles that increases in density after the oxidation process. The Co NP film formed by EPD shows an assembly of NPs separated by surfactant ligands (**Figure 7.3g**). After oxidation for 1.5 hours at 200 °C discrete NPs are still evident in the film, but the particles now form a denser network due to the decrease in inter-particle spacing (**Figure 7.3h**). TEM samples of the interior were prepared to ensure that the NPs in the interior of the film are similar to those shown on the surface with the SEM images, i.e., not sintered and exist as discrete particles. TEM results of the NPs from oxidized film show aggregation, but the NPs are not sintered into bulk material (**Figure 7.3i**).

These EPD films show very rigid contact between the NP film and the copper current collector for both cobalt NP films and the films formed after oxidation. Both the EPD as-deposited cobalt film and the oxidized film are no longer soluble in typical NP solvents such as hexane, even with an ultra-sonication procedure. This excellent physical connectivity property might be the source of good electrical conducting pathways.

Elemental analysis of carbon atoms was performed for both the initial cobalt nanoparticles and the cobalt oxide nanoparticles, in order to investigate the change of the organic surfactant ligands that are initially present on the surface of the cobalt nanoparticles. The elemental analysis is performed for carbon by high temperature combustion followed by IR detection. The initial carbon weight percent of cobalt NP sample was about 6.7 wt % and this carbon weight significantly decreased to 0.84 wt % after the oxidation of the sample at 200 °C in air, indicating that most of the organic components are burned off through the heating process. The 0.84 wt% of carbon is

significantly less than that is required for monolayer coverage of carbon on the 14 nm sized NPs.

Thickness measurements show a contraction of the volume after oxidation (**Table 7.1**). Three cobalt NP films with different thicknesses – 470 nm, 1000 nm, and 1500 nm – were prepared through EPD. Surprisingly, all the samples showed about a 25% reduction in thickness after oxidation despite the increased particle sizes from the Kirkendall hollowing (**Table 7.1**). Even when the shrinkage of the volume due to the organic ligands elimination is considered, this 25% reduction is surprising because the NP size actually increases about 40% during oxidation and the density of Co_3O_4 (6.11 g/cm^3) is also lower than that of $\epsilon\text{-Co}$ (8.64 g/cm^3). This contraction of the film implies that the NPs are filling the porous spaces and settling on more stable sites during oxidation process.

Table 7.1 Thickness and volume analysis of three samples with different thicknesses.

Sample	Thickness		Volume change after oxidation	Density of Co_3O_4 NP Film
	Cobalt NP film	Cobalt oxide NP film		
1	465 nm	347 nm	25% reduction	2.72 g/cm^3
2	1001 nm	725 nm	28% reduction	2.12 g/cm^3
3	1497 nm	1136 nm	24% reduction	2.23 g/cm^3

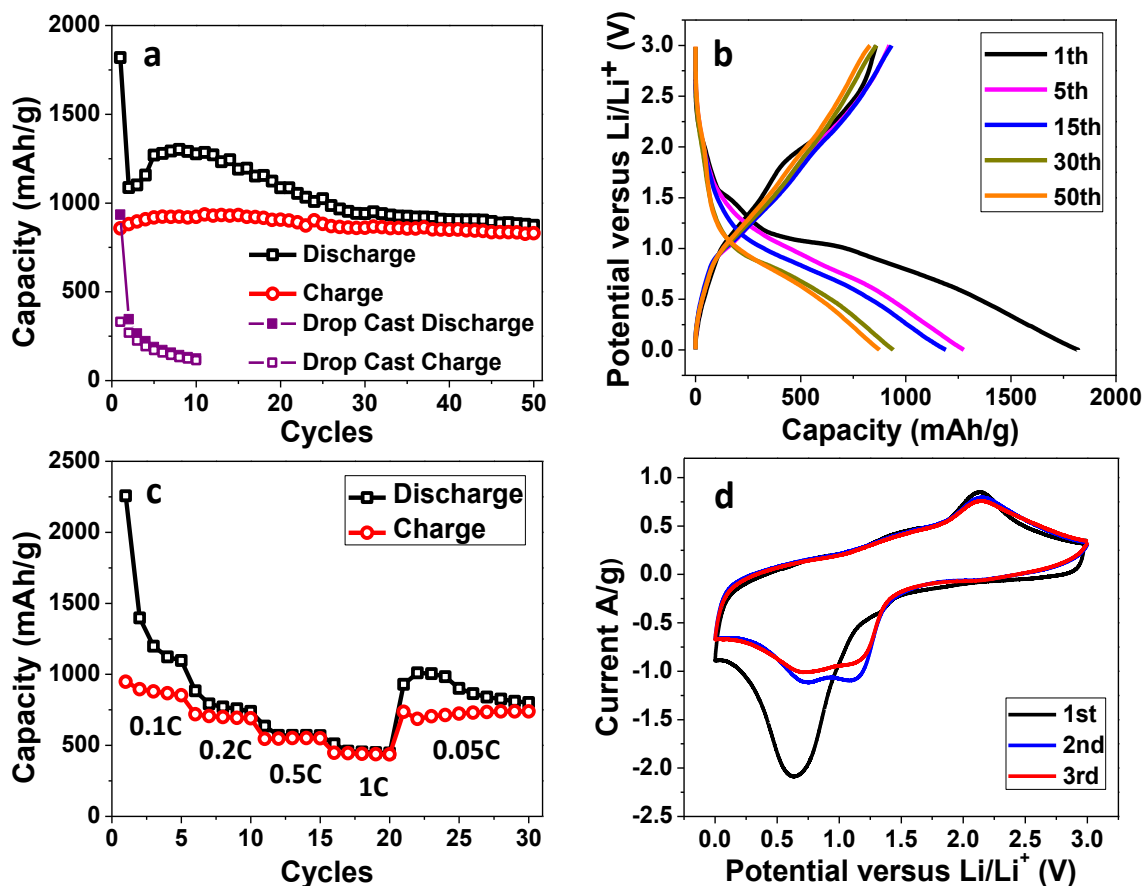


Figure 7.4 Electrochemical performance of EPD Co_3O_4 NP films without carbon black and polymeric additives: (a) Capacity retention at C/20 rate showing the charge (red circles) and discharge (black squares). The purple solid squares and purple open squares show the discharge and charge capacities of drop casted film, respectively. (b) Galvanostatic charge-discharge curves and (c) cycling performance at various current rates showing charge (red circles) and discharge (black squares) (d) Cyclic voltammetry at 50 mV/s rate.

Our EPD-formed Co_3O_4 NP films show higher density than the tap density of a mixture of the same Co_3O_4 NPs with carbon black and Polyvinylidene fluoride (conventional slurry method): $2.12 - 2.72 \text{ g/cm}^3$ for the EPD films versus 1.76 g/cm^3 for the mixture and its dried slurry, based on the Co_3O_4 NP mass. The EPD nanoparticle films also show higher density than the Co_3O_4 NP dried slurry mixture pressed under 160 MPa (2.18 g/cm^3). (See supplementary materials)

The electrochemical performance of these additive-free Co_3O_4 nanoparticle films were tested by using the films as a working electrode in a Swagelok-type electrochemical cells. The cells were completed by using Li foil as the counter electrode, 1 M LiPF_6 in a 50:50 w/w mixture of ethylene carbonate and diethyl carbonate as an electrolyte, and a polypropylene separator (Celgard 2400). **Figure 7.4a** shows the charge/discharge capacity of the film through 50 cycles at C/20 rate considering C as 900 mAh/g. Even after 50 cycles of charge/discharge the capacity is retained near the theoretical capacity (890 mAh/g), much higher than graphite (372 mAh/g) that is commercially used as the anode material of Li-ion batteries. However, the working voltage of our Co_3O_4 EPD film is higher than that of graphite. **Figure 7.4b** shows the galvanostatic discharge (lithiation) – charge (delithiation) curves at C/20 which exhibits high capacity for the first discharge (1820 mAh/g) and decreased throughout cycles. This huge reduction in capacity after the first cycle is due to characteristic irreversible reactions.^{12, 44} Additionally, there is a small capacity contribution from copper oxide thin layer of copper current collector which might be formed during oxidation. As a control experiment, an electrochemical measurement was conducted with a bare copper plate (no NP film) that was treated with the same

oxidation process. This heat-treated copper plate shows a capacity of about 240 mAh/g for the first discharge, but drops to 30 mAh/g for the second cycle, and becomes negligible after several cycles indicating that there is a small contribution to the overall capacity only for first few cycles (see **Figure F.2**). **Figure 7.4c** shows the cycling performance at various current rates. This result reveals the excellent recovery of these novel films after 20 cycles of high current rates. However, at a low current rate (C/20) the samples show discharge capacity increasing for first several cycles which indicates additional reactions for low current rate (**Figure 7.4a** and **7.4c**). Insight into the redox reaction is given (**Figure 7.4d**) by a cyclic voltammetry (CV) measurement with lithium as a counter electrode at 0.5 mV/s. The peaks of the CV cycle for the EPD films are well matched with other Co_3O_4 nanomaterials.^{8, 12, 48} The first cycle of CV shows broad oxidation peaks around 1.5 V and 2.15 V and one reduction peak at 0.63 V that becomes two peaks in the second cycle around 1.26 V and 0.84 V.

In order to understand how our EPD films differ from films formed by other techniques we compared our EPD method against drop-casted films and conventional slurry coated film with polymeric binder and carbon black. Drop-casting is a widely used method to form NP films.^{49, 50} The drop-cast film of NPs was prepared by depositing cobalt nanoparticles dispersed in solvents with different boiling points (B.P.) such as hexane (low B.P.) and tetrachloroethylene (high B.P.) onto a substrate by evaporation of solvents and then calcinating the particles under identical conditions (200 °C for 2 hours in air). The conventional film is prepared by mixing Co_3O_4 NPs with PVDF (Polyvinylidene fluoride) and carbon black. (See supplementary) The

total amount of NPs deposited through drop-casting and the conventional film is controlled to be that of the EPD films. We have investigated the mechanical stability of all three samples with Co_3O_4 nanoparticles: 1) NP films assembled through EPD, 2) NP films formed by drop-casting, and 3) NP films with PVDF and carbon black prepared through conventional methods. A bending test and an adhesion test were carried out to examine the mechanical firmness. Bending experiments were carried out up to the curvature with 0.35 cm radius. All samples do not show any noticeable cracking (**Figure F.3**). Figure 5a shows the bent EPD NP film. An adhesion test was also used to evaluate the mechanical rigidity. Scotch tape was well-attached to the sample films and pulled off (See supplementary). Surprisingly, the EPD film is very stable while the other films were partially de-adhered by the tape. This is shown in **Figure 7.5b**: after the tapes were removed the conventional and drop cast samples clearly show the black NPs removed from the copper plate (**Fig. 7.5b**, top) and the NPs sticking to the tape (**Fig. 7.5b**, bottom). The EPD film, however, exhibits little to none de-adhesion of NPs from the adhesion test. This excellent mechanical stability might provide a critical benefit for building a battery without additives.

Electrochemical performance was also measured for drop-casted and conventional nanoparticle films. The Co_3O_4 NP films formed by drop-casting and by conventional methods were assembled into a Swagelok-type electrochemical cell and measurements similar to those on the EPD films were carried out. No additional polymer binders and carbon black were added to the drop-cast sample as EPD film. Cyclic voltammetry (CV) measurement of drop-casted film with lithium as a counter electrode displays many spikes due to poor contacts between NPs and the copper

current collector, especially during the deintercalation of lithium ions from cobalt oxide film (**Figure F.4**). This poor contact deteriorates even more as charge/discharge cycles are carried out, while the EPD film shows smooth reduction and oxidation curves over all cycles. The galvanostatic measurement also reveals that the EPD films exhibit much better cycle performance than drop-casted films at C/20 rate. (**Figure 7.4a**) In general, most of the drop-casted films (> 80 %) fail to show the reasonable data without any spikes (see **Figure F.5**) and the cycle performance of the remaining 20% exhibit very poor capacity retention. EPD films, however, show only a small decrease of a capacity after cycling. This result explains why polymeric binder and carbon black are needed in all other NP battery electrodes when the NPs are simply placed (drop-cast) on a current collector. The conventional slurry coated film shows similar cyclability through 50 cycles without any significant difference compared to the EPD film's performance (**Figure F.6**).

The volumetric capacity is calculated based on the volume of the cobalt oxide film formed through EPD and oxidation process. The density of our cobalt oxide EPD film is $2.12 - 2.72 \text{ g/cm}^3$ which means overall packing factor of the film is about 0.35 – 0.45 since the density of Co_3O_4 phase is 6.11 g/cm^3 . Therefore, for the high gravimetric capacity samples (890 mAh/g, measured at a low current rate) the volumetric capacity is $2100 - 2500 \text{ mAh/cm}^3$. This volumetric capacity is much higher than graphite, which is about 800 mAh/cm^3 ^{15, 51} and also higher than other reported nanomaterials.^{15, 52, 53} For a more accurate determination of volumetric capacity, the volume expansion and contraction during discharge/charge cycles will be taken into account in future studies. Future improvements in packing factor are

expected from using a slower EPD process (low V and longer deposition time) to create a higher density of NPs. Preliminary studies indicate that varying the deposition conditions can lead to denser films (~20%), but further study is necessary.

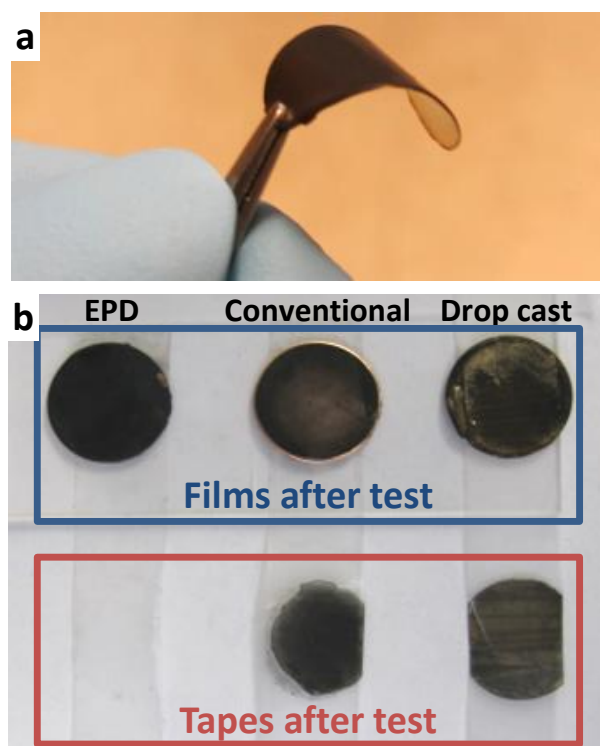


Figure 7.5 Mechanical stability test of Co_3O_4 nanoparticle films: (a) EPD film bends without any noticeable cracks. (b) Scotch tape method is used for adhesion test.

Films in the blue box show the electrodes after the adhesion test. The films are prepared on copper plates by EPD (left), the conventional method (center), and drop-casting (right). The tapes after the test are shown in red box. The tape tested for EPD film (left) shows no noticeable nanoparticles while those for conventional (center) and drop casting (right) film exhibit a significant amount of black film that has de-adhered from the electrodes.

To understand the dependence on film thicknesses and EPD applied voltages, further experiments were carried out in this parameter space. To represent the cyclability, the charge capacity of the 10th cycle of each sample is chosen. **Figure 7.6** shows the correlation between the cycle performance and thicknesses of films at different EPD voltages. The black solid squares and red solid squares represent the 10th cycle charge capacities at a C/20 rate for the 300 V and 600 V EPD deposited samples, respectively. The open black squares, open red squares, and open blue squares display the 10th cycle capacities of the 300 V, 600V, and 150 V samples, respectively, measured at C/10 rate for first 5 cycles and C/5 rate for last 5 cycles. This plot shows that the EPD voltage does not influence the cycle performance significantly within the range from 150 V to 600 V. It however clearly shows that the battery capacity strongly depends on the film thickness. The capacity decreases when the film is thicker than 1 μm , and becomes less than 20% of the theoretical capacity for a 5 μm thick sample. This thickness-dependent capacity indicates that the critical thickness of the film, in order to fully utilize battery performance, is 1 μm . It is likely that this limit is governed by the limited electrical conductivity of the oxide particles. Films with higher packing factors should improve the range of peak-performing thicknesses since higher packing implies additional connectivity pathways between NPs.

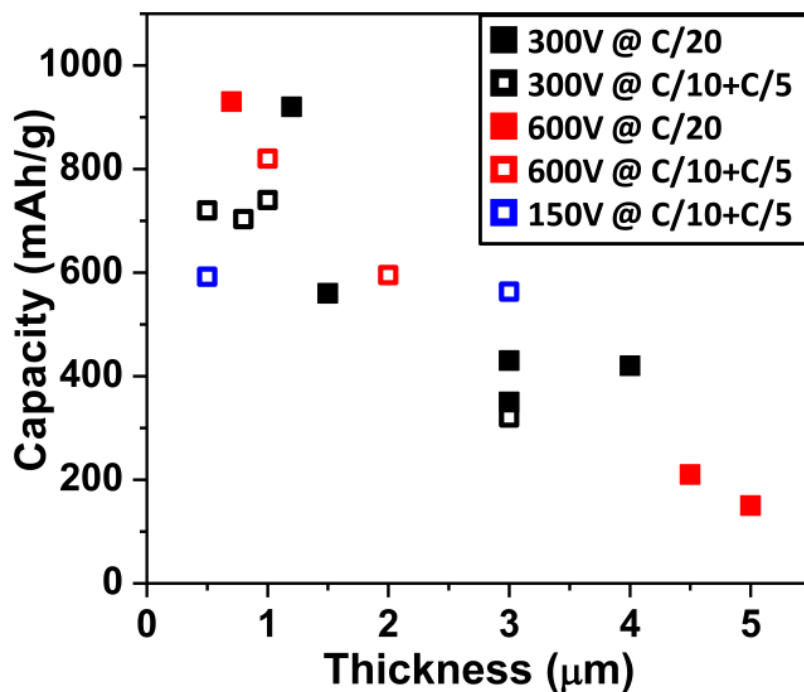


Figure 7.6 Relationship between average film thickness and the charge capacity for different applied voltages during EPD: Capacity was taken at 10th cycle. The black solid squares and red solid squares present 10th cycle capacities at C/20 rate for films assembled at EPD voltages of 300 V and 600 V, respectively. The open black squares, open red squares, and open blue squares show 10th cycle capacities of 300 V, 600V, and 150 V samples, respectively, measured at C/10 rate for first 5 cycles and C/5 rate for remaining 5 cycles.

Due to the absence of binders and carbon black, we can study the morphology evolution during cycles. After the electrochemical measurements were completed, the Swagelok cells were disassembled and the EPD films were cleaned with diethylene carbonate, ethanol, and hexane in order to remove electrolyte residues. The samples

were then scraped off from the copper current collector and put on TEM grids. **Figure 7.7a** shows the TEM image of aggregated small NPs (size: ~5 – 10 nm) after first lithiation process, which reveals that the NPs are no longer individual hollow NPs. This implies that the polycrystalline hollow NPs break into smaller NPs during lithiation. Also after delithiated, NPs are even smaller (size: about 5 nm) (**Figure 7.7b**). These small (~5 nm) NPs remain after 30 cycles of lithiation/delithiation cycle (**Figure 7.7c**). These results suggest the evolution of the NPs during battery operation (**Figure 7.7d**): the initial cobalt oxide NPs are polycrystalline with hollow structure, during the first lithiation step, the polycrystalline hollow NPs break into several pieces, possibly along the grain boundaries, these small NPs can reversibly accommodate lithium ions through cycles. Many nanoparticle systems have been used for size dependent electrochemical properties and each cases show different sizes for the best performance.^{1, 13, 54} In the Co_3O_4 NP system, 5-10 nm may be a stable size for reversible lithiation and delithiation without pulverization.

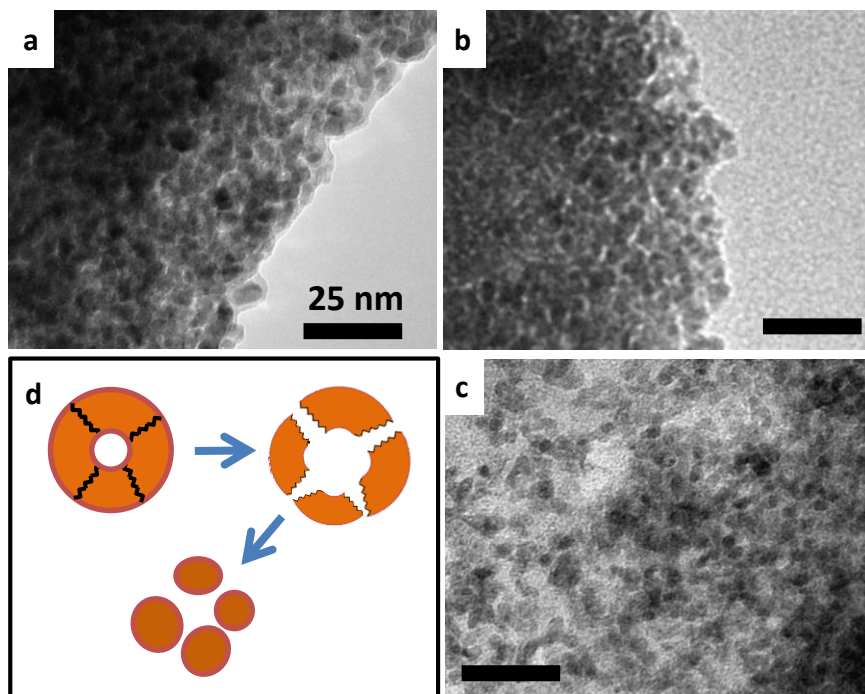


Figure 7.7 TEM images and schematic of nanoparticles through

lithiation/delithiation process: (a) after lithiation, (b) after 1 lithiation/delithiation cycle, and (c) after 30 cycles. The size of the particles are between 5 and 10 nm for (a) and ~5 nm for (b) and (c). (d) Schematic of the evolution of NPs during lithiation. Initial cobalt oxide NP is polycrystalline with hollow structure. During the lithiation process, the NP breaks into several particles and finally become individual NPs.

7.4 Conclusion

We have demonstrated a new method to build high-capacity, additive-free nanoparticle films for Li-ion battery electrodes, eliminating the need for polymeric binders and conductive carbon materials. Removing additives is an effective means to reduce the weight and volume of batteries. Our method employs colloidal synthesis

techniques to produce spherical, monodisperse cobalt metal NPs, which are solution-processable. The critical solution-processing technique that we use to obtain good battery performance for the NP films is electrophoretic deposition (EPD). EPD binds the metal NPs to the surface of the electrode and to each other in an assembly, which is subsequently converted to Co_3O_4 NPs with a polycrystalline hollow structure.

Our cobalt oxide NP films formed without any binders and carbon black show excellent cyclability at low current. This EPD film exhibits superior mechanical stability to other films fabricated by drop-casting or through conventional slurry methods. The electrochemical properties are optimized when the film is 1 μm thick. By scraping off the NPs from current collectors the morphology change is studied after lithiated and delithiated. A stable particle size of 5 – 10 nm is retained through the lithiation/delithiation cycling.

Due to the absence of additive materials this method can provide a good template system to investigate the physical mechanisms and understand the reactions during charge/discharge. This system provides opportunities to utilize colloidal NPs for battery electrodes in a simple and robust manufacturing process.

7.5 References

1. Poizot, P.; Laruelle, S.; Grugeon, S.; Dupont, L.; Tarascon, J. M. *Nature* **2000**, 407, (6803), 496-499.
2. Chan, C. K.; Peng, H. L.; Liu, G.; McIlwrath, K.; Zhang, X. F.; Huggins, R. A.; Cui, Y. *Nat. Nanotechnol.* **2008**, 3, (1), 31-35.
3. Chen, J.; Xu, L.; Li, W.; Gou, X. *Adv. Mater.* **2005**, 17, (5), 582-586.
4. Taberna, P. L.; Mitra, S.; Poizot, P.; Simon, P.; Tarascon, J. M. *Nat. Mater.* **2006**, 5, (7), 567-573.
5. Cabana, J.; Monconduit, L.; Larcher, D.; Palacín, M. R. *Adv. Mater.* **2010**, 22, (35), E170-E192.
6. Park, M.-H.; Kim, K.; Kim, J.; Cho, J. *Adv. Mater.* **2010**, 22, (3), 415-418.
7. Gao, J.; Lowe, M. A.; Abruña, H. c. D. *Chem. Mater.* **2011**, 23, (13), 3223-3227.
8. Wu, Z.-S.; Ren, W.; Wen, L.; Gao, L.; Zhao, J.; Chen, Z.; Zhou, G.; Li, F.; Cheng, H.-M. *ACS Nano* **2010**, 4, (6), 3187-3194.
9. Wang, H.; Cui, L.-F.; Yang, Y.; Sanchez Casalongue, H.; Robinson, J. T.; Liang, Y.; Cui, Y.; Dai, H. *J. Am. Chem. Soc.* **2010**, 132, (40), 13978-13980.
10. Kovalenko, I.; Zdyrko, B.; Magasinski, A.; Hertzberg, B.; Milicev, Z.; Burtovyy, R.; Luzinov, I.; Yushin, G. *Science* **2011**, 334, (6052), 75-79.
11. Jin, B.; Gu, H.-B.; Kim, K.-W. *J. Solid State Electrochem.* **2008**, 12, (2), 105-111.

12. Nam, K. T.; Kim, D.-W.; Yoo, P. J.; Chiang, C.-Y.; Meethong, N.; Hammond, P. T.; Chiang, Y.-M.; Belcher, A. M. *Science* **2006**, 312, (5775), 885-888.
13. Kim, C.; Noh, M.; Choi, M.; Cho, J.; Park, B. *Chem. Mater.* **2005**, 17, (12), 3297-3301.
14. Chen, J. S.; Zhu, T.; Hu, Q. H.; Gao, J.; Su, F.; Qiao, S. Z.; Lou, X. W. *ACS Appl. Mater. Interfaces* **2010**, 2, (12), 3628-3635.
15. Chockla, A. M.; Harris, J. T.; Akhavan, V. A.; Bogart, T. D.; Holmberg, V. C.; Steinhagen, C.; Mullins, C. B.; Stevenson, K. J.; Korgel, B. A. *J. Am. Chem. Soc.* **2011**, 133, (51), 20914-20921.
16. Li, Y.; Lv, X.; Li, J. *Appl. Phys. Lett.* **2009**, 95, (11), 113102-3.
17. Li, C. C.; Li, Q. H.; Chen, L. B.; Wang, T. H. *J. Mater. Chem.* **2011**, 21, (32), 11867-11872.
18. Wu, H.; Chan, G.; Choi, J. W.; Ryu, I.; Yao, Y.; McDowell, M. T.; Lee, S. W.; Jackson, A.; Yang, Y.; Hu, L.; Cui, Y. *Nat Nano* **2012**, 7, (5), 310-315.
19. Zhang, H.-X.; Feng, C.; Zhai, Y.-C.; Jiang, K.-L.; Li, Q.-Q.; Fan, S.-S. *Adv. Mater.* **2009**, 21, (22), 2299-2304.
20. Ban, C. M.; Wu, Z. C.; Gillaspie, D. T.; Chen, L.; Yan, Y. F.; Blackburn, J. L.; Dillon, A. C. *Adv. Mater.* **2010**, 22, (20), E145-149.
21. Jo, G.; Choi, I.; Ahn, H.; Park, M. J. *Chem. Commun.* **2012**, 48, (33), 3987-3989.

22. Sun, Y.; Hu, X.; Yu, J. C.; Li, Q.; Luo, W.; Yuan, L.; Zhang, W.; Huang, Y. *Energy Environ. Sci.* **2011**, 4, (8), 2870-2877.
23. Yao, Y.; McDowell, M. T.; Ryu, I.; Wu, H.; Liu, N.; Hu, L.; Nix, W. D.; Cui, Y. *Nano Lett.* **2011**, 11, (7), 2949-2954.
24. Lai, W.; Erdonmez, C. K.; Marinis, T. F.; Bjune, C. K.; Dudney, N. J.; Xu, F.; Wartena, R.; Chiang, Y.-M. *Adv. Mater.* **2010**, 22, (20), E139-E144.
25. Koo, B.; Xiong, H.; Slater, M. D.; Prakapenka, V. B.; Balasubramanian, M.; Podsiadlo, P.; Johnson, C. S.; Rajh, T.; Shevchenko, E. V. *Nano Lett.* **2012**, 12, (5), 2429-2435.
26. Lee, S.-H.; Kim, Y.-H.; Deshpande, R.; Parilla, P. A.; Whitney, E.; Gillaspie, D. T.; Jones, K. M.; Mahan, A. H.; Zhang, S.; Dillon, A. C. *Adv. Mater.* **2008**, 20, (19), 3627-3632.
27. Finke, A.; Poizot, P.; Guery, C.; Dupont, L.; Taberna, P.-L.; Simon, P.; Tarascon, J.-M. *Electrochem. Solid-State Lett.* **2008**, 11, (3), E5-E9.
28. Leatherdale, C. A.; Kagan, C. R.; Morgan, N. Y.; Empedocles, S. A.; Kastner, M. A.; Bawendi, M. G. *Phys. Rev. B* **2000**, 62, (4), 2669-2680.
29. Ryan, W.; Massoud, E. *Interceram* **1979**, 28, (2), 117-119.
30. Aveline, M. *Ind. Ceram.* **1966**, 581, 28-31.
31. Ortner, M. *Plating* **1964**, 51, (9), 885.
32. Barraclough, M.; Bolton, N.; Collins, A.; Andrews, J. *IEEE Trans. Magn.* **1967**, 3, (3), 531-534.

33. Giersig, M.; Mulvaney, P. *Langmuir* **1993**, 9, (12), 3408-3413.
34. Yeh, S.-R.; Seul, M.; Shraiman, B. I. *Nature* **1997**, 386, (6620), 57-59.
35. Wong, E. M.; Searson, P. C. *Chem. Mater.* **1999**, 11, (8), 1959-1961.
36. Islam, M. A.; Herman, I. P. *Appl. Phys. Lett.* **2002**, 80, (20), 3823-3825.
37. Islam, M. A.; Xia, Y.; Telesca, D. A.; Steigerwald, M. L.; Herman, I. P. *Chem. Mater.* **2003**, 16, (1), 49-54.
38. Islam, M. A.; Xia, Y.; Steigerwald, M. L.; Yin, M.; Liu, Z.; O'Brien, S.; Levicky, R.; Herman, I. P. *Nano Lett.* **2003**, 3, (11), 1603-1606.
39. Yin, Y.; Alivisatos, A. P. *Nature* **2005**, 437, (7059), 664-670.
40. Puentes, V. F.; Krishnan, K. M.; Alivisatos, A. P. *Science* **2001**, 291, (5511), 2115-2117.
41. Gonzalo-Juan, I.; Krejci, A. J.; Dickerson, J. H. *Langmuir* **2012**, 28, (11), 5295-5301.
42. Li, H.; Liao, S. *J. Mater. Chem.* **2009**, 19, (29), 5207-5211.
43. Chen, Y.; Liew, K. Y.; Li, J. *Appl. Surf. Sci.* **2009**, 255, (7), 4039-4044.
44. Lou, X. W.; Deng, D.; Lee, J. Y.; Feng, J.; Archer, L. A. *Adv. Mater.* **2008**, 20, (2), 258-262.
45. Ha, D.-H.; Moreau, L. M.; Bealing, C. R.; Zhang, H.; Hennig, R. G.; Robinson, R. D. *J. Mater. Chem.* **2011**, 21, (31), 11498-11510.

46. Dinega, D. P.; Bawendi, M. G. *Angew. Chem. Int. Ed.* **1999**, 38, (12), 1788-1791.
47. Yin, Y. D.; Rioux, R. M.; Erdonmez, C. K.; Hughes, S.; Somorjai, G. A.; Alivisatos, A. P. *Science* **2004**, 304, (5671), 711-714.
48. Gu, Y.; Jian, F.; Wang, X. *Thin Solid Films* **2008**, 517, (2), 652-655.
49. Talapin, D. V.; Murray, C. B. *Science* **2005**, 310, (5745), 86-89.
50. Yu, D.; Wang, C.; Guyot-Sionnest, P. *Science* **2003**, 300, (5623), 1277-1280.
51. Beaulieu, L. Y.; Larcher, D.; Dunlap, R. A.; Dahn, J. R. *J. Electrochem. Soc.* **2000**, 147, (9), 3206-3212.
52. Magasinski, A.; Dixon, P.; Hertzberg, B.; Kvit, A.; Ayala, J.; Yushin, G. *Nat. Mater.* **2010**, 9, (4), 353-358.
53. Yoon, S.; Jo, C.; Noh, S. Y.; Lee, C. W.; Song, J. H.; Lee, J. *Phys. Chem. Chem. Phys.* **2011**, 13, (23), 11060-11066.
54. Liu, X. H.; Zhong, L.; Huang, S.; Mao, S. X.; Zhu, T.; Huang, J. Y. *ACS Nano* **2012**, 6, (2), 1522-1531.

APPENDIX C

F SUPPLEMENTARY INFORMATION FOR CHAPTER 7

Electrochemical Measurement

All the electrochemical performances were tested by using the nanoparticle (NP) films as a working electrode in a Swagelok-type electrochemical cells. The cells were completed by using Li foil as the counter electrode, 1 M LiPF₆ in a 50:50 w/w mixture of ethylene carbonate and diethyl carbonate as an electrolyte, and a polypropylene separator (Celgard 2400) which has 43 nm pore size with 25 μm thickness. The assembling of the cell was carried out in a glove-box with oxygen and water free condition (<2ppm). Galvanostatic electrochemical charge-discharge measurement and cyclic voltammetry were carried out using Maccor series 4000 cycle tester and Solartron analytical cell test model, respectively.

Nanoparticle characterization

TEM images of the nanoparticle samples were obtained using a FEI Tecnai F12 microscope operating at 120 keV. About 200 particles were analyzed for Co and Co₃O₄ nanoparticles to obtain a size distribution. High-resolution TEM (HRTEM) was done by using a FEI Tecnai F20 microscope operating at 200 keV. XRD (X-ray diffraction) spectra were collected using a Scintag theta-theta x-ray diffractometer (Cu K α radiation). SEM images were obtained on a LEO 1550 FESEM at an accelerating voltage of 2 kV.

The thickness analysis

Three Co NP EPD films were prepared with different thicknesses (~470 nm, 1000 nm, and 1500 nm) by controlling the EPD conditions. In order to form the NP films on a flat substrate, the Co NP films were prepared through EPD on silicon wafers which are similar size to the copper current collector used for electrochemical measurements. The thickness of the NP films was measured on initial Co NP EPD film and the same film after oxidation by KLA-TENCOR P10 Profilometer. Three different places of each sample were scanned and averaged.

Tap density and pellet density measurements of mixture

The mixture is made with 80 wt% of our Co_3O_4 NPs and 10 wt% of carbon black (Carbon black super P Conductive, Alfa Aesar) and 10 wt% of PVDF (Polyvinylidene fluoride, Sigma-Aldrich). The mixture was ground with pestle and mortar for 20 minutes before the density measurement. The tap density measurement was carried out as the method reported.^{1,2} The NP mixture was placed in a small cylinder and tapped for 15 minutes by hand. Then the density is calculated based on the measured volume of the mixture and the Co_3O_4 NP mass. Solvent (NMP, N-methyl-2-pyrrolidone, Sigma-Aldrich) was then added to create a slurry from the mixture, the slurry was dried for 24 hours at 80 °C, and the tap density measurements were repeated. No further increase in density was seen under these dried-slurry conditions.

The density of the dried slurry is also measured after pressed under 160 MPa by a Enerpac hydraulic press.

The contributions from copper oxide.

As a control experiment to standard EPD cobalt oxide NP film, an electrochemical measurement was conducted with a bare copper plate (no NP film) that was treated with the same oxidation process. This heat-treated copper plate shows a capacity of about 255 mAh/g for the first discharge, but drops to 35 mAh/g for the second cycle, and become negligible after several cycles indicating that there is a small contribution to the overall capacity only for first few cycles. (**Figure F.2**) In order to obtain the contributions of copper oxide from **Figure 7.4a** sample, the current rate and weight normalization are calculated based on the **Figure 7.4a** sample's weight. Also there was no significant weight change of copper plate after oxidation process.

Adhesion test

The adhesion test was carried out by using the Scotch tape method (Scotch Magic greener tape, 3M). About 1cm wide tape was attached to the sample films formed on a copper plate and left it for 30 seconds and detached slowly.

The NP film preparation by conventional slurry coating

The Co_3O_4 NP slurry was made by mixing 80% of the Co_3O_4 hollow NPs and 10% of PVDF (Polyvinylidene fluoride, Sigma-Aldrich) binder and carbon black

(Carbon black super P Conductive, Alfa Aesar) in a NMP (N-methyl-2-pyrrolidone, Sigma-Aldrich) solvent dispersant. The slurry is deposited on a copper plate and dry under vacuum for 10 hours at 50 °C.

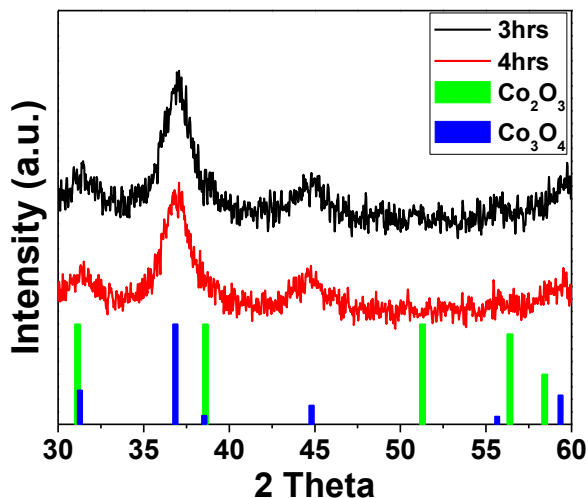


Fig. F.1 XRD of cobalt oxide EPD film which are oxidized for longer time than standard procedure (2hours). The black line and red line show XRD spectra of oxidized for 3 hours and 4 hours respectively. The green bar and blue bar represent the references of Co_2O_3 (JCPDS No. 02-0770) and Co_3O_4 (JCPDS No. 42-1467) respectively.

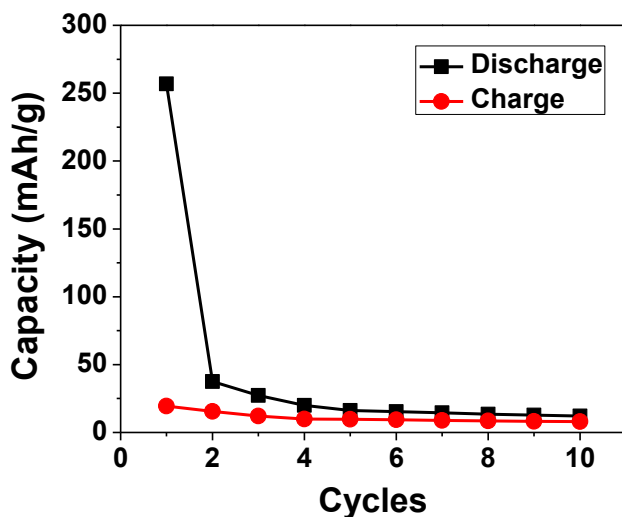


Fig. F.2 Capacity of the oxidized copper plate through cycles. Black line and red line represent the discharge and charge capacity respectively. In order to obtain the contribution of copper oxide from **Fig. 7.4-a** sample, the current rate and weight normalization are calculated based on the **Fig. 7.4-a** sample's weight. Also there was no significant weight change of copper plate after oxidation process.



Fig. F.3 Photographs of bent Co_3O_4 NP films made by EPD, the conventional method, and drop casting. All samples do not show significant cracks by bending up to the curvature with 0.35cm radius.

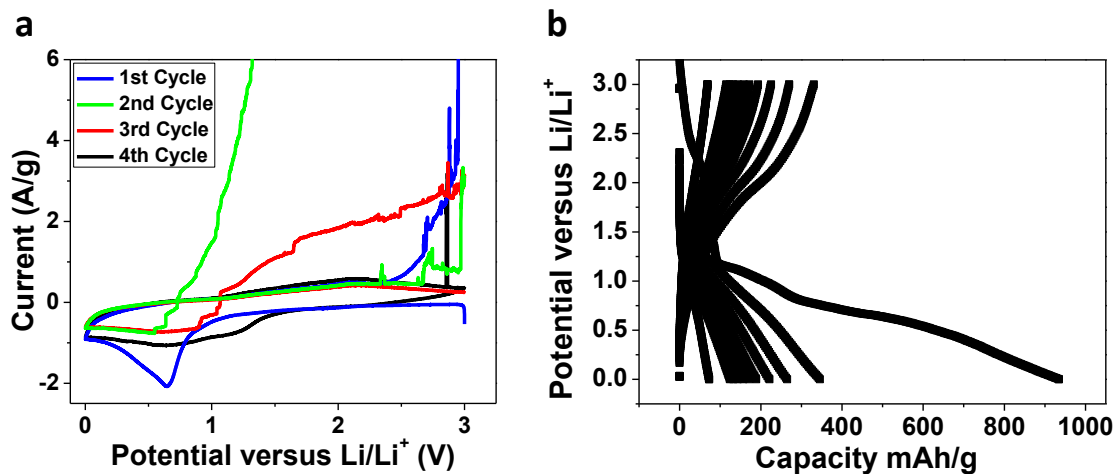


Fig. F.4 Electrochemical performance of drop casted Co_3O_4 NP film without any additives: (a) cyclic voltammogram at 50mV/s (b) Charging-discharging curves at C/20 rate.

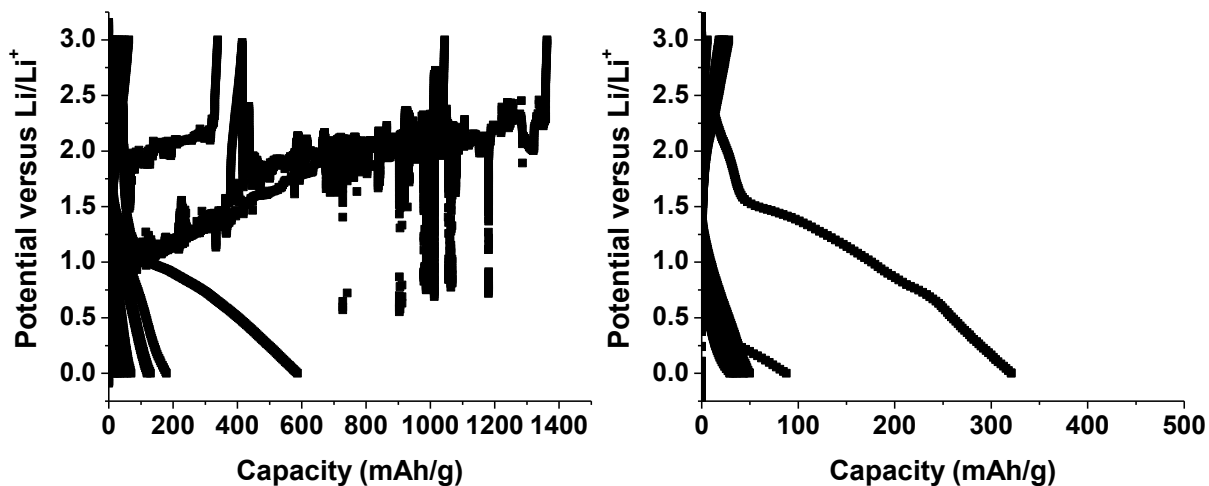


Fig. F.5 Examples of poor galvanostatic charge-discharge curves of drop casted samples. (Left): A sample shows a lot of spikes indicating bad contact between NPs and current collector. (Right): A sample shows small capacity and poor capacity retention. Charging-discharging rate is C/20.

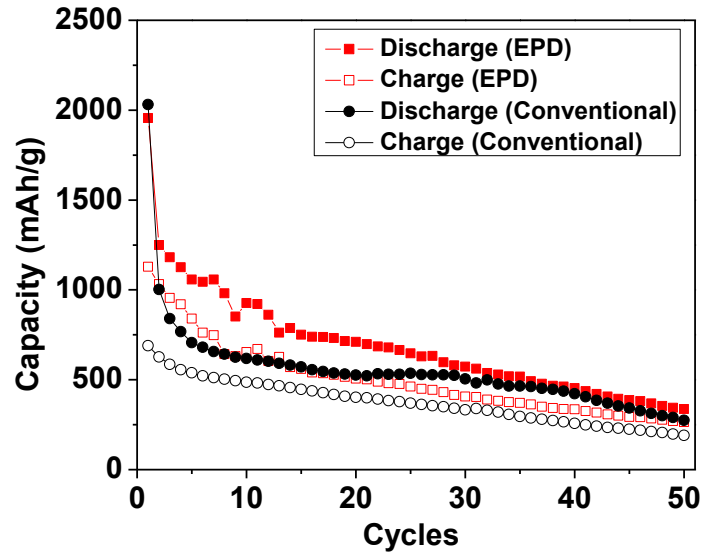


Fig. F.6 The cycle performance of the Co_3O_4 NP films formed by EPD and conventional method with PVDF and carbon black. The charging-discharging rate is $C/5$.

References

1. Sun, C.; Rajasekhara, S.; Goodenough, J. B.; Zhou, F. *J. Am. Chem. Soc.* **2011**, 133, (7), 2132-2135.
2. Qian, J.; Zhou, M.; Cao, Y.; Ai, X.; Yang, H. *J. Phys. Chem. C* **2010**, 114, (8), 3477-3482.

8 CONCLUSIONS AND OUTLOOK

This work was devoted to the synthesis, characterization and utilization of NCs which were chemically transformed. Various pathways for the chemical transformation of NCs were described for the purpose of designing novel NC shapes and phases and for understanding the underlying structural transition mechanisms during such chemical transformations. Kirkendall-hollowed metal oxide and phosphide NCs were synthesized through redox addition transformation routes. The Kirkendall effect in NCs was found to follow a two-step diffusion mechanism which was investigated by several characterization tools including XAS. Unique heterostructured NCs were also synthesized through a cation exchange method in which dual interfaces were created within a spherical NC. This heterostructured NC was found to exhibit a solid-solid phase transformation resulting from cation diffusion and strain at the interfaces. In addition, chemically transformed NCs were combined with the EPD technique, leading to a robust NC film that served as an excellent battery electrode.

8.1 Chemical Transformation of NCs through Redox Addition

First, a stepwise investigation of the structural evolution and the diffusion processes is reported for the chemical transformation from NC ϵ -Co into two successive phases of cobalt phosphide: Co_2P and CoP . This chemical transformation was investigated through a combination of EXAFS, TEM, XRD, SQUID, and DFT calculations. Surprisingly, though both an energetically favored phase change and the

Kirkendall effect are evident, pure phosphide phases are never extant in the NCs, as revealed by EXAFS. Small amounts of excess Co remain, which are undetectable by XRD and magnetic measurements. This residual metal has implications for other nanoscale Kirkendall systems and for the properties of the resulting compounds. Results from EXAFS, TEM, XRD, and density functional theory calculations reveal that the inward diffusion of phosphorus is more favorable at the beginning of the transformation from ϵ -Co to Co_2P by forming of an amorphous Co-P shell, while retaining a crystalline cobalt core. When the major phase of the sample becomes Co_2P , the diffusion processes reverse and atomic cobalt out-diffusion is favored, leaving a void, which is characteristic of the nanoscale Kirkendall effect.

Regarding the synthesis of Ni NCs, unintentional phosphorus (P) doping was found when tri-*n*-octylphosphine (TOP) is used in the coordinating solvent, the use of TOP as a ligand being the most common method for synthesizing monodisperse Ni NCs. The phosphorus doping via TOP of the Ni NCs increases as a function of synthetic temperature and reaction time. This is likely relevant to other synthetic systems which employ TOP and similar strong-binding phosphorus-based ligands, such as triphenyl phosphine. Even with phosphorus content as high as several percent, the crystalline *fcc* Ni lattice is not significantly disrupted. There is, however, a lattice expansion notable in the XRD patterns as a function of at. % P, which enables calculation of the P content of the NCs based on XRD peak position alone, a useful technique in fine-tuning the synthesis. The structure consists of a crystalline *fcc* lattice with P substitutional atoms and distortion only of the Ni atoms surrounding the P substitutional sites. This unintentional P doping significantly impacts the NC

structural behavior, magnetic properties, and catalytic activities, which we have demonstrated through both the experimental and modeled phenomena. The results of this study suggest that the effects of such unintentional doping should be taken into consideration in optimizing NCs for use in applications, and that there may be a significant concentration of XRD-amorphous species present in the NCs, which may interfere with desired properties. Thus, care should be taken when using strong binding surfactant ligands such as TOP in the synthesis of NCs, particularly when they are used in high concentrations.

In the case of nickel phosphide NCs, the structural distinctions between amorphous and crystalline Ni₂P NCs were studied using XAS, XRD, and inductively coupled plasma (ICP). XAS results reveal a significant P concentration in the amorphous NC samples – placing the stoichiometry close to Ni₂P - despite XRD results, which show only *fcc* Ni contributions. By comparing the long-range structural order from XRD to the short-range radial structure from EXAFS we conclude that both techniques are necessary to obtain a complete structural picture of amorphous and crystalline NC phases. Phases are not detectable by XRD when their offsets (deviations) from bulk inter-atomic distances have a standard deviation as high as ~4.82. Phases with lower standard deviation (e.g. <~1.19), however, are detectable by XRD. The possible presence of amorphous phases should be considered when using XRD alone for NC characterization. The results of our study suggest that amorphous phases may be present within NCs that are not detectable based on XRD; these results may apply to a wide range of colloidal NC syntheses.

Finally, the oxidation process from ϵ -Co NCs to two phases of cobalt oxide (CoO and Co₃O₄) was investigated. The phase transition of the NCs occurs through oxidation in air at 200 °C. During this chemical transformation from ϵ -Co to CoO, the single-crystal spherical ϵ -Co NCs convert to polycrystalline hollow CoO NCs due to the nanoscale Kirkendall effect. This morphology remains as the NCs transform, during further heating in air, to the Co₃O₄ phase. The Co₃O₄ NCs can be redispersed in an organic solvent by adding surfactants, thus rendering a method to create solution-processable colloidal, monodisperse Co₃O₄ NCs. DFT calculations and experimental results suggest that a two-step diffusion process is responsible for the Kirkendall hollowing of ϵ -Co into CoO NCs similar to the previously described Co-P system. The first step is O in-diffusion by an indirect exchange mechanism involving interstitial O and vacancies of type I Co sites of the ϵ -Co phase. This indirect exchange mechanism of O has a lower energy barrier than a vacancy-mediated diffusion of O through type I sites. When the CoO phase is established the Co then diffuses outward faster than the O diffuses inward, resulting in a hollow NC. The NC lattice adopts preferred orientations after the single crystalline ϵ -Co NCs are transformed to polycrystalline CoO NCs and Co₃O₄ NCs. The Co₃O₄ NCs possess a high ratio of {110} surface planes, which are known to have favorable catalytic activity.

Knowledge about these transformation methods and structural properties provides a means to tailor the synthesis and composition of the NCs to facilitate their use in applications. In addition, these reports suggest that advanced characterization

techniques such as XAS are crucial to fully resolve the complex atomic structures of the NCs during chemical transformations.

Future research initiatives for the chemical transformation study involving redox diffusion routes can be listed as follows:

- The redox addition of metal NCs has been mainly focused on metal oxides, sulfides, selenides, and phosphides. The conversion reactions from metal NCs to metal carbide or nitride NCs are not well established yet. Generally, the synthesis of metal carbide NCs and nitride NCs requires high temperatures which obfuscates a direct-synthesis approach, but a conversion reaction may provide a low-energy pathway since nuclei formation would not require high reaction temperatures.
- The redox addition reactions were generally focused on the route from metal to metal oxide, phosphide, and sulfide. On the contrary, reduction reactions to convert metal oxide, phosphide, or sulfide NCs back to metal NCs are not well-investigated. Reduction conversions might provide insights to further understand the diffusion mechanisms in NCs.
- During the chemical transformation of NCs, metastable phases or architectures such as Co/Co-P (core/shell) NC were obtained by isolating the intermediate sample. These peculiar NC structures might provide enhanced properties such as electrocatalytic activity since the

amorphous phosphide shell can stabilize the metal core and prevent leaching during the catalytic process. Focus on the various applications of these unique NCs might be the proper means by which to accelerate this research.

- XAS was used to resolve the local atomic structure of NCs during chemical transformations. However the electronic structure of these NCs was not fully determined due to the limitations of the XAS technique. XES (X-ray emission spectroscopy) might be the ideal tool to elucidate the electronic structure, as it can provide valuable information such as local charge- and spin-density. Detailed features of the electronic structure of NC samples during chemical conversions will unlock numerous unknowns such as how the oxidation state of transition metals evolves through chemical transformations. Moreover, the XES technique will allow us to understand the magnetic properties of NCs at the intermediate stages in various chemical transformations.

8.2 Heterostructured NCs through Cation Exchange

Dual interface formation in NCs was demonstrated using a cation exchange reaction to create epitaxial heterostructures within spherical NCs. The heterostructure consists of a copper sulfide layer capped with zinc sulfide (ZnS) grains in spherical NCs and can be tuned by controlling the extent of the cation exchange reaction. This unconventional heterostructure serves as a new route to creating confined 2D layers in

NCs. The cation exchange reaction can effectively produce a 2D atomic layer of copper sulfide within a ZnS NC with epitaxial interfaces between the two materials, and this heterostructure can be a template for investigating unique phenomena in NCs, such as 2D hole gases or 2D quantum wells. During the cation exchange reaction from copper sulfide to zinc sulfide, a solid-solid phase transformation of the copper sulfide phase occurs in the heterostructured NCs. As the cation exchange reaction is initiated, Cu ions replaced by Zn ions at the interfaces are accommodated in intrinsic Cu vacancy sites present in the initial roxbyite ($\text{Cu}_{1.81}\text{S}$) phase of copper sulfide, causing a phase transition to djurleite ($\text{Cu}_{1.94}\text{S}$)/low chalcocite (Cu_2S), which is a more thermodynamically stable phase than roxbyite. This result demonstrates that ion diffusion generated by a cation exchange reaction can initiate a solid-solid phase transition and control the phase of the NCs. The minimization of strain energy in the heterostructured NC then induces a second phase transition back to roxbyite, which forms a better-matched epitaxial interface with zinc sulfide than does djurleite or low chalcocite. The observation of a solid-solid phase transformation in our unique heterostructured NCs provides a new method to control desired phases and an insight into the influence of cation exchange on nanoscale phase transitions in heterostructured materials.

Future research initiatives for the cation exchange reaction creating heterostructured NCs can be listed as follows:

- This strategy of designing heterostructures in NCs might be applicable to other cation species, in addition to Zn, that form wurtzite-structured phases in the cation exchange reaction with roxbyite copper sulfide. NCs exhibiting different capping materials in such a sandwich-like morphology with a copper sulfide layer will yield distinct plasmonic behaviors compared to the NCs with ZnS capping due to the change in dielectric constant of capping material. In addition, new capping materials will lead to a different electronic band alignment allowing a wider tunability of optical and electronic properties.
- This cation exchange was carried out mainly on 22 nm sized copper sulfide NCs. The same reaction for copper sulfide NCs of other sizes will provide insights to resolve the kinetics of the cations during the cation exchange process since the time it takes to convert from roxbyite to Cu_2S would depend on the size of the initial copper sulfide NCs.
- Aligning the orientation of these heterostructured NCs in aggregate will be the key to optimizing the properties of the sandwiched NCs since the properties are strongly dependent on direction (vertical vs. horizontal orientation of the roxbyite layer). Such alignment of the heterostructured NCs may be possible with electrophoretic deposition techniques.

8.3 Additive-Free NC Film for Battery Electrodes

A new fabrication method for NC assemblies was developed for use in Li-ion battery electrodes that requires no additional mechanical support or conductive materials such as polymeric binders or carbon black. Removing additives is an effective means to reduce the weight and volume of batteries. This method employs colloidal synthesis techniques to produce spherical, monodisperse cobalt metal NCs, which are solution-processable. The key solution-processing technique to obtain excellent battery performance for the NC films is electrophoretic deposition (EPD). EPD binds the metal NCs to the surface of the electrode and to each other in an assembly; the Co NCs are subsequently converted to Co_3O_4 NCs with a polycrystalline hollow structure. This NC-film battery made without binders and conductive additives shows high gravimetric (>830 mAh/g) and volumetric capacities (>2100 mAh/cm³) even after 50 cycles. The EPD film exhibits superior mechanical stability relative to other films fabricated by drop-casting or by conventional slurry methods. The electrochemical properties are optimized when the film is 1 μm thick. By scraping off the NCs from the current collectors, the morphology change can be studied after lithiation and delithiation. A stable particle size of 5 – 10 nm is retained through the lithiation/delithiation cycling. Due to the absence of additive materials this method can provide a good template system to investigate the physical mechanisms and reactions during charge/discharge. This system provides opportunities to use colloidal NCs for battery electrodes in a simple and robust manufacturing process.

Future research initiatives for the additive free NC film for battery electrodes can be listed as follows:

- The electrochemical performance of cobalt oxide NC films is limited by the thickness due to low electronic conductivity. To overcome the limitation of the NC film thickness, doping might be a good solution for these cobalt oxide NC films. Ni or Cu doping is common for Co_3O_4 thin films. Such doping might be feasible for cobalt oxide NCs as well by reacting them with Ni and Cu salt precursors.
- With the current set-up and procedure, only metal and metal oxide NCs are viable for creating NC films without additives because of the oxidation step. This system could be extended to a wider range of materials if other techniques for removing organic ligands, such as a ligand exchange process with short inorganic ligands or a $(\text{NH}_4)_2\text{S}$ treatment, are employed.
- The underlying mechanism for the EPD technique with NCs is still unclear. Comprehensive, fundamental studies of the EPD of NCs might be crucial to optimize deposition conditions and enhance the controllability of such features as the thickness and density of the NC films fabricated by EPD. One parameter might be the solvent. By controlling the polarity of the solvent, conductivity of the whole deposition system can be altered, which may lead to different deposition rates.